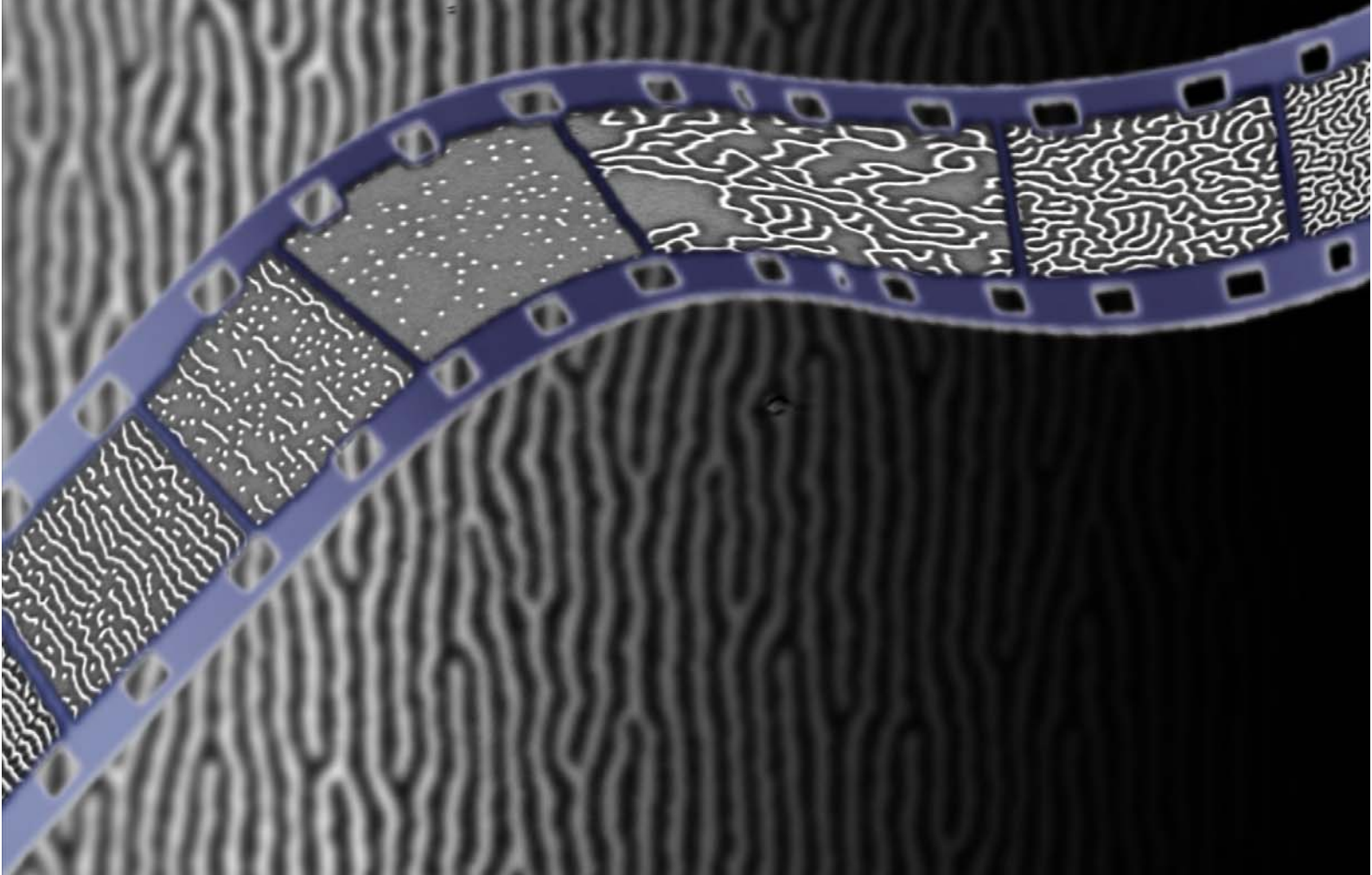


# **The Relation Between Magnetic Hysteresis and the Micromagnetic State**

**Explored by Quantitative  
Magnetic Force Microscopy**



**Nicolas Pilet**



THE RELATION BETWEEN  
MAGNETIC HYSTERESIS  
AND THE MICROMAGNETIC STATE  
EXPLORED BY  
QUANTITATIVE MAGNETIC FORCE  
MICROSCOPY

A thesis submitted in accordance with the requirement  
of the University of Basel for the degree of

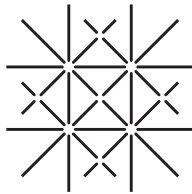
DOCTOR OF PHILOSOPHY

in the Faculty of Philosophy and Natural Science

by

**Nicolas Pilet**

from Rossinière (Vaud), Switzerland



UNI  
BASEL

Genehmigt von der Philosophisch-Naturwissenschaftlichen Fakultät auf  
Antrag von

Prof. Dr. H. J. Hug  
Prof. Dr. H.-J. Güntherodt  
Prof. Dr. G. Güntherodt

Basel, den 19. December 2006

Prof. Dr. Jacob Wirz  
Dekan

*"Le savant n'étudie pas la nature parce que cela est utile;  
il l'étudie parce qu'il y prend plaisir  
et il y prend plaisir parce qu'elle est belle.  
Si la nature n'était pas belle,  
elle ne vaudrait pas la peine d'être connue,  
la vie ne vaudrait pas la peine d'être vécue."*

HENRI POINCARÉ

*"I am among those who think that science has great beauty.  
A scientist in his laboratory is not only a technician:  
he is also a child placed before natural phenomena  
which impress him like a fairy tale."*

MARIE CURIE



# CONTENTS

<i>List of Acronyms and Symbols</i> . . . . .	v
<i>Introduction and Outline</i> . . . . .	1
<b>1. Introduction to Magnetism</b> . . . . .	5
1.1 Dia, Para and Ferromagnetism . . . . .	5
1.2 Relevant Energy Terms . . . . .	8
1.2.1 Exchange energy . . . . .	8
1.2.2 Magnetostatics . . . . .	11
1.2.3 Magnetocrystalline anisotropy . . . . .	13
1.2.4 Magnetoelastic energy . . . . .	14
1.2.5 Zeeman . . . . .	16
1.3 Domains in Ferromagnetic Systems . . . . .	17
1.3.1 The origin of domains . . . . .	17
1.3.2 The domain walls . . . . .	18
1.4 Magnetic Hysteresis Loops . . . . .	22
1.4.1 Magnetisation reversal . . . . .	24
1.4.2 Energies and Magnetic Loop . . . . .	28
1.5 Defects and Domain Wall Motion . . . . .	28
1.6 Magnetism in Thin Films . . . . .	30
1.6.1 Magnetic moment . . . . .	30
1.6.2 Surface lattice constant . . . . .	31
1.6.3 Strain . . . . .	32
1.6.4 Surface magnetic anisotropy . . . . .	33
1.6.5 Inhomogeneous magnetisation . . . . .	34
1.6.6 Summary . . . . .	35
1.7 Nickel . . . . .	36
1.8 Magnetocrystalline Anisotropy . . . . .	38
1.9 Energies Summary . . . . .	38
<b>2. Measurement Methods</b> . . . . .	41
2.1 Introduction to SPM . . . . .	41
2.1.1 Basics of dynamic mode microscopy . . . . .	43

2.2	Introduction to MFM . . . . .	45
2.2.1	Introduction to quantitative MFM . . . . .	46
2.2.2	Calculation of the stray field . . . . .	46
2.2.3	Principles of contrast formation . . . . .	51
2.3	Vibrating Sample Magnetometry . . . . .	58
2.4	LTSFM . . . . .	60
2.4.1	UHV system . . . . .	61
2.4.2	Microscope . . . . .	61
2.4.3	Electronics . . . . .	63
2.5	hr-MFM . . . . .	64
2.6	Tip Preparation . . . . .	66
2.6.1	EBID tip with Fe coating . . . . .	67
2.6.2	ISC tip with Co coating . . . . .	68
<b>3.</b>	<b><i>Cu/Ni(200nm)/Cu/Si(100), a Not So Simple System</i></b> . . . . .	<b>71</b>
3.1	Cu/Ni/Cu : a Well Studied System Yet to Reveal All its Secrets . . . . .	71
3.1.1	Ni films, an interesting system . . . . .	71
3.1.2	Previous studies on Cu/Ni/Cu . . . . .	72
3.1.3	Revisiting magnetometry data . . . . .	74
3.2	Instrumentation and Film Growth . . . . .	74
3.2.1	Instrumentation . . . . .	74
3.2.2	Growth of the film . . . . .	75
3.3	Quantitative Magnetic Force Microscopy . . . . .	76
3.3.1	Simulation of various magnetisation patterns . . . . .	76
3.3.2	Comparison and summary . . . . .	78
3.4	Magnetometry . . . . .	79
3.4.1	Standard interpretation . . . . .	80
3.4.2	Detailed analysis . . . . .	80
3.5	Magnetic Force Microscopy as a Complimentary Method . . . . .	82
3.6	CuNiCu Revisited . . . . .	84
3.7	Conclusions . . . . .	87
<b>4.</b>	<b><i>Tuning the Strain in NiSi with irradiation</i></b> . . . . .	<b>91</b>
4.1	Introduction . . . . .	91
4.1.1	Polycrystalline Ni films . . . . .	91
4.1.2	Tuning anisotropy with ion irradiation . . . . .	91
4.2	Experimental . . . . .	92
4.3	Results . . . . .	95
4.3.1	The effects of irradiation . . . . .	95
4.3.2	Annealing . . . . .	102
4.4	Conclusion and Outlook . . . . .	104



<b>5. Effect of Ion Irradiation on Domains in Ni Films</b> . . . . .	107
5.1 Introduction . . . . .	107
5.1.1 Magnetic hysteresis . . . . .	107
5.1.2 Ion irradiated Ni films at low temperature . . . . .	107
5.2 Instrumentation and Film Growth . . . . .	108
5.3 Results . . . . .	108
5.4 Discussion and Conclusions . . . . .	112
<b>6. Magnetic Return Point Memory</b> . . . . .	113
6.1 The Importance of Magnetic Memory . . . . .	113
6.2 Definitions . . . . .	114
6.2.1 Magnetic return point memory . . . . .	114
6.2.2 Magnetic complementary point memory . . . . .	115
6.3 Previous Works on Return and Complementary Point Memory . . . . .	115
6.4 Experimental . . . . .	118
6.5 Statistical Study on RPM and CPM . . . . .	120
6.5.1 Nucleation field . . . . .	121
6.5.2 Pre-saturation field . . . . .	126
6.6 RPM and CPM Determined from Cross Correlations . . . . .	128
6.6.1 RPM/CPM dependance on defect density . . . . .	130
6.7 The Difference of RPM at Nucleation and Pre-saturation Fields . . . . .	131
6.7.1 Domain wall motion path . . . . .	131
6.7.2 Minor loops . . . . .	133
6.8 Conclusion and Outlook . . . . .	136
<b>7. CoPt Nanodots</b> . . . . .	139
7.1 Nanodots, a Route to Higher Density Recording Media . . . . .	139
7.2 Method . . . . .	140
7.3 Results and Discussion . . . . .	143
7.4 Conclusions . . . . .	145
<b>8. Conclusion and Outlook</b> . . . . .	147
<b>Bibliography</b> . . . . .	168
<b>Acknowledgments</b> . . . . .	169
<b>Appendix</b> . . . . .	171
<b>A. Mathematical Definition</b> . . . . .	173
<b>B. Magnetocrystalline Anisotropy : Supplementary</b> . . . . .	175

---

<i>C. Micromagnetics of Domain Walls</i> . . . . .	177
<i>D. Handy Hints for qMFM in SXM</i> . . . . .	179
D.1 Calibration . . . . .	179
D.2 Simulation . . . . .	184
D.3 Tip Field . . . . .	185
<i>E. Magnetometry Data on Ni/SiO<sub>2</sub>/Si(100)</i> . . . . .	189
<i>F. RPM and CPM influenced by field cooling</i> . . . . .	191
<i>G. Complementary Images Taken on Nanodots</i> . . . . .	193
<i>Publication and Presentation List</i> . . . . .	197
<i>Curriculum Vitae</i> . . . . .	199



## LIST OF ACRONYMS AND SYMBOLS

$A$	exchange stiffness constant	J/m
$\vec{B}$	induction field	T
$B_{s,v}$	surface, volume magnetoelastic anisotropy coefficient	$\frac{J}{m^3}$
$c_L$	force constant	N/m
$\text{Cov}(a, b)$	covariance of $a$ and $b$	
$D$	domain width	nm
$E_{\text{exch}}$	exchange energy	J
$E_{\text{mc}}$	magnetocrystalline energy	J
$E_{\text{me}}$	magnetoelastic energy	J
$E_{\text{ms}}$	magnetostatic energy	J
$E_Z$	Zeeman energy	J
$f_0$	free resonance frequency	Hz
$\vec{H}$	magnetic field	A/m
$H_c$	coercive field	A/m
$(H_{c.n})$	domain wall nucleation coercivity	A/m
$(H_{c.m})$	domain wall motion coercivity	A/m
$\vec{H}_d$	demagnetising field	A/m
$\vec{H}_{\text{ext}}$	external applied field	A/m
$H_{\text{molec}}$	molecular field	A/m
$H^{\text{sat}}$	saturation field	A/m
$\vec{k}$	position vector in 2D-Fourier space = $(k_x, k_y)$	
$k$	magnitude of $\vec{k}$	1/nm

*continued on next page ...*

... continued from previous page

$K_{\text{eff}}$	effective anisotropy coefficient	$\frac{\text{J}}{\text{m}^3}$
$K_{\text{mc}}$	magnetocrystalline anisotropy coefficient	$\frac{\text{J}}{\text{m}^3}$
$K^{\text{s}}$	surface anisotropy coefficient	$\frac{\text{J}}{\text{m}^3}$
$K_{\varepsilon}$	magnetoelastic anisotropy coefficient	$\frac{\text{J}}{\text{m}^3}$
$M$	magnetisation	A/m
$M_{\text{s}}$	saturation magnetisation	A/m
$m$	normalised magnetisation $m = M/M_{\text{s}}$	
$\vec{n}$	direction normal to the sample plane	
$P_{\text{coinc}}$	probability of occurrence by coincidence	
$P_{\text{occur}}$	probability of occurrence	
$P_{\text{occur}}^{\text{min/max}}$	maximum/minimum probability of occurrence	
$t$	film thickness	nm
$x_i$	i refers to internal parameter	
$x_o$	o refers to external parameter	
$x_{\perp}, x^{\perp}$	$\perp$ refers to the perpendicular component	
$x_{\parallel}, x^{\parallel}$	$\parallel$ refers to the parallel component	
$x, y, z$	coordinates	nm
$\Delta f$	frequency shift	Hz
$\delta_{DW}$	domain wall width	nm
$\varepsilon$	strain	
$\phi$	irradiation fluence	$\frac{\text{ions}}{\text{cm}^2}$
$\mu_0 =$	$4\pi \cdot 10^{-7}$	$\frac{\text{V}\cdot\text{s}}{\text{A}\cdot\text{m}} = \frac{\text{H}}{\text{m}}$
$\nabla$	nabla operator	
$\theta_c$	closure angle	$^{\circ}$
$\theta_r$	ripple angle	$^{\circ}$
$\rho(a, b)$	cross correlation of $a$ and $b$	
$\sigma_{DW}$	domain wall energy density	$\frac{\text{mJ}}{\text{m}^2}$
$\sigma_{m,tip}^*(\vec{k})$	tip transfer function	A · m
$\sigma_P$	standard deviation of a given probability	

**Tab. 0.1:** List of most relevant symbols used in this thesis.

---

AFM	Atomic Force Microscopy
CPM	Complementary Point Memory
EBID	Electron Beam Induced Deposition
FFT	Fast Fourier Transform
hr-MFM	High Resolution Magnetic Force Microscope (Swissprobe <sup>©</sup> )
ICF	Instrument Calibration Function
LEED	Low Energy Electron Diffraction
LT	Low Temperature
LTSFM	Low Temperature Scanning Force Microscope (UNIBAS)
MBE	Molecular Beam Epitaxy
MFM	Magnetic Force Microscopy
ML	Monolayer
MOKE	Magneto-Optical Kerr Effect
PLL	Phase-Locked Loop
PMMA	Poly(methyl methacrylate)
PMA	Perpendicular Magnetic Anisotropy
PPMS	Quantum Design Physical Properties Measurement System
qMFM	Quantitative Magnetic Force Microscopy
RBS	Rutherford Backscattering Spectroscopy
RHEED	Reflection High Energy Electron Diffraction
RPM	Return Point Memory
RT	Room Temperature
SEM	Scanning Electron Microscopy
SFD	Switching Field Distribution
SFM	Scanning Force Microscopy
SNR	Signal to Noise Ratio
SPM	Scanning Probe Microscopy
STM	Scanning Tunneling Microscopy
TEM	Transmission Electron Microscopy
UHV	Ultra High Vacuum
VSM	Vibrating Sample Magnetometry
(GI)XRD	(Grazing-Incidence) X-ray Diffraction

**Tab. 0.2:** List of acronyms used in this thesis.



## INTRODUCTION AND OUTLINE

Since the discovery of magnetic lodestones in 600 BC described by ancient Greek philosophers, the mystery of magnetism has continued to intrigue. For thousands of years, these lodestones were more of a curiosity until medieval explorers discovered how to use them to produce a magnetic compass. The compass was studied and explained by William Gilbert in his 1600 treatise on magnetism called "de Magnete"<sup>1-3</sup>. In his work, Gilbert proposed the Earth itself to be magnetic, helping to open up the modern field of magnetism. Only at the start of the nineteenth century was magnetism discovered to be due to elementary magnets analogous to how matter is made up of atoms and molecules. This idea was then developed further by Pierre-Ernest Weiss in 1907<sup>4</sup>, who discovered that these elementary magnets grouped together in ferromagnets to form magnetic domains. In 1933, these domains were experimentally confirmed by Barkhausen<sup>5</sup> after observing that magnetisation was a discontinuous process. He amplified the sound produced by these discontinuous jumps and attributed it to domain switching. In a contemporary study, Bitter developed a technique using a suspension of magnetic colloids to visualise the domains<sup>6</sup>. Domain switching was subsequently found to be lacking as an explanation of magnetisation by Langmuir in 1931<sup>7</sup>, who proposed that the propagation of the walls surrounding the domains was responsible for the magnetisation reversal. This domain wall motion also explained the appearance of hysteresis which characterises the tendency of a magnetic system to behave differently depending on its field history. The study of hysteresis really took off with the advent of magnetometry. These experimental techniques are capable of measuring the average magnetisation of a system as a function of applied field. One of these, vibrating sample magnetometry (VSM), was invented in 1959<sup>8</sup> and has been used ever since as the principle means of accessing a systems magnetic parameters. Since VSM is an volume averaging technique, the microscopic nature of domains remained elusive until the advent of magnetic force microscopy (MFM) in 1987<sup>9</sup>. This powerful technique can image the magnetic field emanating from the surface which gives much needed information about the magnetisation for 100's nm below the surface. This is therefore especially useful when studying magnetic thin films.

The widespread use of magnetic thin films in contemporary data storage

technology, sensors of magnetic field, strain and acceleration, has been made possible by the optimisation of the materials involved, aimed at attaining specific magnetisation structures and hysteresis curve characteristics. However the understanding at the microscopic scale of the reversal process remains a challenge.

This thesis presents a study of magnetism in thin films, more specifically thin films with **perpendicular magnetic anisotropy** (PMA). These magnetic thin films with an easy axis of magnetisation perpendicular to the surface have attracted particular attention due to their potential advantage in high-density magnetic recording media<sup>10–13</sup>. Magnetic thin films with PMA also provide a model system of domain behaviour in a wide variety of materials. More particularly, thin films of nickel have been shown to be of great interest because of their intrinsic magnetic properties favouring PMA<sup>14–17</sup>.

The origin, advantages and removal of PMA in thin films are investigated in this thesis. While both Chapters 3 and 4 present studies of the origin of PMA in nickel films, Chapter 3 explains how the conventional interpretation of the magnetisation loops can give an incorrect picture of both the magnetisation processes and magnetic domain structures in the films. The observations defy explanation based on volume averaged magnetometry measurements but come to light when magnetometry is combined with **quantitative magnetic force microscopy** (qMFM). qMFM revealed a specific magnetisation pattern, namely perpendicular stripe domains with closure caps. Furthermore, the domain wall is shown to be as important as the domain itself in the average magnetisation. These new findings come from using the well established method of magnetometry complimented by the latest qMFM techniques. Chapter 4 concentrates on how ion irradiation can be used to remove PMA. Furthermore, it shows how temperature variation can be used to control the perpendicular component of the magnetisation.

A common theme through this thesis is the coercivity of the ferromagnetic film. **Hysteresis** lies at the very foundation of the magnetic recording industry<sup>10,12</sup>. Hysteretic systems are employed as recording media because they retain their magnetic state for a long period after a writing operation, namely they exhibit **magnetic memory**. This memory has been extensively studied and exploited. However, despite decades of intense study and significant recent advances<sup>18,19</sup>, a fully satisfactory microscopic understanding of magnetic hysteresis is still lacking<sup>20,21</sup>. The origin of hysteresis and its relation to the micromagnetic state has been studied in Chapters 3, 4 and 5. Our novel results show how **domain wall motion** can be hysteresis free (Chapter 3 and 4).

**Domain nucleation** and wall motion were studied in more detail in Chapter 4, in which we show that increasing the defect density does not necessarily increase the hysteresis. Indeed, it can even decrease it by acting on the domain nucleation and therefore on the domain density. The low pinning action of the



---

domain wall is shown to be due to the small size of the domain, implying short distance to travel for the domain wall to allow the magnetisation reversal. Thus, the hysteresis is shown to depend strongly on the micromagnetic domain structure and particularly on the domain width.

The **reproducibility** of the domain nucleation and wall motion is a key factor in microscopic memory<sup>20</sup> and is studied in Chapter 6. The effect of defects on this microscopic reproducibility is shown to be more complicated than the common understanding. We show that defects act as nucleation centres for domains during the magnetisation reversal. This implies a good reproducibility of the way domains nucleate after saturation. On the other hand, defects also act to break up the domains while a demagnetised sample is brought towards saturation. This decreases the reproducibility of the domain evolution on a minor loop excursion.

Chapter 7 presents a study of a perpendicular magnetised array of nanoislands. This has been previously proposed with a view to high density recording media<sup>10</sup>. The hysteresis of such systems has to be characterised and controlled. We show that decreasing the island size under 50 nm increases the coercivity distribution, to detriment of their archival potential.

In summary, this thesis presents novel information about the mechanism leading to hysteresis and the related micromagnetic state. Yet, it also improves the understanding of magnetic measurements two folds. It highlights the danger of quick interpretation of magnetometry. Moreover, it presents a novel way of using state-of-the-art qMFM.





# INTRODUCTION TO MAGNETISM

The goal of this chapter is to introduce some concepts useful for interpreting the results presented in this dissertation. It should not be regarded as an in-depth discussion on magnetism. Although it is well known that “Magnetism” is inherently a quantum mechanical phenomena, discussion about energies in a thermodynamical way is enough to explain most of the results in this thesis. Therefore the definition of the magnetic energies will mainly be considered. The reader interested in a more complete description of magnetism can consult the following excellent texts (in order of complexity)<sup>22, 23, 18, 24</sup>.

## 1.1 Dia, Para and Ferromagnetism

Magnetism at the atomic scale can arise from two different origins, the orbital motion of the electron and the electron spin for incompletely filled orbitals (Hund’s rule). In metals like Fe, Co, Ni or oxides like  $\text{Fe}_3\text{O}_4$  or NiO, the magnetic moment ( $\mu_b$ ) is largely given by the spin<sup>25</sup>. In presence of an external magnetic field ( $\vec{H}$ ), two basic effects can be described<sup>26</sup> : **diamagnetism** and **paramagnetism**. The first of these is a consequence of Faraday’s Law of induction : the external magnetic field induces a current, which in turn induces a magnetic field, directed opposite to the external field. This is called the diamagnetic effect. The diamagnetic moment created by an external field is negative relative to this field. The second effect occurs if there is a resultant nonzero magnetic moment in the atom (spin moment, orbital moment or both). In such a case, the external field tends to orient the intrinsic atomic magnetic moment in its own direction, resulting in a positive moment parallel to the field. This is the paramagnetic moment. It is clear from the definition that all substances possess diamagnetism. However, it is not always possible to see it as in many instances, the effect is masked by a more powerful paramagnetic effect. The **magnetisation** ( $\vec{M}$ ) is defined as the magnetic moment per unit volume. Since the magnetisation is proportional to  $\vec{H}$ , diamagnetic and paramagnetic materials can be described by a constant called **magnetic**

**susceptibility** ( $\chi$ ) which is defined as follows :

$$\chi = \frac{\vec{M}}{\vec{H}}. \quad (1.1)$$

By definition,  $\chi$  is negative/positive for diamagnetic/paramagnetic materials, respectively. Since the thermal agitation acts against the external field lining up the spins, the susceptibility depends on the temperature. The higher the temperature, the lower the magnetisation for a certain external field. For the susceptibility in the paramagnetic case ( $\chi_p$ ), this behaviour is given by the Curie Law

$$\chi_p = \frac{C}{T} \quad (1.2)$$

where  $C$  is the Curie constant and  $T$  is the temperature.

The induction field  $\vec{B}$  is defined as the resultant field (external field plus material induced field) :

$$\vec{B} = \mu_0(\vec{H} + \vec{M}) \quad (1.3)$$

where  $\mu_0 = 4\pi \cdot 10^{-7}$  H/m is the permeability of free space. A material can also be described by its permeability which is defined as :

$$\mu = \frac{\vec{B}}{\vec{H}} \quad (1.4)$$

Both paramagnetism and diamagnetism are called “weak magnetisms” since the external field only has, at room temperature, a weak effect in aligning the moments. Indeed, the thermal energy is large relative to the magnetic energy.

Further important magnetic behaviours can arise from the interaction between the atomic moments. In some cases the situation is such that, from the point of view of these interactions, the spontaneous formation of atomic magnetic ordering in the material is energetically favourable. Indeed, this ordering may exist even without external field and can occur in different ways (see figure 1.1). The most simple ordering is to have all atomic moments parallel aligned. This is called **ferromagnetism**. Another common case is to have atomic moments aligning in an antiparallel way, therefore called **antiferromagnetism**.

*Ferromagnetism* : The aligned atomic moments give rise to a spontaneous magnetic moment called the **saturation magnetic moment**. The internal interaction tending to line up the magnetic moment is called the **exchange field, molecular field** or **Weiss molecular field**. Even if the exchange field is not a “real” magnetic field (field corresponding to a current density), one can use it as an equivalent magnetic field “ $H_{\text{molec}} = \lambda M$ ”. The magnitude of

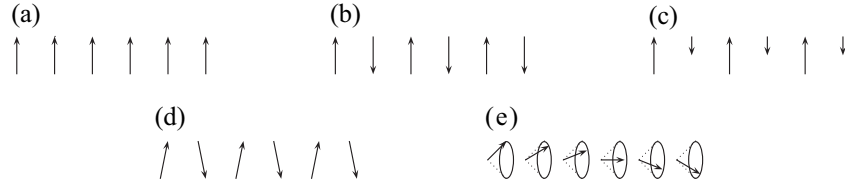


**Fig. 1.1:** Different ordering of atomic magnetic moments : (a) Ferromagnet, (b) Antiferromagnet, (c) Ferrimagnet, (d) Canted antiferromagnet and (e) Helical spin array.

this equivalent field can be as big as  $\mu_0 H_{\text{molec}} \approx 10^3 \text{ T}$  and is much larger than external fields in normal conditions. The orienting effect of the exchange field is in competition with thermal agitation. Above a certain temperature, the **Curie temperature** ( $T_C$ ), the spontaneous magnetisation vanishes, as the spin order is destroyed. Thus, the sample changes from ferromagnetic phase to paramagnetic phase at  $T_C$  for increasing temperature. The temperature dependance of the susceptibility for ferromagnetic material no longer follows the Curie Law but the Curie-Weiss Law:

$$\chi_p = \frac{C}{T - T_c}. \quad (1.5)$$

It can be seen that, at  $T_C$ , the susceptibility is infinite. Therefore, a finite magnetisation can exist for a zero field (spontaneous magnetisation).

*Antiferromagnetism* : As seen previously, in an antiferromagnet the spins are ordered in an antiparallel arrangement with zero net magnetic moment. However, as in a ferromagnet, the temperature play a key role. The antiferromagnetic order is cancelled for a temperature above the “**Néel temperature**” ( $T_N$ ). The susceptibility of a antiferromagnet is not infinite at the Néel temperature, but has a knee, as shown in Fig. 1.2(c).

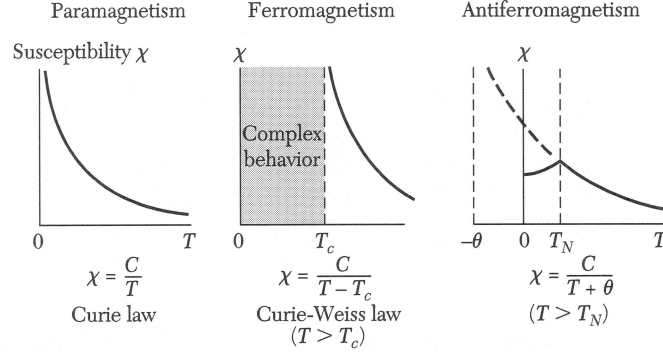


**Fig. 1.2:** Temperature dependence of the magnetic susceptibility in (a) paramagnets, (b) ferromagnets and (c) antiferromagnets. For antiferromagnets, the susceptibility has a maximum value at  $T_N$  where there is a well defined kink in the curve of  $\chi$  versus  $T$ <sup>22</sup>.

## 1.2 Relevant Energy Terms

In magnetism, as in all natural phenomena, the ground state is the one minimising the total energy. Therefore, it is crucial to distinguish and understand the relevant energies involved in magnetic materials. We describe here these energies.

### 1.2.1 EXCHANGE ENERGY

As seen previously, parallel alignment of atomic moments can be explained by the molecular field. This description is convenient in order to understand the situation but it does not explain the origin of this coupling between two atomic moments. Furthermore, to explain the strength of the alignment, this molecular field must be of the order of  $10^9 \frac{\text{A}}{\text{m}}$  corresponding to  $B = 10^3 \text{ T}$ , larger than any man-made field. The mechanism of this strong exchange interaction is not simply a magnetic interaction but an electronic interaction and can only be explained by quantum mechanics<sup>23(chap. 4&5), 24(chap. A1&A2)</sup>. Two cases must be considered separately :

- Ionic solids and insulators where the electronic states of the ions are highly localised and may be treated as atomic states.
- Covalent bonds and metallic solids where charge is delocalised from each of the atomic sites and builds up between atoms.

### *Ionic solids and insulators*

The coupling between two atomic moments in ionic solids is induced by two different interactions. The first one is the **Coulomb interaction**, expressed as  $\frac{e^2}{4\pi\epsilon_0 r_{12}}$ , where  $r_{12}$  refers to the distance between the electrons 1 and 2. The second one is related to the fermionic character of the electron, which implies the **Pauli exclusion principle**. When the electrons are well localised the Pauli principle can be taken into account by introducing an exchange energy term in the Hamiltonian, called the “Heisenberg exchange interaction” ( $E_{exch} = -2\mathcal{J}_{ij} \sum_{i<j}^{nn} \vec{S}_i \vec{S}_j$ , where  $i$  and  $j$  label spins on different atomic sites and  $\mathcal{J}_{ij}$  is the exchange energy of two electrons in state  $i$  and  $j$ ). Without entering into detail, it is useful to know that the exchange energy is of the order of  $10^{-20} \frac{\text{J}}{\text{atom}}$  ( $0.05 \frac{\text{eV}}{\text{atom}}$ ). This is consistent with a Curie temperature of  $T_C \sim 600 \text{ K}$ . By considering the energy of a particular atom,  $i$ , interacting with its  $j$  nearest neighbours, the energy becomes  $E_{exch}^i = -2\mathcal{J} S_i \cdot \sum_j S_j$ . The entire material energy is  $E_{exch} = \sum_i E_{exch}^i$ . This representation of the energy suggests that the energy is composed by a magnetic moment ( $\mu_m$ ) proportional to  $S_i$  in an effective field ( $H_{molec}$ ), also called **Weiss molecular field**, proportional to  $\sum_j S_j$ . Thus, the discrete pairwise interactions can be replaced by assuming that the magnetic moment at site  $i$  ( $\mu_m^i := g\mu_B S_i$ ), interacts with  $H_{molec}$ . The latter is given by the net effect of the nearest neighbour spins :

$$H_{molec} = \frac{2\mathcal{J}}{\mu_0 g \mu_B} \sum_j S_j, \quad (1.6)$$

and the exchange energy by :

$$E_{exch}^i = \mu_0 \mu_m^i \cdot H_{molec} = \mu_0 g \mu_B S_i H_{molec}. \quad (1.7)$$

In conclusion the molecular field is a Coulomb interaction that occurs in systems whose wavefunctions obey the Pauli exclusion principle.

### *Covalent bonds and metallic solids*

In the case of metals the situation is much more complicated. The electrons cannot be considered as localised anymore. These electrons are called **itinerant electrons** and the magnetism caused by them is called **itinerant magnetism**. The picture of local magnetic moments in individual atoms is not valid anymore and the magnetic moments per atom are smaller than the pure spin moment given by Hund’s first rule. For example, the magnetic moment of nickel per atom is  $0.6 \mu_B$ , instead of  $2 \mu_B$ . Since atoms are brought together to form a solid, the electronic levels broaden into bands\*. Therefore, exchange

---

\* The electronic states are continuous within the band.

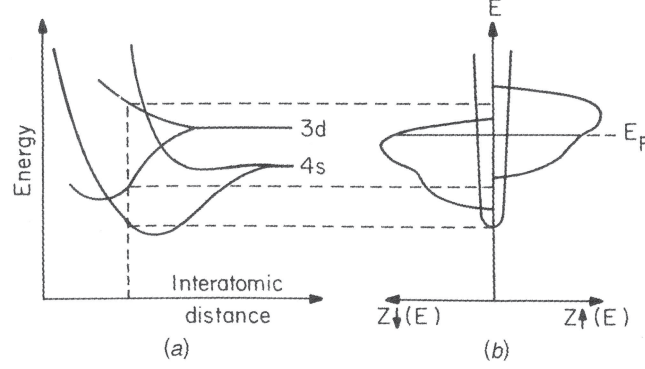


**Fig. 1.3:** (a) Evolution of electronic 4s and 3d states at large interatomic spacing to bands at smaller spacing. (b) Density of states of 4s and 3d states shifted to reflect exchange preference for spin of one direction<sup>23</sup>.

in metals is usually modeled by band structure calculations (see Fig. 1.3(a)). A shift between the spin up and spin down bands (Fig. 1.3(b)) induces an exchange interaction. An easy way to understand magnetic exchange in metals is to consider an equivalent to Hund's first rule : electrons fill states with parallel spins first. This minimises their Coulomb repulsion because they occupy different orbital states, having minimal spacial overlap. However, there is a cost to putting all electrons in the spin up band to satisfy Hund's rule. That cost is greater as the states in the band are spread over a broader energy range. Therefore, there is a competition between exchange energy gain  $\mathcal{J}$  (shifting the spin subbands relative to each other, thus favouring parallel spins) and kinetic energy cost (in favour of paired spins). This competition, schematically shown in Fig. 1.3(b), is expressed quantitatively as the **Stoner criterion** for the occurrence of magnetism in band-like systems :  $\mathcal{J}(E_F)Z(E_F) > 1$ . We can conclude that ferromagnetism is favoured in systems with strong exchange integrals (strong Coulomb effects) and large density of state at the Fermi energy. One can write the exchange energy density as following :

$$e_{exch} = A \left( \frac{\partial \theta}{\partial x} \right)^2 \xrightarrow{3D} A \sum_{i=1}^3 \left( \frac{\nabla M_i}{M_s} \right)^2, \quad (1.8)$$

with  $A$  the exchange energy constant (value for Ni in table 1.1).



## 1.2.2 MAGNETOSTATICS

*Demagnetising field*

When a magnetised sample has surfaces through which flux lines emerge with a normal component, “free poles” exist at the end of the surfaces creating a magnetic dipole. Depending of the shape of the sample, the closing path of least energy of this dipole is through the sample (see Fig. 1.4(a)&(b)).

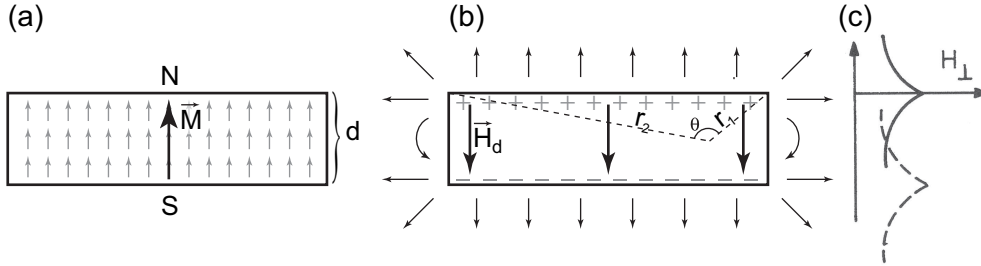


**Fig. 1.4:** (a) Magnetic dipoles inside a magnetised sample. (b) Free magnetic monopoles at surfaces and field lines that they give rise to. (c) Variation of the amplitude of the perpendicular component of the internal field with position inside the sample<sup>23</sup>.

This field,  $\vec{H}_d$ , going from the north pole to the south pole inside the sample is called the **demagnetising field** (since it opposes the magnetisation that set up the dipole). This dipole can be expressed as  $q_m \cdot d$  where  $d$  is the distance between the two magnetic monopoles ( $q_m$ ) (also called **magnetic charges**). The magnetic surface charge density is given by the component of the magnetisation normal to the surface :  $\sigma_m = \vec{M} \cdot \hat{n}$ , where  $\hat{n}$  is the unit vector normal to the surface. Figure 1.4(b) shows the case of a flat magnetically charged sample of infinite length in direction normal to the paper and finite length in the plane of the paper. The field component parallel and perpendicular to the charged surface are given by<sup>23</sup> :

$$H_{i,\parallel} = \frac{\sigma_m}{2\pi} \ln \frac{r_2}{r_1} \quad (1.9)$$

$$H_{i,\perp} = \frac{\sigma_m}{2\pi} \theta, \quad (1.10)$$

where  $r_1$ ,  $r_2$  and  $\theta$  are defined in Fig. 1.4(b). Note that the parallel field vanishes in the middle of the surface ( $r_1=r_2$ ) and that the internal perpendicular field very close to the surface is given by  $H_{i,\perp}(\theta = \pi) = \frac{1}{2}\vec{M} \cdot \hat{n}$ . Since, for a very thin film, the internal demagnetising field is the addition to the field produced by both poles, it's equal to  $-M$ . For a thicker sample the internal field from each surface drops off with distance from the surface. The

dependance is given in figure 1.4(c). The demagnetising field is the strongest near the surface charges and the weakest in the middle. To have a complete overview of the magnetostatic situation, it is necessary to consider the Maxwell's equations to derive the boundary conditions. Considering the interface between the media 1 and 2,  $\vec{\nabla} \cdot \vec{B} = 0$  implies<sup>23</sup>  $(\vec{B}_2 - \vec{B}_1) \cdot \hat{n} = 0$  and therefore  $(\vec{H}_2 - \vec{H}_1) \cdot \hat{n} = (\vec{M}_1 - \vec{M}_2) \cdot \hat{n}$ . From  $\vec{\nabla} \times \vec{H} = \vec{J}$  it results that  $\hat{n} \times (\vec{H}_1 - \vec{H}_2) = \vec{K}$ , where  $\vec{K}$  is the interfacial current density. In other terms, across an interface between two media with different magnetic properties, the normal component of the induction is always continuous ( $\vec{B}_{\perp,1} = \vec{B}_{\perp,2}$ ) and the tangential component of the field is continuous if there is no surface currents ( $\vec{H}_{\parallel,1} = \vec{H}_{\parallel,2}$ ).

To sum up, for a general thickness, assuming the sample is magnetised perpendicular to the surface and very close to the interface, we have<sup>23</sup> :

$$\begin{aligned} \text{inside : } H_i &= -\frac{M_i}{2} \quad \& \quad \text{outside : } H_o = \frac{M_i}{2} \\ \implies B_i &= \mu_0(H_i + M_i) = \mu_0 \frac{M_i}{2} \quad \& \quad B_o = \mu_0(H_o + \underbrace{M_o}_0) = \mu_0 \frac{M_i}{2} \end{aligned}$$

If an external field  $H_{ext}$  is applied to change  $M_i$  its magnitude adds to  $H_i$  and  $H_o$ .

$$\begin{aligned} H_i &= H_{ext} - \frac{M_i}{2} = H_{ext} - H_d \quad \& \quad H_o = H_{ext} + \frac{M_i}{2} \\ B_i &= \mu_0 \left( H_{ext} + \frac{M_i}{2} \right) = B_o. \end{aligned}$$

Far from the sample, there is only the external field. If the sample is thick, inside the sample, the demagnetising field is lower and therefore the internal field bigger than a point close to the interface.

### Energy

In the case of a flat sample\* the energy can be given by equation 1.11.

$$\frac{E_{ms}}{V} = e_{ms} = -\mu_0 \vec{M}_i \cdot \vec{H}_d = -\mu_0 M_i H_d \cos\theta = \frac{1}{2} \mu_0 M_i^2 \cos^2\theta, \quad (1.11)$$

where  $e_{ms}$  is the density of magnetostatic energy ( $E_{ms}$ ) and  $\theta$  the angle between the magnetisation and the surface. If the magnetisation is perpendicular to the surface, the equation is simply :

$$e_{ms} = \frac{\mu_0}{2} M_i^2. \quad (1.12)$$

---

\* In the general case<sup>23</sup>, one has to take into account the demagnetisation factor  $N$  and the energy is given by  $+\frac{\Delta N}{2} \mu_0 M_s^2 \cos^2\theta$ .

### 1.2.3 MAGNETOCRYSTALLINE ANISOTROPY

#### *Phenomenology of anisotropy*

As it is suggested by the name, the magnetocrystalline anisotropy describes the tendency of a sample to align its magnetisation preferably along one crystallographic axis.

- *uniaxial anisotropy* In the case of a uniaxial anisotropy (i.e. for cobalt), the situation is usually described by the magnetocrystalline energy ( $E_{mc}$ ), written as a series. Note that only even powers have to be taken into account, as opposite ends of a crystal axis are equivalent magnetically.

$$E_{mc} = \sum_{n=1 \rightarrow \infty} K'_n \sin^{2n} \theta = K'_1 \sin^2 \theta + K'_2 \sin^4 \theta + \dots, \quad (1.13)$$

where  $K'_1, K'_2, \dots$  are empirical constants and  $\theta$  is the angle between the magnetisation vector and the crystallographic axis\*.

- *cubic anisotropy* In the case of a cubic anisotropy (i.e. for iron or nickel), the situation is more complicated. One has to use the cosines of the magnetisation direction with respect to the cubic axes of the crystal ( $\alpha_1, \alpha_2, \alpha_3$ ) to expand the energy. As in the uniaxial case, only even powers are needed. Furthermore, the  $2^{nd}$  order ( $\alpha_1^2 + \alpha_2^2 + \alpha_3^2$ ) does not contribute, as it is an isotropic term. In addition, thanks to the cubic symmetry, the expression has to be invariant under interchange of  $\alpha_i$ . Therefore, the first term contributing to the anisotropy energy is the  $4^{th}$  order and the second one is the  $6^{th}$  order.

$$E_{mc} = K_1(\alpha_1^2 \alpha_2^2 + \alpha_2^2 \alpha_3^2 + \alpha_3^2 \alpha_1^2) + K_2(\alpha_1^2 \alpha_2^2 \alpha_3^2) + \dots \quad (1.14)$$

Usually, the second term is small and only the first two terms are considered (or even only the first one, for example in the case of iron). The case of nickel is more complex (see section 1.8) and it is necessary to use up to three terms ( $8^{th}$  order).

#### *Origin of the magnetocrystalline anisotropy*

The origin of the magnetocrystalline anisotropy lies in the coupling of the spin part of the magnetic moment to the electronic orbital shape and orientation (spin-orbit coupling), and in the chemical bonding of the orbitals with their local environment (crystalline electric field). If the local crystal field seen by an

---

\*  $n = 0$  can be omitted as it doesn't depend on the angle and therefore is not useful to describe the anisotropy.

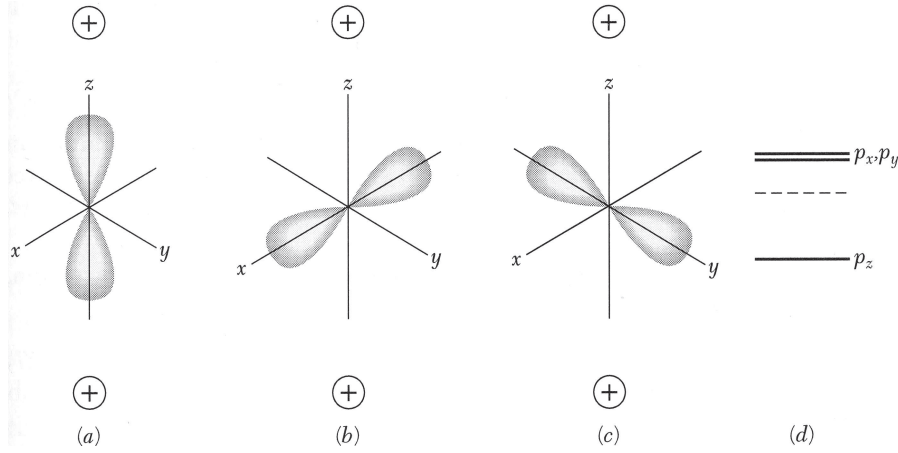


**Fig. 1.5:** An orbital momentum  $L = 1$  is placed in the uniaxial crystalline electric field of the two positive ions along the  $z$  axis. In the free atom, the states  $m_L = \pm 1, 0$  have identical energies. In the crystal, the atom has a lower energy when the electron cloud is close to positive ions (a), than when it is oriented midway between them, as in (b) and (c)<sup>22</sup>. If the spin-orbit coupling ( $\vec{L} \cdot \vec{S}$ ) is appreciable, the spin also prefers a particular crystallographic directions and the material exhibits a strong anisotropy.

atom is of low symmetry and if its bond electrons have an asymmetric charge distribution ( $L_z \neq 0$ ), then the atomic orbitals interact anisotropically with the crystal field (Fig. 1.5). It means that certain orientations are energetically favourable. Furthermore, if there is coupling between the direction of the spin and the orbital angular momentum, the spin also prefers a specific orientation relative to  $\vec{L}$ .

While applying a field rotated relative to the crystal, if the spin-orbit coupling is strong, the torque on the spin due to the field may also act on the orbital moment. When the crystal is of low symmetry, a very large magnetocrystalline anisotropy results. A large field may cause large anisotropic strains. This phenomena is called **magnetostriction**.

#### 1.2.4 MAGNETOELASTIC ENERGY

##### *Origin of magnetoelastic energy*

The magnetoelastic energy is nothing else than the magnetocrystalline energy coupled to the strain, as introduced above (magnetostriction). Lets investigate the case where temperature variation is the origin of the strain (see figure 1.6(a)). The dot/dashed line shows the normal behaviour of a non magnetic material (linear dependance of the length versus the temperature). The dashed line is shifted to illustrate the volume expansion that accompanies

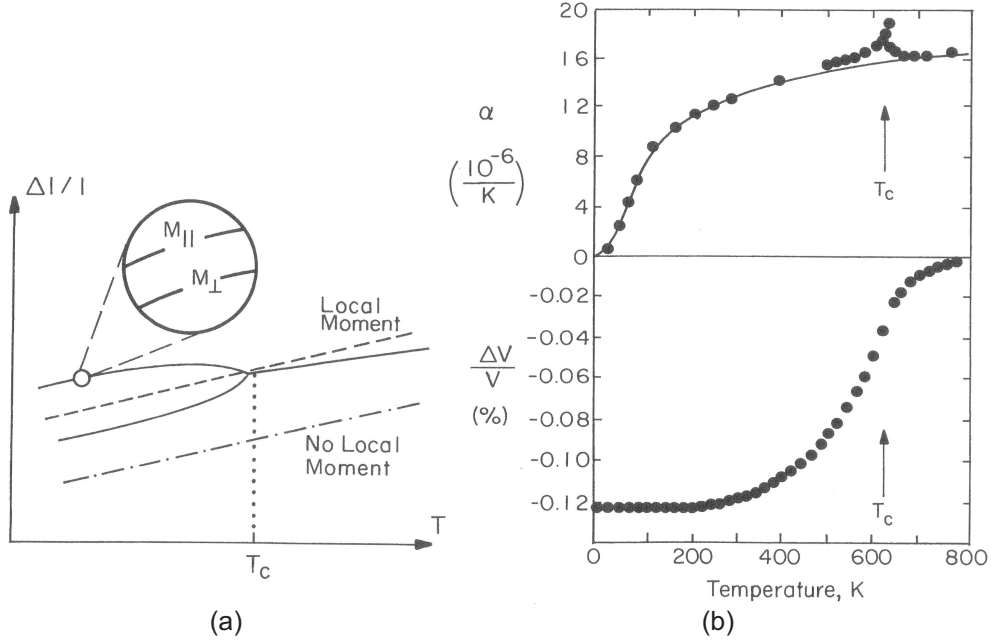


**Fig. 1.6:** (a) Schematic of the thermal expansion of a magnetic material. The circle inset shows the small anisotropic strain depending on the magnetisation direction (only below  $T_c$ ). (b) Thermal expansion and volume expansion coefficient of Ni<sup>23,27</sup>.

the formation of a local magnetic moment. Finally the solid line shows the dependance while raising the temperature from below to above the Curie temperature. It can be seen that because the local magnetic moment does not vanish immediately above  $T_C$ , but merely loses its long range ordering, the internal volume expansion associated with it does not vanish completely above  $T_C$ . Whereas below  $T_C$ , additional magnetovolume effects due to long range magnetic ordering are turned on. They may add or subtract from the volume expansion due to the presence of a local moment. Figure 1.6(b) shows the case for nickel. The lower graph shows the volume expansion  $\omega = \frac{\Delta V}{V}$  versus temperature and the top graph shows the linear coefficient of linear expansion  $\alpha = \frac{\Delta l}{l} \frac{1}{\Delta T}$  versus the temperature. It is noteworthy that the fractional volume deficit at 4.2 K relative to the extrapolated high temperature ( $T \gg T_c$ ) volume is of the order of  $-0.12\%$ . In addition to these isotropic effects called **volume magnetostriction**, a smaller anisotropic strain can be seen below  $T_c$  (Fig. 1.6(a) circle inset). This magnetisation orientation dependant strain ( $\lambda = \frac{\Delta l}{l}$ ) is called **Joule magnetostriction** or **anisotropic magnetostriction**. To describe anisotropic magnetostriction in a material one can refer to its dimensionless magnetostrictive constant ( $\lambda_s$ ), the strains produced at mag-

netic saturation, or its magnetoelastic coupling coefficients ( $B_{ij}$  [Pa or N/m]), the magnetic stresses causing  $\lambda_s$ .

The inverse effect is of great importance for this thesis. Stressing or straining a magnetic material can produce a change in its preferred magnetisation direction. This is called **piezomagnetism** or **stress-induced anisotropy**. Whereas it is easy to magnetise a material in the tensile stress direction ( $\sigma > 0$ ) if  $\lambda_s$  is positive, it is harder to magnetise the material if  $\sigma > 0$  and  $\lambda_s < 0$  and if  $\sigma < 0$  and  $\lambda_s > 0$ .

Naturally, the magnetostrictive constant is different along the three crystallographic directions in the case of a non-isotropic material. For example in Ni,  $\lambda_{100} = -46 \cdot 10^{-6}$  and  $\lambda_{111} = -25 \cdot 10^{-6}$ . Thus, magnetising nickel contracts the crystal in the magnetisation direction. The contraction is bigger in the  $\langle 100 \rangle$  direction.

In a very similar way to the magnetocrystalline anisotropy, this strain dependant component of the energy, the **magnetoelastic energy** ( $E_{me}$ ), can be expressed as a series. Equation 1.15 gives the first term (second order) valid for cubic material :

$$E_{me} = B_1(\alpha_1^2 \varepsilon_{xx} + \alpha_2^2 \varepsilon_{yy} + \alpha_3^2 \varepsilon_{zz}) + B_2(\alpha_1 \alpha_2 \varepsilon_{xy} + \alpha_2 \alpha_3 \varepsilon_{yz} + \alpha_3 \alpha_1 \varepsilon_{zx}) + \dots, \quad (1.15)$$

where  $\alpha_i$  are the cosines of the magnetisation direction with the three coordinate axes, given by the cubic geometry of the crystal,  $\varepsilon_{ij}$  is the strain tensor and  $B_i$  are the magnetoelastic coefficients. The latter express the coupling between the strain tensor and the direction of the magnetisation, similar to  $\lambda_{100}$  and  $\lambda_{111}$ .

A comparison of the relative energies' importance ( $E_{ms}$ ,  $E_{mc}$  and  $E_{me}$ ) is given for nickel in Sect. 1.9. It must be said that magnetostriction coefficients are temperature-dependant. For example, nickel magnetostriction decreases with increasing temperature. The variation is quite small for temperatures lower than room temperature, but it becomes important for higher temperatures ( $400 \text{ K} \rightarrow T_c = 627 \text{ K}$ )<sup>23(chap. 7.6)</sup>.

### 1.2.5 ZEEMAN

The Zeeman energy is the potential energy of a magnetic moment in a field, or for a large number of moments the potential energy per unit volume :

$$e_Z = -\mu_0 \vec{M} \cdot \vec{H} = -\mu_0 M H \cos\theta, \quad (1.16)$$

where  $\theta$  is the angle between the magnetisation and the applied magnetic field.

## 1.3 Domains in Ferromagnetic Systems

At temperatures below the Curie temperature, ferromagnets should exhibit a magnetic moment equal to the saturation moment. However, in reality, an external field may be needed to drive the sample to saturation, due to the presence of domains. Although the electronic magnetic moments are aligned on a very small scale, different regions of magnetisation direction can exist. These are called **domains**, and in each domain, the magnetisation is saturated. For example, if domains with magnetisation oriented up and down exist and if the area covered by both domains is equal, the overall magnetisation is zero (Fig. 1.7b,c&d).

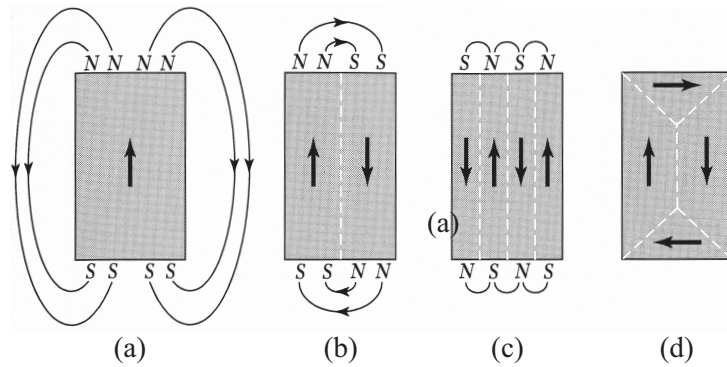


**Fig. 1.7:** Schematics showing how domain nucleation minimises the magnetic energy.

### 1.3.1 THE ORIGIN OF DOMAINS

Domain structures arise from the possibility of lowering the magnetostatic energy of a system by going from a saturated configuration with high magnetic energy to a domain configuration with a lower energy. Figure 1.7 shows how domain formation can minimise the magnetostatic energy. Case 1.7(a) shows a single domain with a high magnetostatic energy due to the large distance the field has to travel outside the sample in order to close the field lines. In other words, this high energy is due to the accumulation of magnetic charges at the extremities of the domain. Splitting this domain in two domains magnetised in opposite directions Fig. 1.7(b) reduces the magnetostatic energy by approximately a factor of two. In Fig. 1.7(a)-(c), the magnetic energy is reduced by a factor  $1/N$  ( $N$  is the number of domains) because of the reduced spatial extension of the field<sup>22, 23(chap. 2.6.3), 28</sup>.

Going from Fig. 1.7(a)→(c), the formation of domains decreases the magnetostatic energy but also costs energy via the creation of a change of mag-

netisation angle by  $180^\circ$  (see Sect. 1.3.2). The width of the domains is given by the point where adding a domain wall costs more than the gain in the magnetostatic energy. We consider here only  $180^\circ$  domains since they are relevant for the discussion of the results presented in this thesis. Note that the magnetic anisotropy cost can be kept low by having domains oriented with other angles\*.

### 1.3.2 THE DOMAIN WALLS

Various types of domain wall structure exist. Although some are complicated, we focus here on simple structures only. However, one must keep in mind that domain structures always arise from the possibility of lowering the energy of a system, by going from a saturated configuration with high magnetic energy to a domain configuration with a lower energy.

#### *Bloch walls*

Although forming a domain by a  $180^\circ$  domain wall costs no anisotropy energy, it does incur a large exchange energy cost. This energy cost can be diminished by having transition regions between two domains which are not infinitely small<sup>†</sup>. This transition, called **Bloch wall**, is represented in figure 1.8. Here,

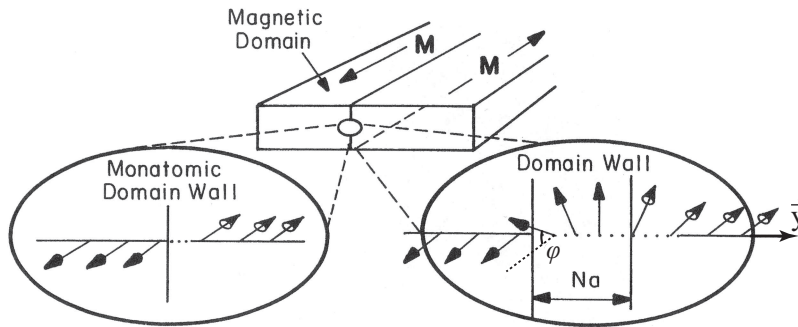


**Fig. 1.8:** Schematics representing a monatomic  $180^\circ$  domain wall versus Bloch domain walls. The energy of the second case can be three orders of magnitude smaller than in the first case<sup>23</sup>.  $N$  is the number of spins necessary to rotate  $180^\circ$  in the second case.

\* Indeed, in materials of cubic anisotropy, when  $\langle 100 \rangle$  direction is the easy axis ( $K_1 > 0$ ), a  $90^\circ$  domain does not cost magnetic anisotropy energy (for symmetry reasons). In the case of nickel (cubic anisotropy with  $\langle 111 \rangle$  being the easy magnetisation axis),  $109^\circ$  and  $71^\circ$  domains do not cost any magnetic anisotropy energy.

<sup>†</sup> An infinitely small transition region supposes a change of magnetic moment direction across a single atomic plane.



the exchange energy is lower when the change is distributed over many spins. From Sect. 1.2.1, we know that the energy cost to have a transition of  $\varphi^\circ$  between two spins is :

$$E_{exch} = -2J\vec{S}_1\vec{S}_2 = -2JS^2\cos\varphi, \quad (1.17)$$

where  $J$  is the exchange energy and  $\vec{S}_i$  design the spin vectors.

If we assume that transition region is spread over a large number of spins, the angle between each spins is very small and  $\cos\varphi = 1 - \frac{1}{2}\varphi^2$ . If  $N$  steps are needed to change the direction by  $\pi$ , the exchange energy is given by :

$$E_{exch,ij} \simeq \text{constant} + JS^2\left(\frac{\pi}{N}\right)^2. \quad (1.18)$$

By considering that the wall is formed by  $N$  spin pairs (each with the same relative angular deviation) and that each line of spins occupies an area  $a^2$  on the wall surface (Fig. 1.8), the energy density can be calculated :

$$\sigma_{exch} \approx \frac{NE_{exch,ij}}{a^2} = JS^2\frac{\pi^2}{Na^2} \quad (1.19)$$

It is clear from Eqn. (1.19) that a wall with larger surface area is favourable in term of exchange energy. However, it costs anisotropy energy<sup>23</sup> ( $\sigma_{anis} = KNa$ ). The equilibrium wall width is given by the minimisation of the sum of the two energy densities:

$$\sigma_{tot} = \sigma_{exch} + \sigma_{anis} \approx JS^2\frac{\pi^2}{Na^2} + KNa \quad (1.20)$$

where  $K$  is the anisotropy energy. Minimising  $\sigma_{tot}$  versus  $N$  gives the domain wall thickness :

$$\delta_{DW} \approx Na = \pi\left(\sqrt{\frac{A}{K}}\right), \quad (1.21)$$

where  $A = \frac{JS^2}{a}$  is the exchange stiffness (in the order of  $10^{-11} \frac{\text{J}}{\text{m}}$ ). This estimation gives a domain wall thickness from 10 nm in high anisotropy systems (such as permanent magnets) to  $0.2 \mu\text{m}$  in systems with small anisotropy. The wall energy density is then given by :

$$\sigma_{DW} \approx 2\pi\left(\sqrt{AK}\right). \quad (1.22)$$

This energy is of the order of  $0.1\text{--}1 \frac{\text{mJ}}{\text{m}^2}$ .

The above calculations assume the magnetisation to be uniform through-

out the sample. In order to determine the magnetisation dependence through the wall thickness, it is useful to allow  $\varphi$  to be a function of the position. A micromagnetic calculation has to be performed to minimise the energy on a local (microscopic) scale. This calculation was done by R.C. O'Handley<sup>23(chap. 8.2)</sup>. The derivation takes into account the anisotropy and the exchange term (c.f. Eqn. (1.8)), function of  $\varphi$  and  $(\frac{\partial\varphi}{\partial y})^2$ , respectively ( $y$  and  $\varphi$  are define in Fig. 1.8). It gives

$$\varphi(y) = \arctan \left[ \sinh \left( \frac{\pi y}{\delta} \right) \right] + \frac{\pi}{2}. \quad (1.23)$$

A simulation for the case of a 200 nm thick Ni film is given in figure 3.2(a). The definition of  $\delta$ , given by the distance between the intersections of the linear fit of  $\varphi$  at  $\varphi = \frac{\pi}{2}$  and  $\varphi = \{0, \pi\}$ , is represented on the graph. In this model the wall thickness is still given by Eqn. (1.21) whereas the wall energy is given by :

$$\sigma_{DW} = 4\sqrt{AK}. \quad (1.24)$$

A 3D simulation of the magnetisation orientation through the domain wall is also plotted in figure 3.2(b). A description of how to consider Bloch domain walls in magnetic force microscopy is given in section 3.3.1.

### *Domain closure*

So far, only the exchange energy and anisotropy energy have been considered. To have a better understanding, the magnetostatic energy must also be considered. Indeed, since inside Bloch walls the component of the magnetisation perpendicular to the surface is not zero, an accumulation of charge exists and therefore the magnetostatic energy is not zero. Minimising this energy can be achieved by having a **domain closure**<sup>22,23,29</sup>. Figure 1.7(d) shows the situation of a domain closure and images of such a wall are presented in figure 1.10(b). Due to the closure, the flux circuit is fully inside the sample and therefore no magnetic field is associated with the magnetisation. Indeed, no component of the magnetisation is normal to the surface, meaning that there is no accumulation of magnetic charges. Therefore, there is no demagnetising field and the magnetostatic energy in this case is zero. This configuration is favourable in term of magnetostatic energy but costs magnetic anisotropy energy. The domain closure can exist if the induced magnetic anisotropy energy is lower than the canceled magnetostatic energy. We will see in Chap. 3 that the closure domain may exhibit more complicated structures, and a quantitative study of such structures will be presented. Section 3.3.1 presents a method to simulate domain closure in the perspective of a qMFM experiment.

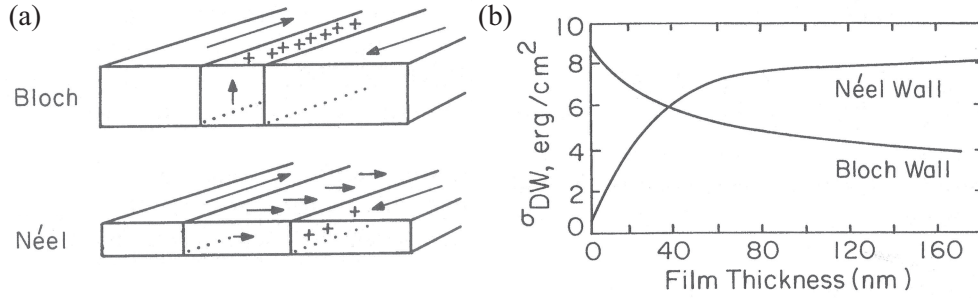


**Fig. 1.9:** (a) Schematics representing Bloch and Néel walls with their magnetic charges. Bloch walls have charged external surfaces and Néel wall have charged internal surfaces. (b) Energy density of Bloch and a Néel walls as a function of the film thickness<sup>23</sup>.

### Néel walls

In a sample with a highly anisotropic geometry (thin film), another possibility to minimise the magnetostatic energy exists.  $E_{ms}$  can be decreased if the spins do not rotate out of the plane, but within the thin film surface plane (Fig. 1.9(a)). In this case the wall is called **Néel wall**. Then, a smaller magnetostatic energy at the internal face of the wall is accepted as the price for removing the larger magnetostatic energy at the top surface. Figure 1.9(b) shows a calculation of the energy density for Bloch walls and Néel walls (including the magnetostatic energy) as function of the film thickness. The Bloch wall energy density increases with decreasing film thickness because of the increased magnetostatic energy due to the appearance of charged surface above and below the wall. The Néel wall energy decreases with decreasing film thickness because it is proportional to the area of the charged surface inside the film. Néel walls are observed to be stable in many types of magnetic films for thickness up to 60 nm\*.

### Cross-Tie walls

The last example to be considered in this section is yet another way for the system to minimise the magnetostatic energy. **Cross-Tie walls** can be explained in the same way as domain presence was justified in section 1.3.1. As seen previously, Néel wall implies a magnetostatic energy at the internal faces of the wall. Figure 1.10(a) shows how the magnetic charges existing in a

\* It has been shown<sup>23</sup> that Néel walls can exist near the surface for much thicker films. Inside the film, the wall is Bloch type and near the surface they depart from the Bloch formation by gradually folding over to lie in the plane of the surface, in order to reduce the magnetostatic energy.

Néel wall can give rise to cross-tie wall. To avoid having too much magnetic charge the polarisation of the wall can alternate, that is to say, the magnetic moment can rotate alternatively “clockwise” and “counterclockwise”. It can be thought of as domains inside the domain wall. Figure 1.10(b), taken by a scanning electron microscope (SEM) with spin polarisation analysis, shows a cross-tie wall in a *NiFe* film. Comparing local magnetisation direction in figures 1.10(a) and (b) gives a good understanding of cross-tie walls.

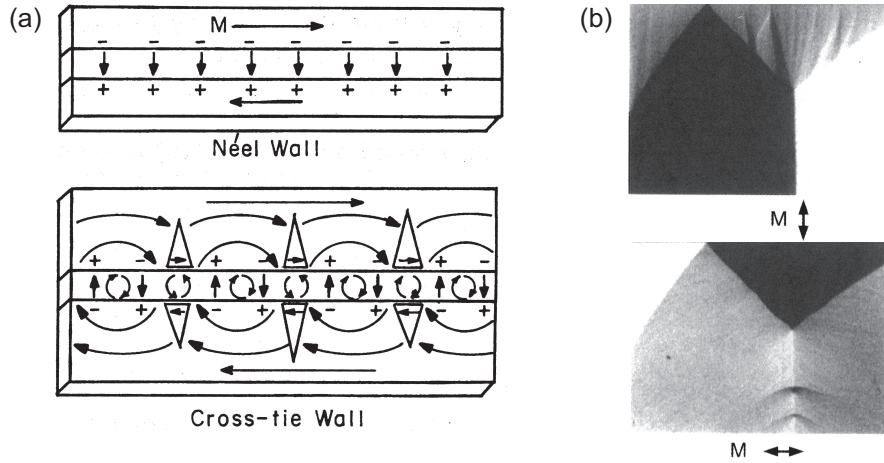


**Fig. 1.10:** (a) (Upper) the charge on a Néel wall. (Lower) the cross-tie wall as a way to minimise the magnetostatic energy. (b) NiFe film imaged by SEM with spin polarisation analysis. The in-plane magnetisation with both vertical and horizontal direction can be addressed: the upper picture shows vertical polarisation contrast; the lower picture shows horizontal polarisation contrast (white is magnetisation to the right, dark to the left and grey vertical). A closure domain with cross-ties on the domain walls can be seen<sup>23</sup>.

## 1.4 Magnetic Hysteresis Loops

Magnetism exhibits a large variety of configurations, depending on the different energy intensities. The evolution of these configurations, while applying an external field, is of great interest. Many of the parameters describing this evolution can be determined by looking at the induction field ( $\vec{B}$ ) dependence on the external field ( $\vec{H}$ ). This function ( $B(H)$ ) is called the **magnetisation curve**, or **hysteresis loop**. Figure 1.11 shows a typical example of such a loop. Important parameters can be extracted from this curve:

- $B_s$ : The saturation induction field is the maximum induction (in a saturated state).

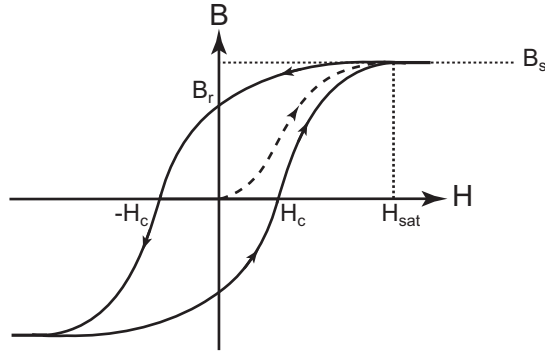


**Fig. 1.11:** Typical hysteresis loop (induction field ( $B$ ) versus magnetic field ( $H$ )) showing  $H_c$ ,  $H_{sat}$ ,  $B_r$  and  $B_s$ . The dashed part represents the start from demagnetised situation (juvenile curve).

- $B_r$ : The remanence induction field is the remanent field after saturation at  $H = 0$ .
- $H_c$ : The coercive field is the field necessary to bring the induction back to zero after the saturation.
- $H_{sat}$ : The saturation field is the field necessary to bring the system to saturation (to have  $B = B_s$ ).

Starting from a demagnetised case ( $H = 0, B = 0$ ), the induction field follows the dashed curve called the **juvenile curve**. Increasing  $H \rightarrow H_{sat}$  brings the system into a saturated state ( $B = B_s$ ). Then  $B$  decreases to zero (for  $H = H_c$ ), changes sign and finally goes into the opposite saturation state when  $H$  is reversed. The  $B(H)$  opening ( $2H_c$ ) comes from an irreversible behaviour while the magnetisation is reversed (It will be seen later that this is mostly due to hindered domain wall motion). This irreversible loop shows an energy loss, given by the area inside the  $B(H)$  curve ( $\int B(H)dH$ ). This is called the **hysteresis loss** and is of the order of  $4B_rH_c$ .

The value of the coercive field ranges over seven orders of magnitude. It is the most sensitive property of ferromagnetic materials. On one hand, some permalloys (*NiFe* alloys) have very low coercive field ( $H_c \approx 1 \frac{\text{A}}{\text{m}}$ )\*. On the other hand, permanent magnets have coercivities in the range of  $10^4$  to  $10^6 \frac{\text{A}}{\text{m}}$ . Materials with low coercivity ( $H_c \lesssim 10^3 \frac{\text{A}}{\text{m}}$ ) are called **soft magnets** and those with high coercivity **hard magnets**, since the magnetisation is easy or difficult to reverse, respectively. Both soft and hard magnets are technologically important. For example, soft magnetic materials are used as field sensors or in transformers where the energy loss has to be small. Hard

\* The earth's magnetic field is about  $30 \frac{\text{A}}{\text{m}}$ .

magnetic materials are used in motor or frictionless bearings. In the field of recording media, materials used are in between these two extremes. They must remain magnetised despite ambient fields from nearby components or electrical currents and yet be reversed by application of a local suitable field  $H > H_c \approx 10^4 - 10^5 \frac{\text{A}}{\text{m}}$ . This thesis mainly concentrates on Ni, a soft magnetic material. For soft magnets, it matters little whether the loop  $M(H)$  or  $B(H)$  is discussed since the shape is essentially the same :  $B = \mu_0(H + M) \propto M$ . In this thesis, we always consider  $M(H)$  loops as we measure the sample properties via magnetometry.

#### 1.4.1 MAGNETISATION REVERSAL

To understand the features of a magnetisation curve, we describe the two possible mechanisms the magnetisation can undergo when reversing. It can happen either by rotation of the magnetisation in the direction of the field, or by motion of domain walls in favour of the domains being in the direction of the applied field. Considering a material with a uniaxial anisotropy of any origin (magnetostatic, magnetocrystalline, magnetoelastic or field induced), the domain walls are assumed to be parallel to the easy axis. We consider in this section a simplistic description of the two following cases : application of a field transverse to the easy direction (Fig. 1.12(a)) and parallel to it (Fig. 1.12(b)). Whereas in the first case, a rotation of the magnetisation occurs, the second case results in domain wall motion.

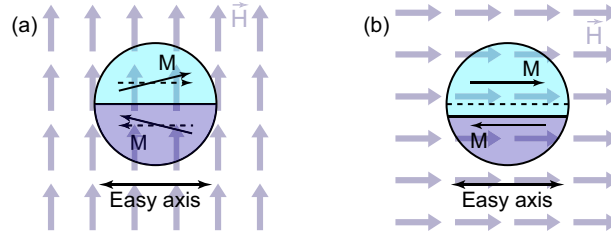


**Fig. 1.12:** Schematic representations of a magnetic material having purely uniaxial anisotropy in the direction of the easy axis. Dashed lines indicate magnetisation configurations for  $H = 0$ . (a) Application of a field transverse to the easy axis. (b) Application of a field parallel to the easy axis.

#### *Field transverse to the easy axis*

The energy density in this situation can be written as :

$$e = e_{\text{anisotropy}} + e_{\text{Zeeman}} = K \cos^2 \theta - M_s H \cos \theta \quad (1.25)$$

where  $\theta$  is the angle between  $\vec{M}$  and the applied field ( $\vec{H}$ ), and  $K$  is the anisotropy constant (taken as positive all along these two paragraphs). This energy density is shown in figure 1.13(a) for  $H = 0$  and for a few values of positive  $H$ . It can be seen that at  $H = 0$ , the stable solution is  $\theta =$

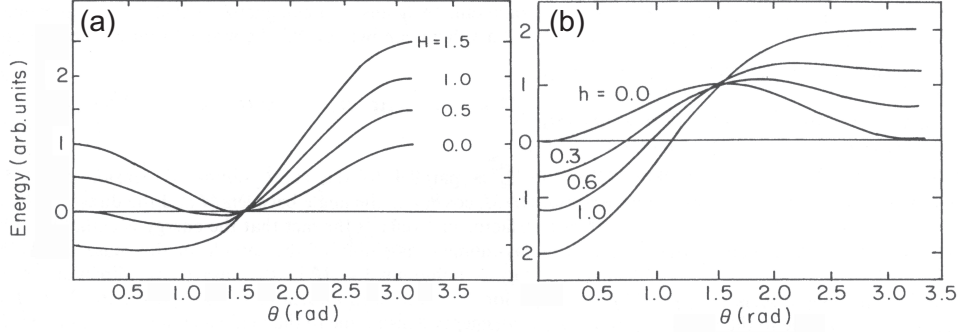


**Fig. 1.13:** Free energy (uniaxial plus Zeeman energy) as a function of angle between magnetisation and applied field, for different applied field strength ( $h = \frac{M_s H}{2K}$ ) in the two cases : (a) hard-axis process (Fig. 1.12(a)) and (b) easy-axis process (Fig. 1.12(b)). Note that in the first case, the stable energy minimum moves from  $\frac{\pi}{2}$  towards zero with applied field. In the second case, there are two local minima of the energy for zero field. One of these vanishes for a given field; the other one is then a stable energy minimum.

$\frac{\pi}{2}$ . As  $H$  increases, this stable point moves to smaller  $\theta$ , indicating that the magnetisation vector is aligning with the applied field. Quantitatively, the equilibrium is given by  $\frac{\partial e}{\partial \theta} = 0$  and  $\frac{\partial^2 e}{\partial \theta^2} > 0$ . This is given by equation 1.26 and 1.27, respectively.

$$(-2K \cos \theta + M_s H) \sin \theta = 0 \quad (1.26)$$

$$-2K \cos 2\theta + M_s H \cos \theta > 0 \quad (1.27)$$

Equation 1.26 has two obvious solutions :  $\theta = 0, \pi$ . Equation 1.27 states that these solutions are stable if  $H > \frac{2K}{M_s}$  and  $H < -\frac{2K}{M_s}$ , respectively. This describes the two saturation states, and also gives the value of the applied field necessary to saturate ( $H_{sat} = \frac{2K}{M_s}$ ). Another solution of Equation 1.26 is given by :

$$2K \cos \theta = M_s H \quad (1.28)$$

This is the equation of motion for the magnetisation in applied fields below saturation ( $-\frac{2K}{M_s} < H < \frac{2K}{M_s}$ ). If  $H = 0$ , the solution is as expected  $\frac{\pi}{2}$ . From the definition of  $H_{sat}$ ,  $K$  can be written as  $K = \frac{H_{sat} M_s}{2}$ . Considering that

the magnetisation in the field direction is  $M = M_s \cos \theta$ ,  $m = \frac{M}{M_s} = \cos \theta$  can be defined as the normalised magnetisation. In the same way, the normalised applied field can be defined as  $h = \frac{H}{H_{sat}}$ . Using these definitions, Eqn. (1.28) can be rewritten as :

$$m = h \text{ for } |h| \leq 1 \quad (1.29)$$

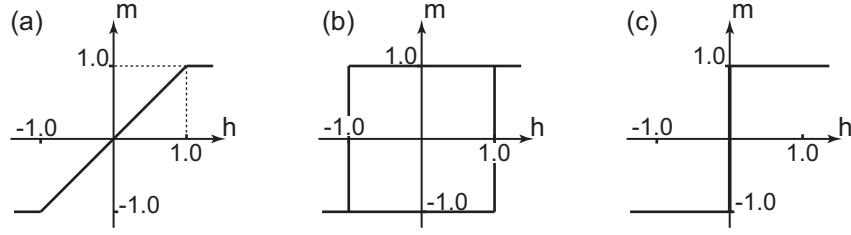


**Fig. 1.14:** Normalised magnetisation curve ( $m(h)$ ) for ideal cases : (a) Hard axis process (Fig. 1.12(a))  $\rightarrow$  rotation of magnetisation. (b) & (c) Easy axis process (Fig. 1.12(b))  $\rightarrow$  domain wall motion impeded by defects (b) or free domain wall motion (c).

We conclude that the magnetisation reversal for a field transverse to the easy direction occurs by the linear rotation of the magnetisation (versus the field), up to the saturation magnetisation (at  $H = H_{sat}$ ), as shown in figure 1.14(a). Note that the presence of domain walls would not change anything since they are parallel to the easy axis : they do not move because there is no energy difference across the domain wall.

### ***Field parallel to the easy axis***

*No domain motion :* Let us assume that the domain is totally pinned (no domain wall motion). Then, the energy density can be written as :

$$e_i = K \sin^2 \theta_i - M_s H \cos \theta_i \quad (1.30)$$

where  $\theta_i$  is the angle between the magnetisation and the applied field in the domain  $i$  (Fig. 1.12(b)). As both domains are along the easy axis, they have the same anisotropy energies. The easy axis aligned field does not apply any torque on the domain magnetisation. The same procedure as above can be applied to find the equilibrium state. Figure 1.13(b) shows the energy density for various normalised fields ( $h = \frac{M_s H}{2K}$ ) from 0 to 1. At zero applied field both  $\theta = 0$  and  $\theta = \pi$  are stable (consistent with the two domains in figure 1.12(b)). With increasing field, these two solutions remain locally stable while  $\theta = 0$  becomes more favourable. For  $h = 1$ , the local stability of the solution



$\theta = \pi$  vanishes and the magnetisation in these domains switches abruptly to  $\theta = 0$ , as shown with the plain curve on figure 1.14(b). The field at which the  $m(h)$  curve cross  $m = 0$  is called the **switching field**. It is due to rotational hysteresis and not to domain wall motion hysteresis (as we considered the domain to be fully pinned).

*With domain motion :* Let us first consider the opposite situation to the previous paragraph, i.e. a smooth and easy wall motion. The field exerts no torque on the domain magnetisation but does exert a torque on the spins making up the wall. Those may rotate to align the wall, therefore shifting the wall in favour of the domain aligned with the applied field. Macroscopically, the difference in Zeeman energy of the two domains represents a field-induced potential-energy difference across the domain wall of  $2M_s H$ . The wall can lower this energy by moving so as to reduce the volume of the unfavourably oriented domains. If there is nothing to slow the motion, the loop resembles the curve with no coercivity on figure 1.14(c). Defect processes can impede wall motion and lead to irreversibility in the  $m(h)$  curve associated with wall motion hysteresis. A coercivity appears, no more related to rotational hysteresis but to wall motion hysteresis (see below).

*Summary* The message from this section can be summarised as following : a square loop with high remanence generally results from application of a field along the easy axis direction of magnetisation and the magnetisation reversal process by wall motion (Fig. 1.14(b)&(c)). A slanted loop with no coercivity, with zero remanence generally results from application of a field transverse to the easy axis direction and the magnetisation reversal process by rotation(Fig. 1.14(a)). These points have been emphasised because one of the main results of this thesis is to show that, even if the above statements are commonly admitted, more care must be taken. In the chapter 3, we show that the  $M(H)$  loop is not sufficient to have a full picture of the magnetisation reversal and that microscopic imaging may be necessary.

Special care must be taken to interpret  $M(H)$  curves for a polycrystalline material. If there is a distribution of the easy direction relative to the applied field direction, each grain responds to the field in a different way. The typical  $M(H)$  curve is then somewhat rounded by summing over a number of grain having different values of  $\theta$ . In this case, the extracted value of any parameter is an averaged value. In this thesis, some results stem from polycrystalline nickel film, with [111] facets. In such a configuration, the easy axis is perpendicular to the film. In terms of anisotropy energy, this is equivalent to a single crystal since the angle between the applied field and the easy axis does not depend on the facet.

### 1.4.2 ENERGIES AND MAGNETIC LOOP

A closer look into the magnetisation loop gives precious information about the energies involved. Let us consider the process of magnetising the sample from the demagnetised state to the saturation state. It is clear in figure 1.15 that the two areas  $A_1$  and  $A_2$  are given by :

$$A_1 = \int_0^{M_s} H(M) dM \quad (1.31)$$

$$A_2 = \int_0^{H_{sat}} M(H) dH. \quad (1.32)$$

$H(M)$  and  $M(H)$  are functions defining the magnetisation curve in terms of the independent variables  $M$  and  $H$ , respectively. Notably, if  $\frac{A_1}{A_2}$  is small, the material is easy to be magnetised, that is to say not much work needs to be done to magnetise the material. Actually,  $\mu_0 A_1$  is the work done “by the field” to bring the sample to the saturated state and  $A_2$  is proportional to the energy given up “by the magnetised material” as it is drawn into a field. Thus,  $A_1$  represents the work done on the sample and  $A_2$  describes the work done by the sample<sup>23(chap. 2.5)</sup>.

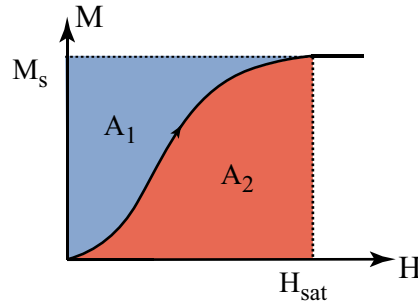


**Fig. 1.15:** Schematic of the  $M(H)$  juvenile loop. The respective definitions of the areas  $A_1$  and  $A_2$  are represented.

## 1.5 Defects and Domain Wall Motion

Defects can come in many forms, such as grain boundary, precipitates, inclusions, surface roughness, . . . . As a general definition, a magnetic defect is seen as a local variation on one of the magnetic properties (anisotropy energy  $K$ , exchange stiffness  $A$ , magnetostatic energy  $E_{ms}$ , . . .). The effect of these defects on the magnetisation is to change the domain wall motion. Two simple cases are shown in figure 1.16. The left case is the presence of non magnetic

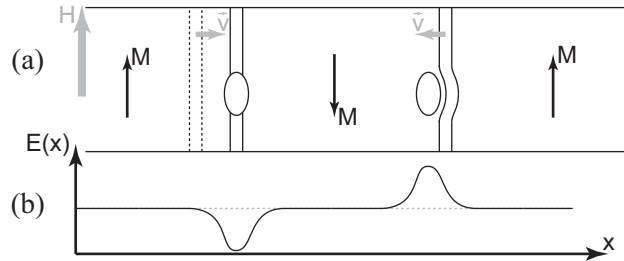


**Fig. 1.16:** (a) Schematic of the two kinds of defects considered, and their influence on wall motion. On the left, a non-magnetic inclusion locally lowers the wall energy by decreasing its area. On the right, particles with different anisotropy or magnetisation than the surroundings present a barrier to the wall motion. (b) Corresponding wall energy as a function of position in the absence of external field<sup>23</sup>.

inclusions or planar defects inside the magnetic material. It eliminates the need for a twist in magnetisation across the defect, lowering locally the wall energy. This local lower energy effectively pins the wall (impedes the motion). The right case represents a magnetic defect having a stronger anisotropy than the rest of the material. The spins in the barrier are pinned in the direction of local anisotropy. The energy to create a wall is therefore larger and this defect acts as a barrier for the wall, preventing the wall moving across the defect.

As seen previously, an applied external field tends to move the walls due to a difference in potential energy across the wall. Clearly, the distribution of defects in the material leads to irregular domain wall motion consisting of jumps from defect to defect, called **Barkhausen jumps**. The wall achieves an average drift velocity which depends on the strength of the applied field and the density of defects. When decreasing the field after saturation, the walls have again to go through the defects. This added difficulty of motion means a tendency of the saturated domain to survive. In other terms, the coercivity is increased. The strength of the pinning effect of a defect depends on two factors :

- The difference between the magnetic properties of the defect and the surrounding material.
- The ratio of the defect size and the domain wall size.

For defects small compared to the domain wall width, the coercivity increases roughly linearly versus defect size. Looking at figure 1.16, it is clear that for defects smaller than the domain wall thickness, increasing the size of a defect induces the filling of a larger fraction of the wall thickness, thus it pins the wall more efficiently. For defects larger than the domain wall width, the

sharpness of the defect (how abruptly the magnetic properties vary between the defect and the surrounding material) must be considered. The coercivity does not depend on the defect size in the case of a sharp transition and varies as the inverse of the defect size in the case of a fuzzy transition<sup>23(chap. 9.3)</sup>. It is commonly accepted that defects, in the framework of domain wall motion, induce an increase of the coercivity. However, one key result of this thesis shows a case of domain wall motion with evident pinning centres acting as nucleation centres but which do not increase coercivity.

## 1.6 Magnetism in Thin Films

The environment of atoms on surfaces differs from that of their bulk counterparts. The symmetry, distance to neighbouring atoms and even the lattice constant are significantly different (usually the lattice constant is smaller at the surface than in the bulk). Accordingly, magnetic moment, Curie temperature, magnetic anisotropy and magnetoelastic coupling may differ at surfaces or in thin films, as compared to bulk. The behaviour at surfaces is therefore an important scientific question, especially since the data storage industries extensively use magnetic films.

### 1.6.1 MAGNETIC MOMENT

To understand and estimate the magnetic moment standing on surfaces, let us consider the result of a simulation done for an 8-monolayer (ML) film of nickel on a copper (001) substrate<sup>23(chap. 16.1)</sup>. Figure 1.17 illustrates the variation of the calculated magnetic moment from layer to layer. The interaction between Ni and Cu atoms at the interface decreases the Ni moment by mixing the Cu itinerant electron character with the Ni  $d$  bands. The central atoms are bulk-like, as the magnetic moment of  $0.56 \mu_B/\text{Ni}$  atoms suggests (cf. table 1.1). The surface layers show an enhanced moment of  $0.74 \mu_B/\text{Ni}$  atoms. This can easily be understood with a simplified picture. In the bulk, the 12-fold coordination of Ni atoms is higher than the 9-fold/8-fold coordination of surface Ni(111)/(100) atoms. Therefore, the surface  $d$  states are left more localised (less itinerant) by the lower coordination. The surface atoms behave more atom-like (a value of  $2 \mu_B/\text{Ni}$  atoms is expected for a 0D atom). The lower coordination implies the intra-atomic exchange to be more effective at the surface. Thus, the magnetic moment per atom can be larger (cf. section 1.2.1). This has been successfully shown experimentally on Co islands grown on Pt(111) by Gambardella *et al*<sup>30</sup> (Fig. 1.18).

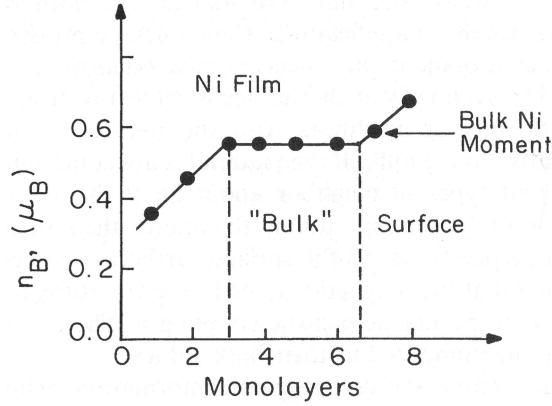


**Fig. 1.17:** Calculation of the variation of the magnetic moment of a 8 ML Ni film on a *Cu* (001) substrate, as a function of the depth. The calculated bulk and surface magnetic moments are  $0.56 \mu_B$  and  $0.74 \mu_B$  per Ni atom respectively (compared with the measured value of  $0.6 \mu_B$ )<sup>23</sup>.

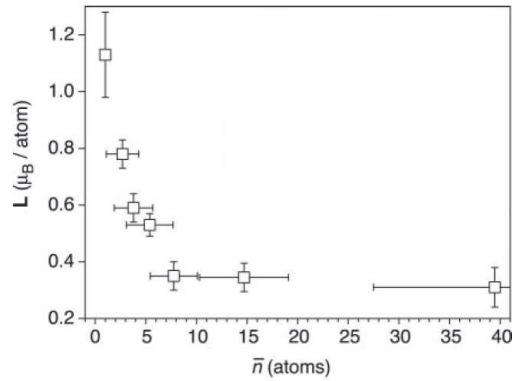


**Fig. 1.18:** Orbital magnetic moment of Co island on Pt(111) versus the average size of these islands. A lower dimensionality exhibits a higher magnetic moment<sup>30</sup>.

### 1.6.2 SURFACE LATTICE CONSTANT

Due to the effect of missing neighbours, the surface lattice is different. Indeed, atomic planes near a surface generally show a spacing normal to the surface that is significantly smaller than in the bulk. This surface relaxation can amount to several percent. This effect is negligible at three or four atomic layers into the material and is therefore important for ultra thin films only.

### 1.6.3 STRAIN

In addition to the surface lattice relaxation of the surface, thin films can exhibit large biaxial in-plane strains<sup>31</sup>. As the effect of strain on magnetism, namely inverse magnetostriction (c.f. section 1.2.4), can be significant in thin films and multilayers, strain is an important parameter when considering the magnetic state of a given sample<sup>32</sup>. Chapter 3 of this thesis deals with the system Cu/Ni/Cu(001) where the most dramatic manifestation of this effect is the existence of strong perpendicular magnetisation over a broad range of the nickel film thickness.

#### *Temperature related strain*

Difference in thermal expansion between the film and its substrate may give rise to film strain associated with a temperature change. This can be induced during the deposition of the film, as an evaporation process involves high energy atoms arriving on the substrate. This is also relevant if high or low temperature measurements are performed on the film. It will be shown by Grazing Incidence X-Ray Diffraction (GIXRD) in chapter 4 that electron evaporated Ni film on Si(100) with a natural SiO<sub>2</sub> oxide is in a strained state as grown. It will also be shown by looking at the magnetic properties that cooling the sample to 9 K induces strain in Ni films.

#### *Sample deformation related strain*

Once the film is grown, deformation of the sample can induce strain. The way the sample is attached to the sample holder to perform measurements is therefore important. This deformation related strain can be used to apply strain in a controlled way, allowing a study of strain related variables, as seen in the work of Lieb *et al*<sup>33-36</sup>. Figure 1.19 shows a method to control the stress applied to the film via the deformation of the sample.

#### *Lattice related strain*

Apart from strain due to temperature or geometry variation, epitaxially grown films can show very large lattice mismatch strains. The misfit strain in the surface plane also gives rise to a perpendicular Poisson strain. The lattice mismatch is defined as  $\epsilon = \frac{(a_s - a_f)}{a_s}$ , where  $a_s$  and  $a_f$  are the the sample and film lattice constant, respectively. If a thin film has a lattice mismatch, layer with smaller product of thickness and stiffness, usually the film, absorbs most of the strain to retain atomic coherence at the interface. This strain depends on the film thickness. The elastic energy per unit area is proportional to  $\epsilon^2 \frac{d}{2}$ , where  $d$  is the film thickness. Thus, this energy increases with film thickness

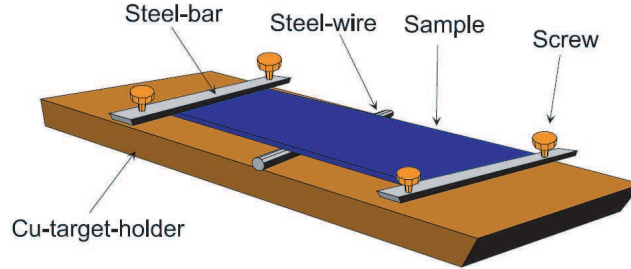


**Fig. 1.19:** Method to control the stress applied to the sample in order to study its effect on certain properties (i.e. the effect on the magnetic anisotropy on Ni films)<sup>33</sup>.

until a critical thickness ( $d_c$ ), where the strain energy exceeds the energy cost for formation of dislocations, which relieve the strain. Then, as the film thickness increases further, the density of dislocation increases and the average film strain decreases. This has been demonstrated in the Cu/Ni/Cu system<sup>37</sup>, where a dependence of the strain in  $\frac{1}{d^{2/3}}$  is shown (see figure 1.20). It is therefore expected that a strong dependence of the magnetic properties can be seen in the Cu/Ni/Cu system for Ni thicknesses larger than 2.7 nm. This is further presented in chapter 3.

#### 1.6.4 SURFACE MAGNETIC ANISOTROPY

##### *Origin*

Bulk magnetocrystalline anisotropy is related to favoured direction of the momentum of the  $d$  electrons on the basis of orbital topology coupled to the spin-orbit interaction (c.f. chapter 1.2.3). Similarly, the surface anisotropy arises from the fact that surface electrons have a reduced probability of being found outside the surface. Motion in the plane of the surface is therefore favoured. As it is associated with an angular momentum perpendicular to the surface plane, the ratio  $L_z^2/(L_x^2 + L_y^2)$  must increase. If the spin-orbit interaction is significant, the  $z$  component of spin perpendicular to the surface is also increased and perpendicular magnetisation may be favoured. This can explain the frequent occurrence of perpendicular magnetisation in a variety of thin-film systems (Fe/Ag(001), Ni/Cu(001) and Co/Pd)<sup>23</sup>.

##### *Phenomenology*

The phenomenological approach is again very similar to the one presented in section 1.2.3. The difference comes from the symmetry being reduced at the surface. Arguments based on the fact that the symmetry negates the

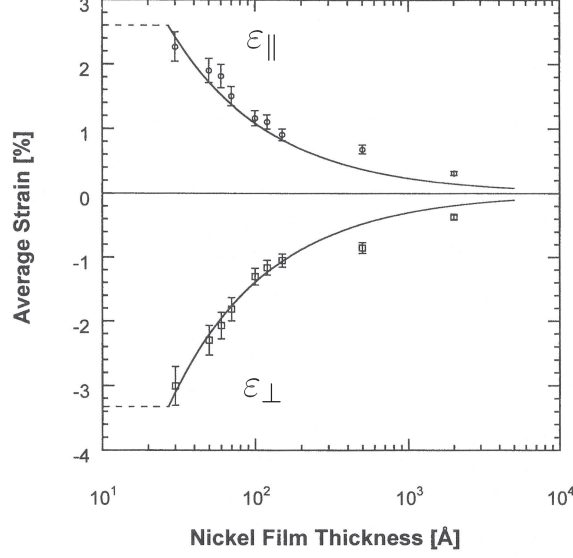


**Fig. 1.20:** In-plane ( $\parallel$ ) and out-of-plane ( $\perp$ ) strain as a function of the nickel film thickness. The data are fitted with the dependance  $\epsilon(d) = \left(\frac{d_c}{d}\right)^{2/3}$ , with  $d_c = 2.7 \text{ nm}$  and  $\epsilon = 2.6\%$ <sup>37</sup>. The in-plane and the out-of-plane strain are related by the Poisson ratio of bulk Ni namely  $-\frac{\epsilon_{\perp}}{\epsilon_{\parallel}} = 1.18 \pm 0.05 \approx 1.28$ .

first three orders are no longer valid. At the surface, the second and higher order terms apply<sup>23(chap. 6, appendix)</sup>. Instead of the formula (1.14), valid for the magnetocrystalline anisotropy, the surface anisotropy may be written as :

$$E_{surface} = K_{s1}\alpha_3^2 + K_{s2}\alpha_3^4 + K_{s3}\alpha_1^2\alpha_2^2 + \dots \quad (1.33)$$

There clearly remains a fourfold anisotropy in the plane of the surface. In addition, there are uniaxial surface terms which, at the first order favour magnetisation perpendicular to the surface if  $K_{s1} < 0$ , and favour magnetisation in the plane of the surface if  $K_{s1} > 0$ . The first term in equation (1.33) is often written as  $K^s \sin^2 \theta$ , in which case  $K^s > 0$  implies perpendicular magnetisation and  $K^s < 0$  magnetisation in the film plane.

### 1.6.5 INHOMOGENEOUS MAGNETISATION

As introduced above, minimising the energy in a magnetic sample implies the formation of in-plane domains to keep the magnetostatic energy low. We also mentioned that thin films and surfaces can exhibit different magnetisation than the bulk. We further reported in section 1.3.2 that Bloch walls can have



a Néel cap ( $\vec{M}$  parallel to the surface) at the surface and that, on thin films, magnetostatic energy can turn the entire Bloch wall into a Néel wall. In films which are so thin that the magnetostatic energy favouring in-plane magnetisation is smaller than those energies that favour out-of-plane magnetisation (mainly the magnetoelastic energy, surface anisotropy and magnetocrystalline energy), the magnetisation in the domains is perpendicular to the film plane. Inside the  $180^\circ$  domain walls, which separate the domains, the magnetisation lies in the film plane. It has been shown by Bochi *et al*<sup>38,39</sup> that, in a system where a Ni film is grown epitaxially between two Cu layers, the magnetisation is perpendicular to the film plane for Ni thicknesses between 2 and 13.5 nm.

Furthermore, thin films may show even more complicated magnetisation. In order to minimise the magnetoelastic energy without too much cost in magnetostatic energy, the magnetisation can take a non-uniform orientation. Figure 3.4 shows two of these situations. In the first case (Fig. 3.4(b)), the magnetisation is in-plane but, to lower the magnetoelastic energy, the magnetisation exhibits some ripples giving rise to a small perpendicular component. These are called **magnetisation ripples**. In the second case (Fig. 3.4(c)), the magnetoelastic energy is such that the domains are perpendicular to the sample plane. To decrease the magnetostatic energy, similarly to the Néel cap in Bloch walls, **closure caps** are formed. Chapter 3 is dedicated to the study of the situation where the magnetisation shows a perpendicular component. It is normally difficult to distinguish closure caps from ripple magnetisation, but we demonstrate that quantitative magnetic force microscopy can make the distinction (c.f. section 3.3).

### 1.6.6 SUMMARY

The magnetisation direction can be predicted by taking into account the interplay between the involved energies. The surface, magnetocrystalline, magnetoelastic (may be separated into a surface term and a volume term) and the magnetostatic terms have to be considered. This can be done by minimising the free energy density ( $f$ ), using a uniform magnetisation model with effective uniaxial anisotropy  $K_{eff}$ <sup>23,37-41</sup> :

$$f = K_{eff} \cdot \sin^2 \theta$$

$$K_{eff} = \underbrace{K_{mc}}_{\text{Magnetocrystalline anisotropy}} + \underbrace{\frac{K^s}{d}}_{\text{Surface anisotropy}} + \underbrace{2\left(B_v + \frac{B_s}{d}\right)\epsilon}_{\text{Volume and surface magnetoelastic anisotropy}} + \underbrace{-\frac{\mu_0 M_s^2}{2}}_{\text{Magnetostatic energy}} \quad (1.34)$$

where the two surface terms (the surface anisotropy and magnetoelastic surface anisotropy) are dependant on the film thickness ( $d$ ).  $\theta$  is the angle between the magnetisation and the normal of the surface,  $\epsilon$  is the film strain,  $M_s$  is the saturation magnetisation and  $\mu_0$  is the vacuum permeability.

This model successfully predicts the magnetisation direction in many cases. However, it fails to describe non-uniform magnetisation such as perpendicular domains with closure caps or rippling magnetisation along an in-plane axis . Chapter 3 elaborates on this more complicated situation.

## 1.7 Nickel

*Nickel* is a grey-silver hard but ductile metal. It is part of the transition metals from group 10 (VIII). Like cobalt and iron, it belongs to period 4 and is ferromagnetic. The main nickel parameters are given in the table 1.1. A schematic of the cubic lattice is shown in figure 1.21. Note that  $[111]$  is the easy magnetisation direction.

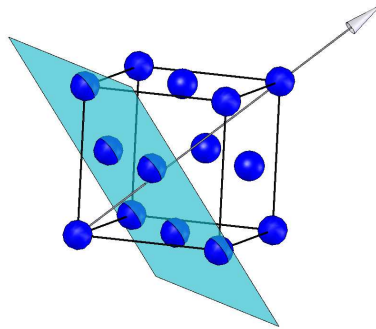


**Fig. 1.21:** Schematic of the fcc cubic lattice of nickel. The arrow represents the  $\langle 111 \rangle$  direction (nickel easy magnetisation axis) while the shaded plane is the  $(111)$  plane. The angle between  $[111]$  and  $[\bar{1}\bar{1}1]$  directions is  $\approx 71^\circ$  and the one between  $[111]$  and  $[\bar{1}\bar{1}\bar{1}] \approx 109^\circ$ .

Symbol	Ni	
Atomic number	28	
Electron configuration	$[Ar]3d^84s^2$	
Crystal structure (c.f. Fig. 1.21)	fcc *	
Easy magnetisation axis (c.f. Fig. 1.21)	$\langle 111 \rangle$	
Magnetic coupling	ferromagnetic	
Oxide (NiO) magnetic coupling	antiferromagnetic	
Magnetic moment per atom	0.6 $\mu_b$	
Exchange energy <sup>23,42</sup>	$A =$	$\approx 1 \cdot 10^{-11} \frac{J}{m}$
Curie Temperature	627 K	
Density	8908 $\frac{kg}{m^3}$	
Saturation magnetisation <sup>43</sup> @ 4K	$M_s =$	$0.49 \cdot 10^6 \frac{A}{M}$
Saturation magnetisation <sup>43</sup> @ 293K	$M_s =$	$0.52 \cdot 10^6 \frac{A}{M}$
Melting temperature	1726 K	
Lattice constant	0.352 nm	
Magneto-crystalline anisotropy coefficients @ 300 K <sup>‡</sup> <sup>44</sup>	$K_1 =$	$-4.5 \cdot 10^3 \frac{J}{m^3}$ †
	$K_2 =$	$-2.3 \cdot 10^3 \frac{J}{m^3}$
Magneto-crystalline anisotropy coefficients @ 4.2 K <sup>44</sup>	$K_1 =$	$-12 \cdot 10^4 \frac{J}{m^3}$
	$K_2 =$	$3 \cdot 10^4 \frac{J}{m^3}$
Magnetoelastic coupling coefficients <sup>23</sup>	$B_1 =$	$6.2 \cdot 10^6 Pa^{\S}$
@ RT	$B_2 =$	$4.3 \cdot 10^6 Pa^{\S}$

\* face centered cubic (can also be body centered cubic (bcc)<sup>45</sup>)

† to have the value in  $\frac{erg}{cm^3}$  multiply these values by 10

‡ c.f. next section

§ Pa  $\equiv \frac{N}{m^2}$

**Tab. 1.1:** Crystallographic, electronic, magnetic and general properties of nickel.

## 1.8 Magnetocrystalline Anisotropy

The nickel magnetocrystalline anisotropy is very sensitive to the presence of impurities<sup>46</sup> and it strongly depends on temperature. At low temperature, as opposed to most materials, fitting the experiment (Eqn. (1.14)) requires more than three orders<sup>44,46\*</sup>. We can see in figure 1.8 the strong dependance of the three anisotropy factors  $K_1$ ,  $K_2$  and  $K_3$  ( $2^{nd}$ ,  $3^{rd}$  and  $4^{th}$  orders, see Eqn. (1.14)). As a comparison, the anisotropy coefficients are also given for Fe. In the case of Fe, it is obvious that only  $K_1$  is important as it is much larger than the higher orders. We also note that, between 300 K and 4 K,  $K_1$  only varies by 14%. In contrast to iron, the first anisotropy coefficient of nickel increases 23 times within the same range. In addition, it can be seen that  $K_2$  and  $K_3$  are large enough to be important. Moreover, they vary so strongly with temperature that they change sign.

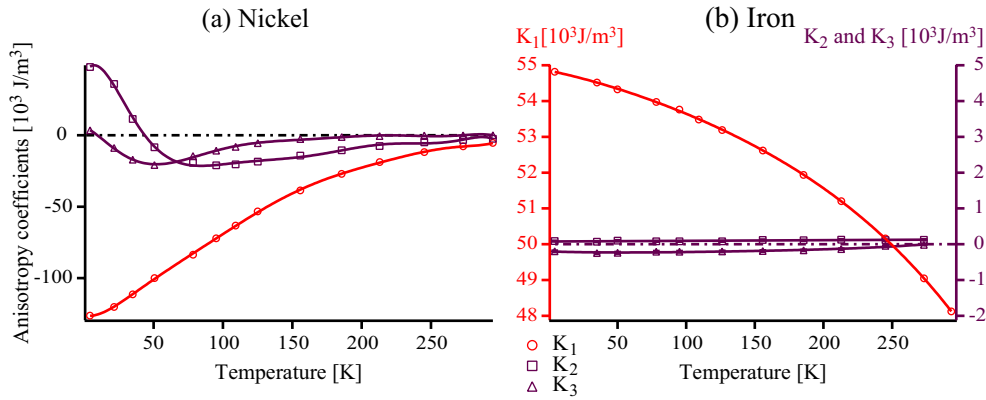


**Fig. 1.22:** Temperature dependance of the three first anisotropy constants<sup>44</sup> of (a) nickel and (b) iron.

## 1.9 Energies Summary

Nickel is of great interest because of its intrinsic magnetic properties. Namely, the small saturation magnetisation (resulting in a relatively small magnetostatic energy density), the large positive bulk magnetoelastic coupling coefficient (giving the high tendency toward perpendicular magnetic anisotropy) and the rather small magnetocrystalline anisotropies at room temperature.

\* Due to this sensitivity, different sources record slightly different values of the magnetocrystalline anisotropy coefficient (c.f. appendix B). In this thesis, the most recent values (including room temperature and 4.2 K) have been used<sup>23</sup>. These are reported on the table 1.1.

Due to these properties, the magnetoelastic anisotropies can be dominant over crystal anisotropy and shape anisotropy. A summary of the relative importance of the energies for Fe and Ni is given in table 1.2

Energy term		Fe	Ni
Magnetostatic	$\mu_0 \frac{M_s^2}{2} [10^6 \frac{\text{J}}{\text{m}^3}]$	1.9	0.14
Magnetocrystalline	$K_1 [10^4 \frac{\text{J}}{\text{m}^3}]$	+4.8	-0.45
Magnetoelastic	$B_1 [10^6 \frac{\text{J}}{\text{m}^3}]$	-2.9	+6.2
Strain for $\frac{\text{Magnetocrystalline}}{\text{Magnetoelastic}} \approx 1$	$\frac{K_1}{B_1}$	1.7 %	0.1 %
Strain for $\frac{\text{Magnetostatic}}{\text{Magnetoelastic}} \approx 1$	$\mu_0 \frac{M_s^2}{2B_1}$	66 %	2.4 %

**Tab. 1.2:** First order anisotropy coefficients for Ni and Fe. The two last columns represent the strain needed to have magnetoelastic energy comparable to magnetocrystalline ( $\frac{K_1}{B_1}$ ) and magnetostatic energies ( $\mu_0 \frac{M_s^2}{2B_1}$ ).

It can be seen that a strain of only 0.1% in nickel gives rise to a magnetoelastic anisotropy comparable to  $K_1$ , whereas a much larger strain (1.7%) is required to give a magnetoelastic anisotropy comparable to the crystal anisotropy in iron. To have a magnetoelastic anisotropy comparable to the magnetostatic effect, strains of 66% and 2.4% are needed for Fe and Ni respectively. Note that strains exceeding about 0.1% are greater than elastic limit of most metals and can exist only in thin films.



# 2

## MEASUREMENT METHODS

### 2.1 Introduction to SPM

Scanning probe microscopy (SPM) refers to all methods involving a sensor (probe) scanning a surface to generate an image. The technique overcomes the resolution limits of far-field techniques (generally half the wavelength used) by scanning close to the surface<sup>47,48</sup>. The resolution in SPM is only limited by the geometrical shape of the probe (Fig. 2.1).

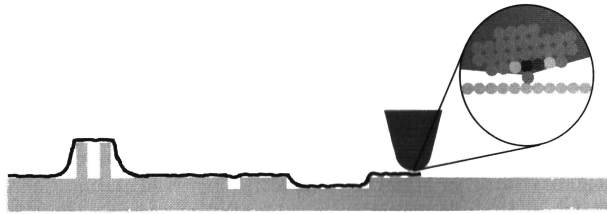


**Fig. 2.1:** The resolution of SPM is limited by the shape of the probe (tip). The image is the convolution of the sample topology and the shape of the tip. If the surface is atomically flat, only the atomic structure of the tip apex is relevant.

As SPM covers a large lateral imaging range (from several  $100\mu\text{m}$  to  $10\text{pm}$ ), it has become an essential tool in the field of nanoscience. In the different SPM techniques, one can have access to a number of different local surface parameters including density of state, topology, chemical bonds, electrostatic forces and magnetic stray field. SPM started with the invention in 1982 of the scanning tunnelling microscope (STM) by G. Binnig and H. Rohrer<sup>49,50</sup>. Here, they used a sharp metallic tip as a probe to scan the surface at a distance of less than  $1\text{nm}$  in vacuum, while applying a voltage between the probe and the surface. The resulting tunnelling current was used as a feedback and kept constant. The tunnelling current is exponentially dependant of the probe-surface distance and flows from the apex atom of the tip,

such that the atomic resolution can be achieved. Since the current from the tip to the sample was measured, both had to be conductive. This prerequisite was overcome with the scanning force microscope (SFM) which was invented by Binnig, Quate and Gerber<sup>51</sup>. In this case, the tip-surface distance is controlled in order to keep the force between tip and sample constant. Therefore, neither the tip nor the surface need to be conductive. The forces acting on the probe involved in the imaging process, (in vacuum) can be:

- *Short range forces*

Short range chemical forces arise from the overlap of electron wave functions and from the repulsion of the ion cores. The range of these forces is therefore comparable to the extension of the electron wave functions (less than 1 nm). Short-range forces can be both attractive or repulsive. Attractive forces are due to the overlap of electron waves reducing the total energy as it happens in a molecular binding. Repulsive forces arise from the Pauli exclusion principle in the case of strong electron wave overlap. The ionic repulsion acts only over small distances where the screening of the ion cores by electrons falls away.

- *Van der Waals forces*

Van der Waals forces are almost always attractive forces. They result from dipole-dipole interaction. They cannot be attributed to chemical bonding since they don't involve electrons moving from one to another atom. The most important forces are not those between permanent dipoles but the so-called dispersion forces. These act between dipoles that arise from fluctuations and dipoles induced in their electric field. They are always present, even with chemically inert noble gas. They depend on the macroscopic tip shape and act over many tens of nanometres.

- *Electrostatic forces*

Electrostatic forces act between localised charges on insulating or semi-conducting samples. Their strength and distance dependence is given by Coulomb's law. They also act if the tip is conducting and are in this case attractive. The average electrostatic force can normally be canceled by controlling the bias between the tip and the sample. Note that a zero bias voltage does not normally correspond to a minimal electrostatic force but to the contact potential difference between tip and sample. Electrostatic forces are long range, so they can be used to determine rough topology by scanning very far away (hundreds of nm away) of the surface while applying a bias between tip and sample.



- *Magnetic forces*

In magnetic force microscopy (MFM), magnetic forces are detected by a tip carrying a magnetic moment. The force acts between this magnetic moment and the stray magnetic field produced by a magnetic sample (ferromagnetic or current distribution). The range of the magnetic forces depends strongly on the decay of the stray field outside of the sample and therefore on the micromagnetic structure of the sample and its thickness. The magnetic forces are longer range than van der Waals and short range forces, therefore MFM measurements can be performed further away from the surface (10-100 nm) than AFM.

This thesis concentrates on MFM which will be introduced in section 2.2. The mode of operation of MFM, namely dynamic mode, will be presented in the next section. The reader who is interested by SPM in general should refer to “Scanning Probe Microscopy” published by Springer<sup>52</sup>.

### 2.1.1 BASICS OF DYNAMIC MODE MICROSCOPY

This thesis presents work carried out with an MFM operated in dynamic mode with quantitative analysis. It is therefore necessary to describe the fundamental concepts of the dynamics of an oscillating cantilever with a tip in proximity to the surface. This section describes the relation between the frequency shift and the force acting on the tip. The sample’s magnetic properties and the force acting on the tip are studied in section 2.2.1.

The oscillating cantilever can be modeled by a damped, driven oscillator. Its equation of motion is described by a non-linear, second-order differential equation<sup>53-55</sup> :

$$m\ddot{z} + \frac{m\omega_0}{Q}\dot{z} + c_L z = F(z) + F_{exc} \cos \omega t \quad (2.1)$$

Here,  $F_{exc}$  is the driving force (excitation force) and  $\omega$  is the angular frequency of the driving force  $\omega = 2\pi f$ .  $Q$ ,  $\omega_0$  and  $c_L$  are the quality factor, angular resonance frequency and force constant of the free cantilever, respectively.  $F$  is the tip-surface interaction force.

In the absence of tip-surface forces ( $F(z)=0$ ), Eqn. (2.1) is the equation of a forced harmonic oscillator with damping and its solution has a transient term and a steady state solution. The steady state term is a sinusoidal function with a phase lag with respect to the excitation force. In a regime where Hook’s law applies, the resonance frequency of the free cantilever ( $f_0$  for  $F(z)=0$ ) is given by :

$$f_0 = \frac{1}{2\pi} \sqrt{\frac{c_L}{m}} \quad (2.2)$$

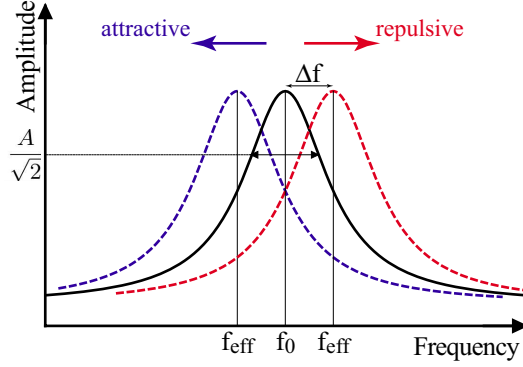


**Fig. 2.2:** Resonance curve for a harmonic oscillator (solid line) and under the influence of attractive/repulsive forces (dashed blue/red lines). The resonance curve is acquired by oscillating the cantilever with a fixed driving force while sweeping the frequency.

In the presence of an external force on the tip (from the sample), the total force acting on the tip  $F_{tot}$  can, for infinitesimally small displacements with respect to the equilibrium position (Taylor expansion) or if the tip-sample force gradient can be assumed constant over the oscillation amplitude of the cantilever, be expressed by:

$$F_{tot}(z) = F(z_0) + \sum_1^{\infty} \frac{1}{n!} \left( \frac{d}{dz} \right)^n F \Big|_{z=z_0} \cdot (z - z_0)^n \approx F(z_0) + \frac{dF}{dz} \Big|_{z=z_0} (z - z_0) \quad (2.3)$$

where  $F_{tot}(z)$  includes the elastic response  $c_L \cdot z$  and the interaction force  $F(z) \neq 0$ . It can be seen as the motion of a harmonic oscillator with an effective spring constant  $c_{eff}$  given by:

$$c_{eff} \equiv -\frac{dF_{tot}}{dz} = c_L - \frac{dF}{dz} \Big|_{z=z_0}. \quad (2.4)$$

Using equation (2.2), the new effective resonance frequency can be calculated :

$$f_{eff} \equiv \frac{1}{2\pi} \sqrt{\frac{c_L - \frac{dF}{dz} \Big|_{z=z_0}}{m}} = f_0 \cdot \sqrt{1 - \frac{1}{c_L} \frac{dF}{dz} \Big|_{z_0}}. \quad (2.5)$$

In an MFM experiment the change in resonance frequency is rarely more than 1% (of the resonance frequency)<sup>56</sup>, so the above relation can be further simplified to

$$\frac{\Delta f}{f_0} = -\frac{1}{2c_L} \frac{dF}{dz} \quad (2.6)$$

with  $\Delta f = f_{eff} - f_0$ . This shows that in this case the resonance frequency of a perturbed harmonic oscillator depends on the gradient of the interaction force. A change in the effective resonance frequency implies a shift of the whole resonance curve (figure 2.2). Note that, in the limit of the above assumption, the resonance curve of a perturbed harmonic oscillator is only shifted (without any shape modifications). It is useful to repeat these assumptions. Firstly, it was assumed that tip-surface interactions induce a frequency shift and not an energy transfer. In an MFM experiment, this is valid, as long as the tip magnetisation, and the sample stray field do not depend on the tip-sample position. Secondly, the force gradient was assumed to be constant over all tip positions during the oscillation. This assumption is valid when using small oscillation amplitudes. Thirdly, the force gradient was assumed to be much smaller than the cantilever force constant ( $dF_{ts}/dz \ll c_L$ ).

## 2.2 Introduction to MFM

SPM using a magnetically sensitive tip is called Magnetic Force Microscopy (MFM). The MFM technique was first introduced in 1987<sup>9,52</sup>. Since then, it has become one of the most common ways to image magnetic surface properties of a sample<sup>57-60</sup>. Apart of the tip being magnetically sensitive, MFM differs from AFM in the tip-sample distance used to image. Indeed, forces involved in the case of AFM are of the order of 1 nN and decay rapidly with tip-sample distance. The tip-sample distance in this case is therefore usually very small or the tip is even in contact with the sample. Magnetic forces are much smaller (two or three order of magnitude) but decay much slower with tip-sample distance. Therefore, the tip-sample distance used in MFM must be sufficiently large not to detect the topography but small enough to still detect the magnetic signal with a reasonable resolution.

Furthermore, the method to control the tip-sample distance is also different<sup>52</sup>. In AFM, the derivative of the forces involved in imaging (short range or van der Waals) does not change sign over a sufficiently large range of tip-sample distance. One can therefore keep this force constant by a feed-back which controls the tip-sample distance. In the case of MFM, the situation is more complex as the derivative of the measured interaction can change sign within one image (Fig. 2.3). Therefore this interaction cannot be used for feed-back. This problem can be solved by two methods. Firstly, a second force which is non-magnetic (tunnelling current or tip-sample capacity) can be used for the feed-back while recording the MFM signal. A similar way is to measure the topology by going very close to the surface. Then this "pre-scanned" topology can be used to guide the tip at a constant tip-sample surface to measure, thus, the magnetic signal. This technique only works in

the absence of piezo/temperature drift. Secondly, the distance can be left unregulated, and the measurement taken at constant average height, measuring thus both topology and magnetic signals. These two signal can be deconvolved by measuring at several different heights (increasing or decreasing the component from topology) or by changing the magnetisation direction of the tip. In this work, the second method was used and the tip-sample distance was chosen such that the topology signal was negligible.

### 2.2.1 INTRODUCTION TO QUANTITATIVE MFM

Quantitative magnetic force microscopy<sup>56,61–63</sup> requires the following steps:

- Calibration of the tip and instrument
  - First, the stray field\* of the calibration sample is computed at the location of the tip (Sect. 2.2.2).
  - Then it is determined how the MFM transforms the stray field into the measured property (Sect. 2.2.3).
- Using the calibration for quantitative analysis of MFM data (Sect. 2.2.3)
  - First, the stray field is calculated from the MFM measurement.
  - Then, if needed, the distribution of the desired physical quantity (e.g. sample magnetisation or current distribution) that generates a stray field that best matches the measured field is assumed.

### 2.2.2 CALCULATION OF THE STRAY FIELD

The stray field emanating from a general ferromagnetic sample can be calculated from<sup>52,64,65†</sup>:

$$\vec{H}(\vec{r}) = - \iiint_{V_s} \vec{\nabla} \vec{M}(\vec{r}') \cdot \frac{\vec{r} - \vec{r}'}{|\vec{r} - \vec{r}'|^3} dV' + \iint_{A_s} \hat{n} \cdot \vec{M}(\vec{r}') \cdot \frac{\vec{r} - \vec{r}'}{|\vec{r} - \vec{r}'|^3} dA' \quad (2.7)$$

where  $V_s$  is the sample volume,  $A_s$  is the sample area,  $\hat{n}$  is the outward unit vector normal to the sample surface (c.f. Fig. 2.3).

It is noteworthy that a general vector field (e.g.  $\vec{M}(\vec{r})$ ) can be written as a sum of a divergence free ( $\vec{\nabla} \cdot \vec{M}_{rot} = 0$ ) and a curl free ( $\vec{\nabla} \times \vec{M}_{div} = 0$ ) part ( $\vec{M} = \vec{M}_{rot} + \vec{M}_{div}$ ). It can be seen in equation (2.7) that only the curl free part of  $\vec{M}$

\* The term **stray field** describes the field outside the sample. Since only this field interacts with the tip to give rise to a magnetic contrast, this is the only field considered in that section.

† The conventions used in this thesis are summarised in appendix A.

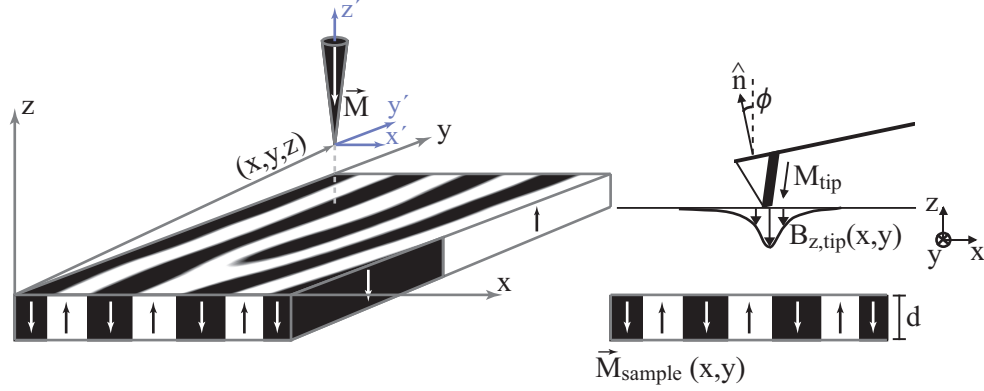


**Fig. 2.3:** Schematics of the situation of a tip scanning in MFM mode : The sample coordinate system has its origin at the sample surface. The tip coordinate system (indicated with primed letters) has its origin at the tip apex. The cantilever is canted and make an angle  $\phi$  to the normal  $\hat{n}$ .

contributes to the stray field. Hence MFM experiments can only give access to the curl free part of the magnetisation field. This is one of the reasons why an infinite number of different magnetisation patterns exist that generate the same stray field. Therefore an MFM experiment cannot, in general, determine the magnetisation pattern. In analogy with the electrostatic field, it can be useful to introduce the magnetic volume charge  $\rho_m$  and the magnetic surface charge  $\sigma_m$ .

$$\begin{aligned}\rho_m &= -\vec{\nabla} \cdot \vec{M} \\ \sigma_m &= \hat{n} \cdot \vec{M}\end{aligned}\quad (2.8)$$

In our case, neither time-varying electrical field nor currents outside the sample exist. Therefore, the magnetic field is curl free\* ( $\vec{\nabla} \times \vec{H} = 0$ ) and thus can be written as the gradient of a scalar magnetic potential  $\phi_m$  :  $\vec{H} = -\nabla \phi_m$ . Going further with the electrostatic field analogy, we can determine that:

- Outside the sample, the magnetisation is zero and therefore the Laplace equation holds (Eqn. (2.9)).
- Inside the sample, where the magnetisation is not zero, the Poisson equation holds (Eqn. (2.10))
- On the sample surface the boundary condition is given by the equation 2.11

---

\* from Maxwell equation

$$\vec{\nabla}^2 \phi_m = \Delta \phi_m = 0 \quad (2.9)$$

$$\Delta \phi_m = -\rho_m \quad (2.10)$$

$$\frac{\partial \phi_{z \leq 0}}{\partial n} - \frac{\partial \phi_{z > 0}}{\partial n} = \sigma_m \quad (2.11)$$

In order to derive some general properties of magnetostatic fields, it is useful to continue the analysis in Fourier space. We use a 2D-Fourier space in which only the  $x$  and  $y$  coordinate are transformed. In this case, it is convenient to write the coordinate triplet  $(x, y, z)$  as  $(\vec{r}, z)$  where  $\vec{r} = (x, y)$ . The Fourier transform is defined by Eqn. (2.12):

$$\begin{aligned} F(\vec{k}) &= \int_{-\infty}^{\infty} f(\vec{r}) e^{i\vec{k} \cdot \vec{r}} dx dy \\ f(\vec{r}) &= \frac{1}{4\pi^2} \int_{-\infty}^{\infty} F(\vec{k}) e^{i\vec{k} \cdot \vec{r}} dk_x dk_y \end{aligned} \quad (2.12)$$

Although the function  $F$  has units of the *spectral density* of  $f$ , we will use the same name and symbol in direct space and Fourier space, differentiated by the coordinate vector ( $\vec{r} = (x, y)$  in the direct space and  $\vec{k} = (k_x, k_y)$  in the Fourier space). In this 2D-Fourier space the nabla operator takes the form  $\nabla = (ik_x, ik_y, \frac{\partial}{\partial z})$ . Considering the situation outside the sample, the Laplace equation holds (Eqn. (2.9)). A general solution is given by equation (2.13), with the coefficients  $\phi(\vec{k})$  determined by the boundary conditions<sup>52</sup>.

$$\phi(x, y, z) = \frac{1}{4\pi^2} \int \phi(k_x, k_y) e^{i\vec{k} \cdot \vec{r}} e^{-\sqrt{k_x^2 + k_y^2} \cdot z} d\vec{k} \quad (2.13)$$

Equation 2.13 has the form of an inverse Fourier transform of  $\phi(\vec{k})$  with  $z=0$ . Therefore, the coefficients  $\phi(\vec{k})$  can be considered as the Fourier transform of  $\phi(\vec{r}, z = 0)$ . Further, by defining  $\phi(\vec{k}, z > 0) \equiv \phi(\vec{k}) \cdot e^{-kz}$ , it is clear that  $\phi(\vec{k}, z)$  is the Fourier transform of  $\phi(\vec{r}, z)$ . It is also clear that the Fourier transform of the magnetic scalar potential ( $\phi(\vec{k}, z)$ ) decays exponentially with  $z$ . It follows (using the definition of  $\phi$ , its general solution, and the definition of  $\nabla$  in 2D-Fourier space) that the Fourier transform of the stray field  $\vec{H}(\vec{k}, z)$  also decays exponentially with  $z$ . Furthermore, it can be shown that, where the Laplace equation holds, the nabla operator takes the form

$$\vec{\nabla} = (ik_x, ik_y, -k), \quad (2.14)$$

and the  $z$  component of the Fourier transform of the stray field is given by :

$$H_z(k_x, k_y, z) = k\phi(k_x, k_y, z). \quad (2.15)$$

It is remarkable that the Fourier transform of the scalar potential  $\phi$  is fully determined by the  $z$  component of the Fourier transform of the field. Since all three components of  $\vec{H}$  can be determined by  $\phi$ , it is sufficient to measure the  $z$  component of the magnetic field to calculate all three components of this field\*.

$$\begin{aligned} \phi(\vec{k}, z) &= \frac{1}{k} H_z(\vec{k}, z) \\ \vec{H}(\vec{k}, z) &= -\vec{\nabla} \phi(\vec{k}, z) \\ \Rightarrow \vec{H}(\vec{k}, z) &= -\frac{\vec{\nabla}}{k} H_z(\vec{k}, z) \end{aligned} \quad (2.16)$$

This is a very important statement which justifies using a tip with a magnetisation perpendicular to the sample surface in MFM. Indeed, measurement with such tips does not restrict the information to the perpendicular component of the stray field but, using Eqn. (2.16), also gives the in-plane component. In conclusion, using Eqn. (2.7), Eqn. (2.9), Eqn. (2.10), Eqn. (2.11) and Eqn. (2.16), the stray magnetic field can be calculated for an arbitrary magnetisation field<sup>56: Appendix A 62,63,66</sup>. The case for a sample with a magnetic domain structure having a uniform magnetisation  $\vec{M}$  throughout their thickness  $d$  is given by the equation (2.17) :

$$\begin{aligned} H_z(\vec{k}) &= \frac{e^{-k \cdot z} \cdot (1 - e^{-k \cdot d})}{2} \begin{pmatrix} -ik_x/k \\ -ik_y/k \\ 1 \end{pmatrix} \cdot \vec{M}(\vec{k}) \\ \vec{H}(\vec{k}) &= -\frac{\vec{\nabla}(\vec{k})}{k} \frac{e^{-k \cdot z} \cdot (1 - e^{-k \cdot d})}{2} \begin{pmatrix} -ik_x/k \\ -ik_y/k \\ 1 \end{pmatrix} \cdot \vec{M}(\vec{k}) \end{aligned} \quad (2.17)$$

The factor  $(1 - e^{-k \cdot d})$  originates from the magnetic surface charge density at the lower surface of the film. The stray field at the position  $\vec{r}$  and a distance  $z$  above the surface of the film can be calculated using the reverse Fourier transform given in Eqn. (2.12).

In summary, we should repeat here that a infinite number of magneti-

---

\* The average value ( $H(k_x = 0, k_y = 0)$ ) can however not be determined that way.

sation patterns exist that generate the same stray field. Therefore, in the best case, the stray field or the magnetic surface charge density can be reconstructed from an MFM image, but not the magnetisation pattern. Further to the reason explained at the beginning of this section, mathematical limitations can be seen in equation (2.17). Indeed, if one wishes to determine the magnetisation pattern from the stray field, equation (2.17) has to be solved for  $\vec{M} = (M_x, M_y, M_z)$ . Since, for  $k = 0$  the first factor vanishes, the average magnetisation cannot be accessed from the stray field (average magnetisation of an infinite film does not generate stray field). Only when some extra information is known about the sample (for example : that the total magnetisation is constant or that the magnetisation is only along  $z$ ), can the magnetisation be determined.

### *Stray field of a thin ferromagnetic film*

As this thesis focuses on thin films, it is instructive to consider the specific case of a slab-like sample with thickness  $d$  and infinite planar dimensions (Fig. 2.4). In order to understand MFM image formation and the interpretation of these images, we calculate the stray field of such a sample. The top surface is at

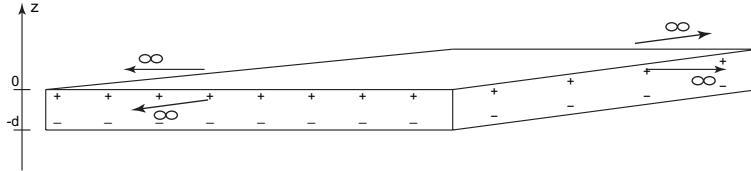


**Fig. 2.4:** Schematics of a thin infinite film of thickness “ $d$ ”.

$z = 0$  and the bottom surface at  $z = -d$ . The magnetisation varies in  $x$  and  $y$  but remains perpendicular to the surface of the sample,  $\vec{M} = (0, 0, \pm M_z(x, y))$ . Such a film only has magnetic surface charges on the top and bottom surfaces and these are equal to  $\pm M_z$ . The boundary conditions are then  $H_z|_{z=+0} = \frac{1}{2}M_z(x, y)$  and  $H_z|_{z=-d+0} = -\frac{1}{2}M_z(x, y)$ . As explained in section 1.2.2, the factor  $1/2$  arises from the fact that the magnetic surface charge generates a stray magnetic field above the upper surface of the sample (outside) and the demagnetising field of the same size but opposite direction below the upper surface of the sample (inside). Using Eqn. (2.13) and the boundary conditions, the Fourier components of the stray field become



$$\begin{aligned}
H_{x,y}(\vec{k}) &= \frac{e^{-k \cdot z} \cdot (1 - e^{-k \cdot d})}{2ki} \cdot k_{x,y} \cdot M_z(\vec{k}) \\
&\equiv \text{HTF}_{x,y}(k) \cdot M_z(\vec{k})
\end{aligned} \tag{2.18}$$

$$\begin{aligned}
H_z(\vec{k}) &= \frac{e^{-k \cdot z} \cdot (1 - e^{-k \cdot d})}{2} \cdot M_z(\vec{k}) \\
&\equiv \text{HTF}_z(k) \cdot M_z(\vec{k})
\end{aligned} \tag{2.19}$$

where  $d$  is the sample thickness,  $M_z(\vec{k})$  is the Fourier transform of the magnetisation  $M_z(\vec{r})$  and  $\text{HTF}_{x,y}(k)$  and  $\text{HTF}_z(k)$  are transfer functions transforming the Fourier transform of the magnetisation to that of the  $xy$  and  $z$  components of the field, respectively. To estimate this stray field, we consider the sample defined above with a magnetisation as a stripe domain pattern with a wavelength  $\lambda$  in the  $x$  direction. Equation 2.19 is interesting in many aspects.

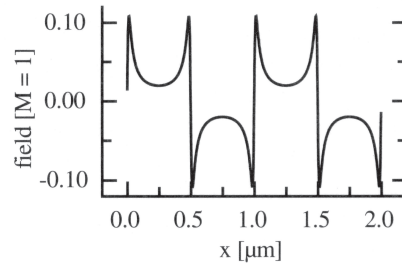


**Fig. 2.5:** Stray field of a thin film sample with unit perpendicular magnetisation and a periodic stripe domain pattern along  $y$  with a wavelength  $\lambda$  100 times larger than the film thickness, measured at a distance  $z = 0.01\lambda$  from the surface (c.f. Fig. 2.3)<sup>52</sup>.

First, it shows that even a perfect magnetic monopole tip has a resolution dependant on the tip-sample distance. Secondly, it can be noted that the field in the centre of the domains becomes small at the surface of the sample, because fields generated by magnetic charges at the top and bottom surface almost compensate (c.f. Fig. 2.5).

### 2.2.3 PRINCIPLES OF CONTRAST FORMATION

The effect of a force on the oscillation of a cantilever has been presented in Sect. 2.1.1. The origin of this force is now investigated in this section. The basis of an MFM experiment is the magnetic tip attached to a cantilever. In order to understand image contrast formation, the interaction of this tip with the sample stray field must be understood, therefore a sufficient knowledge

of the tip is required. Two different methods can be used: the first one is to assume a tip behaviour. Monopole, dipole<sup>67,68</sup> or more complicated models can be used<sup>56,62,63</sup>. Since every tip is different and since very little is known about the geometry and the magnetic layer behaviour of the tip, it can be difficult to find a model suiting the experiment. In addition, it was found that, in case of a dipole tip, the magnitude of the dipole must be dependant on the size of the calibration pattern (or on the characteristic wavelength)<sup>56,68</sup>. Thus a second approach is needed. This one, which is used in this thesis, determines the real tip response function from a carefully designed calibration experiment. This method is greatly simplified when working in Fourier space.

All results in this section are only valid in the limited case when the tip does not affect the sample and vice-versa<sup>18,52,56</sup>, which is a safe assumption in our experiments\*.

### *Calculation of the force applied on the tip*

*Direct space:* The force action on the magnetic tip is given by a convolution of the tip magnetisation distribution with the sample stray field. It can be calculated from the magnetostatic energy of the tip/sample system (c.f. Eqn. (1.11)) :

$$E_{ms}(x, y, z) = \mu_0 \iiint_{V'} \vec{M}_{tip}(x', y', z') \cdot \vec{H}_{sample}(x+x', y+y', z+z') dV' \quad (2.20)$$

where the integration is performed in the primed coordinate system over the full tip volume  $V'^{\dagger}$ . The  $z$  component of the force acting on the tip is then ( $\vec{F} = -\vec{\nabla} E_{ms}$ ):

$$F_z(x, y, z) = -\mu_0 \iiint_{V'} \vec{M}_{tip}(x', y', z') \cdot \frac{\partial}{\partial z} \vec{H}_{sample}(x+x', y+y', z+z') dV'. \quad (2.21)$$

The other components of the force are easily evaluated by replacing the derivative in equation (2.21) by the corresponding lateral derivatives.

The expression in equation (2.21) is rather complicated to evaluate since it is a 3D integration over the full volume of the tip (which is not known except in some simplistic models). Working in Fourier space simplifies the situation greatly.

---

\* The procedure explained below can only be applied on carefully done measurements, i.e. a soft (small  $H_c$ ) magnetic sample needs a weak (small magnetisation) magnetic tip and a strong sample has to be measured with a hard tip, or at large tip-sample distance.

<sup>†</sup> The prime coordinate system is attached to the tip and the non-primed coordinate system is attached to the sample surface as described on figure 2.3.

*Fourier space:* At this step it is useful to change coordinates from  $(x', y', z')$  to  $(\tilde{x}' - \tilde{x}, \tilde{y}' - \tilde{y}, \tilde{x}' - \tilde{z})$  ( $(\tilde{x}', \tilde{y}', \tilde{x}') = (x + x', y + y', z + z')$ ) (c.f. Fig. 2.3). Once written in these new coordinates, the expression of the force (Eqn. (2.21)) takes the form of a convolution of the field ( $\vec{H}_{sample}$ ) and the magnetisation ( $\vec{M}_{tip}$ ). In Fourier space, a convolution becomes a simple multiplication between the first term and the complex conjugate of the second one<sup>69:p.1457</sup>:

$$\begin{aligned}\vec{F}(\tilde{x}, \tilde{y}, \tilde{z}) &= -\mu_0 \iiint_{V'} \vec{H}_{sample}(\tilde{x}', \tilde{y}', \tilde{z}') \vec{\nabla}' \vec{M}_{tip}(\tilde{x}' - \tilde{x}, \tilde{y}' - \tilde{y}, \tilde{z}' - \tilde{z}) d\tilde{V}' \\ &\quad \downarrow \text{2D Fourier transform} \\ \vec{F}(k_{\tilde{x}}, k_{\tilde{y}}, \tilde{z}) &= -\mu_0 \int_{-\infty}^{\infty} \vec{H}_{sample}(k_{\tilde{x}}, k_{\tilde{y}}, \tilde{z}') \vec{\nabla}' \vec{M}_{tip}^*(k_{\tilde{x}}, k_{\tilde{y}}, \tilde{z}' - \tilde{z}) d\tilde{z}'\end{aligned}\tag{2.22}$$

where “\*” denotes the complex conjugate\*. Returning to the previous coordinates, and using a decreasing exponential field dependance versus the product of the k-vector magnitude ( $k = \sqrt{k_x^2 + k_y^2}$ ) and the tip-sample distance ( $z$ ) (c.f. Eqn. (2.13)), the force then takes the following form :

$$\begin{aligned}\vec{F}(\vec{k}, z) &= -\mu_0 \int_{-\infty}^{\infty} \vec{H}_{sample}(\vec{k}, z' + z) \vec{\nabla}' \vec{M}_{tip}^*(\vec{k}, z') dz' \\ &= -\mu_0 \vec{H}_{sample}(\vec{k}, z') \int_{-\infty}^{\infty} e^{-kz'} \vec{\nabla}' \vec{M}_{tip}^*(\vec{k}, z') dz' \\ &= \mu_0 \vec{H}_{sample}(\vec{k}, z') \cdot \sigma_{m,tip}^*(\vec{k})\end{aligned}\tag{2.23}$$

where  $\sigma_{m,tip}^*(\vec{k})$  is the Fourier transform of a tip-equivalent surface charge pattern (or the tip-transfer function), with the surface charges located in a plane at the apex of the tip, parallel to the sample (c.f. Eqn. (2.8)). We have so far calculated the force exerted by the sample on the tip. We can now use this relationship to describe how this force gives rise to image contrast.

### ***Relation between the force and the measured contrast***

From the force vector shown in equation (2.23), we now derive the measured quantity in the MFM experiment. This is either the force  $F_n(\vec{k})$ , or its derivative in dynamic mode  $dF_n(\vec{k})/dn$  (c.f. section 2.1), in the direction of the normal to the cantilever surface, characterised by the vector  $\vec{n} = (0, \sin \phi, \cos \phi)$ , where  $\phi$  is the canting angle between the lever normal and the surface normal

---

\* Note that  $\vec{\nabla} = (ik_x, ik_y, -k)$  is not valid inside the tip. For the tip magnetisation in 2D Fourier space,  $\vec{\nabla}' = (ik_x, ik_y, \frac{\partial}{\partial z})$ .

(see Fig. 2.3). Previous work show that<sup>70</sup>

$$\begin{aligned} F_n &= (\vec{n} \cdot \vec{F}) \\ \frac{d}{dn} F_n &= \vec{n} \cdot \vec{\nabla} F_n. \end{aligned} \quad (2.24)$$

Inserting Eqn. (2.23) and Eqn. (2.16) into Eqn. (2.24), it follows:

$$\begin{aligned} F_n(\vec{k}) &= -\vec{n} \cdot \left( \mu_0 \sigma_{m,tip}^*(\vec{k}) \frac{\vec{\nabla}}{k} H_z(\vec{k}) \right) \\ &\stackrel{\text{LCF}(\vec{k}, \phi) = -\vec{n} \frac{\vec{\nabla}}{k}}{\equiv} \mu_0 \sigma_{m,tip}^*(\vec{k}) \text{LCF}(\vec{k}, \phi) H_z(\vec{k}) \end{aligned} \quad (2.25)$$

$$\frac{d}{dn} F_n = -k \mu_0 \sigma_{m,tip}^*(\vec{k}) [\text{LCF}(\vec{k}, \phi)]^2 H_z(\vec{k}) \quad (2.26)$$

$$= \mu_0 \sigma_{m,tip}^*(\vec{k}) [\text{LCF}(\vec{k}, \phi)]^2 \frac{\partial}{\partial z} H_z(\vec{k}) \quad (2.27)$$

where  $\text{LCF}(\vec{k}, \phi)$  is the **lever canting function**, which describes the effect of the canting angle of the lever on the measurement (further illustration of this effect is given in section 3.2.3 of P.J.A. van Schendel's thesis<sup>56</sup>).

Equation 2.27 represents the relation between the measured quantity and the  $z$  derivative of the stray field. One sees that this relation depends on the tip transfer function (tip equivalent surface charge pattern) and also on the lever canting function.

### *Instrument calibration function*

The relationship described in the previous section enables us to explain the calibration procedure used in this thesis. In addition to  $\sigma_{m,tip}(\vec{k})$ , it is useful to define an *Instrument Calibration Function*  $\text{ICF}(\vec{k})$ , to describe the imaging properties of the instrument for a given feature wavelength (via  $\vec{k}$ ). Indeed, using the LCF instead would require the knowledge of the tip transfer function. The following section presents a calibration procedure in which the *Instrument Calibration Function* (ICF) is determined. The ICF contains the properties of the electronics, the lever (including the canting angle) and the tip. The ICF gives directly the relation between the sample stray field derivative and the measured quantity (frequency shift:  $\Delta f$ ), and can directly be determined from the calibration measurement. The advantage of this method is to allow quantitative measurement of the stray field without having to explicitly know the lever and tip properties. However,  $\sigma_{m,tip}(\vec{k})$  can only be determined if one knows the canting angle and the mechanical properties of the cantilever (force constant and resonance frequency). Using Eqn. (2.6), Eqn. (2.27) and Eqn. (2.14) it is possible to derive  $\text{ICF}_{dH_z}^{\Delta f}(\vec{k})$  defined as the function which

relates the stray field derivative to the measured resonance frequency shift :

$$\begin{cases} \Delta f(\vec{k}) &= \text{ICF}_{\text{d}H_z}^{\Delta f}(\vec{k}) \cdot \frac{\partial}{\partial z} H_z(\vec{k}) \\ \text{ICF}_{\text{d}H_z}^{\Delta f}(\vec{k}) &= -\frac{f_0}{2c_L} \mu_0 \sigma_{m,\text{tip}}^*(\vec{k}) [\text{LCF}(\vec{k}, \phi)]^2 \end{cases} \quad (2.28)$$

where  $f_0$  is the resonance frequency and  $c_L$  the force constant of the free cantilever. Once that calibration function is determined, any image acquired under the same condition (same instrument and tip) can be translated from frequency shift to stray field derivative. The next section describes a way to obtain ICF using a calibration sample.

### **Calibration procedure**

The aim of this procedure is the determination of the ICF defined in Eqn. (2.28). In addition, the calibration procedure developed by van Schendel et al.<sup>56,63</sup>, does not need any assumptions about the distribution of the magnetic charges on the tip. However, the choice of the calibration sample is important. It must have a magnetisation direction perpendicular to the sample plane and homogenous throughout the film thickness ( $M = (0, 0, \pm M_s(x, y))$ ). In addition, the saturation magnetisation value has to be known precisely for the corresponding measurement temperature. The tip/sample interaction must be negligible. Finally, the size distribution of the magnetic domains should be comparable to those of the measured sample.

In the following, the procedure is explained and the parameters used are emphasised at each step. The calibration procedure is based on Eqn. (2.28). The ICF can only be calculated from an MFM measurement if the stray field of the sample is known. This stray field originates from the magnetisation distribution inside the sample which can be determined by applying a discrimination procedure to an MFM image as seen on figure 2.6(b) (*The Sample must be magnetised perpendicular and the saturation magnetisation must be known*).

From this magnetisation pattern, the z-derivative of the stray field can then be computed (see figure 2.6(c)) for a plane parallel to the sample surface, touching the apex of the tip using Eqn. (2.19) and Eqn. (2.16). (*The tip-sample distance and the calibration sample thickness must be known*).

The  $\text{ICF}_{\text{d}H_z}^{\Delta f}(\vec{k})$  is then obtained by a division of the Fourier components of the measurement by those of the stray field derivative as seen in figure 2.6(d) (*The ICF represents the response of the instrument as a function of wave vector  $\vec{k}$* ).

Calibration errors due to sample topography and uncertainties in the estimated magnetisation can be reduced by averaging over several calibration

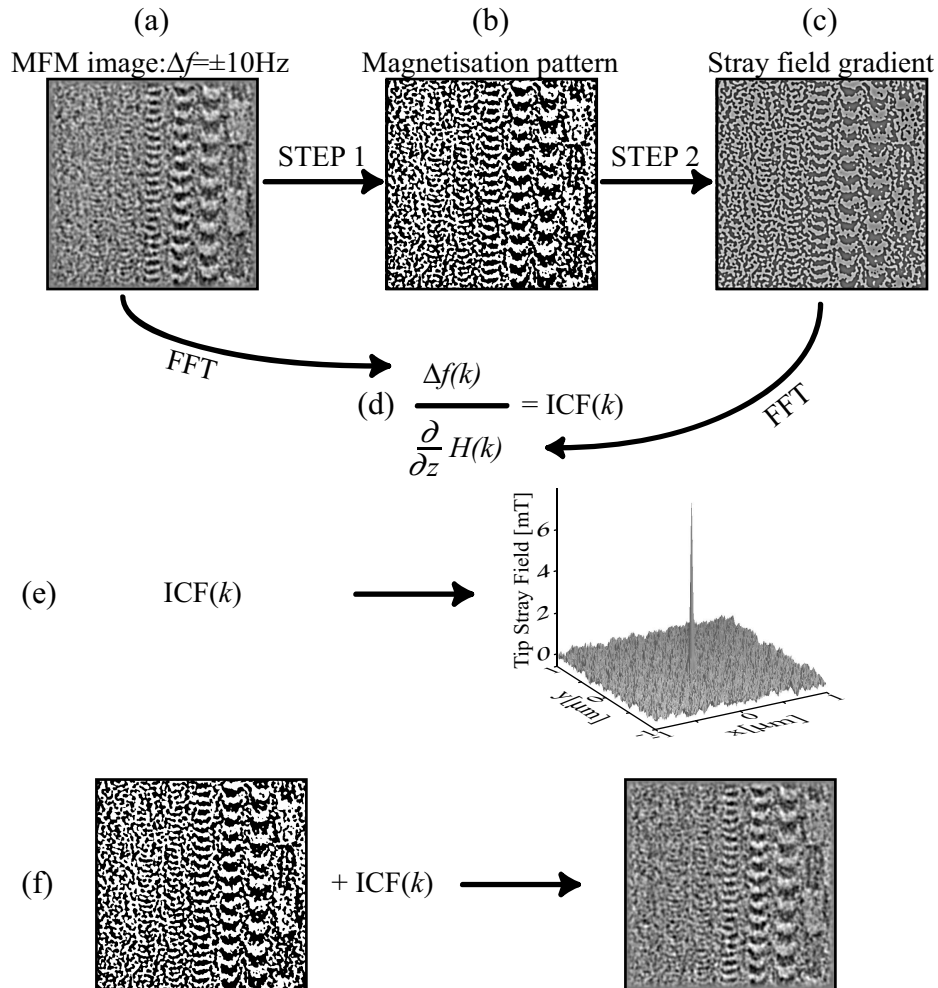


**Fig. 2.6:** Procedure to calibrate an MFM tip (in this case tip D564) : (a) A calibration measurement is done on a sample with perpendicular anisotropy and a large distribution of magnetic domain sizes. (b) The magnetisation pattern is determined by a discrimination process. (c) From the magnetisation pattern the stray field gradient is calculated. (d) Finally the ICF is calculated by dividing the Fast Fourier Transform (FFT) of the acquired image by the FFT of the stray field gradient. Then the ICF can be used to (e) simulate an image from the magnetisation pattern or (f) to calculate the tip stray field.

functions, obtained from different MFM measurements.

The ICF has Fourier space coordinates (2D matrix of complex numbers), thus it cannot be represented as it is. However, it is useful to get an idea of the response of the system versus the frequency measured, by looking at a 1-D representation of the ICF (see for example figure 2.12(b)). This representation is calculated by a circular average of the frequency components having different directions but the same wave vector magnitude  $k$  in Fourier space. The resulting spectrum is called **sensitivity spectrum** and allows the comparison of the sensitivity of the tip to various wave vectors contained in the magnetisation pattern of the sample.

### *Calculation of the tip stray field*

It has been shown above, that to calculate the stray field, using the ICF, the equivalent charge distribution of the tip does not necessary have to be known. However, it can be useful to know the stray field of the tip (for example to evaluate the risk of the tip modifying the sample). If the physical properties of the cantilever are known (canting angle, resonance frequency and spring constant), that can be done using Eqn. (2.28) (c.f. figure 2.6(e)). It gives:

$$\sigma_{m,tip}^*(\vec{k}) = -\frac{2c_L}{\mu_0 f_0} \frac{\text{ICF}_{dH_z}^{\Delta f}(\vec{k})}{[\text{LCF}(\vec{k}, \phi)]^2} \quad (2.29)$$

The stray field of the tip below the plane containing the equivalent charge distribution can be calculated from  $\sigma_{m,tip}^*(\vec{k})$  using the expression:

$$\vec{H}_{tip}(\vec{k}) = -\frac{1}{2} \begin{pmatrix} -ik_x/k \\ -ik_y/k \\ 1 \end{pmatrix} \cdot e^{k(z'-z)} \cdot \sigma_{m,tip}(\vec{k}) \quad (2.30)$$

with  $z$  the distance from the tip to the sample, and  $z' < z$  the distance from the field position to the sample. Knowing  $\sigma_{m,tip}$  (c.f. Eqn. (2.29)), the force on the tip from the field of the sample can be evaluated using equation (2.23). The  $z$  component of the tip field at ( $z = z'$ ) is especially relevant as it is the field from the tip applied on the sample surface. It is given by  $H_{z,tip}(z = z') = -1/2 \cdot \sigma_{m,tip}(\vec{k})$ .

### *Quantitative analysis of MFM Images*

The ICF can also be used to quantitatively analyse an MFM image. In addition to the possibility to calculate the stray field of a sample, the ICF can be used

to simulate a measurement by calculating the stray field derivative of the magnetisation pattern extracted from this measurement (c.f. Eqn. (2.31) and figure 2.6(f)). This is a way to test the validity of the assumption used in the simulation.

$$\begin{aligned}
 \text{Measure } (\Delta f) &\rightarrow \text{Magnetisation pattern} \rightarrow \text{Stray field derivative } \left(\frac{\partial}{\partial z} H_z\right) \\
 &\downarrow \\
 \Delta f_{\text{sim}}(\vec{k}) &= \text{ICF}_{\frac{\Delta f}{dH_z}}(\vec{k}) \cdot \frac{\partial}{\partial z} H_z(\vec{k}) \\
 &\downarrow \\
 \Delta f_{\text{sim}}(\vec{k}) &\stackrel{?}{=} \Delta f
 \end{aligned} \tag{2.31}$$

This simulation assumes a uniform perpendicular magnetisation (similar to the calculation of the ICF). Thus, comparing it with the acquired data allows us to assess the validity of the assumption. In addition, adjustments to the magnetisation pattern can be made to take into account non-perpendicular patterns such as a ripple pattern or closure caps. This quantitative use of MFM is employed in chapter 3, section 3.3.

## 2.3 Complementary Magnetic Analysis : Vibrating Sample Magnetometry

The relevance of the magnetic hysteresis loop for the understanding of a sample's magnetic properties was discussed in section 1.4. The shape of the hysteresis loop gives information about the magnetic reversal mechanism and some of the energies involved can be obtained by an appropriate integration of the curve.

In parallel with MFM, magnetometry measurements to obtain the hysteresis loop were carried out using a vibrating sample magnetometer. The measurement principle consists of detecting a current or voltage induced in a circuit placed close to the magnetic sample in a vibrating motion, hence the name **vibrating sample magnetometry** (VSM). A brief overview of VSM is given in this section.

VSM exploits the fact that a change in magnetic flux ( $\Phi$ ) induces a voltage in the pickup coils. The definition of the magnetic flux in a surface  $S$  is given by

$$\Phi = \int_S d\phi = \int_S \vec{B}^S \cdot d\vec{S} \tag{2.32}$$



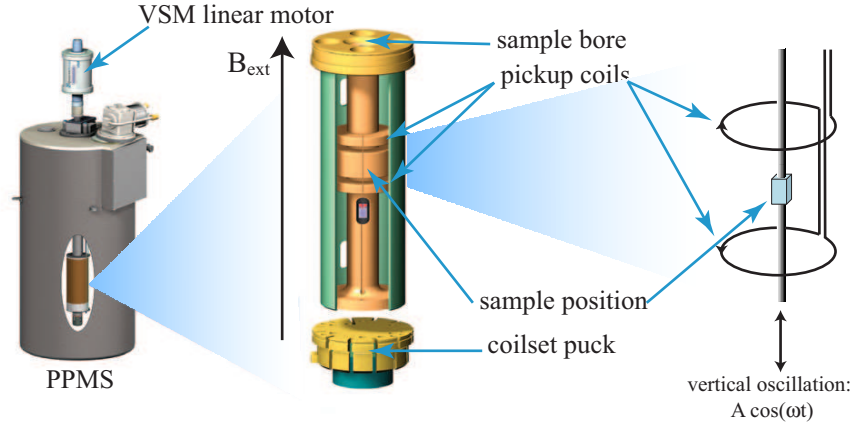


**Fig. 2.7:** *Quantum Design Physical Properties Measurements System (PPMS) with VSM option.* The VSM option for the PPMS consists primarily of a linear motors transport head for vibrating the sample and a oppositely wound coil sets for detection.

where  $\vec{B}^S$  is the magnetic field produced by the sample, and  $d\vec{S}$  is the vector perpendicular to an element on the surface delimited by the pickup coils. If the pickup coil is horizontal,  $d\vec{S}$  is along vertical axis (in  $z$  direction). Furthermore, the surface of the pickup coil can be increased by increasing the coil winding ( $W$ ). Thus equation (2.32) becomes

$$\Phi = AW \cdot B_z^S \quad (2.33)$$

where  $B_z^S$  is the  $z$  component of the magnetic field produced by the sample and  $A$  is the cross-section area of the pickup coil.

If the sample is at a distance  $z$  from the central position of the coil, the vertical component of the magnetic field induced by the magnetic moment of the sample can be written as (Biot-Savart law):

$$B_z^S = \frac{\mu_0 \cdot M}{2\pi \cdot z^3} \quad (2.34)$$

where  $M$  is the vertical component of the magnetic moment of the sample.

For a sinusoidally oscillating sample with an angular frequency of oscillation  $\omega = 2\pi f$  and an amplitude  $\Delta z$  around the position  $z_0$ , the position is given by:

$$z = z_0 + \Delta z \cdot \sin(\omega t) \quad (2.35)$$

and thus the magnetic flux becomes (to the first order):

$$\Phi \approx \frac{AW\mu_0 \cdot M}{2\pi} \cdot \left( \frac{1}{z_0^3} - \frac{3\Delta z \sin(\omega t)}{z_0^4} \right). \quad (2.36)$$

Applying Faradays law of induction  $U_{ind} = -\dot{\phi}$ , the induced voltage in the pickup coils is given by

$$U_{ind} = \frac{3AW\mu_0\Delta z \cdot M \cdot \omega}{2\pi \cdot z_0^4} \cos(\omega t). \quad (2.37)$$

This means that the induced signal in the coils is directly proportional to the component of the magnetisation of the sample parallel to the external field. The acquisition of magnetic moment measurements involves measuring the coefficient of the sinusoidal voltage response from the detection coils. A hysteresis loop measurement consists in measuring the magnetic moment  $M$  as a function of external applied field  $B_{ext}$  generated by a superconducting coil.

To have access to the juvenile curve, the sample can be brought into a demagnetised state prior to a hysteresis loop measurement. A frequently used method to demagnetise a material is to apply an oscillating magnetic field of gradually decreasing magnitude. However the surest method of all would be to heat the material above its Curie temperature and cool it down in zero applied field.

The system used to measure the hysteresis loops presented in this thesis sample is a *Quantum Design Physical Properties Measurements System* (PPMS) with a VSM option (c.f. Fig. 2.7). The measurement is performed by oscillating the sample near a detection pickup coil (doubled to increase the sensitivity) and synchronously detecting the voltage induced. By using a first order gradiometer, consisting of two oppositely wound coils, a relatively large oscillation amplitude (1-3 mm peak) and a frequency of 40 Hz can be reached. The system is able to resolve magnetisation changes of less than  $10^{-9}$  Am<sup>2</sup>. A superconducting coil generates homogeneous field up to 14 T. The system can operate from 300 K down to liquid helium temperature.

## 2.4 LTSFM

All the low temperature\* MFM images presented in this thesis were taken using a homebuilt scanning force microscope operating under ultra high vacuum (UHV)<sup>54–56,71–75</sup>. This section briefly describes this instrument called the

---

\* Most of the measurements were taken at 8.3 K.

**low temperature scanning force microscope (LTSMF).** The LTSMF is housed inside a UHV system (c.f. section 2.4.1). The microscope can be run at temperatures as low as 5 K in a magnetic field up to 7 T (c.f. section 2.4.2). An interferometer system allows the detection of the tip displacement via an optical fibre. The measurements can be run in various SFM modes employing electronics including a phase locked loop, an amplitude feedback loop and a tip-sample feedback (c.f. section 2.4.3).

#### 2.4.1 UHV SYSTEM

The UHV-system consists of two main UHV-chambers as shown in the side view schematic in figure 2.8(a). The whole UHV system has a base pressure of  $1 \times 10^{-10}$  mbar. The microscope chamber is attached to the cryostat, and the analysis and preparation chamber are separated from the microscope chamber by a valve. The analysis chamber contains optics for low energy electron diffraction (LEED) and Auger electron spectroscopy. The preparation chamber contains a heatable and coolable xyz-manipulator, a triple electron-beam evaporator\*, a quartz microbalance thickness monitor, a sputter gun, a mass spectrometer and a crystal cleaver. On the rear side of the chamber, a fast entry air lock (not shown) permits an exchange of cantilevers and samples from air to UHV. Over a transport system, samples and cantilevers can easily be transferred from one chamber to the other. The whole UHV-system is mounted on a passive damping table to insulate it from the building noise. The entire system can be baked out at  $\approx 140^\circ\text{C}$ .

#### 2.4.2 MICROSCOPE

The microscope position can be moved from the manipulation position where the tip and sample are changed using a wobble stick manipulator, to the measurement position in the cryostat over a bellows-system, as illustrated in the cross section schematic in figure 2.8(b). Both sample and tip are mounted on special holders described elsewhere<sup>71</sup>, allowing a reproducible positioning ( $\pm 4 - 6 \mu\text{m}$ )<sup>†</sup>. In the measurement position, the microscope sits inside the cryostat. The cone fixed above the microscope contacts a hollow cone inside the cryostat to allow a heat flow in order to keep the microscope cold. In order to control temperature to  $\pm 0.5 \text{ mK}$ , a temperature sensor and a heater are used via a digital feedback loop. To avoid vibration noises, the microscope is spring suspended on the insert and vibration-insulated via Eddy current

---

\* Apart from the EBID tip (c.f. Sect. 2.6.1) all magnetic tips used in this thesis have been prepared by in situ e-beam evaporation.

† This allows to change the tip magnetisation direction without affecting the sample (c.f. Fig. 2.11).

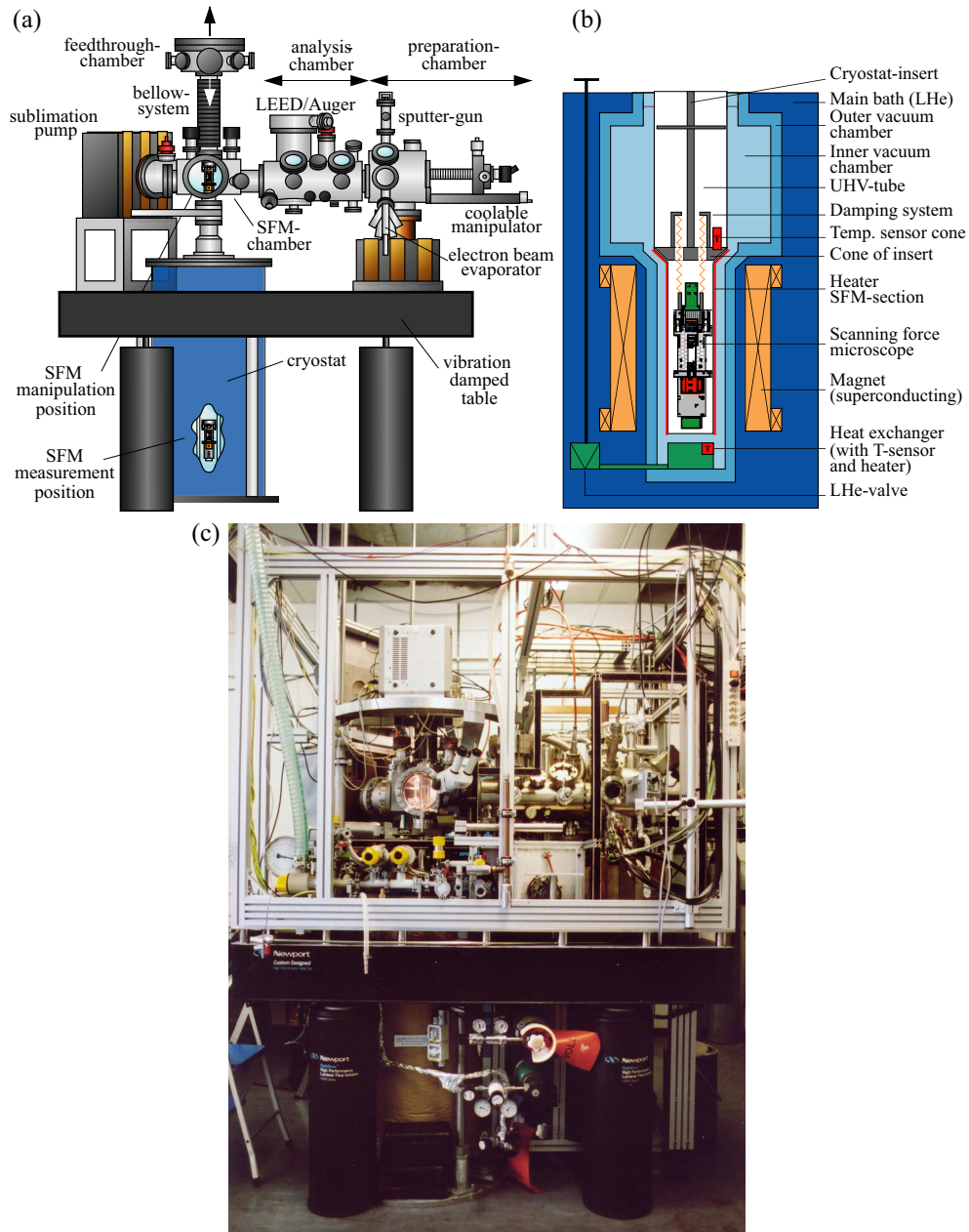


**Fig. 2.8:** Schematics of the LTSFM UHV system. (a) The microscope and preparation chamber can be seen on the left and right respectively. The microscope is attached to the cryostat insert and can be raised for sample and tip manipulation or lowered for measurement at low temperature. (b) The microscope is thermally contacted to the cryostat by the insert copper cone being pressed into the cryostat counterpart.<sup>54</sup> (c) Photo of the LTSFM.

damping. All the electrical wiring and the optical fibre are guided along the cryostat insert.

The sample is mounted on a piezo tube that performs the scan motion in the  $x$ ,  $y$ ,  $z$  directions with a maximum scan range at liquid helium temperature of  $6.5\mu\text{m} \times 6.5\mu\text{m} \times 1.8\mu\text{m}$  respectively. Below the cantilever chip, a piezo actuates the cantilever to oscillate at a given frequency and amplitude. The cryostat also contains a superconducting magnet capable of applying fields up to 7 T perpendicular to the sample surface.

### 2.4.3 ELECTRONICS

A schematic of the scanning and data acquisition electronics as well as the interferometer system is given in figure 2.9. The detection of the cantilever motion is achieved via a fibre-optic interferometer. A cleaved optical fibre end is brought close to (and parallel to) the mirrored backside of the cantilever forming an interferometer\*. If the amplitude of the cantilever is smaller than a quarter of the laser's wavelength and the distance ( $L$ ) between fibre end and cantilever is constant, the interferometer optical signal is proportional to the tip oscillation. In order to keep  $L$  constant, an additional feedback loop is used to drive a piezo on which the fibre is attached. The optical signal is converted by a photodiode into an electric signal (**measurement signal**). This sine-shaped signal is treated by the electronics. The frequency of the sine corresponds to the cantilever frequency and the amplitude can be calibrated using the laser wavelength to calculate the cantilever amplitude<sup>†</sup>, in order to not touch the sample surface with the cantilever chip.

The electronics uses the measurement signal to drive the cantilever at its resonance frequency  $f_0$  with a constant amplitude ( $A_0$ ) and to measure the frequency shift ( $\Delta f$ ) of the cantilever induced by the force interaction (c.f. section 2.1.1). This is achieved using a digital phase locked loop (PLL) developed by Loppacher *et al*<sup>73,74</sup>. As the PLL name implies, a PLL keeps the phase between the cantilever and a reference oscillator locked. The Loppacher system allows the resonance frequency of the cantilever to be measured with a relative accuracy exceeding 1 ppm (part per milion). In addition to the PLL, there is an amplitude feedback and a tip-sample distance feedback (not used in MFM mode but necessary for non-contact AFM mode, c.f. Sect. 2.1 & Sect. 2.2). The recorded data comprises the frequency shift ( $\Delta f$ ), the amplitude ( $A$ ), the voltage applied to drive the cantilever (it gives the dissipation of energy by the cantilever ( $\Gamma$ )) and the variation in tip-sample distance.

These channels are transmitted to the acquisition software (*SCANIT*) developed by Moser *et al*<sup>75</sup>. This software also generates the scan motion ( $x$  and  $y$  scan signal, plus the  $z$  signal to allow slope correction).

\* The cantilever reflection is improved by evaporating an aluminium layer on the backside.

† Note that the cantilever-fibre system is tilted by an angle of  $\phi = 12^\circ$ .

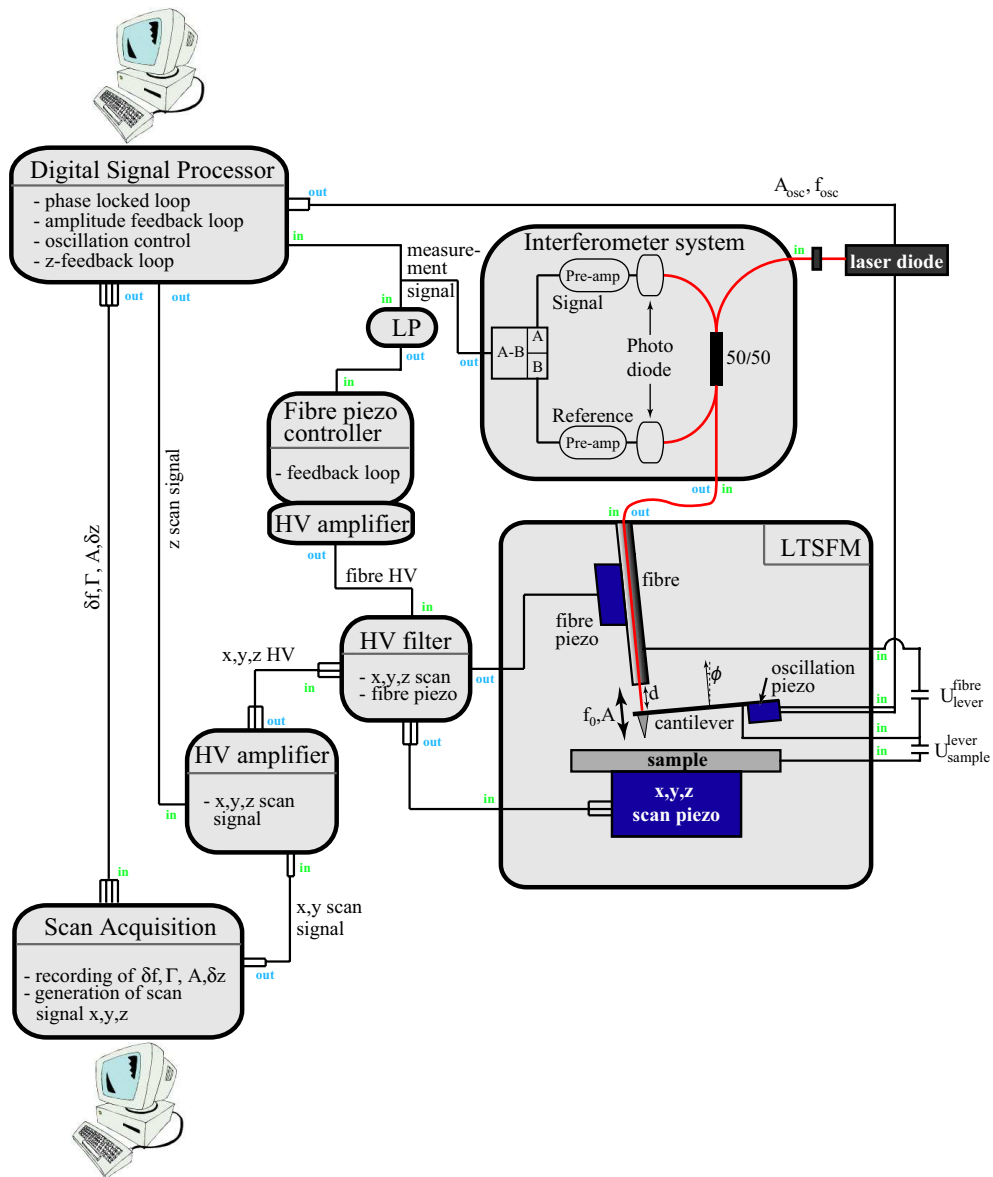


**Fig. 2.9:** Schematic diagram of the LTSFM scanning and data acquisition electronics. The cantilever is driven by a piezoelectric at the frequency  $f_0$  and amplitude  $A$ , detected by an interferometer. <sup>54</sup>

## 2.5 hr-MFM

The high resolution MFM (hr-MFM) used to acquire all room temperature images presented in this thesis is a commercially available instrument sold by a



**Fig. 2.10:** Overview of the hr-MFM instrument including from left to right: The Acquisition computer running the software *Scan Director*, the electronic rack including the *NI Real Time System<sup>TM</sup>*, an oscilloscope, and the high vacuum chamber including the microscope itself<sup>76</sup>.

spin-off company of the university of Basel, *Swissprobe*<sup>©54,76</sup>. The instrument is shown in figure 2.10. It operates at room temperature in a vacuum of  $1 \cdot 10^{-7}$  mbar, achieved in only  $\approx 10$  min. It is mounted on an active vibration isolation with additional internal vibration isolation of the microscope.

The oscillation of the cantilever is detected by a 4-quadrant beam deflection unit for normal and lateral force measurement. Any standard cantilever can be used, with an easy exchange (repositioning precision  $\approx 1 \mu\text{m}$ ). To set the cantilever oscillation, two controllers are used. The amplitude controller keeps the amplitude of the cantilever oscillation constant. The fully digital phase-locked loop (PLL) controller controls the phase of the oscillation and keeps the excitation frequency at the resonance of the cantilever. All loops are set via the software *Scandirector* to allow all common static and dynamic AFM and MFM modes. In addition, a flexible *general scan* concept allows various other measurements such as spectroscopy, which can be used for tip-sample distance estimation. Up to 16 channels can be acquired simultaneously.

The sample stage is optimised for discs up to 120 mm diameter. The coarse motion range in  $r$  and  $\theta$  is 61 mm and  $360^\circ$  respectively. A measurement of the coarse position allows one to find a relative position over the full range with a precision of 100 nm in  $r$  and  $0.0002^\circ$  in  $\theta$ . The maximum  $x, y, z$ , scan range is  $40 \mu\text{m} \times 40 \mu\text{m} \times 6 \mu\text{m}$ .

## 2.6 Tip Preparation

All the tips used in this thesis have been coated with a thin magnetic layer (Fe or Co) to have a strong shape anisotropy of the film which keeps the magnetisation well defined along the tip axis<sup>77</sup>. A brief introduction to tip preparation follows. Some results shown in chapter 3 were performed using a tip obtained by using EBID technique (c.f. section 2.6.1). All the other results were obtained using ultrasharp tips on silicon cantilevers (*Team Nanotec Improved Super Cone* (ISC)) with a thin coating of Co (c.f. section 2.6.2).

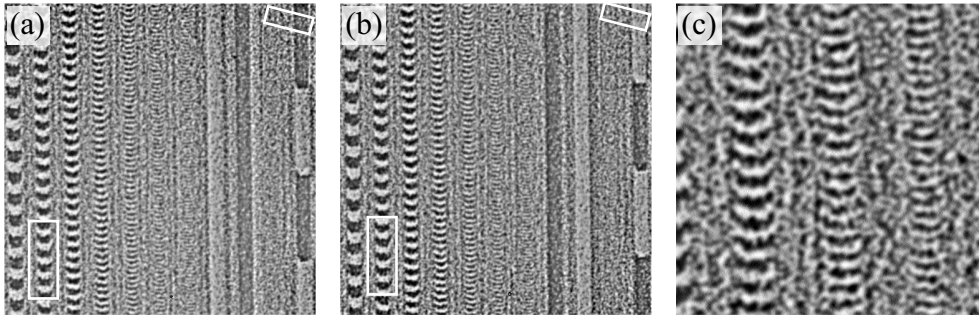


**Fig. 2.11:** (a)  $5 \times 5 \mu\text{m}^2$  area of the perpendicular recording media used to calibrate the tip imaged at 8.3 K by MFM. Various tracks can be seen from DC track to track with 35 nm bit length. (b) Same image at the same temperature after remagnetising the tip in the opposite direction (Note that involves removing the sample during the application of an external field and replacing it after. Thus a reproducible positioning of the sample is required as described in the section 2.4.2). It can be seen that not only the tracks are inverted but also the small spots beside the tracks, showing that they are small domains. (c)  $2 \times 2 \mu\text{m}^2$  MFM image of the same sample.

Two calibration samples were used in this thesis : The tip used for the measurements presented in chapter 3 was calibrated on a Cu/Ni(10nm)/Cu/Si(001) film. The other tips were calibrated using a perpendicular magnetic recording sample exhibiting a strong perpendicular anisotropy\*. Into the magnetic layer, tracks of various bit densities have been written. The bit length ranges from  $2 \mu\text{m}$  down to 21 nm. Besides the tracks, very small domains are formed (c.f. figure 2.11). The thickness and the saturation magnetisation of the coating are 12 nm and  $660 \frac{\text{kA}}{\text{m}}$  respectively.

\* Perpendicular hard drive from Hitachi Global Storage Devices (San Jose, USA).



## 2.6.1 EBID TIP WITH Fe COATING

The tip used to perform the room temperature measurements in chapter 3 is described in this section. A commercial Park Scientific<sup>©</sup> Si<sub>3</sub>N<sub>4</sub> uncoated

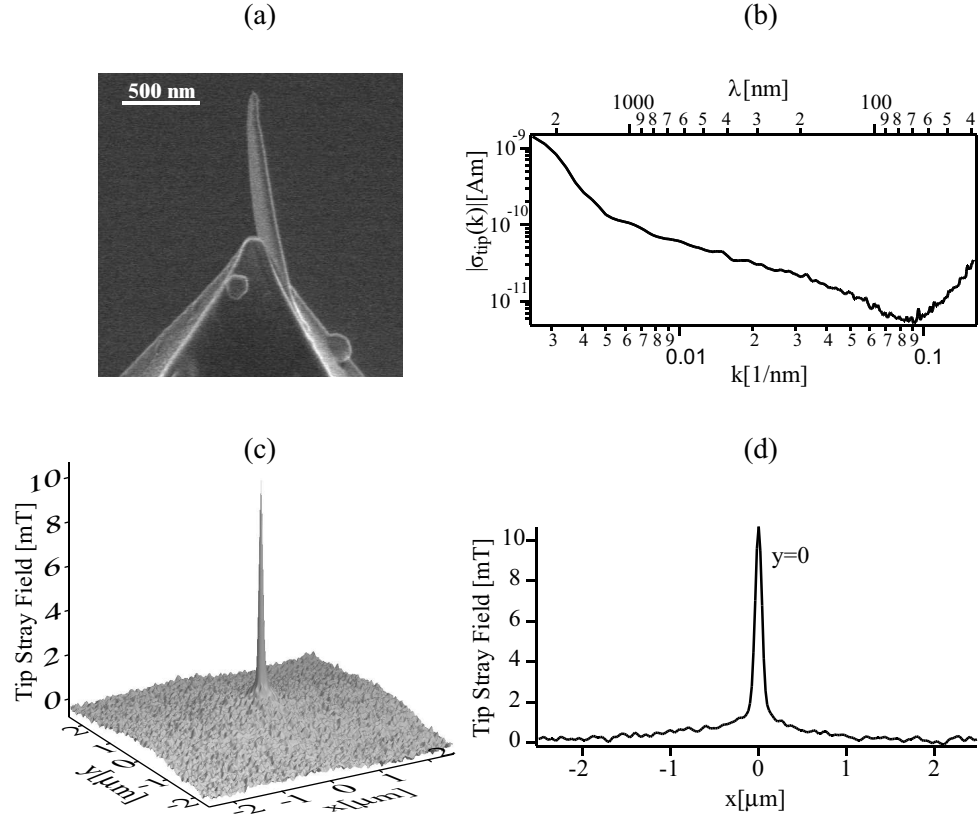


**Fig. 2.12:** (a) SEM image of the EBID tip. (b) ICF extracted from  $5 \times 5 \mu\text{m}^2$  images of Cu/Ni(10nm)/Cu/Si(001). Tip stray field ( $\mu_0 H_{z,\text{tip}}(x, y)$ ) 3D and 2D in (c) and (d) respectively (c.f. Sect. 2.2.3 and App. D.3).

cantilever was used. A needle-like tip has been grown on the pyramid tip by electron beam induced deposition (EBID) of carbon<sup>78,79</sup> (c.f. Fig. 2.12(a)). The needle-like tip was intentionally grown at an angle of approximately twelve degrees to the axis of the pyramid tip, so that it is perpendicular to the surface of the sample (it compensates the angle of  $12^\circ$  between the cantilever and the sample surface (c.f. Sect. 2.4)). This high aspect ratio tip was coated with 10.7 nm iron and 15 nm gold to protect from oxidation. For the coating, thermal evaporation in the  $10^{-7}$  mbar range was used. The evaporation was performed at an angle of  $30^\circ$  to the normal of the lever ( $\hat{n}$  shown in figure 2.3). The resonant frequency and the force constant were  $f_0 = 16500$  Hz and  $c_L =$

0.032 N/m respectively. After the coating, the lever was magnetised in a field of approximately 0.4 T perpendicular to the lever (along  $\hat{n}$ ).

### 2.6.2 ISC TIP WITH Co COATING

The ultrasharp tip from *Team Nanotec GmbH* is cone shaped with a opening angle smaller than  $10^\circ$ . The diameter of the apex of the tip is smaller than 20 nm and the tip height is about  $9\ \mu\text{m}$  (Fig. 2.13(a)). The lever has a spring constant, a free resonance frequency and a length of  $c_L \approx 0.3\ \text{nm}$ ,  $f_0 \approx 40\ \text{kHz}$  and  $l \approx 225\ \mu\text{m}$  respectively. The front end of the cantilever was reflex coated on the backside with 35 nm of aluminium. The magnetic coating is evaporated *in situ* at a pressure of  $10^{-9}$  mBar using an electron beam evaporator after being heated  $\approx 12\ \text{h}$  at  $\approx 120^\circ$ , to remove water. Only one side of the cone shaped tip is coated using an oblique angle evaporation<sup>54</sup>.

Two different magnetic coatings were used in this thesis:

- The first one has been described in a former thesis<sup>55</sup>. A first layer of 1 nm Ti was evaporated at liquid nitrogen temperature as a sticking layer followed by 4 nm Co at room temperature. The tip was then exposed to air for 20 min to oxidise it. This results in  $\approx 2 - 3\ \text{nm}$  Co with a cobalt oxide protecting layer. This tip design provides a high resolution ( $\approx 20\ \text{nm}$ ) and a good sensitivity.
- In order to improve the stability of the tip, we tried to imbed some impurities in the magnetic coating. These defects could increase the coercivity of the tip by hindering the domain wall motion. Thus a small amount of Ti was sandwiched in between two Co layers. The following layers were evaporated: at liquid nitrogen temperature 1 nm Ti plus 1 nm Co and at room temperature  $0.5\ \text{\AA}$  Ti plus 1 nm Co.

The tip coated with this second design was indeed very stable with resolution and sensitivity comparable as the first design. However, no systematic comparison studies were performed. The calibration in figure 2.13 was done for the tip performed using the second design. Before imaging, all cobalt coated tips were magnetised in a field along the tip axis of 1.5 T.

Comparing figure 2.13 and figure 2.12 shows that using a higher aspect ratio tip and decreasing the magnetic coating thickness gives rise to an improved resolution<sup>54</sup>. Indeed, the tip stray field is better localised in the case of the ISC tip (full width at half maximum (FWHM) equal to  $\approx 30\ \text{nm}$ ) than for the EBID tip (FWHM  $\approx 100\ \text{nm}$ ). The maximum stray field is however smaller implying a smaller sensitivity. This has to be expected since the magnetic coating thickness is smaller and since Co has a smaller saturation magnetisation than Fe. The response is higher for larger wavelengths and gets smaller

while imaging smaller wavelengths (c.f. Fig. 2.12(b) and Fig. 2.13(b)). The increasing sensitivity at very small wavelengths is an artefact due to noise in the image<sup>56</sup>.

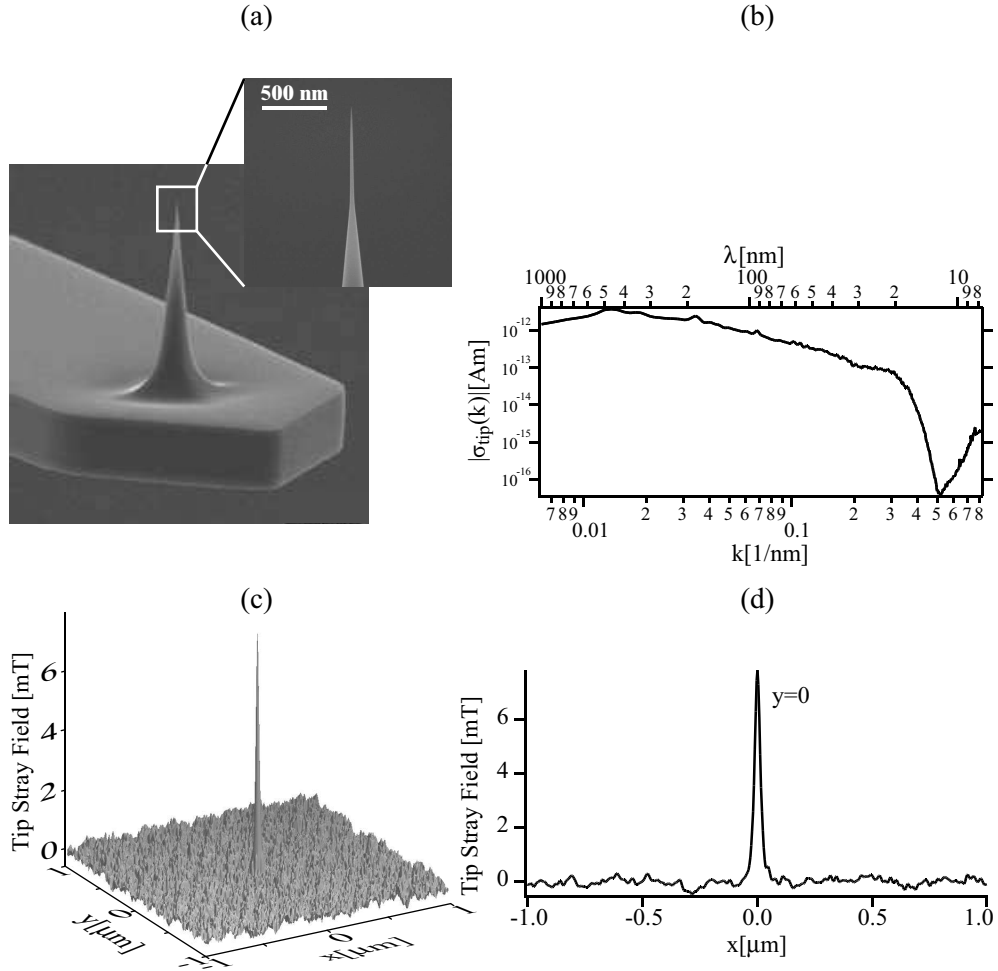


**Fig. 2.13:** (a) SEM image of a standard ISC tip. (b) ICF of an ISC tip coated with a thin cobalt film using the second design. The ICF is calculated from  $2 \times 2 \mu\text{m}^2$  images of a perpendicular recording media. Tip stray field ( $\mu_0 H_{z,\text{tip}}(x, y)$ ) 3D and 2D in (c) and (d) respectively (c.f. Sect. 2.2.3 and App. D.3).





# REMANENCE DUE TO WALL MAGNETISATION COUNTERINTUITIVE

MAGNETOMETRY DATA IN 200 NANOMETRE NICKEL FILMS<sup>17</sup>

## 3.1 Cu/Ni/Cu : a Well Studied System Yet to Reveal All its Secrets

### 3.1.1 Ni FILMS, AN INTERESTING SYSTEM

The widespread use of magnetic thin films in contemporary data storage technology, sensors of magnetic field, strain and acceleration, has been made possible by the optimisation of the materials involved, aimed at attaining specific magnetisation structures and M-H characteristics (c.f. Sect. 1.4). Indeed, magnetic thin films with an easy axis of magnetisation perpendicular to the surface (due to a perpendicular magnetic anisotropy) have attracted particular attention due to their potential advantage in high-density magnetic recording media<sup>10-13,80</sup>. In addition, magnetic thin films with perpendicular anisotropy provide a model system of domain behaviour in a wide variety of materials. Many (material) systems exhibit maze domain patterns that evolve to stripe domains, then large-scale domain growth upon application of an appropriate force<sup>19,81-83</sup>. These processes are often characterised by hysteresis.

More particularly, thin films of nickel have been shown to be of great interest because of their intrinsic magnetic properties (c.f. Sect. 1.9). Namely, the small saturation magnetisation (compared to Co or Fe) results in a relatively small magnetostatic energy density ( $e_{ms,Ni} \sim \frac{1}{10} e_{ms,Fe}$ ) and thus strain induced anisotropies can be dominant over shape anisotropy. Secondly, Ni has a large positive bulk magnetoelastic coupling coefficient<sup>16,84</sup> so the tendency toward perpendicular magnetic anisotropy is high (in Ni/Cu,  $K_\epsilon = 10^5 \text{J/cm}^3$  for 2% misfit strain). Thirdly, the magnetocrystalline anisotropies are rather small at room temperature. Finally, in the case of the Ni/Cu interface, as both metals are fcc with a small lattice misfit, coherent growth is possible and favours good epitaxy. These properties give rise to an unusual sequence of transitions in the direction of the magnetisation.

### 3.1.2 PREVIOUS STUDIES ON Cu/Ni/Cu

The nickel/copper interface was one of the first systems used to study the misfit accommodation in thin films<sup>85,86</sup>. Indeed, the misfit strain of the nickel on copper is about 2.6%, large enough to be considered, but not too large that it could prohibit epitaxial growth<sup>37</sup>. Therefore a lot of interest has been shown in studying the strain<sup>37,84,87-90</sup> of Ni/Cu systems and its effects<sup>16,32,38-40,91</sup>, as a model for the technologically relevant phenomenon of perpendicular magnetisation. From studies of the strain itself, we see that epitaxial nickel on copper is under a biaxial tensile stress due to the lattice mismatch in their bulk form. This lattice mismatch gives rise to an isotropic strain in the (001) plane ( $\varepsilon_{\parallel}$ ) and an out-of-plane compressive strain ( $\varepsilon_{\perp}$ ) due to the Poisson effect. We also see that, in the case of Cu/Ni/Cu the dependance of the strain with Ni thickness ( $t$ ) follows a  $(1/t)^{\frac{2}{3}}$  law (c.f. Sect. 1.6.3). Thus in the case of large thicknesses (for example the 200 nm thick film studied here), the tensile strain is largely relieved\* (c.f. Tab. 3.1). Regarding the effect of this strain on Cu/Ni/Cu properties, we begin by noting that for small Ni thickness  $t$ ,  $3 \text{ nm} < t < 14 \text{ nm}$  (c.f. figure 3.1), a strong perpendicular magnetisation is observed by magneto-optic Kerr effect<sup>40</sup>, vibrating sample magnetometry (VSM)<sup>38</sup>, torque magnetometry<sup>15</sup> and magnetic force microscopy (MFM)<sup>14,39</sup>. It is possible to account for these observations using a uniform magnetisation model with effective uniaxial anisotropy for the free energy<sup>37-40</sup>,  $f = K_{\text{eff}} \sin^2 \theta$ .

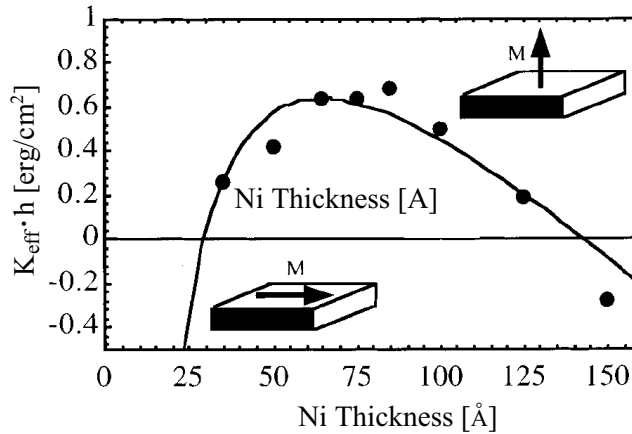


**Fig. 3.1:** Dependence of  $K_{\text{eff}} \cdot h$  on Ni film thickness ( $h$ ) in Cu/Ni/Cu(001) sandwiches. The perpendicular magnetic anisotropy dominates over a large Ni thickness range from 2 nm to 14 nm (after Hug *et al*<sup>14</sup>).

As described in section 1.6.6, the coefficient  $K_{\text{eff}}$  includes contributions

\* by the formation of dislocations.

from the magnetoelastic and interface anisotropies ( $> 0$ ) and the magnetostatic energy  $K_{ms}$  ( $= -\frac{1}{2}\mu_0 M_s^2$ , where  $M_s$  is the saturation magnetisation and  $\mu_0$  is the vacuum permeability). The magnetocrystalline anisotropy  $K_{mc}$  is small and can be neglected (c.f. table 3.1). The magnetoelastic anisotropy  $K_\epsilon$  arises from the Cu/Ni misfit, and a surface anisotropy  $K_s$  is evident for each Ni/Cu interface. When  $K_{eff} > 0$  the perpendicular magnetisation is stable in a field  $H = 0$ .

Sat. magnetisation	$\mu_0 M_s$	0.603 T
Magnetostatic energy	$-\mu_0 \frac{M_s^2}{2}$	-145 kJ/m <sup>3</sup>
Magnetocryst. anis. (c.f. Sect. 1.8)	$K_{mc}$	-4.5 kJ/m <sup>3</sup>
Mag. elastic anisotropy (Eqn. (1.34))	$K_\epsilon$	45 ± 1 kJ/m <sup>3</sup>
Magn. coupl. coeff. <sup>23</sup>	$B_1$	6.2 MPa
Strains <sup>37</sup>	$\epsilon_{xx} = \epsilon_{yy}$	+3.18 10 <sup>-3</sup>
	$\epsilon_{zz}$	-3.8 10 <sup>-3</sup>
Bloch wall width (Eqn. (1.21))	$\delta_{DW} = \pi \sqrt{A/K_\epsilon}$	47 ± 1 nm
Bloch wall energy (Eqn. (1.24))	$\sigma_{DW} = 4\sqrt{AK}$	2.7 $\frac{mJ}{m^2}$

**Tab. 3.1:** Cu/Ni(200 nm)/Cu/Si(001) system parameters (room temperature).

The above model correctly describes a broad range of perpendicular magnetisation observed in the aforementioned references, as well as the thickness dependence of the effective anisotropy. Since perpendicular magnetisation is predicted between 3 nm  $< t < 14$  nm, these thicknesses have extensively been studied<sup>14,37-40,89,90</sup>. Bochi *et al* has pointed out the importance of domain walls in the process of transition from perpendicular to in-plane magnetisation, with domain wall representing more than half of the film surface area for Ni thickness of 14 nm<sup>39</sup>.

In this thesis we present a study of thicker films. The above model predicts that 200 nm thick Ni films must have an in-plane magnetisation. However, although the model describes the case for a uniform magnetisation, it fails to give any information if the magnetisation shows different arrangements\*. Indeed, some previous studies suggest that the magnetisation pattern for such thicknesses may be more complicated, leaving the situation unclear. Hameed

\* Note that domains are not even taken into account (the value of  $\theta$  is taken constant everywhere) and therefore the prediction is only valid in the centre of a big domain.

*et al* have modified a Malek and Kambersky model<sup>92</sup> to include stripe domain structures with tilted partial flux closure domains to explain the structure and the domain size thickness dependance in the MFM images they measure<sup>42</sup>. Ciria *et al* assume that the magnetisation process consists of the evolution of two kinds of domains. One with a large out-of-plane component of the magnetisation and another with magnetisation along the in-plane direction. This explains both magnetometry and magnetoelastic stress measurements<sup>16</sup>. We show here that, using a combination of magnetometry and qMFM measurements, we are able to give a complete description of the magnetisation pattern for Cu/Ni(200 nm)/Cu/Si(001). Domain walls are shown to have great importance since the in-plane magnetisation measured by magnetometry will be shown to come mainly from Bloch walls.

### 3.1.3 REVISITING MAGNETOMETRY DATA

Many of the parameters needed to describe the films' magnetisation are routinely determined from magnetisation loops<sup>23(chap. 9), 18(chap. 4.3.3)</sup> (c.f. Sect. 1.4). Material optimisation strategies therefore depend on this type of measurement and its interpretation, the understanding of which takes on a singular importance.

A striking example is provided by the 200 nm Ni film grown epitaxially in a Cu/Ni/Cu/Si(001) structure, that we selected for convenience in this work. In this system, the observations defy explanation based on volume averaged magnetometry measurements but come to light when magnetometry is combined with high-resolution, qualitative magnetic force microscopy. In this chapter we explain how the conventional interpretation of the magnetisation loops can give an incorrect picture of both the magnetisation processes and magnetic domain structures in the films.

## 3.2 Instrumentation and Film Growth

### 3.2.1 INSTRUMENTATION

The MFM measurements were made at constant average tip-sample distance, in the dynamic variable frequency mode, which determines the shift  $\delta f$  of the cantilever resonance frequency  $f_0$  (c.f. Sect. 2.2). Magnetisation structures ( $M_z$ ) can be inferred from the stray fields ( $H_z$ ) with knowledge of the instrument calibration or the tip transfer function  $\sigma_{m,tip}^*(\vec{k})$ , which was determined as described in section 2.2.1 and 3.3.



### *Room temperature measurement*

The room temperature MFM results were obtained in a vacuum in the  $10^{-7}$  mBar range in a microscope similar to the LTSFM described in section 2.4. With this microscope all images were taken in zero applied field. The cantilever and tip used are described in section 2.6.1. After coating, the tip was magnetised with a field of  $\approx 0.4$  T oriented along the axis of the tip.

### *Low temperature measurement*

The low temperature MFM results were obtained at  $\approx 9$  K in the LTSFM described in section 2.4 allowing us to apply a magnetic field perpendicular to the sample. The cantilever and tip are described in section 2.6.2. After coating, the tip was magnetised with a field of 1.2 T oriented along the axis of the tip.

## 3.2.2 GROWTH OF THE FILM

Our Cu/Ni/Cu/Si(001) films were fabricated by *Molecular Beam Epitaxy* (MBE) at a base pressure in the  $10^{-11}$  mBar range. The first Cu layer on the Si(001) substrate is 50 nm thick. It has been shown by reflection high-energy electron spectroscopy (RHEED)<sup>38</sup> that the Cu films grow epitaxially with (001) orientation and with their [100] axis parallel to the [110] axis of the Si wafer. This  $45^\circ$  rotation of the films about their normal decreases the huge lattice mismatch ( $\approx 50\%$ ) between Cu and Si to approximately 6%, thus making the epitaxial growth of Cu(001) on Si(001) possible. It has also been shown by TEM that no relevant interdiffusion at the interface between Cu and Ni occurs.

RHEED measurement and X-ray diffraction show that Ni grows epitaxially on this layer<sup>37</sup>. The 200 nm Ni film is capped with 5 nm of Cu to provide symmetric interfaces and to prevent oxidation of the Ni. The Cu/Ni lattice mismatch is 2.6 % with the Ni-lattice constant being the smaller of the two. Thus the Ni-films are in a state of tensile strain which, at 200 nm of Ni, is largely relieved by the formation of dislocations. Lattice mismatch between Ni and Cu results in strain, which has been measured by synchrotron X-ray scattering (grazing-incidence diffraction (GIXRD) for in-plane strain and the Bragg diffraction for the out-of-plane strain)<sup>37,93</sup> (c.f. table 3.1). More information about film growth can be found in references<sup>37,38</sup>.

### 3.3 Quantitative Magnetic Force Microscopy

In addition to magnetometry, qMFM was used to access magnetic properties of the sample. This section, starting on the basis introduced in section 2.2, seeks to apply qMFM to various magnetisation arrangements. The aim is to use qMFM to elucidate magnetisation structures other than perpendicular through thickness. This will help to further understand magnetometry data.

#### 3.3.1 SIMULATION OF VARIOUS MAGNETISATION PATTERNS

As explained in section 2.2.3, simulation of an MFM image is important to test the assumptions made about the magnetisation pattern. In this section, a more detailed method to simulate ripple patterns or closure domains is described. This complements the method described in section 2.2.3 for through thickness perpendicular magnetisations.

##### *Domain wall thickness*

As seen in section 1.3.2 the transition between domains is not infinitely sharp. There is a transition region called the domain wall which must be taken into consideration when simulating certain magnetisation patterns. Indeed, a Bloch wall changes the magnetic charge compared to a homogeneously magnetised domain. Therefore it is necessary to estimate the difference between a binary domain surface charge pattern, as used in the calibration of the tip, and the real domain pattern. The  $z$ -component of the magnetisation in an isolated domain wall, parallel to the  $xz$ -plane is given by (c.f. section 1.3.2 and appendix C)

$$m_z(y) = \tanh\left(\frac{\pi y}{\delta_{DW}}\right). \quad (3.1)$$

It is assumed here that a wall correction can be achieved by multiplying the Fourier transform of the square pattern with the Fourier transform of the wall transfer function. This function is computed by dividing the Fourier transform of equation (3.1) by the Fourier transform of a step-like wall<sup>56</sup> :

$$M_{z,\text{walls}}(\vec{k}) = \frac{\frac{k\delta_{DW}}{2}}{\sinh\left(\frac{k\delta_{DW}}{2}\right)} M_{z,\text{square}}(\vec{k}). \quad (3.2)$$

This approximation remains valid as long as the walls are not too curved, and they are so far apart that they do not influence one another<sup>56</sup>.

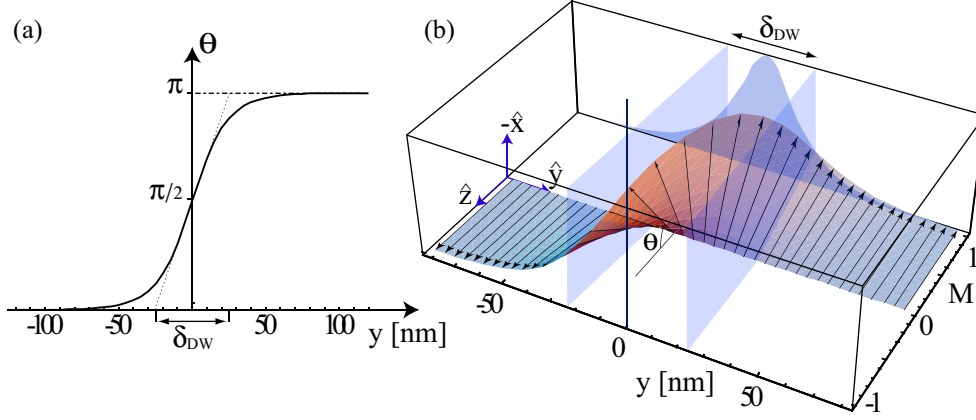


**Fig. 3.2:** Simulation of a Bloch wall for a uniaxial material with  $A = 1 \cdot 10^{-20} \frac{\text{J}}{\text{nm}}$  and  $K_\varepsilon = 45 \frac{\text{kJ}}{\text{m}^3} \Rightarrow \delta_{DW} = 47 \text{ nm}$  (corresponding to the parameters of the 200 nm thick Ni sample of this chapter). (a) The angle between the domain magnetisation and the magnetisation at distance  $y$  inside the domain wall ( $\varphi(y)$ ) is given by equation (1.23). The definition of  $\delta_{DW}$  is represented on the graph ( $\delta_{DW}$  is given by the distance between the intersections of the linear fit of  $\varphi$  at  $\varphi = \frac{\pi}{2}$  and  $\varphi = \{0, \pi\}$ ). (b) Simulation of the magnetisation rotation through a Bloch wall following the procedure described by R. C. O’Handley<sup>23</sup>. The definition of  $\delta_{DW}$  is represented by the blue planes.

### **Ripple pattern :**

Ripples give rise to an out of plane component of the magnetisation varying sinusoidally (c.f. section 1.6.5).

To perform a simulation of the MFM contrast arising from a magnetisation ripples, one may begin with a discrete ( $\pm 1 \cdot M_s$ ) magnetisation pattern. This pattern can then be low-pass filtered to obtain a magnetisation ripple pattern. Alternatively, the discrete magnetisation pattern with infinitely sharp walls can be transformed into a pattern with a domain wall thickness equal to the domain width using the transfer function described by equation (3.2).

The magnitude of the perpendicular magnetisation depends on the angle of the ripple which is simulated, since the perpendicular component of the magnetisation is given by :

$$M_{z,\text{ripple}} = \vec{M}_{\text{ripple}} \cdot \hat{z} = M \cdot \cos\left(\frac{\pi}{2} - \theta_r\right) = M \cdot \sin(\theta_r) \quad (3.3)$$

where  $\theta_r$  is defined as the angle between the ripple and the in-plane magnetisation (c.f. Fig. 3.4).

**Closure domain :**

The case of closure domains is easier to simulate. Since a closure domain implies no uncompensated magnetic charges inside the layer, equation (2.19) can still be used. Indeed, as it can be seen in figure 3.3, the transition between the domain and the closure encloses no charges on average (density of positive charge equal to the density of negative charge in a given volume enclosed by surface  $S$ ). Specifically the magnetisation rotates in a divergence-free way, so the magnetisation flux across the surface  $S$  in figure 3.3 is zero. Only the surface charges enter into consideration and thus the domain itself doesn't produce any contrast in a magnetic force microscopy experiment (this is valid only if the closures extend over the full domain width).

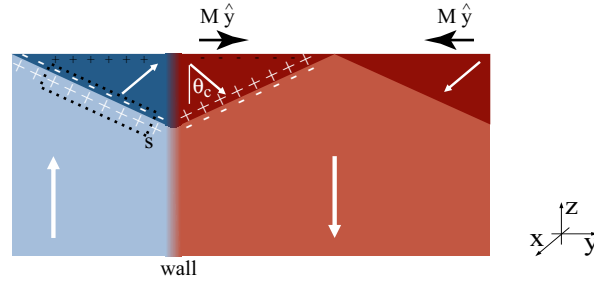


**Fig. 3.3:** Schematic of the canted closure cap. For symmetry reasons no net magnetisation along  $y$  remain. Magnetisation rotates in a divergent-free way from the domain to the closure.

As established above the standard calibration procedure is valid for closure domain simulation. However, the saturation magnetisation value must be decreased by a factor depending on the canting angle. Indeed, the  $z$ -component of the magnetisation is then given by the projection of the magnetisation on the  $z$  axis (c.f. Eqn. (3.4)).

$$M_{z,\text{closure}} = \vec{M}_{\text{closure}} \cdot \hat{z} = M \cdot \cos(\theta_c) \quad (3.4)$$

$\theta_c$  is the angle between the closure magnetisation and the normal to the film (c.f. Fig. 3.4).

### 3.3.2 COMPARISON AND SUMMARY

As it can be seen in figure 3.4 and has been emphasised in the previous paragraphs, perpendicular, ripple or closure capped magnetisation may be differentiated by a careful quantitative MFM experiment. The through thickness perpendicular pattern is shown in figure 3.4(a). The expected frequency shift

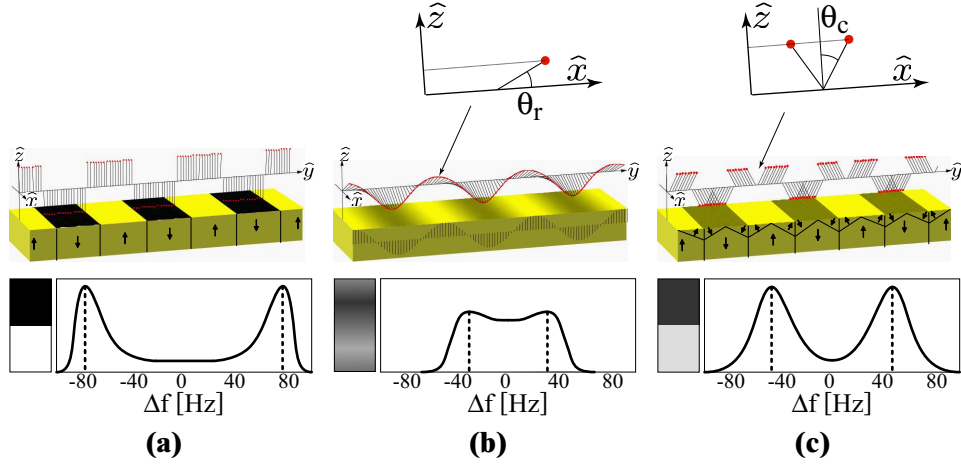


**Fig. 3.4:** Representation of the magnetisation vector and pattern in the case of (a) perpendicular magnetisation (b) ripples (c) perpendicular domain with canted closure cap. The theoretical aspect of the magnetisation pattern and the schematic  $\Delta f$  histogram expected in a MFM experiment is shown for these three cases.

is given by one peak for the black domains and one for the white domains (attractive and repulsive magnetic forces respectively).

In the case of ripples (figure 3.4(b)), it is obvious that the transition between dark and bright domains is smoother, exhibiting the presence of all intermediate frequency shifts. It may also be noted that the total contrast (frequency spread) is weaker, as the magnetisation ripples only at a limited angle ( $\theta_c < \frac{\pi}{2}$ ) around the in-plane direction. The contrast depends on  $\sin \theta_c$ .

The perpendicular magnetisation with a canted closure domain is expected to give rise to a dark and bright contrast similar to the perpendicular magnetisation but with an amplitude diminished by a factor of  $\cos(\theta_c)$ . It must be noted that closure caps with in-plane closure imply no surface charge and therefore no perpendicular component of the magnetisation exactly the same way as in-plane domains. Indeed  $\theta_c = \frac{\pi}{2}$  brings no contrast (in that case contrast may rise only from the domain wall).

## 3.4 Magnetometry

The magnetisation loop  $\vec{M}(\vec{H})$  for the 200 nm film is displayed in Fig. 3.5. Note that the loop is similar to what was observed in previous studies<sup>16,42</sup>. Parameters of this film are indicated in Tab. 3.1.

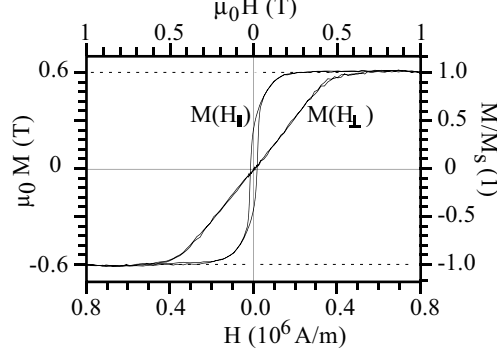


**Fig. 3.5:** Room temperature VSM measurements of the magnetisation versus applied field in a Cu/Ni/Cu/Si(001) sample with a Ni thickness of 200 nm. Fields  $H_{\perp}$  and  $H_{\parallel}$  are applied respectively perpendicular to the film or in-plane (either [100] or [110] with identical result).

#### 3.4.1 STANDARD INTERPRETATION

As can be seen from the figure,  $M(H_{\perp})$  has the form of a hard axis loop with zero remanence, saturating at  $H_{\perp}^{\text{sat}} = 380 \pm 20 \text{ kA/m}$ . Namely the sample need 380 kA/m to be saturated out of the plane, which indicates a net uniaxial anisotropy  $K_{\text{eff}} = -\frac{1}{2}\mu_0 M_s H_{\perp}^{\text{sat}} = -115 \text{ kJ/m}^3$ , favouring in-plane magnetisation. Comparison of this value with the effective anisotropy energy ( $K_{\text{eff}} \simeq K_{\varepsilon} - \frac{1}{2}\mu_0 M_s^2 = -100 \text{ kJ/m}^3$  — cf. Tab. 3.1) supports a homogeneous magnetisation description based on minimisation of the free energy dependent on  $K_{\text{eff}}$ . In addition, the absence of coercivity in this loop suggest that domain wall motion is not involved in this process. The linear behaviour is then explained by  $90^\circ$  rotation process of an initially in-plane magnetisation.

The in-plane magnetisation loop  $M(H_{\parallel})$  saturates more easily than the perpendicular loop, as is expected for an easy magnetisation direction. Further,  $M(H_{\parallel})$  displays remanence and coercivity (of about 42% and  $16 \pm 2 \text{ kA/m}$  respectively), both of which suggest domain wall pinning. Accordingly, the conventional uniform magnetisation interpretation of this magnetisation loop is that the film has in-plane anisotropy. However, upon careful observation several inconsistencies in this interpretation appear, which ultimately demand its change.

#### 3.4.2 DETAILED ANALYSIS

Ciria *et al* have previously shown that although magnetisation measurements in 200 nm Ni film suggest an in-plane anisotropy, their magnetoelastic stress measurement pointed to a complex in-plane and out-of-plane domain struc-

ture. Indeed, a careful look at the magnetometry data also suggests a rather unusual situation.

Notice that if the plane of the film is “easy”, then an applied field that saturates the magnetisation in-plane produces a configuration which essentially minimizes the anisotropy energy. Except for rather small demagnetisation fields for an in-plane magnetisation, removing the applied in-plane field should not destabilise this in-plane magnetisation. That is, a large remanence would be expected. And yet a remanence of only 42% is determined experimentally (Fig. 3.5), indicating that a substantial fraction of the magnetic moments is swinging away from the previously saturated direction\*. In fact, the magneti-

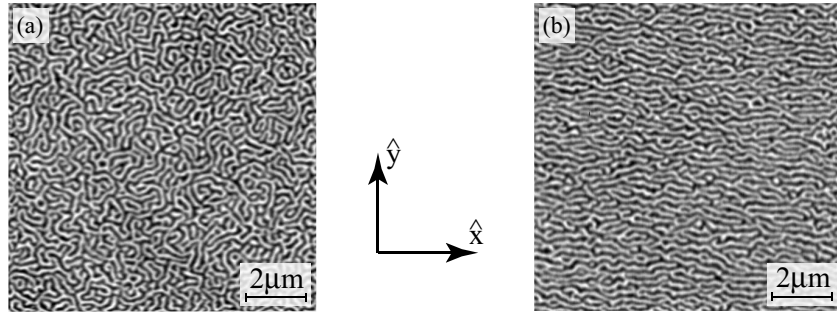


**Fig. 3.6:** MFM images of Cu/Ni/Cu/Si(001) structures with a Ni thickness of 200 nm. (a) As received film in the absence of an applied field. (b) Image of the film relaxed to zero field after saturation in-plane (along  $\hat{x}$ ).

sation swings out of plane, as is readily seen in the MFM measurements of Fig. 3.6. These images of as-received film (maze pattern, Fig. 3.6(a)) and of films previously saturated in-plane and allowed to relax to zero field (stripe pattern<sup>†</sup>, Fig. 3.6(b)) suggest perpendicular magnetisation and an anisotropy energy which is not minimal in the plane<sup>‡</sup>. To further understand the situation, qMFM has been used.

\* Note that this is true for either [100] or [110]  $M(H)$  loops.

<sup>†</sup> The maze pattern to stripe pattern formation is a well known effect<sup>23,82,94</sup>. Coming from the saturated state and decreasing the field the domain nucleate in a spot like feature. To minimise the wall energy, it is then better for the wall to expand in the field direction (the Bloch wall is then aligned with the field minimising the Zeeman energy). The remanent state is therefore given by stripe domain aligned with the in-plane previously applied field.

<sup>‡</sup> Note that the maze domain pattern presented here show an average width of 125 nm, smaller than the one observed by Hameed *and al*<sup>42</sup>. This could be attributed to the fact that the film presented here shows a larger misfit strain and hence a larger perpendicular anisotropy (c.f. Tab. 3.1)

## 3.5 Magnetic Force Microscopy : a Useful Complimentary Method

As described in sections 2.2.3 and 3.3 qMFM can be used to find the magnetisation structure which fits the measured frequency shift pattern,  $\Delta f(M(x, y))$  in the images. In this technique, candidate structures are assumed and their  $\Delta f(M(x, y))$  pattern is simulated and then compared with the measured image to determine which provides the best match.

To determine the tip transfer function ( $\sigma_{m,tip}^*(\vec{k})$ ) a perpendicular sample has to be used. Note that  $\sigma_{m,tip}^*$  is not dependant on the sample. This allows the reduction of noise and artifacts, by averaging\* of the transfer function calculated from various MFM measurements on the same sample but from different areas or even on different perpendicular samples. Here the tip was calibrated using different images taken on the 10 nm thick Ni sample at a well defined tip-sample distance. Then both 10 nm and 7 nm films, which are known to have perpendicular anisotropy<sup>14</sup>, were simulated with the perpendicular magnetisation pattern extracted from figure 3.7 (a)/(d) respectively<sup>†</sup> (c.f. Fig. 3.7). It is noteworthy that the simulation was obtained without any free parameters (the measured tip-sample distance and saturation magnetisation were used). In both simulation a very good agreement is apparent between measured and simulated images. All details of the cross sections including the asymmetry of certain domain walls and the tip response in the centre of large domains are reproduced on the simulation. This confirms that the imaging properties of the MFM tip are well described by the transfer function  $\sigma_{m,tip}^*$  and that the magnetisation is indeed perpendicular to the film surface through the total thickness.

Using the same method of analysis for the 200 nm<sup>‡</sup> film, images shown in Fig. 3.8(a)(b)&(e) are obtained. In this case, although the shape of the pattern is well reproduced by the simulation, the simulated contrast amplitude is too big (overall by a factor 1.6), meaning  $\vec{M}$  is not perfectly perpendicular. Different assumptions degrade or improve the match (as shown in section 3.3, the MFM contrast arising from these assumed magnetisation patterns can be calculated). Simulations of magnetisation ripples (Fig. 3.8(c)), where the magnetisation oscillates out of the plane with amplitude  $\theta(y) \approx \theta_r \sin(k_r y)$ ,

---

\* The complex 2-D matrixes representing the tip transfer function in the Fourier space have to be averaged.

<sup>†</sup> The magnetisation pattern can be extracted with a careful discrimination process. For these thicknesses the domain walls are not relevant since they are smaller than the width of one pixel (19.5 nm).

<sup>‡</sup> Note that in the case of the 200 nm thick film, the perpendicular magnetisation simulation has to take into account the transition between two domains through the domain wall width (47 nm) because this one is bigger than one pixel (Sect. 1.3.2 & 3.3.1).



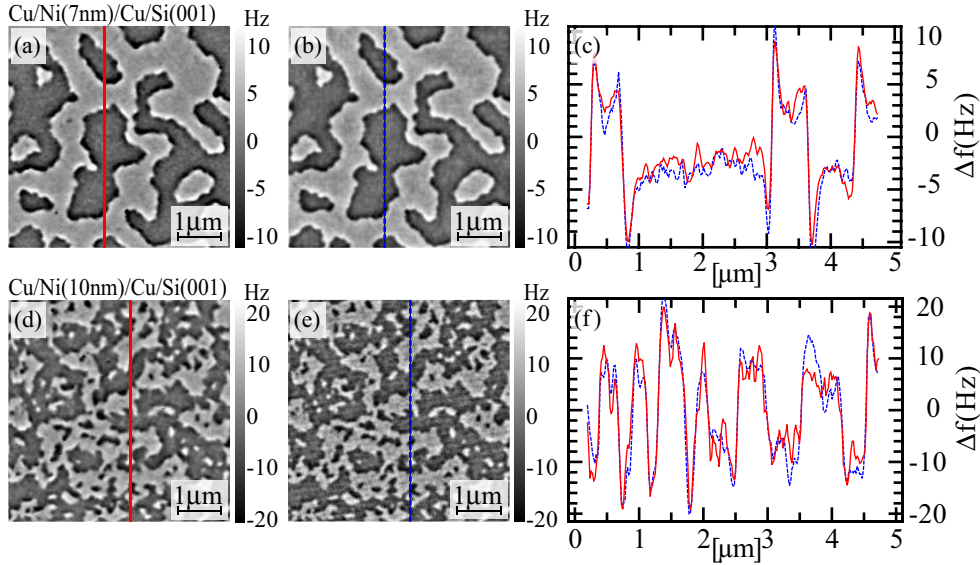


**Fig. 3.7:** Measurement and simulation of the magnetisation of Cu/Ni/Cu/Si(001) structures. (a)/(d) MFM image for 7/10 nm thick Ni, measured at  $33\&31 \pm 1$  nm tip-sample distance respectively. (b)/(e) Image simulated from perpendicular magnetisation pattern extracted from (a)/(d). The simulation was performed using the instrument calibration function  $\sigma_{m.tip}^*(k)$  calculated from 10 nm Ni thick images. The measured tip-sample distance and saturation magnetisation was used. (c)/(f) Comparison of the sections indicated in (a)/(d) (solid line) and (b)/(e) (dashed blue line).

can match the range of measured contrasts for a ripple angle  $\theta_r \approx 39^\circ$  (from in-plane). However, due to the  $\sin(k_r y)$  dependence, ripples are inherently incapable of reproducing sharp contrast changes observed in the MFM data. On the other hand perpendicular domains capped with closure domains<sup>18,42,94</sup> having a canting angle of  $\theta_c \approx 50^\circ$  off the plane normal produce the same pattern as through-thickness perpendicular domains (due to the linearity of the transfer function — c.f. Sect. 3.3.1), and do give the appropriate amplitude (Fig. 3.8(d)).

The above discussion is summarised in the  $\delta f$  histogram of Fig. 3.8(f). It shows that the domain pattern generated by perpendicular domains, adjusted by a factor  $1/1.58$  (corresponding to closures canted at  $51^\circ$ ) closely matches the measured histogram, whereas the ripple simulation has an intermediate frequency shift level that is too high, in accordance with their “fuzzy” magnetisation profile (the transition between dark and bright is not sharp enough). This is further confirmed by a less steep tail of the histogram in the case of ripple pattern. In conclusion, the film is shown to have perpendicular domains

capped with canted closure domains. This quantitative result complements an earlier model results indicating that closures would be consistent with observed domain widths<sup>42,82</sup>.

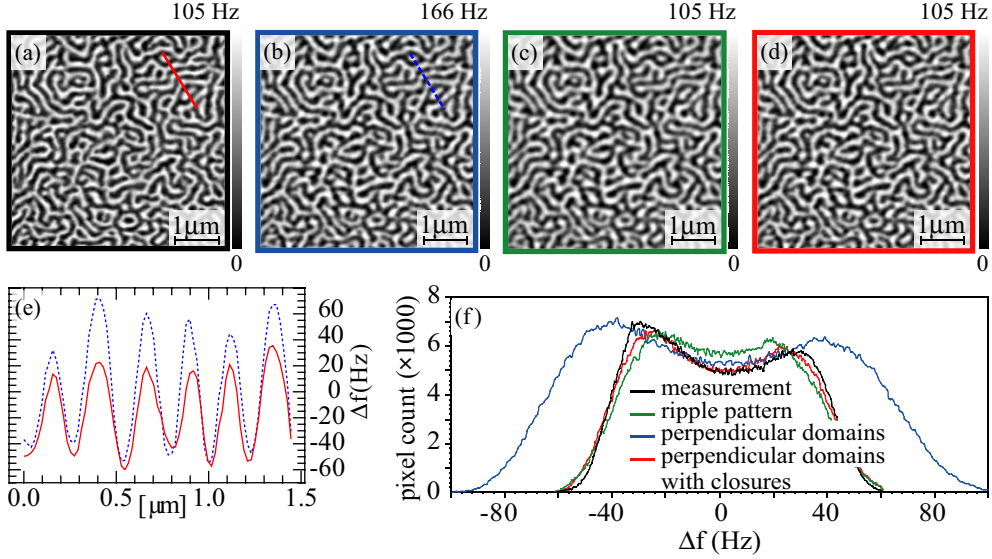


**Fig. 3.8:** (a) MFM image for a 200 nm thick Ni film. (b) Simulation assuming perpendicular domains obtained from (a): Note the higher contrast. (c) Simulation assuming a ripple pattern with  $\theta_r = 39^\circ$ . With a careful look, it occurs that the image is more blurred (d) Simulation assuming closure domain with  $\theta_c = 51^\circ$  (corresponding to contrast adjusted by 1/1.58). (e) Comparison of the sections indicated in (a) and (b). (f) Histogram representing the count of pixels at a given  $\Delta f$  from (a), (b), (c) and (d).

### 3.6 CuNiCu Revisited

The perpendicular anisotropy in 200 nm films thus having been established, our previous interpretations of the magnetisation loop (Fig. 3.5) must be revisited. Indeed, it is recognized that  $M(H_\perp)$  must be a combination of short range domain wall motion processes and closure magnetisation rotation, whereas  $M(H_\parallel)$  must result from long-range rearrangement of domain walls and domain magnetisation rotation. Further clarification is required because coercivity and high remanence are expected for domain wall motion but not for magnetisation rotation. The greater difficulty (smaller susceptibility) of the perpendicular magnetisation of the film via domain wall motion also merits discussion.

In addressing the first point, consider the film saturated in-plane along  $\hat{x}$  as it relaxes to zero field (Fig. 3.6(b)). The magnetisation of the closures lies in the  $yz$  plane and cannot give rise to remanence in  $\hat{x}$  (a slight canting toward  $\hat{x}$  over the underlying Bloch wall could be possible, but minor). Furthermore, the symmetry of the closures requires that their magnetisation have a vanishing average in the direction perpendicular to the domains. Closures therefore cannot be the primary cause of remanence, as other authors have suggested<sup>42</sup>.

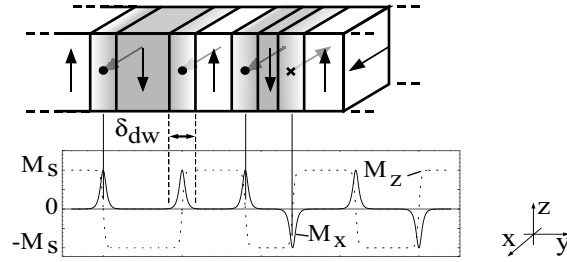


**Fig. 3.9:** Schematic of the magnetisation in the film's Bloch walls. A net magnetisation in  $x$  direction could exist.

On the other hand figure 3.6 shows that the domains remain aligned into the direction of a previously applied in-plane field. This is because the magnetisation of the Bloch walls inside the film remains aligned. This is shown schematically in Fig. 3.9. As is clear from this figure, each wall has a net contribution to the remanence along  $\hat{x}$ , which can be positive or negative, but is not prescribed by symmetry to take either value. However, when the magnetisation relaxes from saturation in  $+\hat{x}$  practically all the magnetic moments in the walls will have a positive component along  $\hat{x}$ . The resulting remanence can be large given the wall density of the present film. Integration of  $\vec{M} \cdot \hat{x}$  over a domain width  $D \simeq 125$  nm yields\*  $M_x = M_s \frac{\delta_{DW}}{D} = 38\% M_s$  (cf. Tab. 3.1), essentially matching the measured remanence of 42%, and in agreement with magnetoelastic stress results<sup>16</sup>. Thus, the remanence is not a net magnetisation of the domains: it is the net magnetisation of the *domain walls*.

Notice that in a maze pattern such as Fig. 3.6(a) the net in-plane magnetisation averages out macroscopically. A transition to this state from Fig. 3.6(b) has a very low driving force (small demagnetisation fields) while requiring a large reconfiguration of the walls. Indeed an in-plane field does predominantly exert a force on domain wall (which are oriented in-plane). In order to align a domain wall with this external field, large reconfiguration of the wall have to happen (c.f. Fig. 3.11). This large reconfiguration with low driving force

\* c.f. appendix C

accounts for the non-zero coercivity observed in the in-plane magnetisation loop.

In contrast to the in-plane loop, the out-of-plane magnetisation loop displays no significant remanence or coercivity. As described below domain wall motion and macroscopic return point memory (RPM)<sup>20</sup> are clearly confirmed via MFM in figure 3.10.

Figure 3.10 represents magnetisation pattern extracted from MFM images. The images were taken at the same height and with the same tip, allowing comparison of the extraction of magnetisation pattern. It was chosen to present magnetisation pattern instead of the original images to make the domain wall motion clearer. Application of a perpendicular field of 100 mT leads to an expansion of the domains favourably oriented relative to the field (dark) at the expense of the others (bright) (compare Fig. 3.10:1&2). When the field is relieved the bright domains expand to represent again  $\approx 50\%$  of the image area (good macroscopic RPM). At a field of 300 mT the maze pattern has completely broken up into a few remaining cylindrical reversed domains. During application of a field of 400 mT the film is saturated, meaning the “dark domains” have expand over the full area and “bright domains” have disappeared (Fig. 3.10: inset 8). Removing the field gives rise to a maze pattern macroscopically similar, namely the remanent domain pattern still have the original length scale and maze-like character.

Note that all the images taken at zero field indicate a vanishing remanent perpendicular magnetisation (50% “dark” domain). However the magnetisation pattern does not recover microscopically. Thus the sample exhibits good macroscopic RPM but no microscopic RPM<sup>20</sup>.

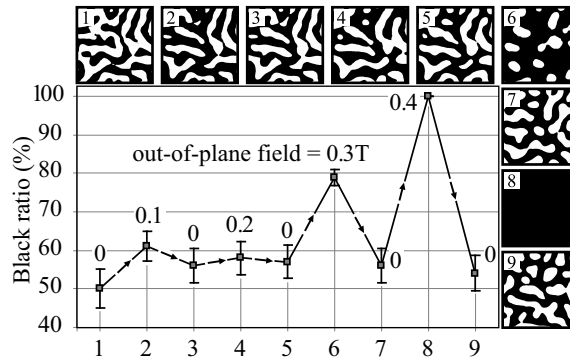


**Fig. 3.10:** Macroscopic return point memory. Total magnetisation level as % black (from MFM images taken at 9.4 K normalised to point 8) after successive field excursions (labels in T).

It is apparent that field excursions up to  $\mu_0 H^\perp = 0.4$  T can move the domain walls so that they can recover the initial magnetisation when  $H^\perp$  is

estimate	expected	measured
$\Delta U_{\perp} \approx \frac{1}{2}\mu_0 M_s^2 - \sigma_{\text{dw}}/D$	123 kJ/m <sup>3</sup>	$E_{\perp} = 121 \pm 3 \text{ kJ/m}^3$
$\Delta U_{\parallel}^+ \approx K_{\varepsilon} - \sigma_{\text{dw}}/D$	23 kJ/m <sup>3</sup>	$E_{\parallel}^+ = 21 \pm 3 \text{ kJ/m}^3$
$\Delta U_{\parallel}^- \approx K_{\varepsilon} - \sigma_{\text{dw}}/D$	23 kJ/m <sup>3</sup>	$E_{\parallel}^- = 32 \pm 3 \text{ kJ/m}^3$

**Tab. 3.2:** Energies for saturation.

removed. Domain wall pinning does not result in appreciable coercivity here because a large magnetisation change can occur by a relatively small displacement of (many) walls between or around pinning centres (c.f. Fig. 3.11). These conclusions do not hold for films with larger domains (thickness around 10 nm and below). In the chapter 5 similar results will be presented and further discussed for a different system (Ni(185 nm)/Si).

The work required to saturate in- or out-of-plane can be quantified from Fig. 3.5 as  $E_{\parallel}$  or  $E_{\perp}$  respectively (c.f. section 1.4.2). The energy differences  $\Delta U_{\perp,\parallel}$  between zero-field and saturated states can also be estimated. In-plane saturation results in peak anisotropy energy  $K_{\varepsilon}$  and negligible magnetostatic energy. Out-of-plane saturation results in the reciprocal case of negligible anisotropy energy and maximum magnetostatic energy. In a remanence state the energy is the wall energy. Tab. 3.2 compares  $\Delta U_{\perp,\parallel}$  with  $E_{\perp,\parallel}$  (domain spacing  $D = 125$  nm). Here the superscripts + and – refer to positive and negative remanence in the initial state\*. A reasonable agreement is apparent despite having neglected the energy of the closures in the initial state, and possibly also additional components in  $\Delta U_{\parallel}^+$  from the removal of wall magnetisation opposing the applied field.

## 3.7 Conclusions

In conclusion, the Cu/Ni/Cu/Si(001) structure with a Ni thickness of 200 nm studied in this chapter is a thin film example which defies a conventional interpretation. The film has perpendicular anisotropy, but the out-of-plane direction is hard to magnetise because of the large magnetostatic energy. 125 nm spaced perpendicular domains with closure domains canted at  $51^{\circ}$  exist in

\* Eqn. (1.31) is well defined for a non hysteretic curve. When there is hysteresis, the energy needed to bring the sample from remanence to saturation depends on the remanent state. Indeed going to positive saturation from a remanent state resulting from previous positive saturation needs only the energy to rotate the domains. Contrastingly, going to positive saturation from a remanent state resulting from previous negative field needs, to first align domain walls and then to rotate the domains. Thus it needs more energy ( $E_{\parallel}^- > E_{\parallel}^+$ )

the demagnetised state. Out of plane magnetisation occurs by domain wall motion, but it has essentially no remanence or hysteresis because the domain width is very small, and large magnetisation changes can take place by small shifts in the domain walls (c.f. Fig. 3.11(a)(d)(e)\*). At large field magnetisation inside the domain walls rotates in the field direction. The in-plane magnetisation for small fields occurs by rearrangement of domain walls over ranges larger than the domain wall spacing (c.f. Fig. 3.11(a)(b)(c)). For large fields, it occurs by magnetisation rotation. It involves coercivity and hysteresis. A 42% remanence observed upon relaxing an in-plane saturation is due almost entirely to the in-plane wall magnetisation of the perpendicular domains.

This study is a good example of a situation where magnetometry alone does not lead to the correct conclusions. Quantitative magnetic force microscopy must also be used in order to fully understand the magnetometry data.

---

\* Note that the schematics represent the different effects of the external field in difference sequences. This schematic is only to aid understanding. In reality, the two effects are certainly not perfectly decoupled.

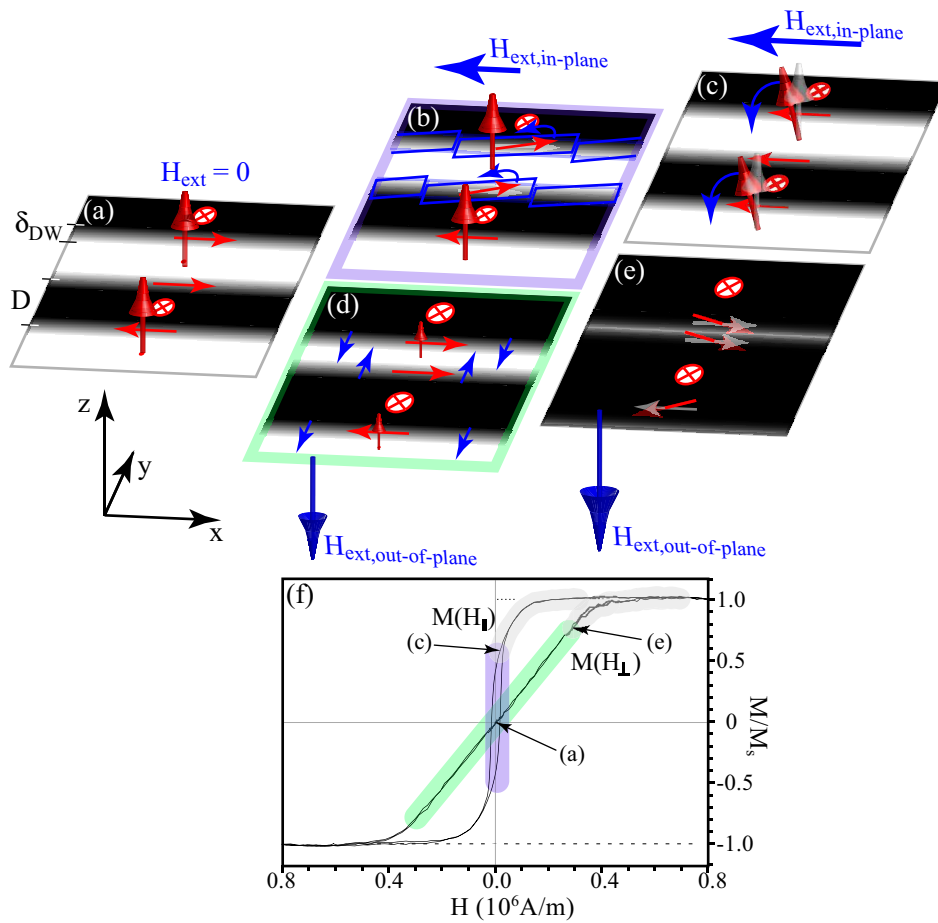


**Fig. 3.11:** New magnetometry interpretation (Top view) : (a) Inside the film remanent situation is represented by 50 % of domain pointing out of the page (up) and 50 % into the page (down). The film surface have closure domains with a canted magnetisation. The Bloch walls between domains are in the plane, pointing left or right. (b) Applying an in-plane field exerts a force on domain walls antiparallel to the external field and reverses their direction. This imply large reconfiguration of the walls. (c) After all the walls are aligned, the magnetisation inside the domains that is perpendicular to the film surface as well as the canted magnetisation of the closure domains have to rotate into the plane. (d) Applying an out-of-plane field exerts a force on domains aligned opposite to the field to shrink them in favour of the one aligned in the field direction. This implies a short domain wall motion ( $1/2D \approx 60 \text{ nm}$ ). (e) After all domains are aligned with the field, the domain walls have to rotate out of the plane. (f) This interpretation is correspondingly shown in the magnetometry loop. The violet and green line highlight the part of the hysteresis loop governed by domain wall motion. The grey parts indicate where magnetisation rotation occurs.







# TUNING THE MAGNETOELASTIC ANISOTROPY IN NICKEL BY IRRADIATION<sup>95–97</sup>

## 4.1 Introduction

### 4.1.1 POLYCRYSTALLINE Ni FILMS

In the last chapter (Chap. 3) the complicated interplay between the different magnetic anisotropy terms of epitaxial Cu/Ni/Cu/Si(001) films was studied<sup>16,17,37–41,98</sup>. The dependence of the anisotropy terms on film thickness and their role for the micromagnetic state was analysed. For films consisting of 200 nm Ni interesting magnetisation phenomena were described.

This chapter is devoted to a simpler thin film system, namely a polycrystalline Ni-film on a naturally oxidised Si-substrate. We found that the growth-induced strain plays an important role for the micromagnetic state and magnetic hysteresis process. To further elaborate the role of the strain, two methods to tune the strain after deposition were studied.

### 4.1.2 TUNING ANISOTROPY WITH ION IRRADIATION

We focus here on the effects of Xe ion irradiation on the magnetisation structure of nickel films. By way of collision cascades and thermal spikes, ion irradiation can lead to sputtering, grain-damage/growth, swelling, noble-gas clusters, voids and blistering in a metal film. The mechanical and microstructural properties of the latter are affected accordingly<sup>99</sup>. It is likewise expected that the magnetisation is affected by irradiation. Indeed, previous studies by Lieb *et al* on ion-irradiated Ni<sup>33,36,100–102</sup> and Fe<sup>34,102,103</sup> films by means of magneto-optical Kerr effect (MOKE) and X-ray diffraction (XRD) have revealed changes in the magnetisation and microstructure upon ion irradiation. Further studies showing the effect of ion irradiation on magnetic anisotropy are summarised in the Fassbender *et al* review article<sup>99</sup>.

Most of these previous studies focus on irradiation of Co/Pt multilayer systems and explain the magnetic anisotropy change in terms of interface mixing and roughening<sup>104–108</sup>. However, Devolder *et al* suggested that the irradiation-induced controlled decrease of the magnetic anisotropy cannot be

solely attributed to Co-Pt intermixing, and that irradiation also significantly releases the tensile strain of the cobalt<sup>109</sup>. More information about how the strain is affected by irradiation is given by studies on irradiated (1 MeV C<sup>+</sup>) Cu/Ni/Cu systems where the strain mainly comes from the lattice mismatch. Studying thin Ni films up to 9 nm capped by copper, Lee *et al* could show that irradiation removes the perpendicular anisotropy therefore reorienting the magnetic easy axis from surface normal to surface parallel. They show this removal is due to a reduction of the interface anisotropy<sup>110</sup>. Furthermore, they mention that reduction of interface magnetic anisotropy is not due to a blurred interface but “has more fundamental origins which are yet to be understood.”

Further investigation of these origins has been carried out by Kim *et al*<sup>93,111,112</sup> on similar films. They could show that irradiation causes the magnetisation to fall back into the film plane. According to their interpretation this is due to the irradiation induced lowering of the magnetic interface anisotropy. This process has been shown to occur via strain relief and without any alloy formation. However, a growth of the grain size of Cu has been seen<sup>111</sup> and the interface between the top Cu layer and the Ni layer has been shown to become rough<sup>112</sup>. Furthermore, they show that irradiation actually reduces the intermixing at the Ni/Cu interfaces. They concluded that the interface demixing is due to the inelastic energy transfer induced thermochemical driving forces being greater than the mixing by elastic collision.

Despite great interest in this field, the understanding of the irradiation-induced process leading to a loss of perpendicular anisotropy is still poor. The systems studied so far are all very thin films, implying a large effect of the chemical and structural properties of the interface. Furthermore, the ion irradiation energy was chosen such that the ions go fully through the film for all systems studied so far. Thus a change of the chemical and structural properties of the interface by irradiation induced interdiffusion, atomic displacement and amorphisation cannot be neglected.

In order to clarify the role of the irradiation on anisotropy we have used simpler thin film systems. Namely, a 185 nm Ni and a 75 nm Ni film were deposited onto a Si(100) wafer coated with its native oxide. The irradiation energies were then chosen such that the ions do not reach the Ni/SiO<sub>2</sub> interface to avoid any chemical or structural changes of the interface.

## 4.2 Experimental

Polycrystalline Ni films were fabricated by electron beam evaporation on naturally oxidised Si(100) (a few nm SiO<sub>2</sub>) substrates at room temperature in a vacuum of  $6 \cdot 10^{-8}$  mbar. Two different Ni-films thicknesses have been pro-

duced. Some of the samples were subsequently irradiated by Xe ions to study a mutual change of their properties. The ion irradiation was done by K. Zhang *et al* in Prof K.P. Lieb's group at Göttingen<sup>35</sup>.

In order to avoid an intermixing of the Ni/Si interface, the ion irradiation energies were appropriately selected:

- Ni-thickness =  $70 \pm 1 \text{ nm}$  : Xe irradiation by 200 keV  $\text{Xe}^+$  ions with fluences of  $4 \cdot 10^{14}$  ions/cm<sup>2</sup> at 100 K. The mean penetration depth of the Xe ions was calculated to be 26 nm and its full width at half maximum (FWHM) 30 nm (c.f. Fig. 4.1).
- Ni-thickness =  $185 \pm 1 \text{ nm}$  : Xe irradiation by 600 keV xenon ions with a fluence of  $1 \times 10^{15}$  ions/cm<sup>2</sup>. The ion energy was tuned to a mean range of 81 nm and a FWHM of 87 nm of the implantation profile.

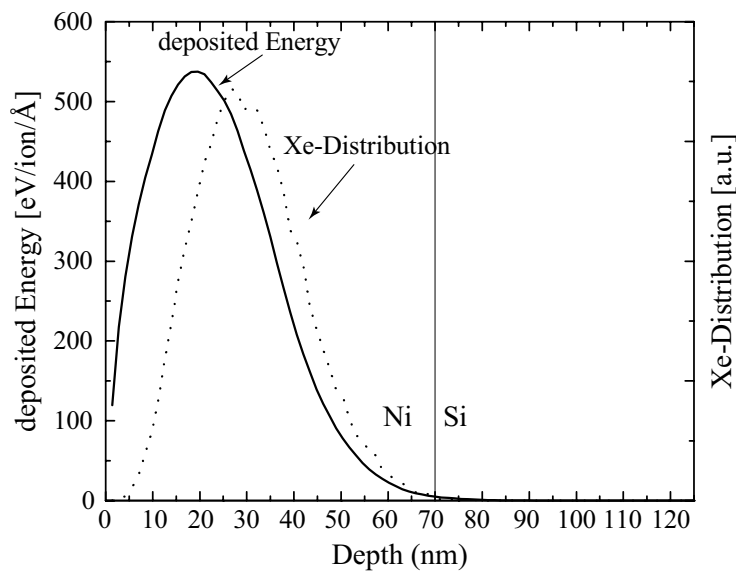


**Fig. 4.1:** Deposited energy and ion range calculated with the *SRIM 2000* code<sup>113,114</sup> for 70 nm thick Ni/Si sample irradiated with 200 keV Xe-ions. Adapted from Zhang's thesis<sup>35</sup>.

In order to confirm the expected intact Ni/Si interface, the as-grown and irradiated films were studied by means of Rutherford backscattering spectroscopy\* (RBS) before and after irradiation (c.f. figure 4.2). The data clearly prove that no or only neglectable interface broadening occurred.

\* With a 900 keV  $^4\text{He}^{++}$  beam. Further information about RBS are available in Lieb and Keinonen survey article<sup>115</sup> (see in particular the *Box 2*) and in Zhang thesis<sup>35</sup>.

The maximum density of the implanted Xe was in both cases 0.15 at.%. The ion implantations and RBS analysis\* were carried out using the Göttingen 530 kV implanter IONAS by Zhang *et al*<sup>35,116</sup>.

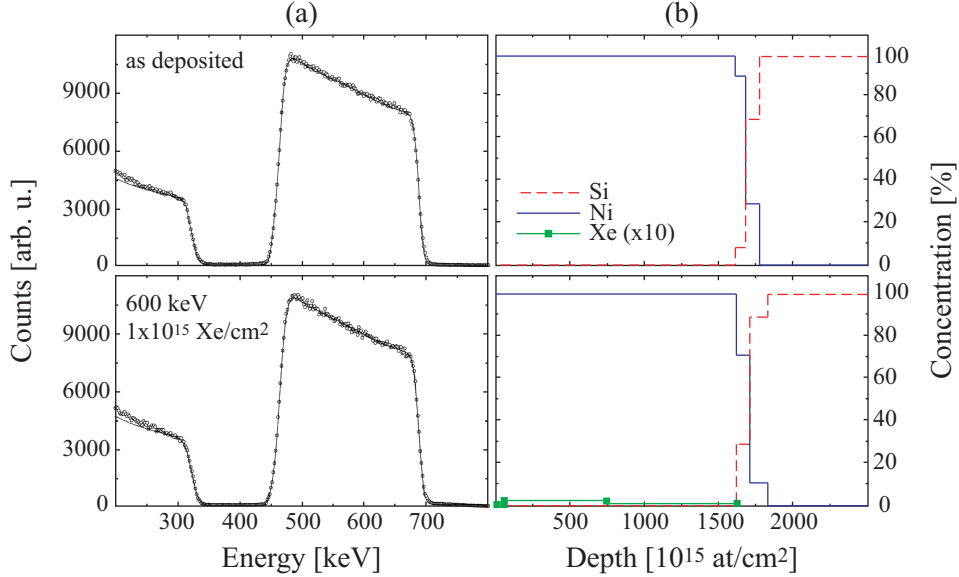


**Fig. 4.2:** RBS measurements and deduced atom concentration profile for the 185 nm Ni thick film: The RBS spectra are almost identical in the as-grown sample as in the irradiated one, as Xe does not penetrate the interface and thus no mixing occurs. Note that the interface width is several nanometres due to the deposition process. The data analysis was performed with the WIN-DF program.

The crystalline structure of the film were analysed by X-ray diffraction (XRD). This study revealed the interface to consist of Ni(111) facets. No change of crystalline orientation and grain size were found after irradiation. This can be understood by considering standard irradiation processes. Ions entering the film lead to the displacement of a large number of Ni atoms in the collision cascade<sup>117</sup>. Subsequent relaxation to their lattice positions and the annealing of most point defects below room temperature means that no surface damage is visible around the cascade<sup>118</sup>.

The magnetic properties were characterised at room temperature by means of MFM and vibrating sample magnetometry (VSM). The room temperature MFM images were taken using a *Swissprobe*<sup>©</sup> *hr-MFM* operating in a vacuum of  $1 \times 10^{-5}$  mbar described in section 2.5. The low temperature MFM images were taken using a homebuilt liquid helium cooled scanning force microscope

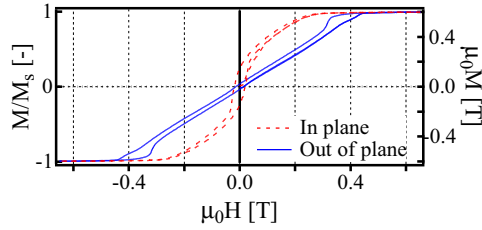
\* Heavy ions in a medium-A matrix (Xe in Ni) has been used to perform the RBS analysis.

described in section 2.4<sup>72</sup>. Both instruments were operated in a dynamic mode described in section 2.1.1. As MFM tips, *Team Nanotec GmbH* silicon cantilevers with an ISC tip coated with 4 nm Co and magnetised in a static field larger than 1 T were used (see Sect. 2.6.2). VSM was taken at room temperature using a *Quantum Design Physical Properties Measurement System (PPMS)* (see section 2.3).

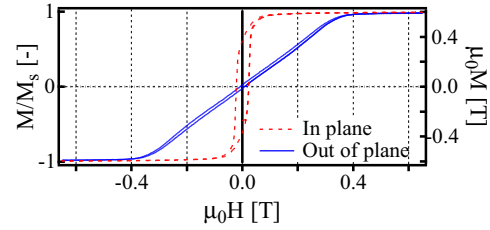
## 4.3 Results

### 4.3.1 THE EFFECTS OF IRRADIATION

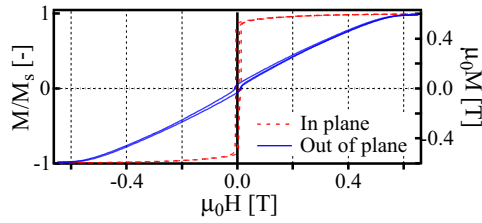
(a) 185 nm, as-grown



(c) 70 nm, as-grown



(b) 185 nm, irradiated



(d) 70 nm, irradiated

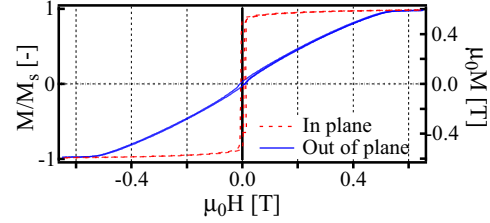


**Fig. 4.3:** Magnetisation versus applied magnetic field loops from VSM. (a) as-grown and (b) irradiated 185 nm thick film, (c) as-grown and (d) irradiated 70 nm thick film

The as-grown and irradiated films with Ni thickness of 185 nm and 70 nm were studied by VSM\* and MFM. For clarity, the values for the 70 nm film will henceforth be given in brackets with a bold font. The as-grown film magnetisation vs. field for the 185(**70**) nm film is shown in Fig. 4.3(a)(c) respectively. The magnetisation saturation for perpendicular fields occurs at a saturation field  $\mu_0 H_{sat}^\perp = 450 \pm 40$ (**400  $\pm$  50**) mT. The perpendicular direction is found harder to saturate than the in-plane direction where the corre-

\* Some additive loops measured at 8.3 K are shown in appendix E.

sponding values are  $\mu_0 H_{sat}^{\parallel} = 330 \pm 30(260 \pm 30)$  mT. A small hysteresis is apparent in both magnetisation loops, with coercivities of  $\mu_0 H_c^{\parallel} = 19(22)$  mT and  $\mu_0 H_c^{\perp} = 14(6)$  mT for in-plane and perpendicular, respectively.

We further point out two characteristics which are indicative of *perpendicular* anisotropy in the two films. First, given the small demagnetisation fields for a uniform in-plane magnetisation, the observed in-plane remanence of 23(62) % for the in-plane loop is too small to be consistent with a magnetisation that fully remains in-plane.

The curved part near saturation indicates magnetisation rotation. The perpendicular loops shows little hysteresis and a linear magnetisation versus field behaviour. From our results on the Cu/Ni(200 nm)/Cu(100) films we know that such hysteresis loops are characteristic for thin film systems that have a magnetisation that does not remain in the film plane due to the presence of perpendicular magnetisation anisotropy but which is too weak to allow a fully perpendicular magnetisation state<sup>17</sup> (c.f. Chap. 3).

The in-plane loop of the 185 nm film shows that 77% of the magnetisation points away from the film plane. Such a large perpendicular amplitude is consistent with an up/down perpendicular magnetisation inside the film and closure domains at the films surfaces. The perpendicular loop of the 185 nm shows a noticeable shoulder which indicates a sudden onset of domain nucleation followed by domain wall motion. It implies the appearance of perpendicular magnetisation domains as the out-of-plane saturating field is removed, an event which is only supported by a perpendicular anisotropy.

MFM measurements confirm the above analysis. Stripe domains with a surprisingly strong perpendicular component of the magnetisation are visible in figure 4.4(a)-(d).

The as-grown\* samples were demagnetised by a slowly oscillating field with a gradually decreasing amplitude applied in the sample plane. This generates a well orientated regular pattern of stripe domains 125(100) nm wide with a frequency shift contrast of 18.5(7.7) Hz<sup>†</sup> (Fig. 4.4(b)(d)). This relatively large contrast is due to a strong perpendicular component of the magnetisation. In Ni films, such a magnetisation state is known to be caused by perpendicular magnetostatic anisotropy, which arises from tensile strain<sup>17,42</sup>. The strained state of the film appearing here at room temperature is due to the evaporation process<sup>119,120</sup>.

The qualitative and quantitative difference in contrast between the 70 nm and the 185 nm thick films can be explained in terms of different configurations

---

\* Note that, since the MFM measurements were performed after demagnetising the sample, the domain state is not as grown. “As grown” refer in this thesis to the fact that the sample has not been irradiated.

<sup>†</sup> The free cantilever resonance frequency  $f_0 = 34240$  Hz

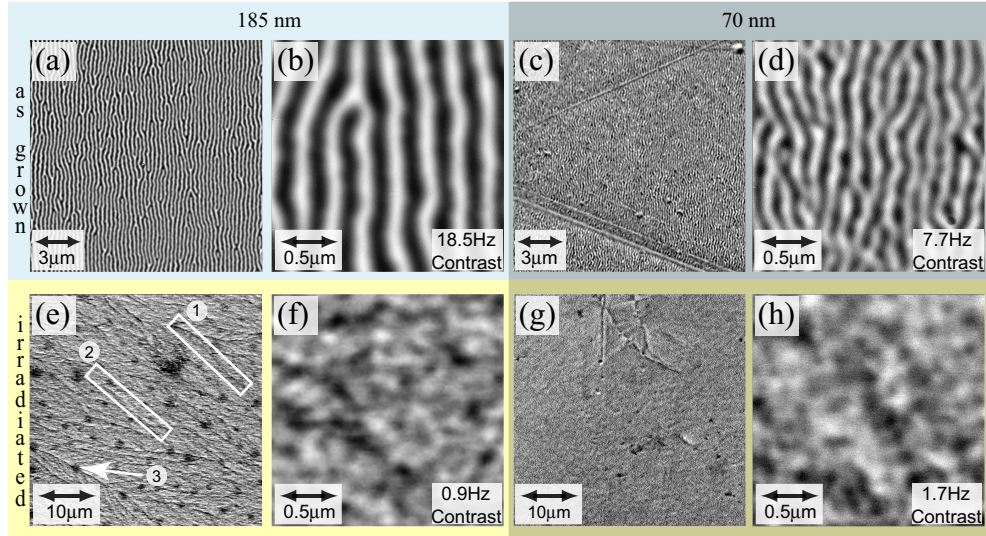


**Fig. 4.4:** MFM taken at RT at  $\approx 60$  nm tip-sample distance of (a)-(d) as-grown sample and (e)-(h) irradiated sample. Images (a)(b)(e)(f) concern the 185 nm thick sample and images (c)(d)(g)(h) the 70 nm thick sample. Detail in image (e) : black line (1), white line (2), black spot (3).

of the magnetisation for different thicknesses. Indeed, whereas the overall contrast difference is largely due to the difference of thicknesses, the increased blurredness of the 70 nm images is likely to be due to ripple magnetisation instead of perpendicular domains. This explanation is further confirmed by the difference seen in the VSM loops (Fig. 4.3) where the 185 nm thick film exhibits a shoulder typically due to nucleation process and the 70 nm does not show any signs of domain nucleation. However, to confirm this model, simulations must still be carried out. The stripe width difference in between the two thicknesses is consistent with theory predictions<sup>23(chap. 16.7.2), 39</sup>. Both differences mentioned above are consistent with previous work on epitaxial Co film<sup>121</sup>.

Qualitatively the  $M(H)$  loops and the MFM images of the as-grown samples confirm the results obtained on the CuNiCu system (c.f. Chap. 3). Both films have a considerable magnetic moment that is out of the film plane. Irradiation with Xe ions drastically changes this situation. The magnetisation loops of the irradiated samples are markedly different from the loops of the as-grown samples (Fig. 4.3(b)(d) and (a)(c) respectively). The in-plane loops show a sharp transition to saturation, displaying a square shaped loop with almost 100% remanence. This indicates the absence of a positive anisotropy to pull the magnetisation out of the plane, counter to the as-grown film. The

perpendicular direction remains hard, but the 185 nm thick Ni film loop does not have the nucleation shoulder when going from saturation to zero. The more rounded shape and the absence of the shoulder indicate magnetisation rotation rather than the nucleation of domains followed by domain wall motion.

These differences to the as-grown case become more prominent when the local micromagnetic structure is investigated with MFM. The MFM image of the irradiated film in Fig. 4.4(f)(h) shows an approximately 20(4) times weaker  $\Delta f$  contrast which evidences the reduction of the perpendicular component of the magnetisation.

The main features of the large scale image of the 185 nm thick irradiated sample (Fig. 4.4(e)) are faint line like structures (white boxes) overlaid by micrometre sized dark spots (white arrow). The line like features are interpreted as domain walls between domains with in-plane magnetisation. These domain walls are expected to be Bloch walls inside the film with a Néel cap at the surface<sup>122</sup>. Two types of Bloch walls exist (c.f. figure 3.2). Depending on whether the wall magnetisation rotates towards the tip or away from it, a black or white line results (Fig. 4.4(e) white boxes 1 and 2 respectively). The dark spots will be discussed later.

The 70 nm thick sample also exhibits two kind of features as shown in figure 4.4(g). Some lines are visible at the top of the image and black spots are distributed around the image. Further investigation have been carried out to find the origin of the lines. As seen in figure 4.5 the lines continue up from image in figure 4.4(g) for tens of microns. It is interpreted as a scratch in the Ni film. Indeed, it is known that scratches in a film with magnetisation parallel to the film plane may lower the energy of domain wall creation<sup>18,123</sup>. The line like features in figure 4.5(a) are interpreted as cross-tie walls (c.f. Sect. 1.3.2) and thus confirm the magnetisation to be in-plane. To confirm that the contrast generated by the vertical line is indeed of magnetic origin, two MFM images were acquired at the same sample location with two opposite states of the tip magnetisation\* (c.f. Fig. 4.5(b)). Indeed comparing the image in Fig. 4.5(a) and (b) show that the contrast generated by the line-like features is inverted after inverting the tip magnetisation. However the black spots and the white spot are not inverted, therefore coming from topology of the surface. MFM imaging reveals these bright and dark spots to be holes in the film and debris respectively as seen in figure 4.6(b).

The topography images were acquired in tapping mode<sup>†</sup>. While the image of the 185 nm film shows bubbles (figure 4.6(a)) the corresponding data

\* The Swissprobe<sup>©</sup> high resolution magnetic force microscope allows one to re-magnetise the tip and re-approach in the same area, allowing the deconvolution of the magnetic contrast from the topology.

<sup>†</sup> "Science is the topography of ignorance.", Oliver Wendell Holmes, Sr.



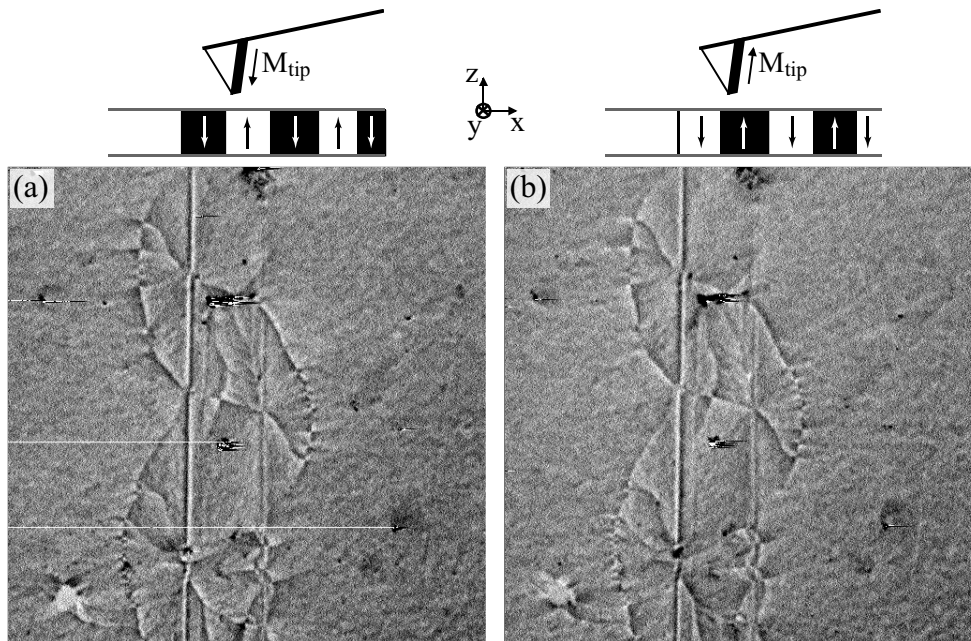


**Fig. 4.5:** MFM images taken on the 70 nm Ni thick sample after irradiation ( $40\ \mu\text{m} \times 40\ \mu\text{m}$ ). (a) and (b) images are taken with opposite tip magnetisation.

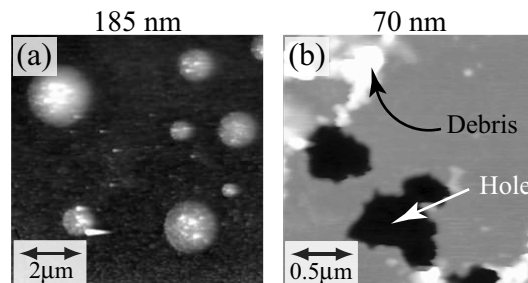


**Fig. 4.6:** AFM tapping mode image taken at RT (a) on 70 nm Ni thick sample and (b) on 185 nm Ni thick after irradiation.

acquired on the 70 nm film shows craters and nearby debris (figure 4.6(b)).

Both topography images in figure 4.6 can be explained by Xe bubble formation during the irradiation. This process is well known but normally occurs for higher fluences. In the case of the thicker film, Xe forms bubbles due to the non solubility in Ni. In the case of the thinner film, the Ni layer is not able to handle the bubble and a fast expansion occurs causing a hole (through

the full film) and associated debris.

The change from a stripe domain structure with out-of-plane magnetisation (Fig. 4.4(a)-(d)) to a domain state with in-plane magnetisation (Fig. 4.4(e)-(h)) clearly shows that strain is relieved. Grazing-incidence X-ray diffraction (GIXRD, Cu-K line) was used to study the dependence of the lattice constant and thus determine the strain state of the as grown 70 nm Ni film and after various irradiation fluences up to  $4 \cdot 10^{14}$  ions/cm<sup>2</sup>. The results shown in Fig. 4.7

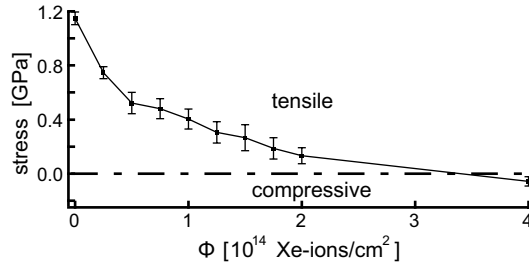


**Fig. 4.7:** 70 nm Ni film stress measured after various fluences ( $\phi$ ) of 200 keV Xe-irradiation by means of 3°-GIXRD

indicate a large tensile stress of 1.2 GPa after deposition, which is rapidly relaxed upon ion bombardment. It reaches zero for about  $3 \times 10^{14}$  ions/cm<sup>2</sup> and then becomes compressive, due to the storage of non-soluble noble-gas ions and defect accumulation<sup>124</sup>. Similar correlations between strain and magnetism were found after ion implantation in thin iron films<sup>34</sup>.

Our results show that irradiation can be used to change and completely remove the tensile strain and consequently the magnetoelastic anisotropy. A confirmation that the system has not otherwise been affected can be obtained from a measurement at low temperature. Cooling recovers the tensile strain because of the different thermal expansion coefficients of Ni and Si. The films were therefore studied by MFM at 9 K. The images in figure 4.9 and figure 4.8 show the 70 nm and the 185 nm thick films respectively, at room temperature and 9 K both before and after irradiation. All images in figure 4.8 and figure 4.9 are  $2 \mu m$ , taken with 50 nm\* tip-sample distance. Thus all contrasts and features sizes can be compared for a given temperature. However no comparison of the contrast is possible between low temperature measurements and measurements done at 9 K since the instrument and the tip are different (ICF are different and thus contrast changes may not be due to sample, c.f. equation (2.28)). The stripe domain observed in the as-grown film

\* Since not all measurements were available at this specific height due to technical limits (the minimum tip-sample distance is mainly limited by the cleanness of the sample), the image height was corrected to be 50 nm using the exponential dependence of the stray field

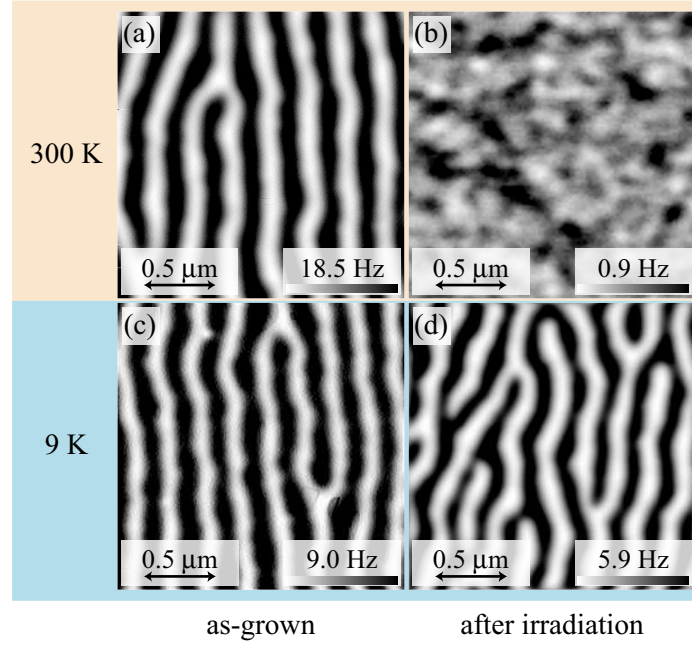


**Fig. 4.8:** MFM measurements performed on the 185 nm thick Ni film. (a) and (b) images are taken at 300 K (RT) before and after irradiation (As shown in Fig. 4.4(b)&(f)). (c) and (d) MFM images are taken at 9 K (LT) before and after irradiation.

(Fig. 4.9(a) & Fig. 4.8(a)) was not observed after irradiation at room temperature (Fig. 4.9(b) & Fig. 4.8(b)), however, as expected, at low temperature the stripe domains are now observed in both the as-grown and irradiated samples (Fig. 4.9(c)-(d) & Fig. 4.8(c)-(d)). This is recognised to be due to the thermal strains imposed on the Ni/SiO<sub>2</sub> boundary further coupled to the magnetocrystalline anisotropy which increases at low temperature<sup>23</sup>. However it can be seen that the strain of the irradiated sample is not fully recovered at low temperature since the frequency shift contrast of the irradiated sample is slightly lower than that of the as-grown sample even at low temperature. The contrast of the 70 nm thick film is sharper at low temperature which could mean that ripples become perpendicular domains. The width of domains in both film thicknesses were not affected by the cooling.

---

versus the tip-sample distance as described in equation (2.19).

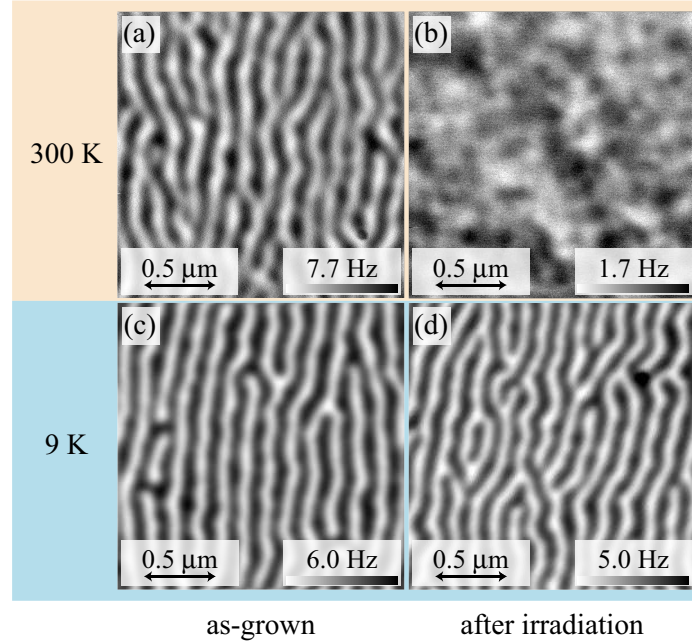
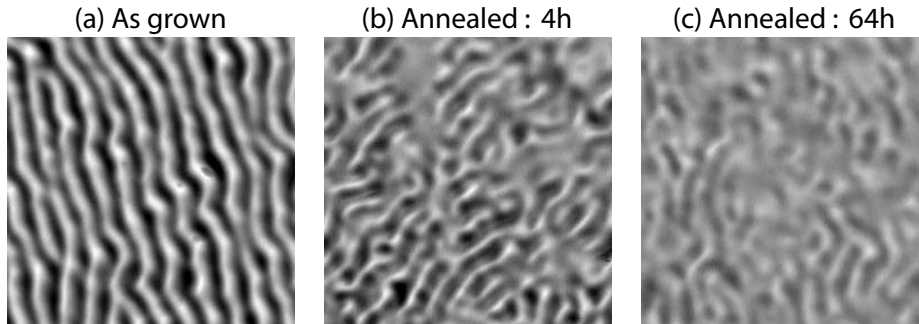


**Fig. 4.9:** MFM measurements performed on the 70 nm thick Ni film. (a) and (b) images are taken at 300 K (RT) before and after irradiation (As shown in Fig. 4.4(d)&(h)). (c) and (d) MFM images are taken at 9 K (LT) before and after irradiation.

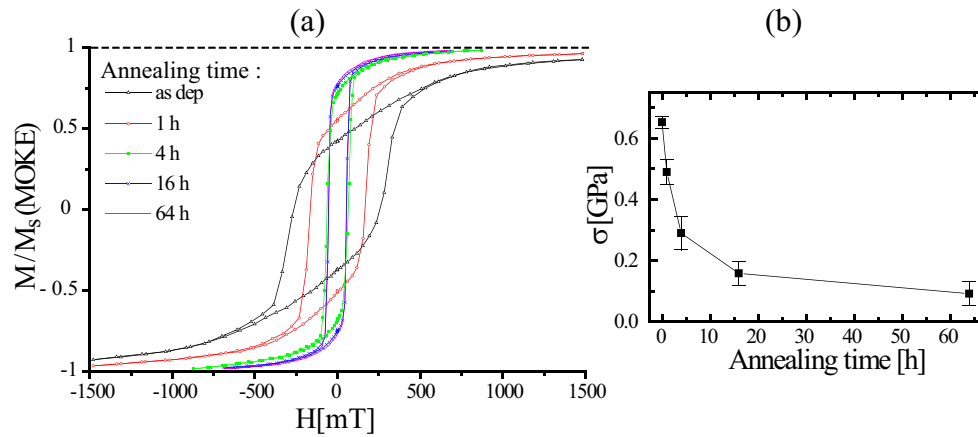
### 4.3.2 ANNEALING

The perpendicular magnetic anisotropy found for the Ni films has been shown to be due to strain. Irradiation removes this strain and consequently the perpendicular anisotropy. An alternative method to remove strain, namely annealing, is presented in this section. This has been done for several annealing times for the 70 nm film<sup>97</sup>. Figure 4.10 presents MFM images of (a) the as grown sample, and after (b) 4 h and (c) 16 h of annealing at 220°C in high vacuum. To allow a visual comparison of the MFM images all data are displayed with the same  $\Delta f$ -range as for the data obtained on the as-grown film. With increasing annealing time, the contrast decreases and the image becomes more blurred. Annealing thus decreases the perpendicular anisotropy. However, in contrast to irradiation, even after 64 h annealing at 220°C the perpendicular anisotropy has not been fully removed. This observation is consistent with hysteresis loops acquired by magneto-optical Kerr effect (MOKE)\*.

\* MOKE, as VSM, measure an area of a few millimetres square. The MOKE measurements were performed at Göttingen by K. Zhang on the apparatus described in G.A. Müller



**Fig. 4.10:** MFM measurements performed on a 70 nm thick Ni film. (a), (b) and (c) images are taken at 300 K (RT) as grown, after 4 h and after 64 h annealing respectively. All images are  $2 \mu\text{m} \times 2 \mu\text{m}$  and the contrasts have been normalised to 4.5 Hz.



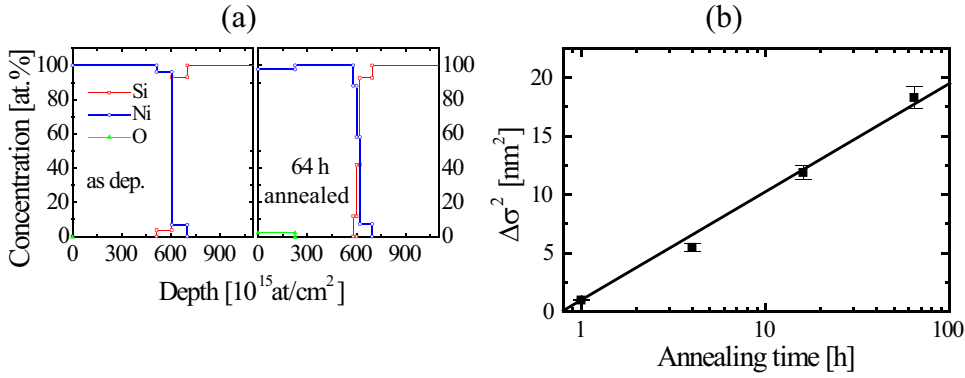
**Fig. 4.11:** (a) Hysteresis loops measured by mean of MOKE for sample with various annealing times. (b) Film stress deduced from XRD measurements for 0, 1, 4, 16 and 64 h annealed sample at  $220^\circ\text{C}$ .

Figure 4.11(a) shows in-plane hysteresis loop measured on the as-grown sample and after various annealing time up to 64 h. Annealing increases the remanence by decreasing the perpendicular anisotropy, which tends to align the magnetisation out of the plane. The coercivity also decreases with annealing time consistent with the results obtained by irradiation.

The annealing induced strain relief has also been confirmed by grazing incidence x-ray diffraction (figure 4.11(b)). A comparison of the strain removal

induced by irradiation (Fig. 4.7) with that achieved by annealing (Fig. 4.11(b)) reveals that some tensile strain remains even after 64 h. This confirms the MFM results that still show a remaining perpendicular magnetisation after 64 h annealing (Fig. 4.10(c)).

However, one must be careful in comparing irradiation and annealing results. Indeed it was shown by RBS that irradiation does not affect the interface, which is not true for annealing as shown in figure 4.12.



**Fig. 4.12:** Atom concentration profiles and interface mixing deduced from RBS measurements : (a) The interface between Ni and Si is very abrupt in the as-grown sample. This interface becomes diffuse after 64 h annealing. (b) To quantify the interface mixing, the interface width ( $\sigma$ ) defined as  $2\sigma$  being the distance between the depth positions with the atom concentration at 84% and 16%<sup>126</sup> has been plotted versus the annealing time. One can see that the increase of  $\sigma$  follows a logarithmic law. The fit in the graph represents  $\Delta\sigma^2 = 1 + 9.26 \cdot \log(t)$ ,  $t$  being the annealing time.

## 4.4 Conclusion and Outlook

In conclusion, our analysis shows that 185(70) nm films of Ni on oxidised Si substrates have a perpendicular anisotropy and a surprisingly strong perpendicular magnetic moment. Irradiating the films with Xe ions without affecting the Si/Ni interface relieves the film strain, causing the magnetisation to fall back into the film plane as the magnetoelastic component of the anisotropy vanishes. Reintroducing strain in the film by cooling down to 9K recovers the perpendicular anisotropy, confirming that irradiation did not adversely affect the crystallinity of the film or its interface to the substrate. Irradiation is thus seen to be effective in selectively removing only the magnetoelastic part of the

films magnetic anisotropy after film deposition. Annealing has been shown to be a second method to relieve the film strain. Although a long annealing time is needed to reach similar strain relief effects as Xe irradiation, annealing has the advantage to not introduce any foreign ions.

Further AFM and MFM experiments have to be done in order to elucidate the mechanism of strain relaxation by irradiation. The work presented here could be enhanced by imaging samples irradiated at the same energy but various fluences. This could bring additional information about the magnetic configuration as well as about the irradiation effect on the sample. In addition, further simulations need to be performed to test the hypothesis of the presence of ripples in the 70 nm thick film and the expected perpendicular domains with closure caps in case of the 185 nm thick film.







# EFFECT OF ION IRRADIATION ON DOMAIN NUCLEATION AND WALL MOTION IN NICKEL FILMS<sup>127</sup>

## 5.1 Introduction

### 5.1.1 MAGNETIC HYSTERESIS

The coercivity of ferromagnetic films (or lack thereof) is exploited in many technological applications, including magnetic storage media<sup>10,12</sup>. To the extent that the macroscopic magnetisation in a material depends on the relative volume fractions of opposing domains, reversal domain nucleation and domain wall motion will largely control the characteristics of the hysteresis<sup>128</sup>. Domain nucleation plays an important role in the hysteresis process<sup>81</sup>. Therefore the nucleation process has been intensively investigated both theoretically and experimentally<sup>81,123,129–132</sup>. The domain wall motion has also sparked strong interest<sup>82,133,134</sup> and many studies on various different materials with perpendicular anisotropy investigate the importance of wall nucleation and motion in the coercivity<sup>128,135–146</sup>. The nucleation coercivity ( $H_{c,n}$ ) and the motion coercivity ( $H_{c,m}$ ) was previously defined<sup>134</sup>.

Magnetometry can be used to determine these values. However, as discussed in chapter 3 it remains difficult to draw conclusions on the magnetisation reversal process solely from magnetometry data. Methods to image the micromagnetic state such as MFM are clearly required<sup>17,146–152</sup>. Here an MFM and magnetometry study of the hysteresis process of as grown and irradiated Ni film is presented.

### 5.1.2 ION IRRADIATED Ni FILMS AT LOW TEMPERATURE

Chapters 3 and 4 have shown the importance of the magnetoelastic component of the anisotropy in Ni films. Furthermore, chapter 4 has shown that irradiation can effectively remove this anisotropy causing the magnetisation to fall into the film plane. In addition, measurements at low temperature have shown the ability to recover perpendicular magnetisation of an irradiated sample by cooling. Therefore, the magnetisation behaviour of both as-grown and irradiated sample can be studied and compared at low temperature. It has

been shown in previous chapters that magnetisation reversal for field applied perpendicular to the sample surface occurs mainly by domain wall motion. It is known that this motion and the preceding domain nucleation can be affected by ion irradiation differently depending also on the ion species and ion energy<sup>99</sup>. Both the number of domain walls existing for a given field history, and their mobility is affected by irradiation. In the present chapter we focus on the effects of Xe<sup>+</sup> irradiation of Ni films through microscopic observations of domain wall motion with quantitative magnetic force microscopy (qMFM)<sup>62</sup>.

## 5.2 Instrumentation and Film Growth

The sample used for this study is the 185 nm Ni film already described in chapter 4, section 4.2. The fabrication, characterisation and irradiation parameters can also be found there.

The macroscopic characterisation of the magnetic hysteresis, remanence, coercive and saturating fields, as well as the salient features of the magnetisation loop of the as-grown and irradiated samples were obtained at 8.3 K with the vibrating sample magnetometer (VSM) described in section 2.3. The micromagnetic characteristics of the films, not accessible to magnetometry, were obtained from MFM images.

The MFM images were taken at 8.3 K using the homebuilt scanning force microscope described in Sect. 2.4. The microscope is located within a superconducting magnet capable of applying fields up to 7 T perpendicular to the sample surface. The instrument was operated in the dynamic mode described in section 2.1.1. All images presented in this chapter were taken at the same tip-sample distance and with the same tip (*Team Nanotec GmbH* silicon cantilever with 4 nm Co coated tip), so as to enable a reliable comparison between images at different fields. The tip calibration as described in section 2.2.3 is given in section 2.6.2. Under these conditions, the average normalised (perpendicular) magnetisation can be calculated from the ratio of up domains to down domains<sup>62,146,153</sup>.

## 5.3 Results

To ensure comparable initial conditions, both irradiated and as-grown samples were demagnetised by means oscillating fields applied in the film plane. Their amplitudes were decreased from 1.2 T to zero. In all cases, stripe domains well aligned with the demagnetising field direction<sup>19</sup> were obtained (c.f. figure 5.1). The high contrast in the images arises from a large component of magnetisation perpendicular to the film plane. Consistent with chapter 4, the contrast

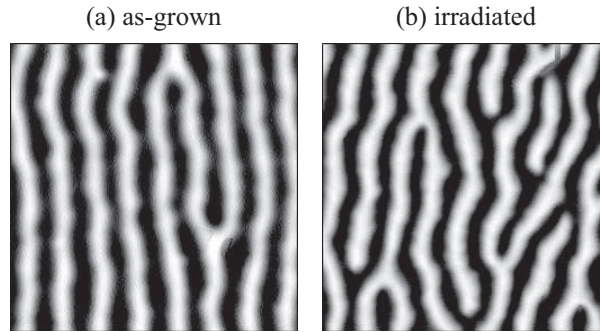


**Fig. 5.1:** MFM images ( $2 \times 2 \mu\text{m}^2$ ) taken at 8.3 K. The width of the stripe domains is  $\sim 125$  nm in both cases.

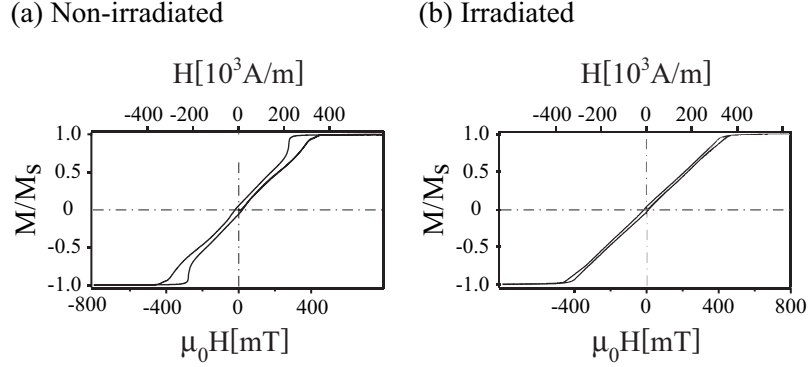
and domain morphology here can be seen to arise from the perpendicular magnetic anisotropy (PMA) in these films. At room temperature the PMA arises from growth induced strain. This strain and consequently the PMA can be removed by ion irradiation<sup>95,111,112</sup>. The magnetisation is then in the film plane. The cooling to 8.3 K re-introduces an in-plane biaxial strain because of the large differential expansion coefficient of Ni and the Si-substrate. PMA is then recovered even in the irradiated sample. The MFM image (Fig. 5.1(b)) showing a stripe domain pattern typical for perpendicular magnetisation accordingly confirms the recovery of the PMA. Thus, a comparative study of the irradiated and as-grown\* films via MFM images is possible.

Figure 5.2 shows perpendicular magnetisation loops (at 8.3 K) for as-grown and irradiated films<sup>†</sup>. From Fig. 5.2(a) it is seen that the coercive field of the as-grown film is only  $\mu_0 H_c = 20 \pm 2$  mT.  $M(H)$  is linear with increasing applied fields up to the saturation field  $\mu_0 H = 450 \pm 20$  mT. Decreasing the field from 800 mT (i.e. after saturation) a sharp shoulder in  $M(H)$  can be observed. This indicates the delayed nucleation of reversed domains. For comparison, a magnetisation loop from the irradiated sample is shown in Fig. 5.2(b). In this case the saturation field is  $\mu_0 H = 490 \pm 40$  mT. Surprisingly, the coercive field is only  $\mu_0 H_c = 12 \pm 2$  mT and thus even smaller than that of the as-grown film with fewer defects. The delayed nucleation seen in the as-grown films is not observed. This indicates that the irradiation induced defects serve as nucleation centres.

Additional differences between the films become apparent upon detailed study of the micromagnetic structure with MFM. Images taken at selected

\* Note that, since the MFM measurements were performed after demagnetising the sample, the domain state is not as grown. “As grown” refer in this thesis to the fact that the sample structure has not been modified.

<sup>†</sup> The in-plane magnetisation loops (at 8.3 K) are shown in appendix E. In this appendix is also shown the magnetisation loops measured at room temperature.



**Fig. 5.2:** VSM loops taken at 8.3k of the (a) as-grown and (b) irradiated samples. The applied field is perpendicular to the film.

points on the raising and decreasing branches of the magnetisation loop, as shown in Fig. 5.3(a) and (b) for the as-grown and irradiated films, respectively. The starting point for the image sequences are the images also shown in figure 5.1.

For the as-grown sample, increasing the applied field reveals that the domains with magnetisation opposite to the field (bright domains) narrow, shrink in length and finally vanish completely (Fig. 5.3(a)I-IV). Subsequently reducing the field does not immediately result in the re-appearance of these domains. Domains do not nucleate until the field drops (Fig. 5.3(a)V-VIII). At field values just slightly lower than 270 mT the white domains already make up more than 25 % of the imaged sample area. This confirms the sudden drop in magnetisation measured by VSM (Fig. 5.2(a)). When the field is further lowered, the reverse domains increase in length and slightly in width until bright and dark areas are essentially equal (Fig. 5.3(a)IX-XV).

The corresponding micromagnetic behaviour of the irradiated sample is different. As the field is increased from zero, the bright (i.e. reverse) domains break up at multiple locations along the each stripe, forming small spot-like domains (Fig. 5.3(b)I-III). With increasing field these domains shrink and finally vanish (Fig. 5.3(b)III-V). Images taken at points on the decreasing branch of the magnetisation loop show a high areal density of nucleation points. These domains then grow in both width and length until at zero field the bright and dark areas are equivalent. Notice that the average length of contiguous reversal domains is significantly shorter than for the as-grown sample.

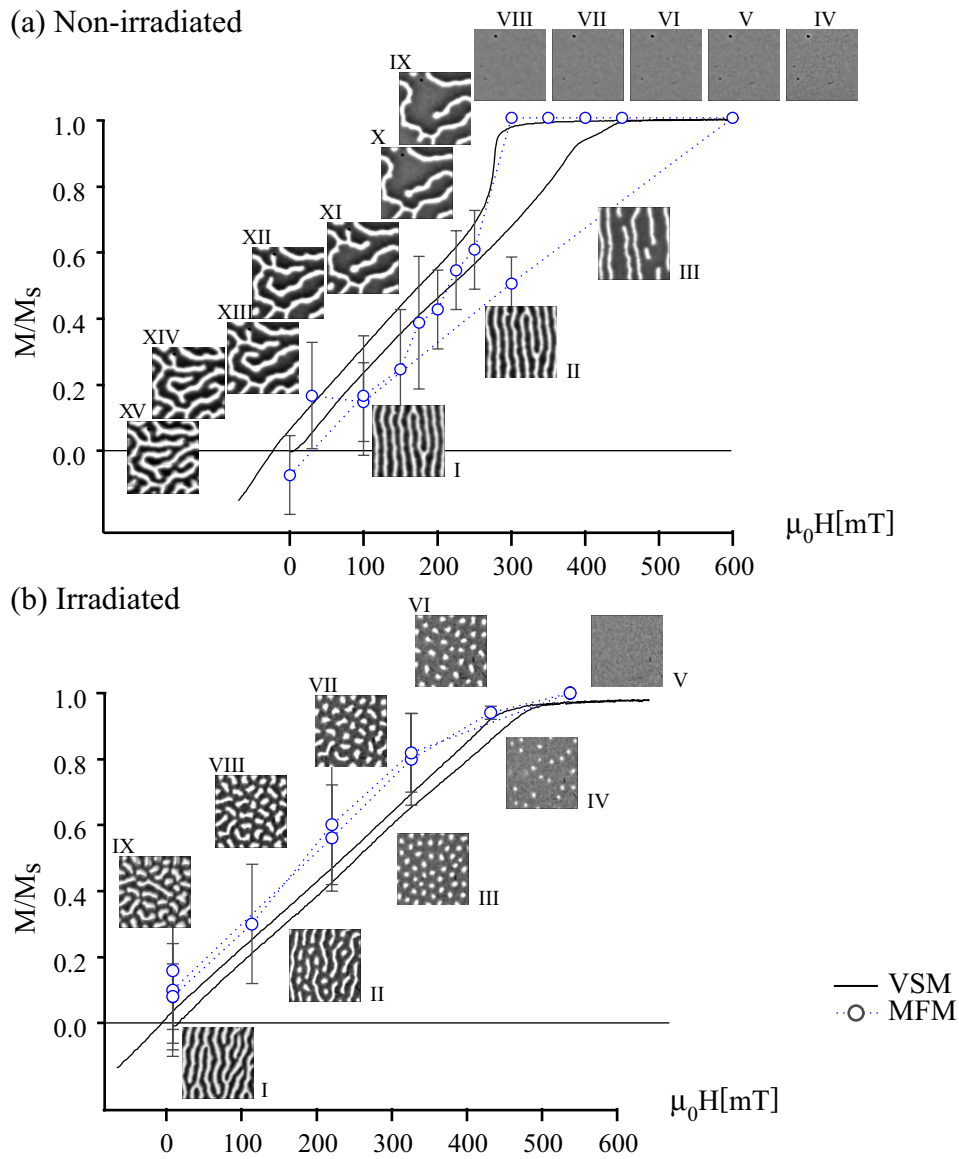


**Fig. 5.3:** Comparison between MFM images ( $4\mu\text{m}^2$ ) and perpendicular VSM loops. The points represent the average normalised magnetisation calculated from the MFM images. The dotted line represents the loop as determined by MFM averages. The solid line corresponds to the VSM loop (c.f. Fig. 5.2).

## 5.4 Discussion and Conclusions

The magnetisation determined from the black and white ratio visible in the MFM images corresponds well with the magnetisation values measured by MFM (Fig. 5.3)\*. The reversal process is governed by the nucleation of measured domains followed by subsequent domain wall motion. Surprisingly, the process is very similar for the as-grown and the irradiated films. Particularly the absence of a hysteresis for the irradiated film seems surprising.

As was pointed out previously<sup>17</sup> (c.f. Chap. 3) this is a direct consequence of the large density of domains. The narrow width of the domains (125 nm) requires minimal wall motion for a large magnetisation change. Thus domain wall motion can occur between existing pinning centres.

The MFM data however, clearly reveals the various roles of the defects for the magnetisation reversal process. When the field is increased the defects will lead to a breaking up of the domains into smaller domains (as seen by comparing Fig. 5.3(a) II – IV and Fig. 5.3(b)II – IV). The area of these breached domain segments can then easily decrease because the walls can move sufficiently between the defects. Once the film is saturated, and the field is again decreased, the defects facilitate domain nucleation (domain nucleation occurs at one order of magnitude more points after irradiation as seen by comparing inset IX in Fig. 5.3(a) and inset VI in Fig. 5.3(b)<sup>†</sup>).

In summary, the irradiation of Ni film with Xe leads to defect that have a strong influence on the domain wall mobility. Nevertheless, the hysteresis of the irradiated film is smaller than that of the as-grown film. This is because the defects facilitates domains nucleation. This enhances the areal density of domains that can subsequently grow by a motion of the domain walls between the defects<sup>136</sup>.

---

\* VSM gives an average magnetisation over several  $\text{mm}^2$ , whereas the magnetisation calculated by MFM is an average over  $4\ \mu\text{m}^2$ . This explain the small variations between the two results seen on figure 5.3.

<sup>†</sup> Fig. 5.3(b)VI shows 37 nucleation centres, whereas it is not possible to affirm that Fig. 5.3(a)IX contains even one nucleation centre (it could contain a maximum of 5).

## MACROSCOPIC AND MICROSCOPIC MAGNETIC RETURN POINT MEMORY<sup>154</sup>

### 6.1 The Importance of Magnetic Memory

Hysteresis lies at the very foundation of the magnetic recording industry. Hysteretic systems are employed as recording media because they retain their magnetic state for a long period after a writing operation, namely they exhibit **magnetic memory**. This memory has been extensively studied and exploited. However, despite decades of intense study and significant recent advances<sup>18(chap. 5.6.1), 19</sup>, a fully satisfactory microscopic understanding of magnetic hysteresis is still lacking<sup>20,21,155</sup>. Due to the central importance of memory in recording media, various types of memory have been studied. The macroscopic magnetisation returns to the same value after a cycle through the major hysteresis loop, “remembering” the previous state. This will be defined as macroscopic return point memory. Another memory is complementary point memory, which will be defined in the next section. It has been shown how important these memories are in terms of applications<sup>156</sup> as well as in terms of fundamental microscopic understanding of magnetism<sup>20,133,157–164</sup>.

Hysteretic behaviour and thus magnetic memory in general can be varied by the introduction of appropriate disorder into the system. Over the past 40 years, this technique has developed into a high art form<sup>10,12</sup>. Further, it has been shown that this disorder also affects return point and complementary point memories<sup>157</sup>.

Until recently, information about the reproducibility of the domain configuration was extracted from the associated magnetic avalanches via observation of the Barkhausen noise<sup>157,165–167</sup>. Microscopic theories were built on information provided by Barkhausen measurements and macroscopic information from standard magnetometry methods. If the Barkhausen noise repeats perfectly for every cycle of the major loop, one could conclude that avalanches occur in the same time and therefore that the microscopic spatial evolution of the domain is also identical. However, this is not a direct measurement. To date, various experimental methods have been developed to directly observe the evolution of the microscopic domain state with the applied field. Pierce

*et al* used the scattering of polarised x-rays to test the domain evolution in Fourier space. Here we use low temperature MFM to study the domain configuration as a function of the applied field in direct space. Samples with high and low defect densities were studied.

## 6.2 Definitions

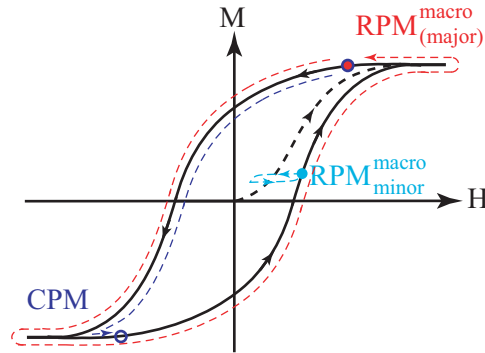


**Fig. 6.1:** Representation of major and minor macroscopic return point memory RPM and complementary point memory CPM. RPM concerns the magnetisation at one point on the hysteresis curve and the same point after an excursion along the full major loop (red point). The  $\text{RPM}_{\text{minor}}^{\text{macro}}$  concerns the magnetisation before and after an excursion on a minor loop as represented in light blue. CPM involves points on the hysteresis curve at equal and opposite magnetic fields showing the equivalent magnetisation.

### 6.2.1 MAGNETIC RETURN POINT MEMORY

In his 1905 dissertation at Göttingen, Madelung defined macroscopic return-point memory (RPM) as follows: Suppose a magnetic system on the major hysteresis loop is subjected to a change in the applied field that causes an excursion along a minor hysteresis loop inside the major loop; if the applied field is readjusted back to its original value and the sample returns to its initial magnetisation, then macroscopic RPM is said to exist. It is convenient to name this kind of return point memory minor loop return point memory  $\text{RPM}_{\text{minor}}^{\text{macro}}$ . Then  $\text{RPM}^{\text{macro}}$  without any subscript index shall describe the return to the initial magnetisation state after a full hysteresis loop. (c.f. figure 6.1 red path).

Madelung's macroscopic characterisation immediately raises the question of how the ferromagnetic domains behave on a microscopic level. Do the



domains remember (i.e. return precisely to) their initial states, or does just the ensemble average remember? Indeed, many microscopic configurations lead to the same macroscopic magnetisation. We present here a study of these questions on a microscopic scale. For such a microscopic study it is useful to define microscopic return point memory (RPM). RPM is said to exist if the sample returns to its initial magnetisation pattern (on a microscopic scale). Thus RPM implies  $\text{RPM}^{\text{macro}}$  but the opposite is not true.

### 6.2.2 MAGNETIC COMPLEMENTARY POINT MEMORY

Besides  $\text{RPM}^{\text{macro}}$  and RPM, it is further important to study macroscopic and microscopic magnetic memory when returning to the point-mirror symmetric point on the magnetisation loop. This kind of magnetic memory is called complimentary point memory ( $\text{CPM}^{\text{macro}}$ ) and microscopic complimentary point memory (CPM) respectively (c.f. figure 6.1 blue path). The work of Pierce *et al* and our own work shows that, on a reasonably large sample area, perfect RPM and CPM does not occur\*. Instead, only partial RPM and partial CPM exists. Mathematically, this partial memory will be described by the cross-correlation coefficient between two data-sets.

## 6.3 Previous Works on Return and Complementary Point Memory

Since the Madelung definition, one hundred years ago, return point memory remains largely unstudied from both a theoretical and experimental aspect. Third-generation synchrotron sources recently made available fully coherent, quasicontinuous beams of x-rays. Pierce *et al* have used this availability to perform a reconstructionless x-ray speckle metrology using coherent, resonant, magnetic x-ray scattering. They show that the speckle pattern acts as a fingerprint of the domain configuration and allows the ensemble of microscopic magnetic domains to be monitored versus the applied field history. They investigated Co/Pt multilayer films with different defect densities by repeated cycling over the hysteresis loop. The macroscopic magnetisation returns to the same value after each cycle for all samples studied. However, a high but incomplete RPM was only found for the highly disordered samples and RPM was found to be higher for the locations on the hysteresis loop characteristic

---

\* Note that RPM equal to unity can be observed in certain systems such as exchange bias systems where frozen spins act as a memory of the micromagnetic pattern even at saturation<sup>61,168</sup>.

for domain nucleation\*. Pierce *et al* have also studied CPM and have found that the disordered samples also exhibit CPM but smaller than RPM. However, the RPM-CPM difference does not exceed 10% and it remained unclear whether the difference was caused by an instrumental bias<sup>164</sup>. Pierce *et al* have also studied the evolution of the RPM and CPM at different positions on the magnetisation curve as shown in figure 6.2. This shows that both RPM and CPM effects are maximum at domain nucleation and they diminish to rather small values just before reaching saturation.

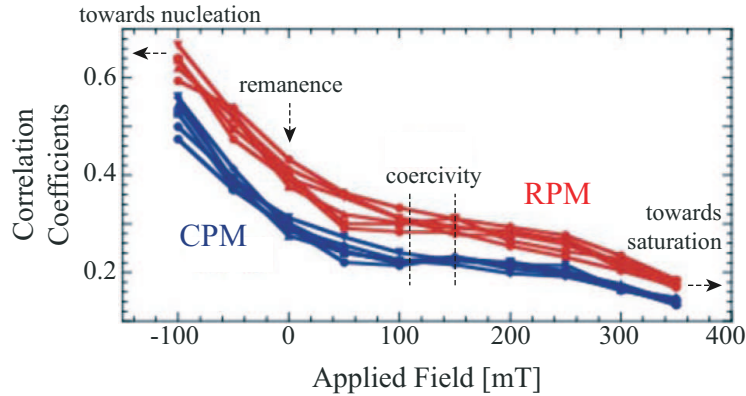


**Fig. 6.2:** Measured RPM and CPM values versus the applied field for high defect density samples.<sup>157</sup>

In order to explain their results, namely the incomplete RPM and CPM and  $CPM < RPM$ , Pierce *et al* have compared the predictions of various theories on magnetic hysteresis with their experimental results.

The experimental observation that CPM is always smaller than RPM can be understood in the context of two theories:

1. A hamiltonian with a local random field including a large component obeying spin inversion symmetry and a small component that breaks the spin-reversal symmetry<sup>158–160</sup>.

Pierce *et al* proposed that the spin-reversal symmetry may be broken by frozen magnetic impurities or by a wide distribution of domain coercivity leading to incomplete saturation<sup>157</sup>. Although it seems reasonable

---

\* X-ray speckle spectroscopy gives microscopic information since the change of any area of the sample changes the entire speckle pattern. However working in Fourier space gives only the intensities and excludes the phase information (except in holography experiments). The reconstruction in real space is therefore normally impossible. Pierce *et al* have overcome this problem by reducing the entire image analysis to a correlation coefficient between two images. They have then a way to measure the RPM and CPM values but not an ideal tool to understand it.

that his experimental results could be explained by such a model, a quantitative modeling at non-zero temperature has not been attempted.

2. An alternative explanation is based on a spin-reversal symmetry Hamiltonian but with a spin dynamics that breaks spin-reversal symmetry. Deutsch *et al* used the Landau-Lifshitz-Gilbert-Bloch-Bloembergen formalism and show dynamic symmetry breaking<sup>158,162,163</sup>. However, these numeric results still have rather large error bars and the difference between RPM and CPM is not much higher than these error bars.

To further explore these effects Katzgraber *et al* have numerically studied paradigmatic models for random magnets. This shows that simple systems with Ising spin symmetry reproduce RPM and CPM increasing for increasing disorder, with RPM always bigger than CPM<sup>164</sup>. They have used three models (Edwards-Anderson spin glass, random-field Ising model (RFIM) and spin glass with diluted random field), and they always obtain CPM and RPM even at finite temperature. They also show that both memory effects increase with increasing disorder. Moreover, they show that while spin glasses show identical CPM and RPM because of their spin reversal symmetric hamiltonian, RFIM always shows an RPM considerably larger than CPM because of the lack of spin-reversal symmetric hamiltonian. Finally, the spin glass with diluted random fields breaking spin-reversal symmetry reproduces the experimental results of Pierce *et al*.

In conclusion, the experimental results by Pierce *et al* can be understood qualitatively by two distinct theories, one includes the breaking of spin-reversal symmetry into the spin-dynamics, while the other attributes the symmetry breaking to the hamiltonian<sup>158</sup>.

Pierce *et al* also found that both RPM and CPM values become smaller when going from nucleation towards saturation. We show in this chapter this behaviour is attributed to a variety of possible paths for domain evolution after a defect-determined domain nucleation.

However, to date, it remains unclear whether the observed difference in CPM and RPM arises from the physics of the sample or is due to a slightly non-symmetric experimental set-up. Further, the small difference between CPM and RPM may be within the (non-determined) error bars. Thus, experiments carried out in real space are of undoubted importance.

## 6.4 Experimental

For our MFM study of RPM and CPM, a sample with a large number of defects within the imaging area of our instrument ( $6.8 \times 6.8 \mu\text{m}^2$ ) is required. CoPt multilayer samples with a perpendicular magnetic anisotropy with different defect densities, similar to those studied by Pierce *et al*, were fabricated by plasma deposition. However, all these samples showed only a few defects within the maximum scan area of our MFM. In addition, the hysteresis loop appears rather rectangular at low temperature. Domain nucleation and subsequent domain growth thus occurred in an extremely narrow field region, and as such, these samples were not suitable for our MFM study of RPM and CPM. As an alternative we used irradiated 185 nm thick polycrystalline Ni films deposited onto a Si-substrate. The effect of the ion irradiation on the magnetic anisotropy and on the hysteresis loop has been described in chapter 4 and chapter 5. All the MFM measurements were taken at 8.3 K in order to have a large perpendicular anisotropy\* with the tip described in section 2.6.2 and with the same average tip-sample distance for all compared images. For fields applied perpendicular to the sample surface a linear hysteresis loop that shows almost no hysteresis ( $\mu_0 H_c = 12 \pm 2 \text{ mT}$ ) and saturates at  $\mu_0 H_{sat} = 490 \pm 40 \text{ mT}$  was observed. MFM images showed nucleation at many locations within the limited scan area, and subsequent domains growth.

All RPM and CPM data was measured at 8.3 K with the LTSFM described in section 2.4. This instrument allows the application of fields up to 7 T perpendicular to the sample surface. The application of a homogeneous magnetic field generates a torque on the cantilever, leading to a cantilever deflection and consequently to a change of the tip-sample distance. Hence, for any major change in field the scanning motion of the tip is stopped and the tip is retracted from the surface of the sample sufficiently to avoid an accidental tip-crash. Then the tip has to be re-approached to a pre-selected tip-sample distance after each change of field. This operation, the charging (de-charging) of the superconductor magnet and also the image acquisition ( $\approx 7 \text{ min}$ ) requires a rather noticeable amount of time. As a consequence the number of field sweeps and therefore the total number of images was limited to 36. Thus, the RPM and CPM values were studied at two points on the hysteresis loop only. Figure 6.3 shows the  $M(H)$  loop of the 185 nm Ni on Si at 8.3 K irradiated by 600 keV xenon ions with a fluence of  $1 \times 10^{15} \text{ ions/cm}^2$  as measured by vibrating sample magnetometry.

The MFM images shown in panels (a)-(e) illustrate the dependence of the domain structure when the field is increased from zero to saturation (corre-

---

\* As shown in chapter 4 the magnetisation of the irradiated Ni film is in-plane at room temperature.

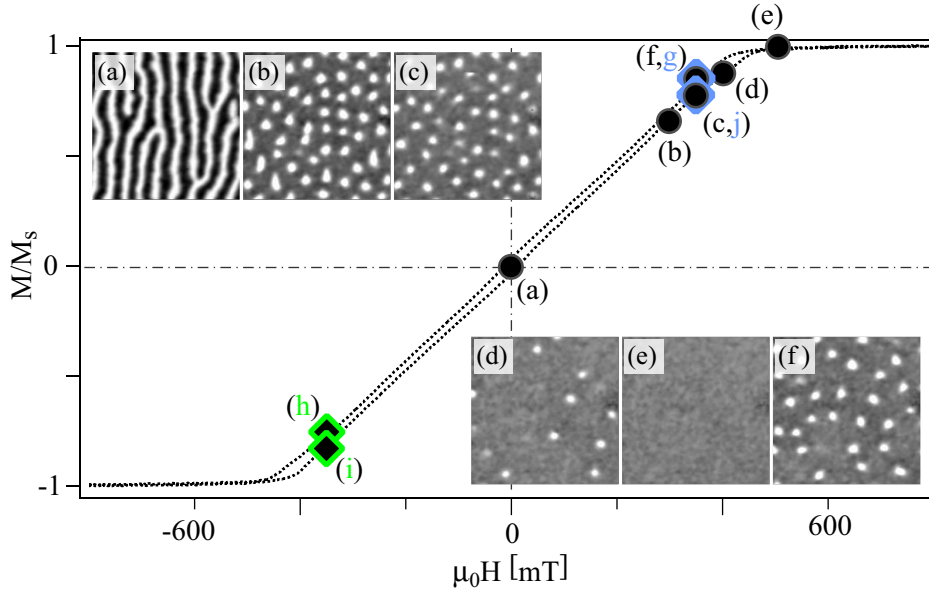


**Fig. 6.3:** Hysteresis loop measured by VSM at  $\approx 8$  K and corresponding MFM  $2 \times 2 \mu\text{m}^2$  images. MFM images taken at point (g) and (i) or (h) and (j) are shown in figures 6.4 or 6.6 respectively.

sponding to the circles drawn into the VSM loop shown in Fig. 6.3). Panel (f) shows the nucleation of domains at 350 mT after returning from a field of 500 mT. Several  $4 \times 4 \mu\text{m}^2$  images were then measured at +350 mT (Fig. 6.3 blue diamond (g)) and -350 mT (Fig. 6.3 blue diamond (i)) when decreasing from +1 T and -1 T respectively, to determine RPM and CPM at the point on the loop when domain nucleation occurs (c.f. Fig. 6.4 & Fig. 6.6 respectively). Note that the  $\pm 1$  T field used here is much larger than the field required for saturation,  $\mu_0 H_{sat} = 490 \pm 40$  mT. MFM images were also recorded on points (h) and (j) (c.f. Fig. 6.3), at the point where the domains vanish before reaching saturation, named as the pre-saturation field (these images will be discussed in section 6.5.2). Note that the MFM images recorded in positive and negative fields have the same appearance, i.e. white spots on a dark background. This is because the magnetisation of the MFM tip flips to an orientation parallel to the external applied field when it becomes larger than the coercivity of the tip ( $\approx 200$  mT). For clarity, table 6.1 illustrates the path on the hysteresis loop that was explored to acquire the images shown in figures 6.3, 6.4 & 6.6.

Point	Description	Image number
$2 \times 2 \mu\text{m}^2$		
(a)	Sample cooled in 0 T	Fig. 6.3
(b)	Field raised to +300 mT	Fig. 6.3
(c)	Field raised to +350 mT	Fig. 6.3
(d)	Field raised to +400 mT	Fig. 6.3
(e)	Field raised to +500 mT	Fig. 6.3
(f)	Field decreased to +350 mT	Fig. 6.3
$4 \times 4 \mu\text{m}^2$		
(h <sub>1</sub> )	Field decreased to -350 mT	Fig. 6.8
(i <sub>1</sub> )	Field increased to -350 mT returning from -1 T	Fig. 6.6
(j <sub>1</sub> )	Field increased to +350 mT	Fig. 6.8
(g <sub>1</sub> )	Field decreased to +350 mT returning from +1 T	Fig. 6.4
	⋮	
(h <sub>8</sub> )	Field decreased to -350 mT	Fig. 6.8
(i <sub>8</sub> )	Field increased to -350 mT returning from -1 T	Fig. 6.6
(j <sub>8</sub> )	Field increased to +350 mT	Fig. 6.8
(g <sub>8</sub> )	Field decreased to +350 mT returning from +1 T	Fig. 6.4
(h <sub>9</sub> )	Field decreased to -350 mT	not shown
(i <sub>9</sub> )	Field increased to -350 mT returning from -1 T	not shown
(j <sub>9</sub> )	Field increased to +350 mT	not shown

**Tab. 6.1:** Path on the hysteresis loop used to acquire the images shown in figures 6.3, 6.4 & 6.6.

## 6.5 Statistical Study on RPM and CPM

The study of RPM and CPM requires the comparison of the micromagnetic states at specific points on the  $M(H)$  loop after cycling through the hysteresis loop. The work of Pierce *et al* was based on diffraction patterns of circularly polarised x-ray beams transmitted through the sample. Contrastingly, we acquired MFM data that can either be analysed by a visual point-to-point correlation, or by performing cross-correlation calculations between different MFM images in real space.

The most criticised point of the work of Pierce *et al* is their comparison of their CPM and RPM values. They found that CPM is always smaller than RPM but the size of the error bars they have attributed to their data points is still intensively debated. Our real space data allows the direct comparison of domain patterns. Hence, error analysis is simpler.

In the following we first discuss the various images obtained at points  $g_k$  ( $k = 1 \cdots 8$ , +350 mT returning the field from +1 T) and points  $i_k$  ( $k = 1 \cdots 9$ ,

-350 mT returning the field from  $-1$  T). At these points on the hysteresis loops multiple domains have nucleated (Sect. 6.5.1). The images taken at points  $h_k$  and  $j_k$  ( $k = 1 \cdots 9$ ,  $\mp 350$  mT near the saturation) are presented in section 6.5.2. These two different hysteresis loop locations are further compared in section 6.7.

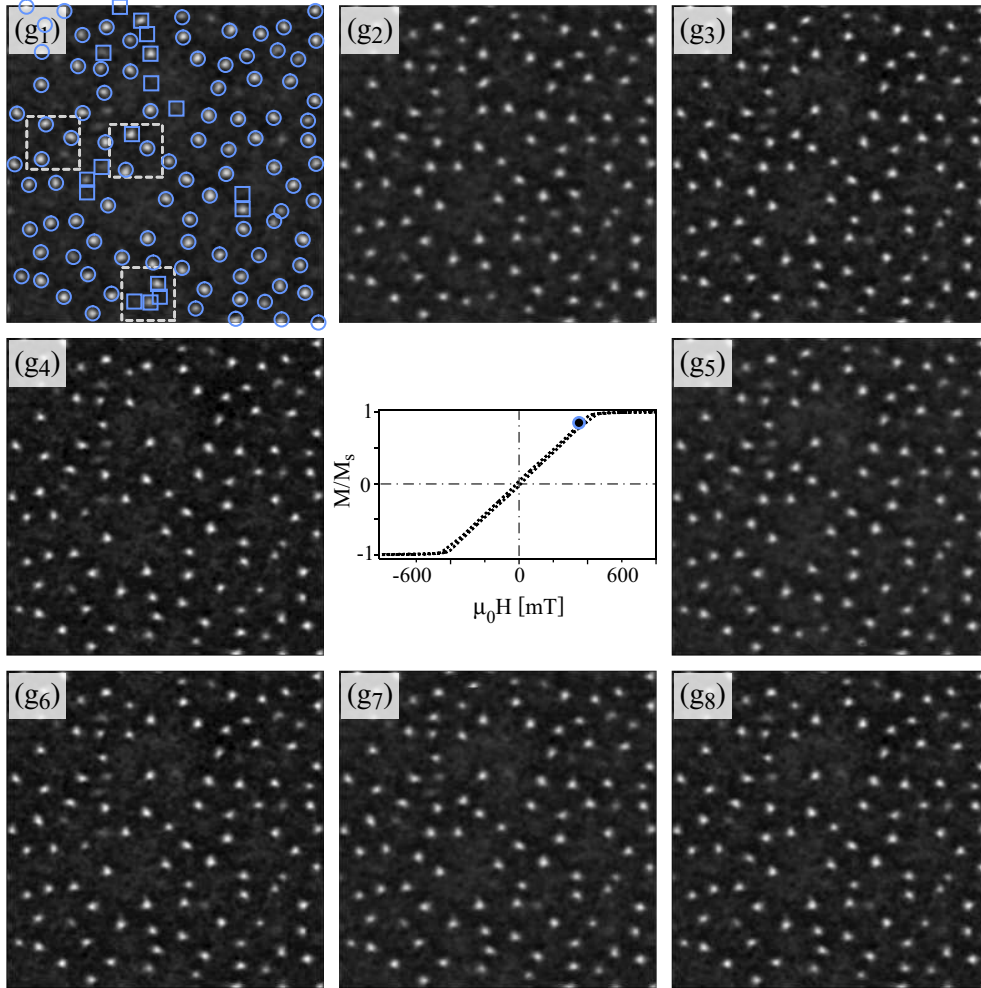
### 6.5.1 NUCLEATION FIELD

Figure 6.4 shows the MFM data obtained at points  $g_1 \cdots g_8$  in a field of  $+350$  mT. At this field many circular domains have nucleated. The comparison of the images reveals that the overall domain patterns are very similar. This indicates a high RPM. The blue squares in panel  $g_1$  of figure 6.4 highlight domains that appear in only a few images. The blue circles in panel  $g_1$  of figure 6.4 highlight those circular domains which are present in all images. Most of these domains appear in exactly the same spot. However a few of them move between two spatially close positions. Figure 6.5 shows a selection of subimages extracted from the images  $g_1 \cdots g_8$  at three different positions ((a),(b) and (c)). These positions are highlighted by dashed grey squares in panel  $g_1$  of figure 6.4.

The subimages extracted at position (a) show a situation where two of the three domains always nucleate at exactly the same location. The third domain, however, chooses between two spatially close points (Fig. 6.5(a): point highlighted by arrow). This can either be due to two spatially close nucleation centres with almost the same energy or one nucleation centre but with a different path of domain wall motion due to an almost symmetrical energy landscape (the path of the domain walls will be further studied in section 6.7.1). Some of the domains appear only in certain images. Thus the probability for domain nucleation is smaller than 1 (Fig. 6.5(b): point highlighted by arrow). Finally areas exist where the nucleation of domains is correlated (Fig. 6.5(c)). This may be due to the presence of the stray field of one domain that increases the energy to nucleate another domain in the close vicinity of the first one. Note that all these cases reduce the RPM values.

The local RPM on a nucleation centre can be 100 %, but the average value over the whole image is not 100 % because not all of the nucleation centres appear in each image. Having 93 domains out of 110 that always nucleate in the same place, we expect an RPM  $> 84\%$ . A calculation based on the cross-correlation of different images will be presented in section 6.6.

This section concentrates on the estimation of the difference between RPM and CPM. Thus, as described above, images were also taken at complementary negative fields as shown in figure 6.6. A visual comparison with figure 6.4 reveals that most domains nucleate in the same locations for positive and negative field. To allow a detailed comparison, we superimpose circles and



**Fig. 6.4:**  $4 \times 4 \mu\text{m}^2$  images of a 185 nm Ni film on Si. Images  $(g_1)$ - $(g_8)$  are taken with  $+350 \text{ mT}$  perpendicular applied field on consecutive major loops.

squares for both the positive fields (see panel  $g_1$  of Fig. 6.4) and the negative fields (see panel  $i_1$  of Fig. 6.6) into one image (see Fig. 6.7). In order to differentiate the data acquired in positive and negative fields the corresponding shapes are green and blue respectively. Note that the positive field overlays have been shifted by one pixel for clarity.

Most of the green and blue shapes overlap. Hence most domains nucleate at the same location for positive and negative fields. This indicates that the defects leading to domain nucleation can be described with a spin-independent Hamiltonian. However, some locations exist where a domain nucleates only



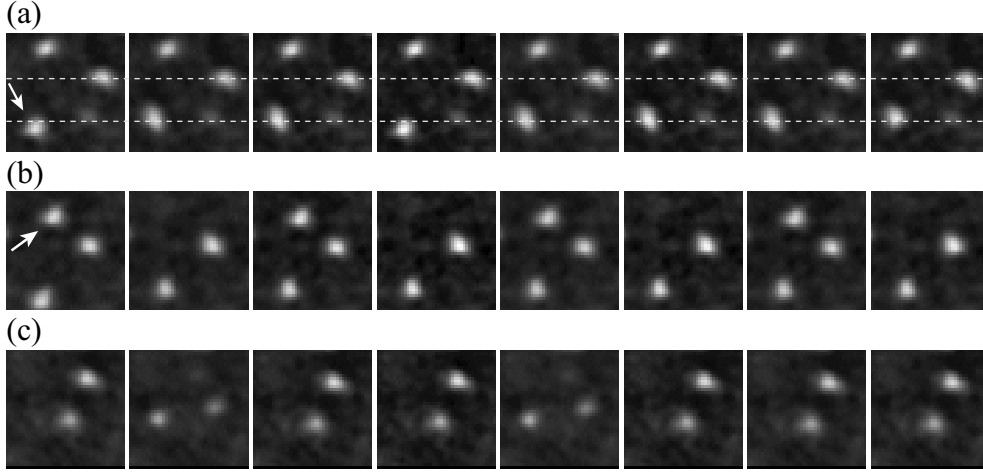


**Fig. 6.5:** Zoomed area of images from figure 6.4. (a) The two points on the top of the images nucleate always at exactly the same place, whereas the one at the bottom move slightly from one image to another one. (b) This two nucleation centres are correlated, if one point nucleates, its corresponding also nucleate.

for one but not for the other field direction. This is already a strong indication that CPM is in fact smaller than RPM but both values are of an appreciable size. However this is not yet a proof because it may be a coincidence that the domains nucleate for one but not for the other field direction. In the following, we use statistical methods to estimate the probability for such a coincidental situation. We select 6 points for which domain nucleation is not symmetrical from images  $g_1 \cdots g_8$  and  $i_1 \cdots i_9$  (the points are numbered in the figure 6.7). The counts of the occurrence of each of the six points is shown in table 6.2.

A first estimation of the probability of occurrence can simply be gained from counting (Tab. 6.2 second column). However, the small number of MFM images acquired reduces the accuracy of the determined probabilities. To improve the estimation of occurrence the *Bootstrap* method has been applied for each of the points<sup>169–171</sup>. The results for the mean probability of occurrence ( $P_{\text{occur}}$ ) and its standard deviation ( $\sigma_{P_{\text{occur}}}$ ) are summarised in table 6.3 for all 6 points.

Assuming that a domain appears exactly  $n$ -times in a total of an extremely large number of  $N$  images recorded for one field but does by coincidence not occur a single time in a total of  $M$  images acquired in the opposite field can be calculated as:

$$P_{\text{coinc}} = \left(1 - \frac{n}{N}\right)^M. \quad (6.1)$$

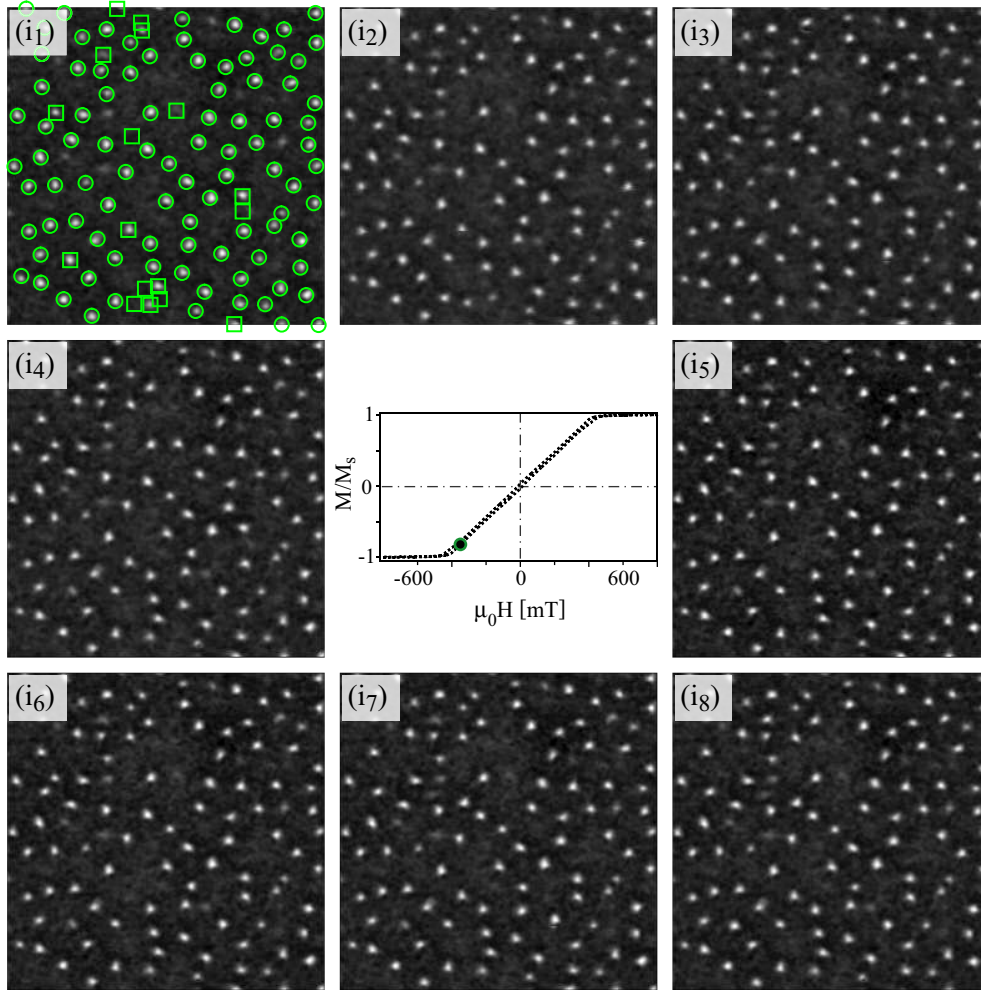


**Fig. 6.6:** Similar measurements as in Fig. 6.4 but for complementary negative fields.  $(i_1)$ - $(i_8)$   $4 \times 4 \mu\text{m}^2$  images were taken at  $-350$  mT (shown on the loop) after a full major loop between each image.

However,  $N$  and therefore  $n$  are not a large numbers. Therefore the probability of occurrence and its error have been estimated by the Bootstrap method (see table 6.3 first three columns)

$P_{\text{coinc}}$  calculated by equation (6.1) becomes larger when  $n/N$  approaches a small number. In order to calculate  $P_{\text{coinc}}^{\text{max}}$ , an upper limit for  $P_{\text{coinc}}$ , we use the smallest reasonable estimate for the probability of occurrence. For this purpose we use  $P_{\text{occur}}^{\text{min}} \equiv \langle p \rangle - 3.4 \cdot \sigma$  where for  $\langle p \rangle$  and  $\sigma$  the Bootstrap

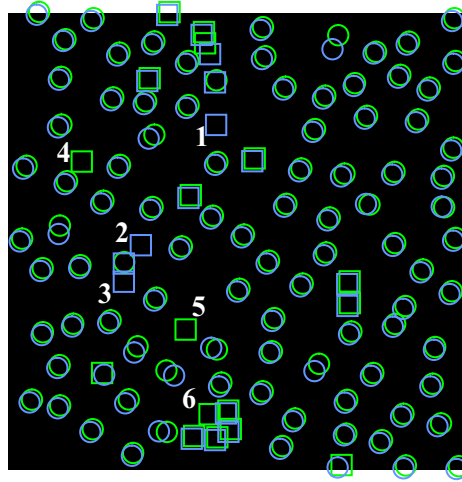


**Fig. 6.7:** Superposition of the pattern in blue/green extracted from images Fig. 6.4/Fig. 6.6 for positive/negative applied field respectively. The circles/squares highlight areas nucleating every time/intermittently over eight consecutive full major loops. The pattern for negative applied field (green) has been slightly shifted for clarity.

Point	Counts	Probability of occurrence
1	01000000	13 %
2	01101011	63 %
3	01101011	63 %
4	111111001	78 %
5	111100111	78 %
6	000000001	11 %

**Tab. 6.2:** The points 1,2 and 3 appear only with positive applied field and the points 4,5 and 6 appear only with negative applied field. The counts are extracted from the MFM images (Fig. 6.4 & Fig. 6.6). The numbers correspond to those in Fig. 6.7. The probability of occurrence and the standard deviation is calculated using a Bootstrap sampling.

values are used\*. The  $P_{\text{coinc}}^{\text{max}}$  can thus be calculated by

$$P_{\text{coinc}}^{\text{max}} = \left(1 - P_{\text{occur}}^{\text{min}}\right)^M \quad (6.2)$$

\* Assuming a binomial distribution, the chance of the probability being smaller than  $p - 3.5\sigma$  is given by  $\frac{1}{\sqrt{2\pi}} \int_{-\infty}^{-3.4} e^{-\frac{1}{2}x^2} dx = 3.37 \cdot 10^{-4}$ . Hence the confidence that this minimum value of occurrence is small enough is 99.966 %.

Point	$P_{\text{occur}}$	$\sigma_{P_{\text{occur}}}$	$P_{\text{occur}}^{\text{min}}$	$1 - P_{\text{occur}}^{\text{min}}$	$P_{\text{coinc}}^{\text{max}}$
1	0.13	0.11	0	1.00	1.00
2	0.62	0.16	0.08	0.94	0.53
3	0.62	0.16	0.08	0.94	0.53
4	0.78	0.14	0.30	0.71	0.04
5	0.78	0.14	0.30	0.71	0.04
6	0.11	0.10	0	1.00	1.00
Total error probability ( $P_{\text{coinc, all points}}^{\text{max}}$ )					$7.80 \cdot 10^{-4}$

**Tab. 6.3:** Error estimation on RPM/CPM difference by a statistical calculation.

with  $M = 8$  and  $9$  dependent of the point. The results for each of the 6 points are summarised in table 6.3(last three columns). The total probability that all points simultaneously occur in one field but not in the other by coincidence ( $P_{\text{coinc, all points}}^{\text{max}}$ ) can then be calculated by the product of the probabilities for each single point. Note that point 2 and 3 are fully correlated and thus have been counted as a single point since this calculation is valid only for independent points. We find an extremely low value, namely  $7.8 \cdot 10^{-4}$ . Thus the probability that our observation of  $\text{CPM} < \text{RPM}$  is due to a coincidence and not a real physical effect is only  $7.8 \cdot 10^{-4}$ !

In conclusion, figure 6.7 shows good return point memory as well as good complementary point memory. In addition it is shown that CPM is lower than RPM with a very small error probability.

### 6.5.2 PRE-SATURATION FIELD

The MFM images recorded at pre-saturation field (at points (h) and (j) (see Fig. 6.3 and Tab. 6.1)) are shown in figure 6.8. Contrasting with the nucleation points, the pre-saturation points show a very small RPM consistent with previous work<sup>20,146,157</sup>. It is clear in figure 6.8 that the images are very different, but a closer look shows some minor similarities. It is not possible in this case to compare each point since the correlation is so poor.

Another way to highlight those similarities is by superposing the 9 images (from 9 consecutive major loops). Then, the pixels appearing more often look bright whereas pixels appearing rarely look dark. That has been done in figure 6.9 adding the nine different magnetisation patterns and normalised to unity. Therefore black pixels ( $= 0$ ) represent regions saturated for all nine images and white pixels ( $= 1$ ) represent areas not saturated for a single image. Figure 6.9(a)&(b) shows the result with normalised contrast for positive and

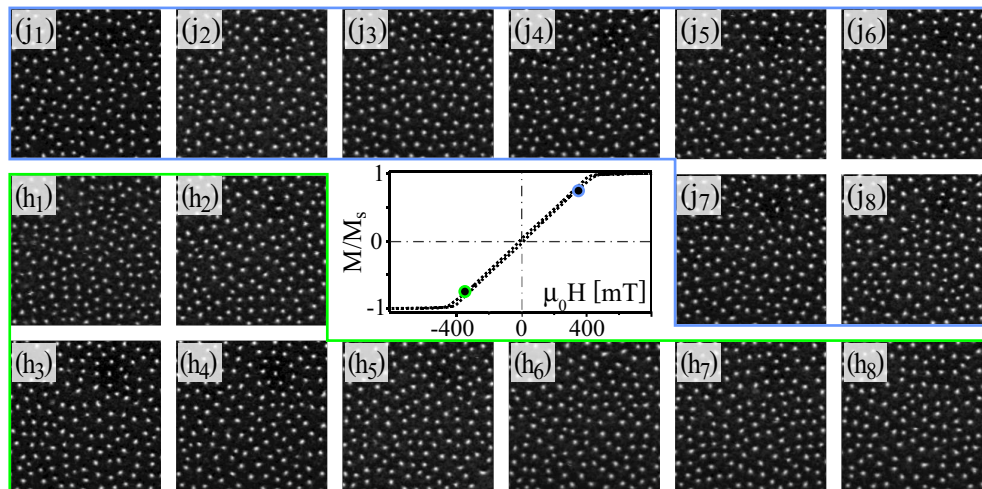


**Fig. 6.8:** Measurement on nine consecutive major loops in pre-saturation state (only 8 images are shown). The images highlighted in red/green are measured with positive/negative applied field as shown in the loop.

negative field respectively. The normalisation implies that pixels with unity intensity are always present and exhibit RPM. It can be seen in figure 6.9(a) that only two points show perfect RPM (figure 6.9(a) arrows). For negative fields (Fig. 6.9(b)) none of the pixels are always present but some of them are present 8 times over 9. For clarity, a discrimination level has been applied to plot as black every pixel present less than 6 times over 9. This is shown on Fig. 6.9(c)&(d) for positive and negative fields respectively. The most relevant points (largest area) have been marked in figure 6.9(c) and superimposed on figure 6.9(d) to be able to have some information on the CPM. The correlation is even poorer between positive and negative field than between different major loops at the same field (only three points correlate). In summary, RPM is very small and CPM is even smaller.

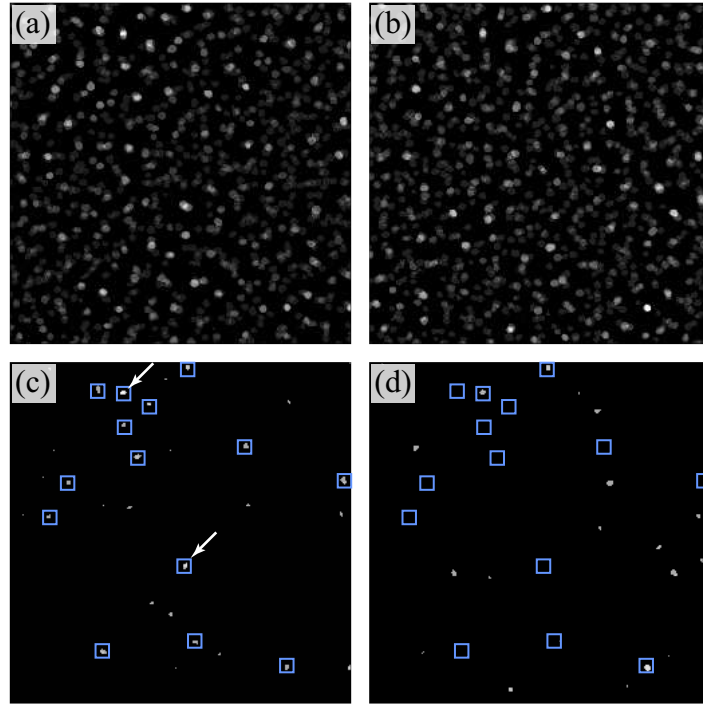


**Fig. 6.9:** Pre-saturation field images analysis : (a)/(b) Superposition of nine images taken at pre-saturation positive/negative field respectively. 0 means zero occurrence and 1 means 100% occurrence. (c)/(d) discrimination process to hide every pixel appearing less than  $\frac{6}{9}$  times. The blue squares show the relevant point in image (c) and are overlaid on image (d) to help the comparison.

## 6.6 RPM and CPM Determined from Cross Correlations

In the previous section our discussion on RPM and CPM was based on the visual inspection of the locations of domain nucleation. Using appropriate statistical methods we found that CPM is lower than RPM with an extremely high confidence of 0.99922. We have also estimated the RPM value of  $\pm 350$  mT at the nucleation field ( $> 84\%$ ) and found that the RPM value of  $\mp 350$  mT at the pre-saturation field is very low.

Here we use cross correlation between various images to calculate RPM, CPM and their error, similarly to Pierce *et al.* The cross correlation between

two images ( $a$  and  $b$ ) is calculated as<sup>20,162</sup> :

$$\rho(a, b) = \frac{\text{Cov}(a, b)}{\sqrt{\text{Cov}(a, a)\text{Cov}(b, b)}} \quad (6.3)$$

where the covariance  $\text{Cov}(a, b)$  of two images in real space is given by :

$$\text{Cov}(a, b) = \frac{1}{n} \sum_{k=1}^n (x_k - \bar{x})(y_k - \bar{y}) = \frac{1}{n} \sum_{k=1}^n x_k y_k - \bar{x}\bar{y}. \quad (6.4)$$

The sum is over all pixels and  $n$  is the pixel number.

In order to increase the signal-to-noise ratio we do not directly use the MFM grey-scale images, because the data also contain a contribution from the topography of the sample and measurement noise. While the topography contribution may lead to an overestimation of the cross correlation value, the noise would decrease the evaluated value. Instead of the measured MFM data we use the so-called magnetisation patterns extracted from the MFM data\*.

Because 9 consecutive loops were measured, many different pairs of images can be used to calculate averages and errors of the RPM/CPM values. The data is plotted in figure 6.10. The green and blue histograms represent the values measured of RPM/CPM for nucleation field and pre-saturation field, respectively. The dashed bars and solid bars represent the values of RPM and CPM respectively. One can clearly see that for the nucleation field  $\text{RPM} = 0.87 \pm 0.05$ , whereas  $\text{CPM} = 0.80 \pm 0.04$ . The pre-saturation field data shows an RPM much smaller ( $0.22 \pm 0.04$ ) and a CPM even smaller ( $0.18 \pm 0.03$ )<sup>†</sup>. This shows that RPM is high at the nucleation field. RPM at the pre-saturation field is much smaller. In agreement with the results of Pierce *et al*, CPM is smaller than RPM for both points on the hysteresis loop. However, the error bar of the RPM and the CPM values are relatively large, while the difference between the RPM and CPM is small. Thus the statement that CPM is smaller than RPM cannot be made with high confidence. Note that this remains one of the most criticised points of the work of Pierce *et al*.

Here the advantage of a visual comparison of the real space images (see Sect. 6.5) over a statistical method based on the cross correlation of data-sets becomes apparent. As revealed by a visual comparison of Fig. 6.6 and Fig. 6.4 a difference between RPM and CPM occurs in only a few locations. However, the probability that this occurs by coincidence was found to be extremely low, i.e.  $7.8 \cdot 10^{-4}$ .

---

\* The magnetisation pattern is obtained by a discrimination process of the measured image. This can be done because all the measurements have been taken with the same tip-sample distance.

<sup>†</sup> The values indicated here are the mean and the standard deviation of all possible relevant correlation calculated from the images taken on 4 points of nine consecutive major loops.

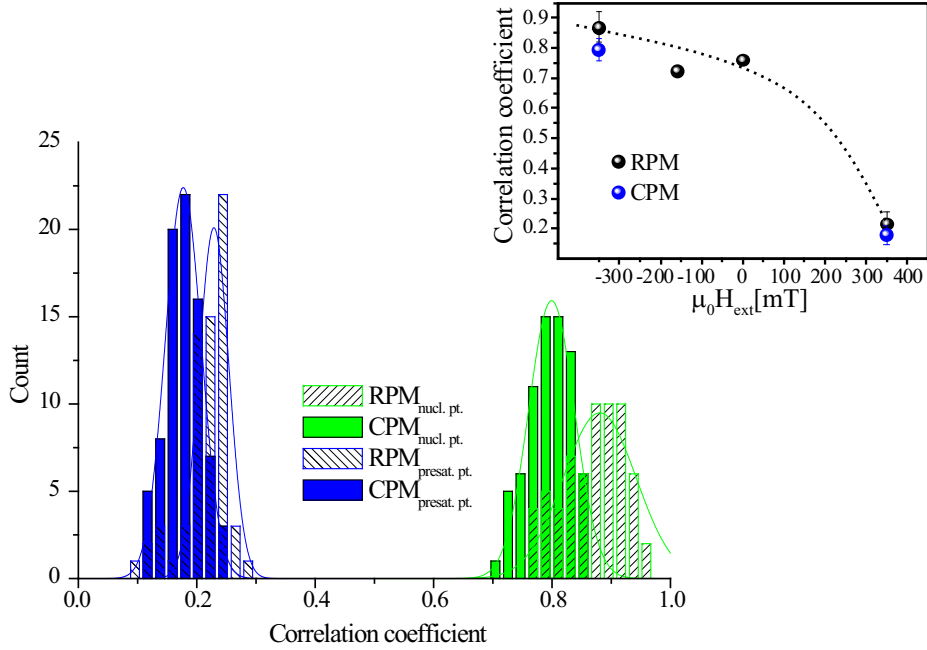


**Fig. 6.10:** Histogram of CPM and RPM values obtained by comparing the different relevant images taken on the nine different major loops. The green and blue show memories for nucleation and pre-saturation field respectively. The plain and dashed histograms stand for CPM and RPM respectively. The inset show the dependance of RPM/CPM versus the applied field (position in the hysteresis loop). The dotted line is a guide for the eyes using qualitatively the dependance shown in previous work<sup>20</sup>. The error bar is the standard deviation on the values measured by comparing different pairs of images. Since the two middle points were calculated from only 4 images, the error could not be estimated by statistical means.

### 6.6.1 RPM/CPM DEPENDANCE ON DEFECT DENSITY

Two Ni film samples were measured to investigate the effect of defects. The first one as presented above was irradiated with Xe ions to induce defects, the second one was non-irradiated. The same measurements as presented in section 6.5.1 have been performed on the low density defect sample. However, as seen in figure 5.3 in chapter 5 the nucleation centres density is so low that it is not possible to find the state where domains nucleate. The hysteresis loop exhibits a shoulder and the transition between  $M/M_s = 1$  and  $M/M_s = 0.8$  is very fast. Since the domain expansion implies a loss of RPM/CPM, we were unable to measure those values. It may be possible with a larger scanning area (to increase the probability to find a nucleation centre). The fact that



the RPM/CPM is not measurable for low density samples is consistent with the conclusions of Pierce *et al* who do not see RPM/CPM for their lowest defect density sample.

## 6.7 The Difference of RPM at Nucleation and Pre-saturation Fields

One of the remaining challenge is to explain the large difference between RPM(CPM) at nucleation and pre-saturation field. The comparison of the as-grown and irradiated samples revealed that the irradiation induced defects serve as nucleation centres (see chapter 5). This explains the high RPM(CPM) in these samples. One may thus expect that these defects also play an important role near saturation that would lead to a high RPM(CPM) at the pre-saturation field. However, the comparison of the locations that show a high RPM at the pre-saturation field (panels c Fig. 6.9) with a typical domain pattern at the nucleation field (Fig. 6.4) reveals a low spatial correlation (see figure 6.11).

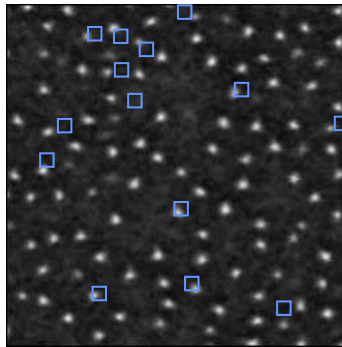


**Fig. 6.11:** The high occurrence points extracted from figure 6.9 overlaid in blue on a typical image in the nucleation state (positive field).

In order to further understand the decay of RPM and CPM for fields between nucleation and saturation, two additional experiments are presented in the following sections.

### 6.7.1 DOMAIN WALL MOTION PATH

As discussed in previous sections the irradiation induced defects act as nucleation centres. This is because the defects lower the energy for domain nucleation. Subsequent domain growth then requires domain wall motion. For this process it is energetically favourable that the total domain wall length remains

minimised and that domain wall motion occurs along paths with no or only small defects. For the irradiated sample which contains many defects, and consequently leads to a high domain density, a large change of the magnetisation can be achieved with little domain wall motion. Thus many different domain wall motion paths are possible. This is clearly visible in figure 6.12(a)-(d). Each of the panels represents an overlay of the magnetisation patterns obtained from MFM images acquired at 380 mT, 320 mT, 160 mT and 0 mT\*. The comparison of panels (a) to (d) reveals that although a high RPM ex-

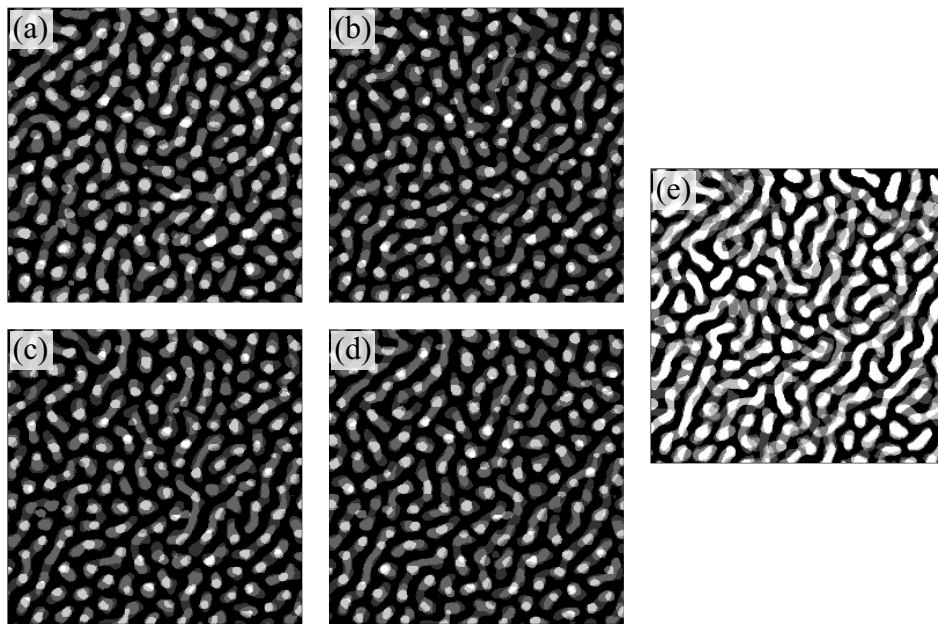


**Fig. 6.12:** (a) Superposition of 4 magnetisation patterns extracted from images taken at four different decreasing fields after saturation (380-320-160-0 mT). (b)-(d) Same as (a) but on three consecutive major loops. (e) superposition of the magnetisation patterns extracted from the four consecutive major loops at 0 mT.

ists for the nucleation field, the development of the zero-field magnetisation pattern is rather irreproducible.

To compare the different domain wall motion paths, figure 6.12(e) shows the superposition of the images taken at 0 mT for the four different loops. The white areas represent areas with 100% RPM. It is apparent that the major part of the white area arises from the original nucleation centres.

In conclusion, using MFM, we have shown that the lowering of the RPM while decreasing the field after nucleation is due to non-reproducible domain

---

\* the magnetisation pattern from the image taken at 320 mT has been multiplied by a factor of 2 to highlight the nucleation points

wall paths. RPM is conserved at the nucleation centres and in regions where the domain wall paths are reproducible. The further loss in RPM when the applied field reaches the pre-saturation field trivially follows from the irreproducible domain wall motion. As shown in figure 6.12, the domains grow from the nucleation centres. The point of nucleation then remains part of the reversed domain for all fields. The irreproducible domain wall motion then leads to a correspondingly irreproducible pattern of point-like domains near saturation (see figure 6.13).

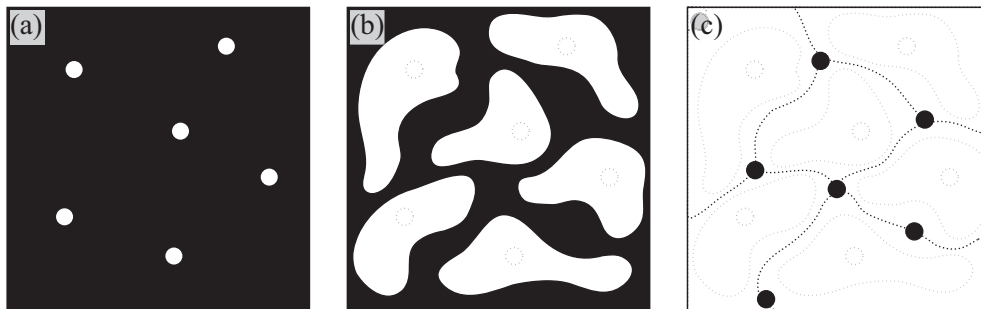


**Fig. 6.13:** (a) The domains grown from nucleation centres. (b) The point of nucleation remains part of the reversed domain for all fields. (c) The domain wall motion leads to a pattern of point like domains near saturation.

### 6.7.2 MINOR LOOPS

The loss of RPM(CPM) from the point of domain nucleation to the zero-magnetisation state\* was found to be due to random domain wall motion (see Sect. 6.7.1 and Fig. 6.12). The rapid decay of RPM towards the zero-magnetisation state ( $H = H_c = 130 \pm 20$  mT) is also nicely visible in figure 6.2 that re-plots the data of Pierce *et al*<sup>157†</sup>. In addition, we have observed that RPM(CPM) decreases further when approaching the saturated state. We have shown that the locations of the last reversed domains before reaching saturation are different from the nucleation positions (c.f. Fig. 6.11). However, this does not explain the small value of RPM(CPM) near saturation. One may expect that defects that resist magnetisation reversal exist, that would lead to high RPM(CPM).

In order to probe the development of RPM from the zero-magnetisation state towards saturation, MFM data were acquired before and after having performed minor magnetisation loops. Figure 6.14(a) shows the MFM data

\* Note that for our sample  $M = 0$  is obtained at  $H \approx 0$ .

† A similar decay can be seen on figure 4 of the 2003 Pierce *et al* article<sup>20</sup>

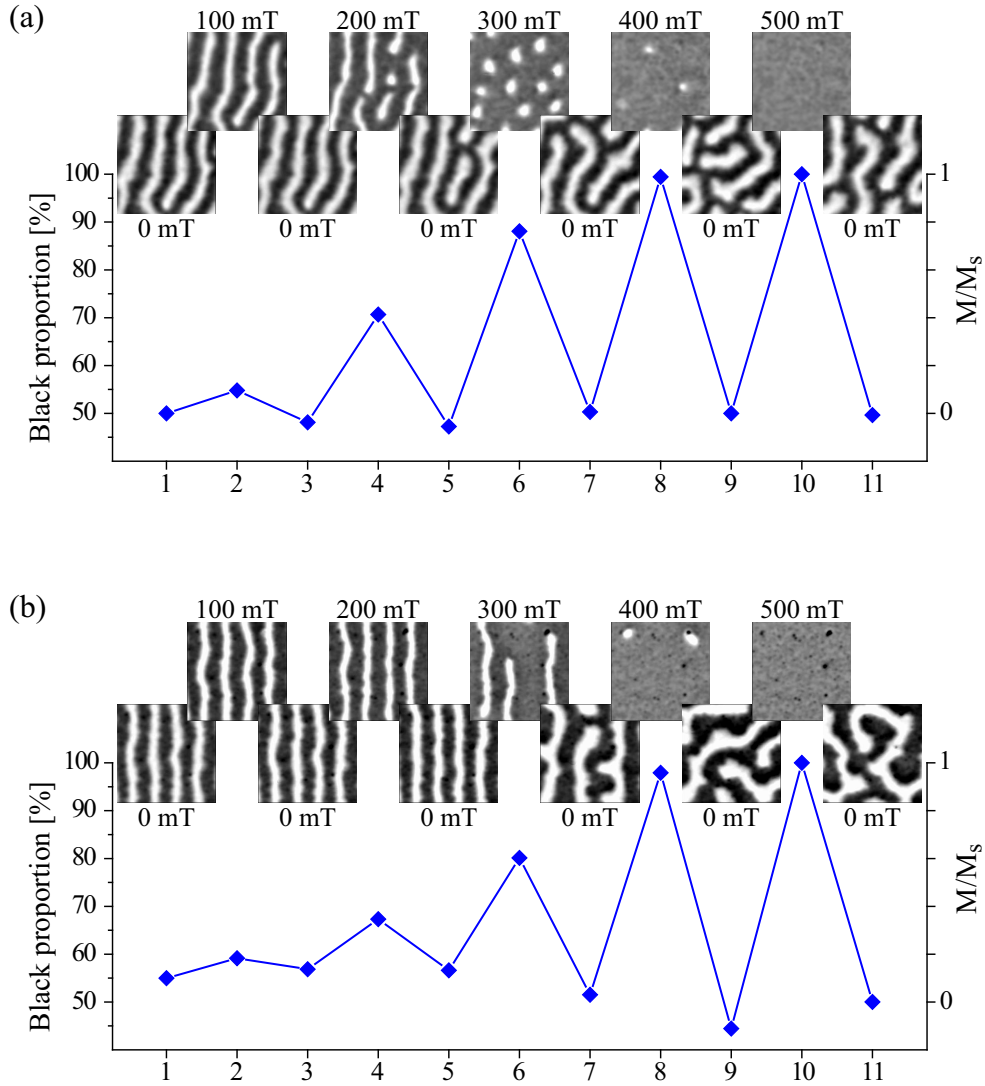


**Fig. 6.14:** Minor loop measurement for (a) a low defect density sample and (b) a high defect density sample. The  $y$  axis represents the average magnetisation over the image area. The  $x$  axis shows the parameter number corresponding to the measurement history shown in table 6.4. All images are  $1 \times 1 \mu\text{m}^2$

and the magnetisation extracted from the images for the field excursions documented in table 6.4 for the irradiated sample.

While the initial stripe domain pattern fully recovers after a field excursion of 100 mT (Fig. 6.14(a) points 1,2 and 3), two of the domains break up into smaller pieces at 200 mT (Fig. 6.14(a) point 4). And while one of the

Point Number	1	2	3	4	5	6	7	8	9	10	11
Field [mT]	0	100	0	200	0	300	0	400	0	500	0

**Tab. 6.4:** Minor loop field excursion performed to acquire the MFM images in figure 6.14.

domains recombines after the field is removed (Fig. 6.14(a) point 5) the other domain remains in a broken-up state.  $\text{RPM}_{\text{minor}}$  is thus reduced. A further loss of  $\text{RPM}_{\text{minor}}$  occurs after a field excursion to 300 mT, 400 mT and finally after having reached the saturation state at 500 mT. The irradiation induced

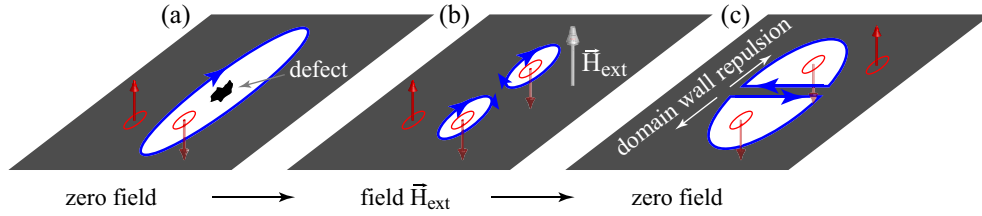


**Fig. 6.15:** (a) A defect due to irradiation lead to (b) the breaking up of a domain into two pieces while an external field is applied. (c) When decreasing the field back to zero the recombination is hindered by the opposite orientation of the magnetisation in the two wall pieces.

defects clearly serve as nucleation centres for reversed domains, i.e. lead to the breaking up of an initiated domain (Fig. 6.15, panel (a)) into two pieces. Once a domain is broken up into two domains (Fig. 6.15, panel (b)) the recombination is hindered by the opposite orientation of the magnetisation in the two wall pieces (Fig. 6.15, panel (c)). Even if their walls are driven into close vicinity by removing the external field that enlarges the domain site, the  $360^\circ$  turn of the magnetisation stabilises the broken-up state. Hence the domain grows into different directions in order to re-establish the zero magnetisation state.

In summary, we find that the defects lead to a breaking up of the initial domains when a field is applied. Once a domain is broken-up into two pieces, the recombination after removing the field is hindered by the opposite orientation of the domain wall facing each other. It thus seems that a high defect density may even decrease  $\text{RPM}_{\text{minor}}$  more rapidly when a field is applied. This is nicely confirmed by a corresponding study with the as-grown sample (see Fig. 6.14(b)).

In this sample RPM has been shown to be so small that we could not measure it with our scan range (see Sect. 6.6.1). Surprisingly, the as-grown (less defective) sample shows a higher  $\text{RPM}_{\text{minor}}$  than the irradiated sample

when performing minor loops. The application of a small field leaves the stripe domains intact but only changes their width. The  $\text{RPM}_{\text{minor}}$  decreases only when applying a 300 mT field and then decreases very rapidly while applying larger field\*.

## 6.8 Conclusion and Outlook

Pierce *et al*<sup>20</sup> have measured macroscopic and microscopic RPM and CPM. Both values were found to become smaller when going from nucleation to zero magnetisation state and finally to saturation. Pierce *et al* also showed that CPM is smaller than RPM but the difference was of the same order as the error bar, meaning that the debate on this topic remained open. In contrast to the work of Pierce *et al*, our MFM data were acquired in real-space. We were therefore able to demonstrate that the high RPM(CPM) at nucleation field is due to defects in the sample and that CPM is in fact smaller than RPM with extremely high confidence.

Note that presently two distinct theories exist to explain that  $\text{CPM} < \text{RPM}$ . One attributes the lower CPM to a random field with a spin-asymmetric Hamiltonian, while the second theory is based on a spin-reversal symmetric Hamiltonian but attributes the spin asymmetry to a spin asymmetric damping term in the Landau-Lifshitz equation. Based on our measurement that shows spatially well localised points that break spin-reversal symmetry, we believe that at least in our sample the magnetisation process is governed by a spin-asymmetric random field. We have recently performed further experiments where the ratio of  $\frac{\text{CPM}}{\text{RPM}}$  was compared for zero field and field-cooled samples. The field cooled samples showed considerably more locations that have RPM but no CPM (c.f. appendix F). However the data is not yet fully analysed at the time of completion of this thesis. This would definitely point toward the theory including a random field (coming from the defects) with a spin-asymmetric Hamiltonian.

In order to compare our data to previous work by Pierce *et al*, cross-correlation coefficients were calculated between a large selection of images. From such calculations we were able to evaluate  $\text{RPM}(\text{CPM})$  and the corresponding error bars at the nucleation and pre-saturation fields. The paths of the domain walls when reducing the magnetisation from a domain nucleation state towards zero magnetisation were imaged. We showed that the domain wall motion is rather irreproducible. This explains the loss of  $\text{RPM}(\text{CPM})$ .

---

\* The average magnetisation appears to take values below zero for points 7, 9 and 11 in the figure 6.14. This is an artefact due to the small averaged area. Indeed, the shape of the domains change drastically and the importance of the border of the image is not negligible for such a small image.

In addition, the reason for the low RPM(CPM) at the pre-saturation field was analysed by performing various minor loops. Note that, to date there is a common understanding that a high defect density leads to a high RPM. However, our minor-loop  $\text{RPM}_{\text{minor}}$  study of the as grown Ni film and the irradiated film clearly shows that this is not the case at least for small field excursion. Surprisingly, the sample with fewer defects showed a higher  $\text{RPM}_{\text{minor}}$ . We found that this is due to collective domain wall motion.

We currently believe that the size of the RPM does not only depend on the defect density but is also governed by the kind of the energetically most favourable domain pattern. Small width stripe or maze domain patterns seems to cause a higher RPM. Clearly further experiments are needed to further elaborate this last point.







## E-BEAM LITHOGRAPHY AND MFM TO THE LIMIT : A STUDY OF Co/Pt NANODOTS<sup>172</sup>

### 7.1 Nanodots, a Route to Higher Density Recording Media

The annual increase in the areal density of hard disc drives has mainly been achieved by scaling, which requires a reduction in grain sizes in order to achieve an acceptable signal to noise ratio (SNR). However, if grains' volume is reduced too far, their thermal energies become comparable to the anisotropy energy of the grains and can induce random reversals in the magnetisation<sup>10,12,173</sup>. Coupled with the requirement of a reasonable number of grains per bit to attain satisfactory SNR, this phenomenon imposes a lower limit to the size of bits, known as the superparamagnetic limit<sup>174,175</sup>. Note that materials with a sufficiently high anisotropy exist such that the superparamagnetic limit is far off. However, such materials require extremely high writing fields that are difficult to achieve. The fabrication of single domain islands out of continuous thin film magnetic media is one method which has been suggested as a possible route to higher density magnetic data storage<sup>10,176–179</sup>.

Single domain islands, in which the easy axis of magnetisation lies perpendicular to the plane and is derived from interface or crystalline anisotropy rather than shape, have been proposed for patterned media<sup>175</sup>. Materials of this nature can be made thin, and the resulting islands could be used with emerging perpendicular recording technology. Co/Pt multilayers are therefore good candidates for patterning because of their strong interfacial perpendicular anisotropy, large coercivities and high squareness<sup>12,128,180</sup>.

There have been several studies on the patterning of Co/Pt and similar materials using different techniques including: deposition onto patterned resist<sup>181</sup>, ion beam patterning using stencil masks<sup>182</sup>, ion irradiation patterning of magnetically hard and soft areas<sup>183</sup>, focused ion beam patterning<sup>184,185</sup> and deposition onto pre-patterned substrates<sup>186</sup>. The latter technique has produced the best results, with 30 nm diameter magnetic islands with a periodicity of 60 nm. It does however suffer from the drawback of sidewall deposition

which could introduce coupling between the dots and the trench.

MFM has been shown to be a powerful technique to investigate the magnetic properties of nano-objects due to the high resolution and sensitivity achievable<sup>11,60,131,187–195</sup>. In the same way that hysteresis curves were reconstructed for Ni films via MFM imaging at different field (c.f. Chap. 5), this has been done for pattern media\*<sup>127,135,153,196</sup>. In previous chapters, MFM was used to study the anisotropy, the hysteresis and the domain nucleation and wall motion of Ni films. Here we concentrate on studying the switching field distribution (SFD) of patterned Co/Pt nanodots.

Preliminary studies of writing errors in patterned media indicate that to attain acceptable error rates, the switching field distribution (SFD) of the islands needs to be very narrow. Therefore, the evaluation of the SFD of practical islands is of great interest<sup>197,198</sup>. Recent developments in high resolution magnetic force microscopy enable a lateral resolution below 10 nm, which allows imaging of 25 nm nanodots. In this chapter, we present the direct measurement of the SFD of Co/Pt island arrays, with islands ranging from 25 nm to 100 nm diameter. These arrays have been fabricated by patterning predeposited Co/Pt multilayers using an e-beam lithographically defined hard mask and ion milling for pattern transfer.

## 7.2 Method

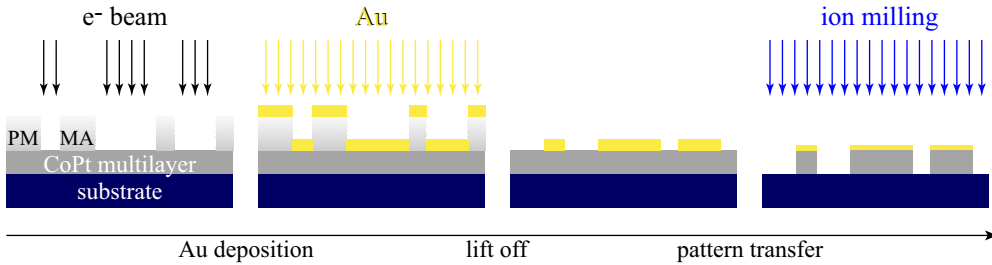


**Fig. 7.1:** Schematic diagram of the four principal stages in the island fabrication process.

Thin film Co/Pt multilayers, with a  $\text{Pt}(10\text{ nm})/(\text{Co}(0.4\text{ nm})/\text{Pt}(1\text{ nm}))_{15}$  structure have been deposited onto Si substrates using e-beam evaporation at  $200^\circ\text{C}$ . The pressure during deposition was  $1.0 \sim 2.1 \cdot 10^{-7}$  mbar and the resulting film's coercivity was 200 mT. Resist (PMMA\*) was then spun onto

\* In a pattern film, MFM allows each dot to be counted, giving the percentage of switched elements as function of the external field.

\* Poly(methyl methacrylate)

the multilayers and patterned by direct e-beam lithography at 20 keV, using a *LEO 1530 Gemini FEG SEM* and *Raith Elphy Plus Lithography System* with a laser interferometer stage. After development, e-beam evaporation was used to deposit 65 nm of Au. The Au layer from the unexposed regions was removed by liftoff, leaving Au nano-pillars which were used as a hard mask to transfer the pattern into the magnetic layer using  $\text{Ar}^+$  milling at 2 keV and 18 mA<sup>†</sup>. The patterning process is illustrated in figure 7.1. Islands, ranging

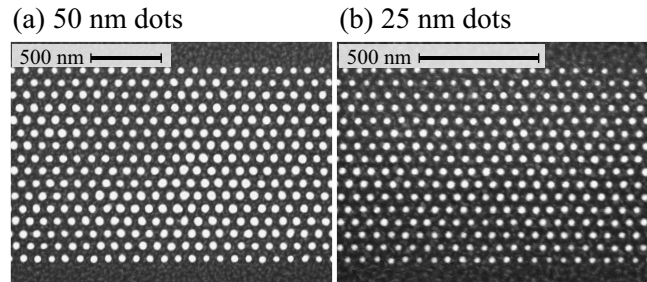


**Fig. 7.2:** SEM images of island patterns, showing (a) 50 nm islands on a 100 nm pitch and (b) 25 nm islands on a 60 nm pitch. The areal density of the 25 nm islands is approximately  $210 \frac{\text{Gb}}{\text{in}^2}$

from 20 nm with a separation of 50 nm up to 500 nm with a 500 nm separation, were fabricated as illustrated in figure 7.2(a)&(b). The resolution of this technique is comparable to that of Hu *et al*<sup>186</sup>.

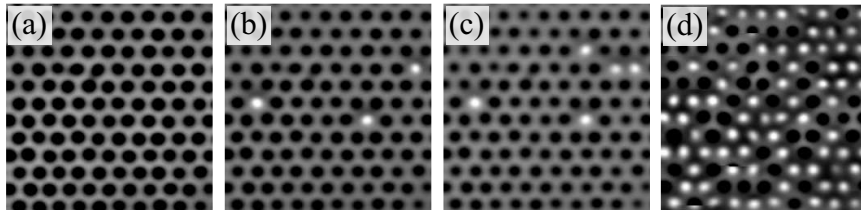


**Fig. 7.3:**  $1 \times 1 \mu\text{m}^2$  MFM images at (a) remanence, (b) -620 mT, (c) -590 mT and (d) coercivity (-430 mT). Images (b) and (c) are one field step (30 mT) apart and show that two islands have a switching field between -590 and -620 mT. In (d) some islands appear to have two domains. These islands were switched by the tip field during imaging.

The MFM images were taken at 11 K using the home built scanning force microscope described in section 2.4 operating at a base pressure of  $1 \cdot 10^{-10}$  mbar<sup>72</sup>.

<sup>†</sup> The 21 nm Co/Pt and part of the seeding layer are etched out, leading to 27 nm thick islands.

The microscope is located within a superconducting magnet capable of applying fields up to 7 T perpendicular to the sample surface allowing for high-resolution in-situ observation of the magnetic structure at different fields applied along the surface normal. The instrument was operated in the dynamic mode described in section 2.1.1<sup>63</sup>. All images presented in this chapter were taken at the same tip sample distance and with the same tip so as to enable a reliable comparison between images at different fields. Under these conditions the switching field of each dot can be observed and thus the switching field distribution (SFD) of the array of magnetic dots can be determined<sup>127,196</sup>.

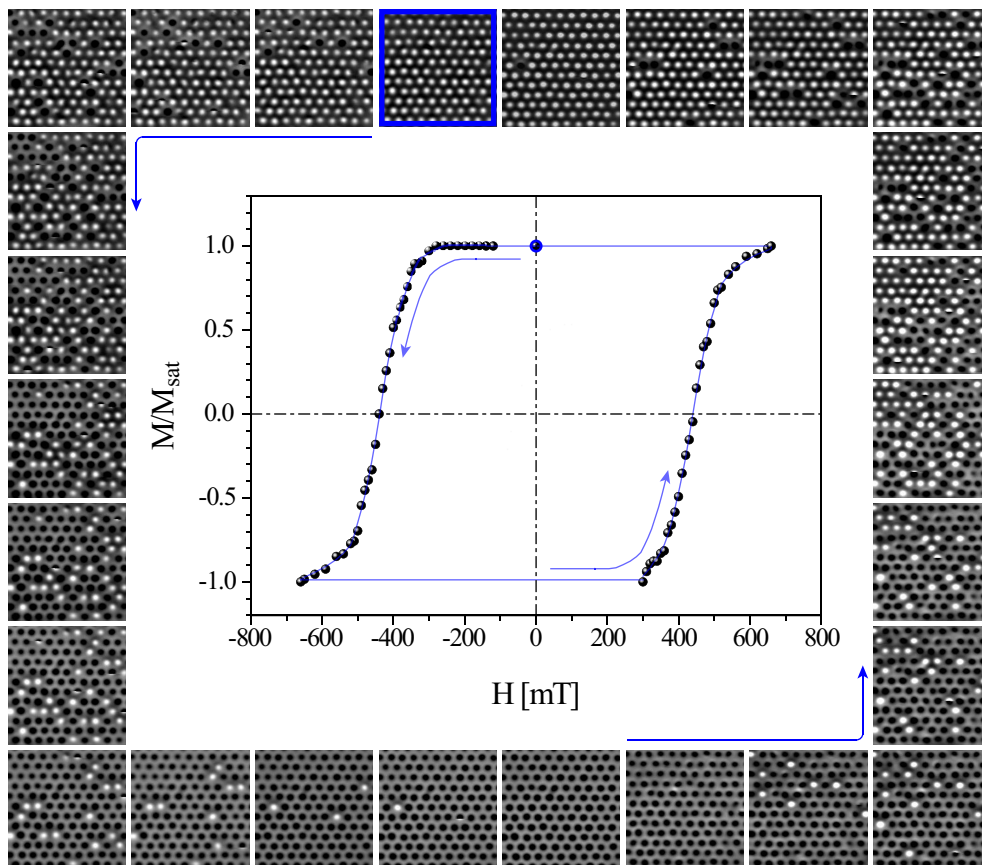


**Fig. 7.4:** The hysteresis loop measured by high resolution MFM for the 50 nm dots and some of the MFM images used to extract the magnetisation. Each point on the loop is calculated from one such  $1 \times 1 \mu\text{m}^2$  MFM image. The line is a guide for the eye. The first image was taken with zero applied field (blue point and blue border image). Negative field was then applied following the path indicated by the arrows.

To image the nanodot array a *Team Nanotec GmbH* silicon cantilever with a 4 nm Co coated tip was used (c.f. Sect. 2.6.2). The magnetic contrast in the image enables the determination of the magnetisation direction of each dot individually, an example being shown in figure 7.3. The dots exhibit perpendicular anisotropy such that the dot is magnetised either parallel or antiparallel to the tip field, appearing dark or bright respectively.

Using the superconducting magnet, the external field normal to the sample plane was increased incrementally and MFM images were taken at each step of the applied field with the applied field left on throughout the MFM imaging. The switching field of each dot was determined by observing changes in dot magnetisation direction between images taken at consecutive field steps. In particular, figure 7.3(b)&(c) present two images at consecutive fields, showing that it is simple to determine that two out of 5 dots have switched in that field step.

## 7.3 Results and Discussion

An example hysteresis loop (50 nm islands) is shown in figure 7.4, which also shows MFM images of the islands at various stages between saturation and coercivity. The SFDs of patterned media with islands of 25, 50 and 100 nm and spacings of 60, 100 and 200 nm respectively were evaluated directly by this method, and their hysteresis loops were then computed by integration of the SFDs. The hysteresis loop and SFDs of the three samples are shown in figure 7.5\*.

The SFDs of the 100 and 50 nm diameter islands are remarkably similar showing no evidence that coercivity increases as size reduces (Fig. 7.5(a)) as was observed elsewhere<sup>131,199</sup>. The 25 nm islands show a reduced coercivity and a broader switching field distribution (Fig. 7.5(b)), which would give rise to an increased write error-rate in a practical storage system. This change could be due to the reduced thermal stability of the lower volume islands, but since the experiments were performed at 11 K and the anisotropy of Co/Pt multilayers is high, it seems much more likely that this is due to edge damage during ion milling. This could take various forms: damage to the interfaces of the multilayer, reducing anisotropy; local irregularities in shape and edge definition giving rise to nucleation sites; or redeposition of milled material onto the outer edge of the islands. Redepleted material would not be multilayered, and so would have a significantly reduced anisotropy, reducing the switching field of the islands. One possibility would be that the resulting structure, with a hard magnetic multilayer core and a soft magnetic outer would have a higher

---

\* Some of the images used to obtain these data for 100 nm and 50 nm dots are shown in appendix G.

thermal stability than its reduced switching field would suggest, in the manner of exchange spring media<sup>200</sup>. Further measurements at different temperatures are required to correctly determine the reversal processes in these islands and their thermal stability.

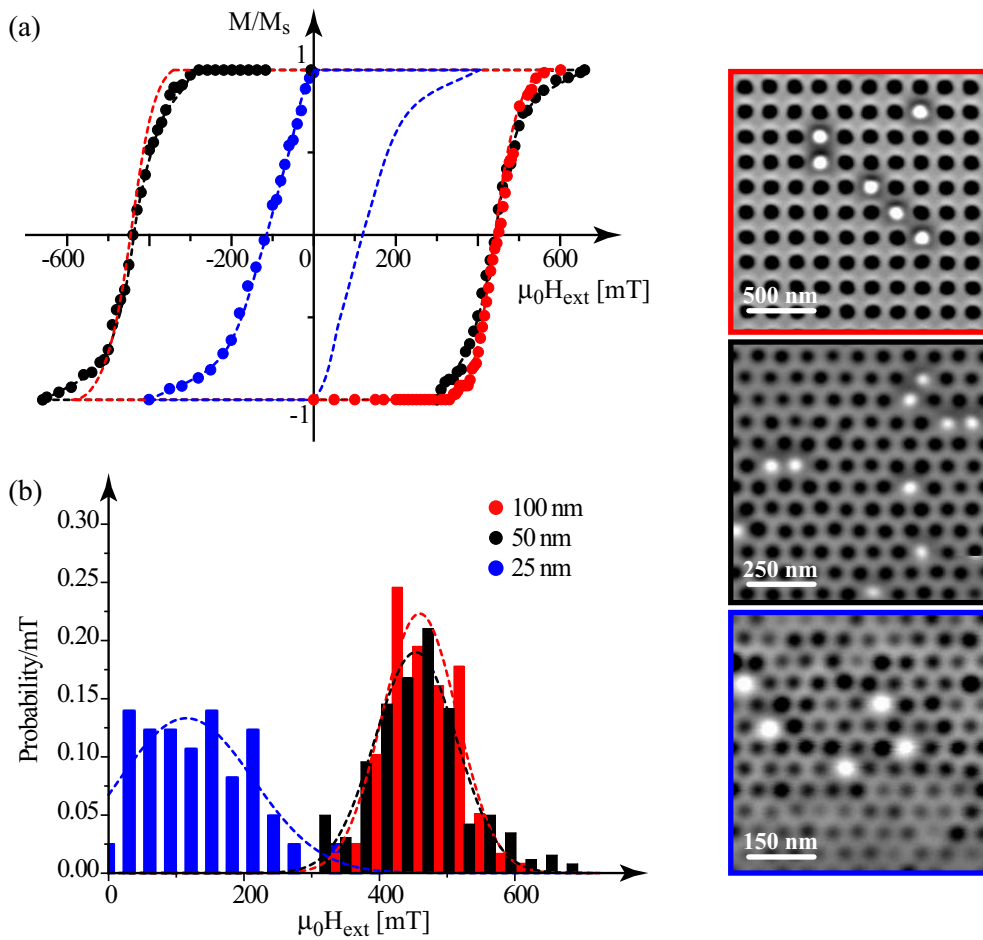


**Fig. 7.5:** (a) Hysteresis loop and (b) SFDs of the three samples measured by high resolution MFM. Dashed line is a guide for the eye in (a) and a gaussian fit in (b). Some of the MFM images used to calculate the hysteresis curve and the SFD are presented in appendix G.

## 7.4 Conclusions

In conclusion, we have performed MFM on magnetic islands as small as 25 nm diameter with a periodicity of 60 nm. We have demonstrated that the SFD of these arrays can be directly determined from high resolution MFM data. Decreasing the island diameter below 50 nm reduces the coercivity and increases the width of the switching field distribution.







## CONCLUSION AND OUTLOOK

In this thesis many novel results have been discussed and concluded in dedicated chapters. Quantitative MFM was certainly the most relevant experimental method used in this thesis. The conclusion and the outlook will thus be focussed solely on this technique.

Although MFM is nowadays widely used by both the recording media industry and academia to study micromagnetism, its full potential is rarely exploited. Most researchers use MFM as a low cost technique to image the magnetic structure of a surface at room temperature and in air. In his 2003 review Hartmann stated<sup>57</sup> of this basic use of MFM: “*the method yields only qualitative information about the magnetic object and it is difficult to improve the resolution to values below 100 nm*”.

The results presented in this thesis demonstrate that the technique of MFM has been considerably developed beyond this level, at least in our research group. Three further levels of sophistication of the MFM technique can now be identified :

- Level 1 :

A lateral resolution of 10 nm is routinely obtained on sufficiently flat samples. This became possible by in-vacuum operation which improves the instruments' sensitivity and allowed the use of sharp, high aspect-ratio tips with an extremely thin ferromagnetic coating. The MFM work done at low temperature profits from an increased instrumental stability and enhanced sensitivity.

The use of magnetic fields (in our case, perpendicular to the sample surface) allows the observation of micromagnetic structure changes along the hysteresis loop\*. In addition, the field can also be used to switch the magnetisation of the tip.

In summary the increased sensitivity obtained by in-vacuum operation and appropriate instrumentation allows the use of improved MFM tips.

---

\* The frequency shift and tip-sample distance due to the external field torque on the lever have to be accounted for.

This leads to a lateral resolution around 10 nm on flat samples. Low temperature and the application of magnetic fields increase the parameter space to reproducibly study the micromagnetic state of the sample.

- Level 2 :

The high resolution, sensitivity and reproducibility obtained in level one enables an improved analysis of MFM images. Different images can be compared by visual inspection. Counting features and applying statistical methods can lead to quantitative information. Furthermore, averaging methods can be used. Average magnetisation over the scan range can be compared to standard magnetometry measurements. Image analysis such as cross correlation functions can be used to compare images.

In summary, the high level of reproducibility of MFM obtained in level 1 allows the application of statistical and other data analysis methods. Hence, the level of pure visual inspection of the MFM images is surpassed.

- Level 3 :

The ultimate level of sophistication is reached when detailed information on the micromagnetic state can be deduced from the MFM measurements. This level is based on levels one and two, and additionally requires tip calibration and quantitative data analytical methods. The calibration of the tip requires a sample with a perpendicular magnetisation and a known saturation magnetisation, as well as the precise determination of the tip-sample distance (error < 1 nm). Clearly, once calibrated, the tip must not change for the full experiment.

In addition, high resolution imaging requires very small tip-sample distances. The measured MFM signal may thus be convolved with the sample topography. Then topography/magnetism separation methods are required.

In summary, MFM data can be understood and evaluated quantitatively. The stray field from the surface of the sample can be evaluated from MFM data when the tip is calibrated. Model magnetisation patterns can then be found that best match the stray field determined from MFM data.

Although high lateral resolution MFM (Level 1) and statistical analysis (Level 2) have been previously used in a few labs around the world, the simulation of MFM images from magnetisation pattern and consequently the deduction of micromagnetic information from MFM images based on calibration of a real tip (as opposed to a tip model) is only used in our lab to date. The work done during this thesis involved second level MFM for all chapters

and also involved the third level of sophistication for the measurements in chapter 3.

The results presented in this thesis show that state of the art MFM can give relevant information about various kinds of sample. However, some improvement of the technique would be needed to routinely employ the technique in an industrial environment. The tip needs to be sensitive enough while retaining high resolution and being magnetically hard. Improvement in this respect are still needed. Namely, fabrication of the tip coating needs to become more reliable. Various different coatings should be used in order to be able to choose the proper tip for a given experiment (sensitivity, resolution, hardness). A “universal” calibration sample should be designed, to allow an easy calibration valid for any kind of sample. Such a sample would have all required spatial wavelengths repeated over the whole sample. Finally the numerical calculation process could also be improved to allow the simulation of various different magnetisation patterns other than through thickness, ripples or closure cap as presented here.



## BIBLIOGRAPHY

- [1] B. Dibner, *The de magnete of Gilbert, Williamroller, DHD*, Isis **51** (1960), no. 165, 365–366.
- [2] M. Ugaglia, *The science of magnetism before Gilbert. Leonardo Garzoni's treatise on the loadstone*, Ann. Sci. **63** (2006), no. 1, 59–84.
- [3] D. P. Stern, *A millennium of geomagnetism*, Rev. Geophys. **40** (2002), no. 3, 1007.
- [4] P. Weiss, *L'hypothèse du champ moléculaire et la propriété ferromagnétique*, J. Phys. Rad. **6** (1907), 661–690.
- [5] H. Barkhausen, *Two with help of new repeating rediscovered appearances by H Barkhausen the silence during unmagnetising of iron*, Phys. Z. **20** (1919), 401–403.
- [6] F. Bitter, *On inhomogeneities in the magnetization of ferromagnetic materials*, Phys. Rev. **38** (1931), no. 10, 1903–1905.
- [7] I. Langmuir and K. J. Sixtus, *Regions of reversed magnetization in strained wires*, Phys. Rev. **38** (1931), no. 11, 2072–2072.
- [8] S. Foner, *Versatile and sensitive vibrating-sample magnetometer*, Rev. Sci. Instrum. **30** (1959), no. 7, 548–557.
- [9] J. J. Sáenz, N. García, P. Grütter, E. Meyer, H. Heinzelmann, R. Wiesendanger, L. Rosenthaler, H. R. Hidber, and H.-J. Güntherodt, *Observation of magnetic forces by the atomic force microscope*, J. Appl. Phys. **62** (1987), no. 10, 4293–4295.
- [10] A. Moser, K. Takano, D. T. Margulies, M. Albrecht, Y. Sonobe, Y. Ikeda, S. Sun, and E. E. Fullerton, *Magnetic recording: Advancing into the future*, J. Phys. D:Appl. Phys. **35** (2002), R157–R167.
- [11] A. Moser, C. Bonhote, Q. Dai, H. Do, B. Knigge, Y. Ikeda, Q. Le, B. Lengsfeld, S. MacDonald, J. Li, V. Nayak, R. Payne, M. Schabes, N. Smith, K. Takano, C. Tsang, P. van der Heijden, W. Weresin,

- M. Williams, and M. Xiao, *Perpendicular magnetic recording technology at 230 Gbit/in<sup>2</sup>*, J. Magn. Magn. Mater. **303** (2006), no. 2, 271–275.
- [12] K. Ouchi, *Recent advances in perpendicular magnetic recording*, IEEE. Trans. Magn. **37** (2001), 1217–1222.
- [13] P. J. Grundy, *Thin film magnetic recording media*, J. Phys. D: Appl. Phys. **31** (1998), 2975–2990.
- [14] H. J. Hug, B. Stiefel, A. Moser, I. Parashikov, A. Klicznik, D. Lipp, H.-J. Güntherodt, G. Bochi, D. I. Paul, and R. C. O’Handley, *Magnetic domain structure in ultrathin Cu/Ni/Cu/Si(001) films (invited)*, J. Appl. Phys. **79** (1996), no. 8, 5609–5614.
- [15] K. Ha and R. C. O’Handley, *Magnetization canting in epitaxial Cu/Ni/Cu/Si(001) films*, J. Appl. Phys. **87** (2000), no. 9, 5944–5946.
- [16] M. Ciria, J. I. Arnaudas, L. Benito, C. de la Fuente, A. del Moral, K. Ha, and R. C. O’Handley, *Magnetoelastic coupling in thin films with weak out-of-plane anisotropy*, Phys. Rev. B **67** (2003), 024429 1–6.
- [17] M. A. Marioni, N. Pilet, T. V. Ashworth, R. C. O’Handley, and H. J. Hug, *Remanence due to wall magnetization and counterintuitive magnetometry data in 200 nm films of Ni*, Phys. Rev. Lett. **97** (2006), 027201 1–4.
- [18] A. Hubert and R. Schäfer, *Magnetic domains*, Springer Verlag, Berlin Heidelberg New York, 2000.
- [19] H. S. Cho, V. R. Inturi, J. A. Barnard, and H. Fujiwara, *Characteristics of stripe domains in FeTaN films observed by magnetic force microscopy*, IEEE Trans. Magn. **34** (1998), no. 4, 1150–1152.
- [20] M. S. Pierce, R. G. Moore, L. B. Sorensen, S. D. Kevan, O. Hellwig, E. E. Fullerton, and J. B. Kortright, *Quasistatic X-ray speckle metrology of microscopic magnetic return-point memory*, Phys. Rev. Lett. **90** (2003), 175502 1–4.
- [21] P. Fischer, *Magnetic soft X-ray transmission microscopy*, Curr. Opin. Solid State Mater. Sci. **7** (2003), no. 2, 173–179.
- [22] C. Kittel, *Introduction to solid state physics*, eighth edition ed., John Wiley & Sons, Inc., 2005.
- [23] R. C. O’Handley, *Modern magnetic materials, principles and applications*, John Wiley & Sons, Inc., 2000.

- [24] S. Blügel, T. Brückel, and C. M. Schneider (eds.), *Magnetism goes nano*, vol. 26, Forschungszentrum Jülich GmgH, Jülich, 2005.
- [25] R. Skomski, *Nanomagnetics*, J. Phys.: Condens. Matter **15** (2003), R841–R896.
- [26] S.V. Vonsovskii, *Magnetism*, 1<sup>st</sup> ed., vol. 1, John Wiley & Sons, Inc., 1974.
- [27] T. G. Kollie, *Measurement of thermal-expansion coefficient of nickel from 300 to 1000 K and determination of power-law constants near curie-temperature*, Phys. Rev. B **16** (1977), no. 11, 4872–4881.
- [28] C. Kittel, *Physical theory of ferromagnetic domains*, Rev. Mod. Phys. **21** (1949), no. 4, 541–583.
- [29] C. Kittel, *Theory of the structure of ferromagnetic domains in films and small particles*, Phys. Rev. **70** (1946), no. 11 and 12, 965–971.
- [30] P. Gambardella, S. Rusponi, M. Veronese, S. S. Dhesi, C. Grazioli, A. Dallmeyer, I. Cabria, R. Zeller, P. H. Dederichs, K. Kern, C. Carbone, and H. Brune, *Giant magnetic anisotropy of single cobalt atoms and nanoparticles*, Science **300** (2003), 1130–1133.
- [31] R. Koch, *The intrinsic stress of polycrystalline and epitaxial thin metal films*, J. Phys. Condens. Matter. **6** (1994), 9519–9550.
- [32] D. Sander, *The correlation between mechanical stress and magnetic anisotropy in ultrathin films*, Rep. Prog. Phys. **62** (1999), no. 5, 809–858.
- [33] K. Zhang, *Stress-induced magnetic anisotropy in Xe-ion-irradiated Ni thin films*, Nucl. Instr. Meth. B **243** (2006), no. 1, 51–57.
- [34] G. A. Müller, E. Carpena, R. Gupta, P. Schaaf, K. Zhang, and K. P. Lieb, *Ion-beam induced changes in magnetic and microstructural properties of thin iron films*, Eur. Phys. J. B **48** (2006), 449–462.
- [35] K. Zhang, *Magnetic texturing of thin nickel films induced by Xe-ion implantation*, Ph.D. thesis, Georg-August-Universität-Göttingen, 2001.
- [36] K. Zhang, K. P. Lieb, G. A. Müller, P. Schaaf, M. Uhrmacher, and M. Münzenberg, *Magnetic texturing of xenon-ion irradiated nickel films*, Eur. Phys. J. B **42** (2004), no. 2, 193–204.

- [37] K. Ha, M. Ciria, R. C. O’Handley, P. W. Stephens, and S. Pagola, *X-ray study of strains and dislocation density in epitaxial Cu/Ni/Cu/Si(001) films*, Phys. Rev. B **60** (1999), no. 19, 13780–13785.
- [38] G. Bochi, C. A. Ballentine, H. E. Inglefield, C. V. Thompson, R. C. O’Handley, H. J. Hug, B. Stiefel, A. Moser, and H.-J. Güntherodt, *Perpendicular magnetic anisotropy, domains, and misfit strain in epitaxial Ni/Cu<sub>1-x</sub>Ni<sub>x</sub>/Cu/Si(001) thin films*, Phys. Rev. B **52** (1995), no. 10, 7311–7321.
- [39] G. Bochi, H. J. Hug, D. I. Paul, B. Stiefel, A. Moser, I. Parashikov, H.-J. Güntherodt, and R. C. O’Handley, *Magnetic domain structure in ultrathin films*, Phys. Rev. Lett. **75** (1995), no. 9, 1839–1842.
- [40] R. Jungblut, M. T. Johnson, J. van de Stegge, A. Reinders, and F. J. A. den Broeder, *Orientational and structural dependence of magnetic anisotropy of Cu/Ni/Cu sandwiches: Misfit interface anisotropy*, J. Appl. Phys. **75** (1994), 6424–6426.
- [41] G. Bochi, O. Song, and R. C. O’Handley, *Surface magnetoelastic coupling coefficients of single-crystal fcc Co thin films*, Phys. Rev. B **50** (1994), no. 3, 2043–2046.
- [42] S. Hameed, P. Talagala, R. Naik, L. E. Wenger, V. M. Naik, and R. Proksch, *Analysis of disordered stripe magnetic domains in strained epitaxial Ni(001) films*, Phys. Rev. B **64** (2001), 184406 1–5.
- [43] J. Crangles, *The magnetic properties of solids*, Edward Arnold (Publishers), 1977.
- [44] P. Escudier, *L’anisotropie de l’aimantation : Un paramètre important de l’étude de l’anisotropie magnéto-cristalline*, Ann. Phys. **9** (1975), no. 3, 125–173.
- [45] V. L. Moruzzi, P. M. Marcus, K. Schwarz, and P. Mohn, *Ferromagnetic phases of bcc and fcc Fe, Co and Ni*, Phys. Rev. B **34** (1986), no. 3, 1784–1791.
- [46] J. J. M. Franse, *Magnetic anisotropy in nickel and iron : The effect of pressure*, J. Phys. Colloq. C1 **32** (1971), 186–192.
- [47] R. Wiesendanger and M. Bode, *Nano- and atomic-scale magnetism studied by spin-polarized scanning tunneling microscopy and spectroscopy*, Solid. State Commun. **119** (2001), no. 4-5, 341–355.



- [48] H.K. Wickramasinghe, *Progress in scanning probe microscopy*, Acta. Mater. **48** (2000), no. 1, 347–358.
- [49] G. Binnig and H. Rohrer, *Scanning tunneling microscopy*, Helv. Phys. Acta **55** (1982), 726–735.
- [50] G. Binnig, H. Rohrer, C. Gerber, and E. Weibel, *7x7 reconstruction on Si(111) resolved in real space*, Phys. Rev. Lett. **50** (1983), no. 2, 120–123.
- [51] G. Binnig, C. F. Quate, and C. Gerber, *Atomic force microscopy*, Phys. Rev. Lett. **56** (1986), no. 9, 930–933.
- [52] E. Meyer, H. J. Hug, and R. Bennewitz, *Scanning probe microscopy*, Springer Verlag, Berlin Heidelberg, 2004.
- [53] R. García and R. Pérez, *Dynamic atomic force microscopy methods*, Surf. Sci. Rep. **47** (2002), 197–301.
- [54] P. Kappenberger, *Exchange bias effect and hard disk media studied by means of quantitative magnetic force microscopy*, Ph.D. thesis, Universität Basel, 2005.
- [55] I. Schmid, *The role of uncompensated spins in exchange biased systems*, Ph.D. thesis, Universität Basel, 2006.
- [56] P. J. A. van Schendel, *Investigation of magnetisation structures in ferromagnetic and superconducting samples by magnetic force microscopy*, Ph.D. thesis, Universität Basel, 1999.
- [57] M. R. Koblischka and U. Hartmann, *Recent advances in magnetic force microscopy*, Ultramicroscopy **97** (2003), no. 1-4, 103–112.
- [58] U. Hartmann, *Magnetic force microscopy*, Annu. Rev. Mater. Sci. **29** (1999), 53–87.
- [59] S. Porthun, L. Abelmann, and C. Ladder, *Magnetic force microscopy of thin film media for high density magnetic recording*, J. Magn. Magn. Mater. **182** (1998), 238–273.
- [60] A. Moser, M. Xiao, P. Kappenberger, K. Takano, W. Weresin, Y. Ikeda, H. Do, and H. Hug, *High-resolution magnetic force microscopy study of high-density transitions in perpendicular recording media*, J. Magn. Magn. Mater. **287** (2005), 298–302.
- [61] P. Kappenberger, I. Schmid, and H. J. Hug, *Investigation of the exchange bias effect by quantitative magnetic force microscopy*, Adv. Eng. Mater. **7** (2005), no. 5, 332–338.

- [62] H. J. Hug, B. Stiefel, P. J. A. van Schendel, A. Moser, R. Hofer, S. Martin, H.-J. Güntherodt, S. Porthun, L. Abelmann, J. C. Lodder, G. Bochi, and R. C. O'Handley, *Quantitative magnetic force microscopy on perpendicularly magnetized samples*, J. Appl. Phys. **83** (1998), no. 11, 5609–5620.
- [63] P. J. A. van Schendel, H. J. Hug, B. Stiefel, S. Martin, and H.-J. Güntherodt, *A method for the calibration of magnetic force microscopy tips*, J. Appl. Phys. **88** (2000), no. 1, 435–445.
- [64] B. Thidé, *Electromagnetic field theory*, <http://www.plasma.uu.se/CED/Book/>, November 2006, UPSILON BOOKS (free on-line textbook).
- [65] J.D. Jackson, *Classical electrodynamics*, 2<sup>nd</sup> ed., J. Wiley and Sons, August 1998.
- [66] C. Schönenberger and S. F. Alvarado, *Understanding magnetic force microscopy*, Z. Phys. B **80** (1990), 373–383.
- [67] K. L. Babcock, V. B. Elings, J. Shi, D. D. Awschalom, and M. Dugas, *Field-dependence of microscopic probes in magnetic force microscopy*, Appl. Phys. Lett. **69** (1996), no. 5, 705–707.
- [68] L. Kong and S. Y. Chou, *Quantification of magnetic force microscopy using a micronscale current ring*, Appl. Phys. Lett. **70** (1997), no. 15, 2043–2045.
- [69] C. Cohen-Tannoudji, B. Diu, and F. Laloë, *Mécanique quantique II*, vol. Nouveau tirage, 1996, Hermann, éditeur des sciences et des arts, 1996.
- [70] D. Rugar, H.J. Mamin, P. Guethner, S.E. Lambert, J.E. Stern, I. McFadyen, and T. Yogi, *Magnetic force microscopy: General principles and application to longitudinal recording media*, J. Appl. Phys. **68** (1990), no. 3, 1169–1183.
- [71] B. Stiefel, *Magnetic force microscopy at low temperatures and in ultrahigh vacuum*, Ph.D. thesis, University of Basel, 1998.
- [72] H. J. Hug, B. Stiefel, P. J. A. van Schendel, A. Moser, S. Martin, and H.-J. Güntherodt, *A low temperature ultrahigh vacuum scanning force microscope*, Rev. Sci. Instrum. **70** (1999), no. 9, 3625–3640.
- [73] C. Loppacher, *Nichtkontakt-Rasterkraftmikroskopie mit digitalem Phasenregelkreis*, Ph.D. thesis, University of Basel, 2000.

- [74] C. Loppacher, M. Bammerlin, E. Battiston, M. Guggisberg, D. Müller, H. R. Hidber, R. Lüthi, E. Meyer, and H.-J. Güntherodt, *Fast digital electronics for application in dynamic force microscopy using high-Q cantilevers*, Appl. Phys. A **66** (1998), S215–218.
- [75] A. Moser, *Untersuchungen von Hochtemperatursupraleitern mit dem Rasterkraftmikroskop*, Ph.D. thesis, University of Basel, 1995.
- [76] www.swissprobe.com  
info@swissprobe.com.
- [77] S. Porthun, L. Abelmann, S. J. L. Vellekoop, J. C. Lodder, and H. J. Hug, *Optimization of lateral resolution in magnetic force microscopy*, Appl. Phys. A, Mater. Sci. Process. **66** (1998), S1185–S1189.
- [78] M. Ruhrig, S. Porthun, and J. C. Lodder, *Magnetic force microscopy using electron-beam fabricated tips*, Rev. Sci. Instrum. **65** (1994), no. 10, 3224–3228.
- [79] M. Ruhrig, S. Porthun, J. C. Lodder, S. McVitie, L. J. Heyderman, A. B. Johnston, and J. N. Chapman, *Electron beam fabrication and characterization of high-resolution magnetic force microscopy tips*, J. Appl. Phys. **79** (1996), no. 6, 2913–2919.
- [80] K. R. Coffey, M. A. Parker, and J. I. K. Howard, *High anisotropy  $L1_0$  thin films for longitudinal recording*, IEEE Trans. Magn. **31** (1995), no. 6, 2737–2739.
- [81] D. P. Jackson and B. Gantner, *Energetics of interacting magnetized domains*, Phys. Rev. E **64** (2001), 056230 1–4.
- [82] T. Eimüller, R. Kalchgruber, P. Fischer, G. Schütz, P. Guttman, G. Schmahl, M. Köhler, K. Prügl, M. Scholz, F. Bammes, and G. Bayreuther, *Quantitative imaging of magnetization reversal in FeGd multilayers by magnetic transmission X-ray microscopy*, J. Appl. Phys. **87** (2000), no. 9, 6478–6480.
- [83] A. Asenjo, D. García, J.M. García, C. Prados, and M. Vázquez, *Magnetic force microscopy study of dense stripe domains in Fe-B/Co-Si-B multilayers and the evolution under an external applied field*, Phys. Rev. B **62** (2000), no. 10, 6538–6544.
- [84] M. Ciria, J. I. Arnaudas, A. del Moral, and R. C. O’Handley, *Magnetoelastic stress in Cu/Ni/Cu/Si(100) epitaxial thin films*, Phys. Rev. B **70** (2004), 054431 1–6.

- [85] J. W. Matthews and J. L. Crawford, *Accommodation of misfit between single-crystal films of nickel and copper*, *Thin Solid Films* **5** (1970), no. 3, 187–198.
- [86] U. Gradmann, *Struktur und Ferromagnetismus sehr dünner epitaktischer Ni-Flachenschichten*, *Ann. Phys.* **17** (1966), no. 1-2, 91–106.
- [87] C. A. Chang, *Reversed magnetic-anisotropy in deformed (100)Cu-Ni-Cu structures*, *J. Appl. Phys.* **68** (1990), no. 9, 4873–4875.
- [88] S. Müller, B. Schulz, G. Kostka, M. Farle, K. Heinz, and K. Baberschke, *Pseudomorphic growth of Ni films on Cu(001): A quantitative LEED analysis*, *Surf. Sci.* **364** (1996), 235–241.
- [89] J. Lee, G. Lauhoff, and J. A. C. Bland, *Spacer-layer-induced spin re-orientation in Ni/Cu/Ni sandwiches*, *Europhys. Lett.* **35** (1996), no. 6, 463–468.
- [90] J. Lee, G. Lauhoff, M. Tselepi, S. Hope, P. Rosenbusch, J. A. C. Bland, H. A. Durr, G. van der Laan, J. P. Schille, and J. A. D. Matthew, *Evidence for a strain-induced variation of the magnetic moment in epitaxial Cu/Ni/Cu/Si(100) structures*, *Phys. Rev. B* **55** (1997), no. 22, 15103–15107.
- [91] S. Kuriki, *Uniaxial magnetic-anisotropy in epitaxial Ni(110) films*, *IEEE Trans. Magn.* **12** (1976), no. 2, 107–113.
- [92] Z. Malek and V. Kambersky, *K teorii doménové struktury tenkých vrstev magneticky jednoosých materiálů*, *Czech. J. Phys.* **8** (1958), 429–434.
- [93] H. M. Hwang, J. C. Park, D. G. You, H. S. Park, K. Jeong, J. Lee, T. G. Kim, and J. H. Song, *Spin-reorientation transition of epitaxial Cu/Ni/Cu(001) structure*, *J. Appl. Phys.* **93** (2003), no. 10, 7625–7627.
- [94] U. Rüdiger, J. Yu, L. Thomas, S. S. P. Parkin, and A. D. Kent, *Magneto-resistance, micromagnetism, and domain-wall scattering in epitaxial hcp Co films*, *Phys. Rev. B* **59** (1999), 11914–18.
- [95] N. Pilet, T. V. Ashworth, M. A. Marioni, H. J. Hug, K. Zhang, and K. P. Lieb, *Microstructural and magnetic effects of Xe- and Ni-irradiation of Ni(70 nm)/Glass/Si(100) thin films*, in preparation, 2007.
- [96] K. Zhang, K. P. Lieb, D. G. Merkel, M. Uhrmacher, N. Pilet, T. V. Ashworth, , and H. J. Hug, *Ion-induced magnetic texturing of Ni films: Domain structure and strain*, *Nucl. Instr. Meth. B*, in press, 2006.

- [97] K. Zhang, K. P. Lieb, N. Pilet, T. V. Ashworth, M. A. Marioni, and H. J. Hug, *Microstructural and magnetic properties of thermally mixed Ni/Si layers*, in preparation, 2007.
- [98] S. M. Cherif, A. Layadi, J. Ben Youssef, C. Nacereddine, and Y. Rousigne, *Study of the magnetic anisotropy in Ni/Cu and Ni/glass thin films*, *Physica B* **387** (2007), no. 1-2, 281–286.
- [99] J. Fassbender, D. Ravelosona, and Y. Samson, *Tailoring magnetism by light-ion irradiation*, *J. Phys. D: Appl. Phys.* **37** (2004), R179–R196.
- [100] K. Zhang, K.P. Lieb, P. Schaaf, M. Uhrmacher, W. Felsch, and M. Münzenberg, *Ion-beam-induced magnetic texturing of thin nickel films*, *Nucl. Instr. Meth. B* **161** (2000), 1016–1021.
- [101] K. Zhang, K. P. Lieb, V. Milinovic, M. Uhrmacher, and S. Klaumünzer, *Interface mixing and magnetism in ni/si bilayers irradiated with swift and low-energy heavy ions*, *Nucl. Instr. Meth. B* **249** (2006), 167–171.
- [102] K. P. Lieb, K. Zhang, V. Milinovic, P. K. Sahoo, and S. Klaumunzer, *On the structure and magnetism of Ni/Si and Fe/Si bilayers irradiated with 350-MeV Au ions*, *Nucl. Instr. Meth. B* **245** (2006), no. 1, 121–125.
- [103] G. A. Müller, R. Gupta, K. P. Lieb, and P. Schaaf, *Determination of spin distributions in ion-beam magnetic textured iron films by magnetic orientation Mossbauer spectroscopy*, *Appl. Phys. Lett.* **82** (2003), no. 1, 73–75.
- [104] C. Chappert, H. Bernas, J. Ferré, V. Kottler, J.-P. Jamet, Y. Chen, E. Cambril, T. Devolder, F. Rousseaux, V. Mathet, and H. Launois, *Planar patterned magnetic media obtained by ion irradiation*, *Science* **280** (1998), 1919–1922.
- [105] H. Bernas, T. Devolder, C. Chappert, J. Ferré, V. Kottler, Y. Chen, C. Vieu, J. P. Jamet, V. Mathet, E. Cambril, O. Kaitasov, S. Lemerle, F. Rousseaux, and H. Launois, *Ion beam induced magnetic nanostructure patterning*, *Nucl. Instr. Meth. B* **148** (1999), no. 1-4, 872–879.
- [106] C. T. Rettner, S. Anders, J. E. E. Baglin, T. Thomson, and B. D. Terris, *Characterization of the magnetic modification of Co/Pt multilayer films by He<sup>+</sup>, Ar<sup>+</sup>, and Ga<sup>+</sup> ion irradiation*, *Appl. Phys. Lett.* **80** (2002), no. 2, 279–281.
- [107] J. Ferré, T. Devolder, H. Bernas, J. P. Jamet, V. Repain, M. Bauer, N. Vernier, and C. Chappert, *Magnetic phase diagrams of He ion-*

- irradiated Pt/Co/Pt ultrathin films*, J. Phys. D: Appl. Phys. **36** (2003), 3103–3108.
- [108] G. J. Kusinski and G. Thomas, *Physical and magnetic modification of Co/Pt multilayers by ion irradiation*, Microsc. Microanal. **8** (2002), no. 4, 319–332.
- [109] T. Devolder, S. Pizzini, J. Vogel, H. Bernas, C. Chappert, V. Mathet, and M. Borowski, *X-ray absorption analysis of sputter-grown Co/Pt stackings before and after helium irradiation*, Eur. Phys. J. B **22** (2001), 193–201.
- [110] J.-S. Lee, K.-B. Lee, Y. J. Park, T. G. Kim, J. H. Song, K. H. Chae, J. Lee, C. N. Whang, K. Jeong, D.-H. Kim, and S.-C. Shin, *Modification of interface magnetic anisotropy by ion irradiation on epitaxial Cu/Ni/Cu(002)/Si(100) films*, Phys. Rev. B **69** (2004), 172405 1–4.
- [111] T. G. Kim, Y. H. Shin, , J. H. Song, M. C. Sung, I. S. Kim, D. G. You, J. Lee, K. Jeong, G. Y. Jeon, and C. N. Whang, *Effects of ion irradiation on epitaxial Cu/Ni/Cu(001) with perpendicular magnetic anisotropy*, Appl. Phys. Lett. **81** (2002), no. 21, 4017–4019.
- [112] T. G. Kim, J. H. Lee, J. H. Song, K. H. Chae, S. W. Shin, H. M. Hwang, J. Lee, K. Jeong, C. N. Whang, J.-S. Lee, and K.-B. Lee, *Interface study of ion irradiated Cu/Ni/Cu(002)/Si magnetic thin film by X-ray reflectivity*, J. Magn. Mater. **299** (2006), 105–111.
- [113] J. F. Ziegler, J. P. Biersack, and U. Littmark, *The stopping and range of ions in solids*, (new edition in 1999) ed., Pergamon Press, New York, 1985.
- [114] *Computer package SRIM*, [www.srim.org](http://www.srim.org).
- [115] K. P. Lieb and J. Keinonen, *Luminescence of ion-irradiated  $\alpha$ -quartz*, to be published in Cont. Phys., 2007.
- [116] M. Uhrmacher, K. Pampus, F.J. Bergmeister, D. Purschke, and K. P. Lieb, *Energy calibration of the 500 kV heavy-ion implanter ionas*, Nucl. Instr. Meth. B **9** (1985), no. 2, 234–242.
- [117] J.R. Tesmer, M. Nastasi, J.C. Barbour, C .J. Maggiore, and J.W. Mayer (eds.), *Handbook of modern ion beam materials analysis*, Materials Research Society, Pittsburgh, 1995.
- [118] N. Nita, R. Schaeublin, and M. Victoria, *Impact of irradiation on the microstructure of nanocrystalline materials*, J. Nucl. Mater. **329-333** (2004), 953–957.

- [119] C. Y. Shih, C. L. Bauer, and J. O. Artman, *Interdependance of magnetic properties and intrinsic stress in mono- and polycrystalline thin nickel films*, J. Appl. Phys. **64** (1988), no. 10, 5428–5430.
- [120] C. J. Tsai and K. H. Yu, *Stress evolution during isochronal annealing of Ni/Si system*, Thin Solid Films **350** (1999), 91–95.
- [121] M. Hehn, S. Padovani, K. Ounadjela, and J. P. Bucher, *Nanoscale magnetic domain structures in epitaxial cobalt films*, Phys. Rev. B **54** (1996), no. 5, 3428–3433.
- [122] M. R. Scheinfein, J. Unguris, J. L. Blue, K. J. Coakley, D. T. Pierce, and R. J. Celotta, *Micromagnetics of domain walls at surfaces*, Phys. Rev. B **43** (1991), no. 4, 3395–3423.
- [123] J. A. Cape and G. W. Lehman, *Magnetic somain structures in thin uniaxial plates with perpendicular easy axis*, J. Appl. Phys. **42** (1971), no. 13, 5732–5756.
- [124] J. K. Steele and D. I. Potter, *The disappearance of voids during 180 keV Ni<sup>+</sup> bombardment of nickel*, J. Nucl. Mater. **218** (1995), 95–107.
- [125] G.A. Müller, *Ion-beam induced changes of magnetic and structural properties in thin Fe films*, Ph.D. thesis, Georg-August-Universität Göttingen, 2004, [http://webdoc.sub.gwdg.de/diss/2004/mueller\\_georg/mueller\\_georg.pdf](http://webdoc.sub.gwdg.de/diss/2004/mueller_georg/mueller_georg.pdf).
- [126] K. Zhang, K.P. Lieb, V. Milinovic, and P.K. Sahoo, *Swift heavy ion irradiation of a-Si/Fe/c-Si trilayers*, J. Appl. Phys. **100** (2006), 053501 1–7.
- [127] N. Pilet, T. V. Ashworth, M. A. Marioni, H. J. Hug, K. Zhang, and K. P. Lieb, *Effect of ion irradiation on domain nucleation and wall motion in Ni films*, J. Magn. Magn. Mater., in press, 2006.
- [128] G. N. Phillips, K. O’Grady, Q. Meng, and J. C. Lodder, *Domain structure and magnetization processes in magneto-optic Co/Pt thin films*, IEEE Trans. Magn. **32** (1996), 4070–4072.
- [129] P. Herget, B. Knight, J. A. Bain, T. E. Schlesinger, and H. Awano, *Magnetically defined domain isolation for studies of nucleation and growth coercivities*, IEEE Trans. Magn. **41** (2005), no. 10, 3763–3765.
- [130] D. Guarisco, Z. H. Li, B. E. Higgins, Y. Wu, and A. LeFebvre, *Perpendicular drive integration*, IEEE Trans. Magn. **42** (2006), no. 2, 171–175.

- [131] T. Thomson, G. Hu, and B. D. Terris, *Intrinsic distribution of magnetic anisotropy in thin films probed by patterned nanostructures*, Phys. Rev. Lett. **96** (2006), no. 25, 257204 1–4.
- [132] W. Y. Lee, A. Hirohata, H. T. Leung, Y. B. Xu, S. M. Gardiner, C. C. Yao, and J. A. C. Bland, *Magnetization reversal in mesoscopic  $Ni_{80}Fe_{20}$  wires: A magnetic domain launching device*, IEEE Trans. Magn. **36** (2000), no. 5, 3018–3020.
- [133] V. Basso, *Hysteresis models for magnetization by domain wall motion*, IEEE Trans. Magn. **34** (1998), no. 4, 2207–2212.
- [134] P. Herget, T. E. Schesinger, and D. D. Stancil, *Mechanism for domain expansion in MAMMOS*, IEEE Trans. Magn. **41** (2005), no. 10, 2860–2862.
- [135] G. Hu, T. Thomson, T. Rettner, S. Raoux, and B. D. Terris, *Magnetization reversal in Co/Pd nanostructures and films*, J. Appl. Phys. **97** (2005), no. 10, 10J702 1–3.
- [136] F. Schuler, *Magnetic films : Nucleation, wall motion, and domain morphology*, J. Appl. Phys. **33** (1962), no. 5, 1845–1850.
- [137] K. Fukumoto, W. Kuch, J. Vogel, F. Romanens, S. Pizzini, J. Camarero, M. Bonfim, and J. Kirschner, *Dynamics of magnetic domain wall motion after nucleation: Dependence on the wall energy*, Phys. Rev. Lett. **96** (2006), no. 9, 097204 1–4.
- [138] G. P. Zhao, M. G. Zhao, H. S. Lim, Y. P. Feng, and C. K. Ong, *From nucleation to coercivity*, Appl. Phys. Lett. **87** (2005), no. 16, 162513 1–3.
- [139] S. B. Choe and S. C. Shin, *Magnetic domain reversal dynamics in Co/Pd nanomultilayers*, J. Magn. Magn. Mater. **209** (2000), no. 1-3, 84–89.
- [140] S. B. Choe, D. H. Kim, and S. C. Shin, *Domain reversal dynamics in ferromagnetic thin films of Co/Pd nanomultilayers*, J. Korean Phys. Soc. **40** (2002), no. 3, 421–434.
- [141] S. B. Choe and S. C. Shin, *Domain reversal behavior in perpendicular magnetic nanoscale thin films*, Current Applied Physics **2** (2002), no. 6, 503–507.
- [142] O. Pietzsch, A. Kubetzka, M. Bode, and R. Wiesendanger, *Observation of magnetic hysteresis at the nanometer scale by spin-polarized scanning tunneling spectroscopy*, Science **292** (2001), no. 5524, 2053–2056.



- [143] J. Pommier, P. Meyer, G. Penissard, J. Ferré, P. Bruno, and D. Renard, *Magnetization reversal in ultrathin ferromagnetic-films with perpendicular anisotropy domain observations*, Phys. Rev. Lett. **65** (1990), no. 16, 2054–2057.
- [144] A. Kirilyuk, J. Ferré, J. Pommier, and D. Renard, *Domain-wall dynamics in ultrathin Au/Co/Au films*, J. Magn. Magn. Mater. **121** (1993), no. 1-3, 536–538.
- [145] T. Kleinefeld, J. Valentin, and D. Weller, *Micromagnetic properties and domain dynamics of CoPt thin-films*, J. Magn. Magn. Mater. **148** (1995), no. 1-2, 249–250.
- [146] J. Schmidt, G. Skidmore, S. Foss, E. D. Dahlberg, and C. Merton, *Magnetization reversal processes in perpendicular anisotropy thin films observed with magnetic force microscopy*, J. Magn. Magn. Mater. **190** (1998), no. 1-2, 81–88.
- [147] G. A. Gibson, J. F. Smyth, S. Schultz, and D. P. Kern, *Observation of the switching fields of individual permalloy particles in nanolithographic arrays via magnetic force microscopy*, IEEE Trans. Magn. **27** (1991), no. 6, 5187–5189.
- [148] R. Proksch, E. Runge, P. K. Hansma, S. Foss, and B. Walsh, *High-field magnetic force microscopy*, J. Appl. Phys. **78** (1995), no. 5, 3303–3307.
- [149] R. D. Gomez, I. D. Mayergoyz, and E. R. Burke, *Magnetic imaging in the presence of an external-field-eraser process of thin-film recording medium*, IEEE Trans. Magn. **31** (1995), no. 6, 3346–3348.
- [150] D. Romel, E. R. Burke, and I. D. Mayergoyz, *Magnetic imaging in the presence of external fields: Technique and applications*, J. Appl. Phys. **79** (1996), no. 8, 6441–6446.
- [151] A. Jander, P. Dhagat, R. S. Indeck, and M. W. Muller, *MFM observation of localized demagnetization in magnetic recordings*, IEEE Trans. Magn. **34** (1998), no. 4, 1657–1659.
- [152] R. Engel-Herbert, T. Hesjedal, J. Mohanty, D. M. Schaadt, and K. H. Ploog, *Magnetization reversal in MnAs films: Magnetic force microscopy, SQUID magnetometry, and micromagnetic simulations*, Phys. Rev. B **73** (2006), 104441 1–7.
- [153] M. V. Rastei, R. Meckenstock, and J. P. Bucher, *Nanoscale hysteresis loop of individual Co dots by field-dependent magnetic force microscopy*, Appl. Phys. Lett. **87** (2005), 222505 1–3.

- [154] N. Pilet, T. V. Ashworth, M. A. Marioni, H. G. Katzgraber, and H. J. Hug, *Return point memory and complementary point memory presented in real space by in field MFM*, in preparation, 2007.
- [155] P. Fischer, T. Eimuller, G. Schutz, P. Guttman, G. Schmahl, K. Pruegl, and G. Bayreuther, *Imaging of magnetic domains by transmission X-ray microscopy*, J. Phys. D: Appl. Phys. **31** (1998), no. 6, 649–655.
- [156] O. Perkovic and J. P. Sethna, *Improved magnetic information storage using return-point memory*, J. Appl. Phys. **81** (1997), no. 3, 1590–1597.
- [157] M. S. Pierce, C. R. Buechler, L. B. Sorensen, J. J. Turner, S. D. Kevan, E. A. Jagla, J. M. Deutsch, T. Mai, O. Narayan, J. E. Davies, K. Liu, J. H. Dunn, K. M. Chesnel, J. B. Kortright, O. Hellwig, and E. E. Fullerton, *Disorder-induced microscopic magnetic memory*, Phys. Rev. Lett. **94** (2005), no. 1, 017202 1–4.
- [158] M.S. Pierce, C.R. Buechler, L.B. Sorensen, S.D. Kevan, E.A. Jagla, J.M. Deutsch, T. Mai, O. Narayan, J.E. Davies, Kai Liu, G.T. Zimanyi, H.G. Katzgraber, O. Hellwig, E.E. Fullerton, P.Fischer, and J.B. Kortright, *Disorder-induced magnetic memory: Experiments and theories*, Accepted by Physical Review B 01/25/07, January 2007.
- [159] E. A. Jagla, *Numerical simulations of two-dimensional magnetic domain patterns*, Phys. Rev. E **70** (2004), no. 4, 046204 1–7.
- [160] E. A. Jagla, *Hysteresis loops of magnetic thin films with perpendicular anisotropy*, Phys. Rev. B **72** (2005), no. 9, 094406 1–6.
- [161] J. M. Deutsch, A. Dhar, and O. Narayan, *Return to return point memory*, Phys. Rev. Lett. **92** (2004), no. 22, 227203 1–4.
- [162] J. M. Deutsch and T. Mai, *Mechanism for nonequilibrium symmetry breaking and pattern formation in magnetic films*, Phys. Rev. E **72** (2005), no. 1, 016115 1–11.
- [163] J. M. Deutsch, T. Mai, and O. Narayan, *Hysteresis multicycles in nanomagnet arrays*, Phys. Rev. E **71** (2005), no. 2, 026120 1–7.
- [164] H. G. Katzgraber and G. T. Zimanyi, *Hysteretic memory effects in disordered magnets*, Phys. Rev. B **74** (2006), no. 2, 020405 1–4.
- [165] J. R. Petta, M. B. Weissman, and G. Durin, *Barkhausen pulse structure in an amorphous ferromagnet: Characterization by high-order spectra*, Phys. Rev. E **57** (1998), no. 6, 6363–6369.

- [166] S. Zapperi and G. Durin, *New perspectives for the Barkhausen effect*, Comput. Mater. Sci. **20** (2001), no. 3-4, 436–442.
- [167] D. Spasojevic, S. Bukvic, S. Milosevic, and H. E. Stanley, *Barkhausen noise: Elementary signals, power laws, and scaling relations*, Phys. Rev. E **54** (1996), no. 3, 2531–2546.
- [168] P. Kappenberger, S. Martin, Y. Pellmont, H. J. Hug, J. B. Kortright, O. Hellwig, and E. E. Fullerton, *Direct imaging and determination of the uncompensated spin density in exchange-biased CoO/(CoPt) multilayers*, Phys. Rev. Lett. **91** (2003), no. 26, 267202 1–4.
- [169] [http://en.wikipedia.org/wiki/Bootstrapping\\_\(statistics\)](http://en.wikipedia.org/wiki/Bootstrapping_(statistics))  
[http://en.wikipedia.org/wiki/Bootstrap\\_%28statistics%29](http://en.wikipedia.org/wiki/Bootstrap_%28statistics%29)  
[http://bcs.whfreeman.com/ips5e/content/cat\\_080/pdf/moore14.pdf](http://bcs.whfreeman.com/ips5e/content/cat_080/pdf/moore14.pdf)  
software (S-Plus):  
<http://www.insightful.com/Hesterberg/bootstrap/>  
<http://statwww.epfl.ch/davison/BMA/library.html>  
software (Excel sheet):  
<http://people.revoledu.com/kardi/tutorial/Bootstrap/examples.htm>.
- [170] B. Efron, *1977 Rietz lecture bootstrap methods: Another look at the jackknife*, Ann. Stat. **7** (1979), no. 1, 1–26.
- [171] B. Efron, *Nonparametric estimates of standard error: The jackknife, the bootstrap and other methods*, Biometrika **68** (1981), no. 3, 589–599.
- [172] B. D. Belle, F. Schedin, N. Pilet, T. V. Ashworth, E. W. Hill, P. W. Nutter, H. J. Hug, and J. J. Miles, *High resolution MFM study of e-beam lithography patterned Co/Pt nanodots*, J. Appl. Phys., in press, 2007.
- [173] D. Weller and A. Moser, *Thermal effect limits in ultrahigh-density magnetic recording*, IEEE Trans. Magn. **35** (1999), no. 6, 4423–4439.
- [174] R. M. H. New, R. F. W. Pease, and R. L. White, *Submicron patterning of thin cobalt films for magnetic storage*, J. Vac. Sci. Technol. B **12** (1994), no. 6, 3196–3201.
- [175] B. D. Terris and T. Thomson, *Nanofabricated and self-assembled magnetic structures as data storage media*, J. Phys. D: Appl. Phys. **38** (2005), no. 12, R199–R222.
- [176] H. J. Richter, A. Y. Dobin, R. T. Lynch, D. Weller, R. M. Brockie, O. Heinonen, K. Z. Gao, J. Xue, R. J. M. van der Veerdonk, P. Asselin,

- and M. F. Erden, *Recording potential of bit-patterned media*, Appl. Phys. Lett. **88** (2006), no. 22, 222512.
- [177] Z. Z. Bandic, E. A. Dobisz, T. W. Wu, and T. R. Albrecht, *Patterned magnetic media: impact of nanoscale patterning on hard disk drives*, Solid. State Technol. **1** (2006), S7.
- [178] B. D. Terris, T. Thomson, and G. Hu, *Patterned media for future magnetic data storage*, Microsyst. Technol. **13** (2007), no. 2, 189–196.
- [179] H. Sato and T. Homma, *Fabrication of magnetic nanodot arrays for patterned magnetic recording media*, J. Nanosci. Nanotechnol. **7** (2007), no. 1, 225–231.
- [180] C. J. Lin, G. L. Gorman, C. H. Lee, R. F. C. Farrow, E. E. Marinero, H. V. Do, H. Notarys, and C. J. Chien, *Magnetic and structural-properties of Co/Pt multilayers*, J. Magn. Mater. **93** (1991), 194–206.
- [181] M. Thielen, S. Kirsch, H. Weinforth, A. Carl, and E. F. Wassermann, *Magnetization reversal in nanostructured Co/Pt multilayer dots and films*, IEEE Trans. Magn. **34** (1998), no. 4, 1009–1011.
- [182] B. D. Terris, L. Folks, D. Weller, J. E. E. Baglin, A. J. Kellock, H. Rothuizen, and P. Vettiger, *Ion-beam patterning of magnetic films using stencil masks*, Appl. Phys. Lett. **75** (1999), no. 3, 403–405.
- [183] T. Devolder, C. Chappert, V. Mathet, H. Bernas, Y. Chen, J. P. Jamet, and J. Ferré, *Magnetization reversal in irradiation-fabricated nanostructures*, J. Appl. Phys. **87** (2000), no. 12, 8671–8681.
- [184] C. T. Rettner, M. E. Best, and B. D. Terris, *Patterning of granular magnetic media with a focused ion beam to produce single-domain islands at  $> 140$  Gbit/in<sup>2</sup>*, IEEE Trans. Magn. **37** (2001), no. 4, 1649–1651.
- [185] T. Aign, P. Meyer, S. Lemerle, J. P. Jamet, J. Ferré, V. Mathet, C. Chappert, J. Gierak, C. Vieu, F. Rousseaux, H. Launois, and H. Bernas, *Magnetization reversal in arrays of perpendicularly magnetized ultrathin dots coupled by dipolar interaction*, Phys. Rev. Lett. **81** (1998), no. 25, 5656–5659.
- [186] G. Hu, T. Thomson, M. Albrecht, M. E. Best, B. D. Terris, C. T. Rettner, S. Raoux, G. M. McClelland, and M. W. Hart, *Magnetic and recording properties of Co/Pd islands on prepatterned substrates*, J. Appl. Phys. **95** (2004), no. 11, 7013–7015.

- [187] L. Gao, S. H. Liou, M. Zheng, R. Skomski, M. L. Yan, D. J. Sellmyer, and N. I. Polushkin, *Magnetic force microscopy observations of the magnetic behavior in Co-C nanodot arrays*, J. Appl. Phys. **91** (2002), no. 10, 7311–7313.
- [188] G. Hu, T. Thomson, C. T. Rettner, and B. D. Terris, *Rotation and wall propagation in multidomain Co/Pd islands*, IEEE Trans. Magn. **41** (2005), no. 10, 3589–3591.
- [189] L. V. Melo and P. Brogueira, *Magnetic dynamic behavior of nanomagnets studied by magnetic force microscopy with external field*, Mater. Sci. Engineer. C **23** (2003), no. 6-8, 935–938.
- [190] S. A. Koch, R. H. T. Velde, G. Palasantzas, and J. T. M. De Hosson, *Magnetic versus structural properties of Co nanocluster thin films: A magnetic force microscopy study*, Appl. Phys. Lett. **84** (2004), no. 4, 556–558.
- [191] S. A. Koch, R. H. T. Velde, G. Palasantzas, and J. T. M. De Hosson, *Magnetic force microscopy on cobalt nanocluster films*, Appl. Surf. Sci. **226** (2004), no. 1-3, 185–190.
- [192] J. Bai, H. Takahoshi, H. Ito, H. Saito, and S. Ishio, *Dot-by-dot analysis of magnetization reversal in perpendicular patterned CoCrPt medium by using magnetic force microscopy*, J. Appl. Phys. **96** (2004), no. 2, 1133–1137.
- [193] G. Q. Li, H. Takahoshi, H. Ito, T. Washiya, H. Saito, S. Ishio, T. Shima, and K. Takanashi, *Mechanism of magnetization process of island-like  $L1_0$  FePt films*, J. Magn. Magn. Mater. **287** (2005), 219–223.
- [194] B. C. Choi, B. R. Pujada, Y. K. Hong, M. H. Park, H. Han, S. H. Gee, and G. W. Donohoe, *Micromagnetic domain structures and magnetization switching mechanism in submicrometer thin-film elements*, IEEE Trans. Magn. **41** (2005), no. 10, 3109–3111.
- [195] P. Eames and E. D. Dahlberg, *Characterization of domain states in sub-micron sized permalloy particles with perpendicular anisotropy*, J. Appl. Phys. **91** (2002), no. 10, 7986–7988.
- [196] X. B. Zhu, P. Grütter, V. Metlushko, Y. Hao, F. J. Castano, C. A. Ross, B. Ilic, and H. I. Smith, *Construction of hysteresis loops of single domain elements and coupled permalloy ring arrays by magnetic force microscopy*, J. Appl. Phys. **93** (2003), no. 10, 8540–8542.

- [197] H. J. Richter, A. Y. Dobin, O. Heinonen, K. Z. Gao, R. J. M. van der Veerdonk, R. T. Lynch, J. Xue, D. Weller, P. Asselin, M. F. Erden, and R. M. Brockie, *Recording on bit-patterned media at densities of 1 Tb/in<sup>2</sup> and beyond*, IEEE Trans. Magn. **42** (2006), no. 10, 2255–2260.
- [198] R. Murillo, M. H. Siekman, T. Bolhuis, L. Abelmann, and J. C. Lodder, *Thermal stability and switching field distribution of CoNi/Pt patterned media*, Microsyst. Technol. **13** (2007), no. 2, 177–180.
- [199] B. D. Terris, M. Albrecht, G. Hu, T. Thomson, and C. T. Rettner, *Recording and reversal properties of nanofabricated magnetic islands*, IEEE Trans. Magn. **41** (2005), no. 10, 2822–2827.
- [200] D. Suess, T. Schrefl, S. Fahler, M. Kirschner, G. Hrkac, F. Dorfbauer, and J. Fidler, *Exchange spring media for perpendicular recording*, Appl. Phys. Lett. **87** (2005), no. 1, 012504 1–3.
- [201] H. Arnold and G. W. Elmen, *Permalloy, an alloy of remarkable magnetic properties*, J. Franklin Inst. **195** (1923), 621–632.
- [202] E. P. Wohlfahrt, *Iron, cobalt and nickel*, Ferromagnetic Materials, vol. volume I, North-Holland Publishing Company, Holland, 1980.

## ACKNOWLEDGMENTS

The work presented in this thesis would not have been possible without the participation of many people in and outside the Institute of Physics at the University of Basel. Here, I would like to extend my warmer thanks to all these people.

Firstly, I address my sincere thanks to my thesis advisor, Prof Hans J. Hug for providing me with the opportunity to accomplish this fascinating thesis in his group. His everyday optimism and incredible dynamism were certainly helpful on many occasions. His vast knowledge of general physics and particularly in magnetism were most helpful throughout. Finally his precise way of thinking is certainly an excellent model to follow.

I would also like to warmly thank my co-advisor, Prof H.-J Güntherodt. He acted as an excellent supervisor by always taking a long term view of the projects, encouraging in the difficult moments and helping to find projects for the future.

I would like to also thank Prof G. Güntherodt for kindly accepting to be the external examiner for my thesis.

I wish to express my warmer thanks to my friend and colleague Dr. Tim Ashworth with whom I did all the measurements presented in this thesis. I profited greatly from his knowledge in surface physics. I would also like to thank him for his “english” way to be, always friendly. Specially the fact that his conception of a physics group is not limited to the lab but also includes a social life which contributed a lot to improve my stay in Basel.

I would like to thank Dr. Miguel Marioni for sharing his wide knowledge on all aspects of magnetism. The many discussions we had were always helpful.

In writing this thesis, I was greatly helped by the people reading through the draft of the dissertation. Prof Hans J Hug, Dr Tim Ashworth and Dr Laetitia Bernard have greatly improved the quality of this manuscript by suggesting numerous improvements. I thank them sincerely for the huge work they did on this final step.

I benefited a lot from the excellent skills of our technician, Yves Pellmont, who was always happy to help even when I made difficult requests. The lab was brightened up thanks to his permanent good mood.

This thesis is based on many external collaborations. The input from K. Zhang, M. Ciria, B. Belle and A. Moser in making the samples used in this thesis was most appreciated. Many thanks to Prof K. P. Lieb who opened the doors for me to the world of irradiation. His friendly encouragements were also gratefully received.

Although staying behind the scenes, the staff of the electronics and mechanical workshops, as well as administrative personnel provided me with efficient support. I am in particular grateful to Germaine Weaver and Audrey Fisher (administration), Sascha Martin (mechanical workshop) and Andi Tonin (electronics workshop).

I would also like to thank Dr. B. Hoogenboom who helped me in the early stage of my PhD and introduced me, among other things, to some helpful noise measurements. I also want to thank persons who help in different ways to realise this work: Dr. P. Kappenberger, Dr H. Katzgraber (for teaching me the Bootstrap method), Dr A. Drechsler, Prof. G. Tarrach and M. Romanelli (for helping me with the swissprobe instrument), Dr P. Reinman, Dr H. R. Hidber, D. Visan (compiler of the Buddha Bar music collections) and anyone else I may have forgotten.

Thanks to my family, who, despite their completely different orientation, encouraged me during this PhD project. Thanks for the trust you placed in me.

My final and also my biggest thanks are to Laetitia Bernard who supported me all along this project. Not only the many discussions we had to inspire me, but also that without her artistic ability most of the images in this thesis would certainly not look as good as they do. More generally the help she provides in the writing step is numerous. Last but not least, she endured the long working hours and the not always good mood involved in finishing this thesis. Thank you!



# APPENDIX





## MATHEMATICAL DEFINITION

This appendix presents some definitions of mathematical notations used in this thesis. In this thesis, vectors are denoted with an arrow ( $\vec{A}$ ) and the sign *nabla* ( $\vec{\nabla} = \left(\frac{\partial}{\partial x}, \frac{\partial}{\partial y}, \frac{\partial}{\partial z}\right)$ ) is used to describe divergence, gradient, laplacian, .... Finally, while scalar product is written as a dot ( $\cdot$ ) or omitted when the situation is clear enough ( $\vec{\nabla} \vec{A}$ ), the vectorial product is written as a cross ( $\times$ ). Since this thesis only uses cartesian coordinates, we define :  $\vec{A}(x, y, z) = (A_x, A_y, A_z)$  and a scalar  $\psi(x, y, z)$ .

- The Divergence (div):

$$\vec{\nabla} \cdot \vec{A} = \vec{\nabla} \vec{A} = \frac{\partial A_x}{\partial x} + \frac{\partial A_y}{\partial y} + \frac{\partial A_z}{\partial z}$$

- The Gradient (grad):

$$\vec{\nabla} \cdot \psi = \vec{\nabla} \psi = \left( \frac{\partial \psi}{\partial x}, \frac{\partial \psi}{\partial y}, \frac{\partial \psi}{\partial z} \right)$$

- The Curl:

$$\vec{\nabla} \times \vec{A} = \left( \frac{\partial A_z}{\partial y} - \frac{\partial A_y}{\partial z}, \frac{\partial A_x}{\partial z} - \frac{\partial A_z}{\partial x}, \frac{\partial A_y}{\partial x} - \frac{\partial A_x}{\partial y} \right)$$

- The Laplacian (div grad):

$$\vec{\nabla} \left( \vec{\nabla} \psi \right) = \vec{\nabla}^2 \psi = \nabla^2 \psi = \Delta \psi = \frac{\partial^2 \psi}{\partial x^2} + \frac{\partial^2 \psi}{\partial y^2} + \frac{\partial^2 \psi}{\partial z^2}$$





# MAGNETOCRYSTALLINE ANISOTROPY : SUPPLEMENTARY

Magnetocrystalline anisotropy in $10^3 \frac{J}{m^3}$	
R.C. O'Handley's book <sup>23</sup> [from J.J.M. Franse (1971) <sup>46</sup> ]	<i>RT</i> $K_1 = -4.5 \quad K_2 = -2.3$
	<i>4.2K</i> $K_1 = -1.2 \quad K_2 = 0.3$
P. Escudier thesis (1975) <sup>44</sup>	<i>RT</i> $K_1 = -5.5 \quad K_2 = -2.5 \quad K_3 = -0.03$
	<i>4.2K</i> $K_1 = -1.26 \quad K_2 = 0.58 \quad K_3 = 3.5$
K. Zhang thesis <sup>35</sup> [from Arnold (1923) <sup>201</sup> ] at 23°C	$K_1 = -4.5 \quad K_2 = -2.4$
P.J.A. van Schendel <sup>56</sup> [from Wohlfart book (1980) <sup>202</sup> ]	$K_1 = -5.5 \quad K_2 = -2.5$

**Tab. B.1:** Values of the magnetocrystalline energy coefficients of Nickel at different temperatures from various sources.





## MICROMAGNETICS OF DOMAIN WALLS

This appendix does not derive equation (1.23) as it was done by R.C. O’Handley in his book<sup>23</sup>(chap. 8.2). We present here the derivation of equation (3.1) from equation (1.23). First some trigonometric definitions and relations must be recalled :

$$\cos(A + B) = \cos(A) \cdot \cos(B) - \sin(A) \cdot \sin(B) \quad (\text{C.1})$$

$$\sin(\arctan(\alpha)) = \frac{\alpha}{\sqrt{1 + \alpha^2}} \quad (\text{C.2})$$

$$\cosh^2(\alpha) = 1 + \sinh^2(\alpha) \quad (\text{C.3})$$

$$\tanh(\alpha) = \frac{\sinh(\alpha)}{\cosh(\alpha)} \quad (\text{C.4})$$

$$1 - \tanh^2(\alpha) = \frac{1}{\cosh^2(\alpha)} \quad (\text{C.5})$$

The  $z$  component of the normalised magnetisation ( $\frac{M}{M_s}$ ) is given by  $m_z(y) = \cos(\varphi(y))$ . Given Eqn. (1.23) and Eqn. (C.1),

$$m_z(y) = \cos(\varphi(y)) = -\sin\left(\arctan\left[\sinh\left(\frac{\pi y}{\delta_{DW}}\right)\right]\right) \quad (\text{C.6})$$

$$\stackrel{(\text{C.2})}{=} -\frac{\sinh\left(\frac{\pi y}{\delta_{DW}}\right)}{\sqrt{1 + \sinh^2\left(\frac{\pi y}{\delta_{DW}}\right)}} \quad (\text{C.7})$$

$$\stackrel{(\text{C.3})}{=} -\frac{\sinh\left(\frac{\pi y}{\delta_{DW}}\right)}{\cosh\left(\frac{\pi y}{\delta_{DW}}\right)} \quad (\text{C.8})$$

$$\stackrel{(\text{C.4})}{=} -\tanh\left(\frac{\pi y}{\delta_{DW}}\right) \quad (\text{C.9})$$

Note that the negative sign is irrelevant since it just defines whether the magnetisation rotates from  $-1$  to  $1$  or vice-versa.

The  $x$  component of the normalised magnetisation being given by  $m_x(y) = \sin(\varphi(y))$ , we have that  $(m_x(y))^2 = 1 - (m_z(y))^2$ . Therefore, the normalised

component of the magnetisation in the  $x$  direction within the wall is given by

$$\int_{-\infty}^{\infty} m_x(y) \, dy = \int_{-\infty}^{\infty} \sqrt{1 - \tanh^2\left(\frac{\pi y}{\delta_{DW}}\right)} \, dy \quad (\text{C.10})$$

$$\text{Mathematica}^{\text{©}} \quad \delta_{DW} \quad (\text{C.11})$$





# HANDY HINTS FOR qMFM IN SXM

## D.1 Calibration

*Here we show how to compute, plot and save the calibration of a tip using the procedure described in section 2.2.3. Channel 1 must contain an image of a perpendicular sample exhibiting domains as small as possible with a well known saturation magnetisation and thickness.*

```
sxm_read,'D564.002',1,directory='C:\...\...\directory'
```

*We just read the data. Here the file name is “D564.002”. Using the option multi\_adc=1 reads the 1<sup>st</sup> channel of a Scanit<sup>©</sup> file. In the case of a Swissprobe<sup>©</sup> file, this is not necessary.*

```
rm_canting,1,2,12.00;
```

*The canting angle of the cantilever effect on the channel 1 is removed using the procedure described in section 2.2.3.*

```
rm_cal,2,3;
```

*The above line is a technical line related to the format of a sxm channel. In order to take into account the calibration indicated in the header directly in the dataset, one must use rm\_cal.\**

```
sxm_minmax,3,1
```

```
sxm_toplabel,3,'b'
```

*Before going further, it is good to have a look at the channel imported. The “minmax” function allows one to choose the plotted range. It is useful to avoid taking “bad pixels” into account in the plotted range.*

```
mfm_deconvolve,3,-1,4,40,0,0,6.0,0.0,0.0,0,1,[1e-5];
```

```
lp_lambda_filter_sp,4,4,20.0,0.05;
```

*To calculate a better discrimination pattern, it is always good to calculate the image closer, using the exponential dependence*

---

\* It is not the goal here to give a complete introduction to sxm programming. The reader who wants to learn more detail can refer to the sxm help (a .pdf file is available in the sxm installation folder). In addition it is strongly recommended to have a look at the structure of the file, and specially at the structure of the header (with the 3 calibration levels related by calibration factors which are, in the case of the z axis: voltage, pixel and frequency).

of the stray field versus the tip-sample distance as described in equation (2.19). The transitions are then sharper and the discrimination is thus easier. The high frequency noise will be very much amplified so that a low frequency pass filter needs to be applied. It is recommended to filter wavelengths smaller than 2-4 pixels. The filter here was applied on channel 4 itself, filtering every wavelength smaller than 20.0nm\* (exponential decay). As the filtering is done in the Fourier space, it is necessary to smooth out the edge (then the image may be infinitely repeated without sharp transition at the edge). Here the 5 pixels near the border were smoothed out. It is recommended to use the “\_sp” version of the filter specially when calibrating tip used with the Swissprobe<sup>©</sup> instrument;

```
lp_lambda_filter_sp,3,33,20.0,0.05;
```

Depending on the quality of the result (signal to noise ratio) it may be necessary to filter it. The filter should be as small has possible to not lose data (2-3 pixels). This must be done only when the calculation of the stray field diverges (the noise is amplified too much by the simulation). It is usually the case only with measurements taken far away from the sample. Note that it would be equivalent to filter the calibration channel (the whole calibration is a linear process), but the filter function is designed to be applied on a real space channel only.

```
sxm_toplabel,4,'c';
```

Please compare qualitatively and quantitatively the image before (3) and after (4) being going closer.

- `sxm_level,4,5,'c'`

```
image_5=(image_5*2-1);
```

A discrimination process is used in order to get the magnetisation pattern. Note that this is the only “free” parameter. The ratio of a demagnetised sample should be 50%. The magnetisation has to take value -1 and 1 whereas the `sxm_level` output values 0 and 1. The image of the channel 5 must thus be re-scaled

- `image_5(where(image_5 le 0))= -1;`  
`image_5(where(image_5 ge 0))= +1;`

In the case a special care was taken during the measurement to centre the frequency shift around “0”, a parameterless method can be used. All pixels showing a value in

---

\* One have to be really careful in SXM to always indicate non integer with a comma. Otherwise the channel may become integer, with truncated values.

the 'z' axis lower or equal than 0 will take the value -1 and all pixels showing a value greater or equal than 0 will take the value +1. Note that, this second way to do the discrimination is more reproducible. If the quality of the image is good enough, the frequency shift histogram of the image shows two peaks (corresponding to black and white domains). The frequency shift corresponding to the minimum between the two peaks can be taken instead of "0" to perform the discrimination. The histogram can be calculated using `sxm_histogram`.

```
image_5=image_5*660000;
```

Channel 5 has then to be multiplied by the saturation magnetisation to represent the magnetisation pattern. This value can be calculated or, even better measured by magnetometry (i.e. VSM)

```
sxm_toplabel,5,'d'
```

A look at the magnetisation pattern is always useful to check is everything is fine.

```
mfm_sim,5,-1,6,1,0,22.0,5.0,12.0,0;
```

This line is the key point. The `mfm_sim` routine uses Eqn. (2.17)-2.19 to calculate the sample stray field derivative from the magnetisation pattern. The parameter in order are:

- magnetisation pattern channel (input).
- parameter to tell the routine to not take any calibration function into account (a point monopole (= flat) calibration function is then used).
- the sample stray field derivative ( $\frac{d}{dz}H_z(\vec{k})$ ) channel (output).
- 1 selects z-derivative output.
- 0 for no coordinate transform.
- tip-sample distance to calculate the stray field at in nm.
- amplitude used for the measurement. Most of the time, if the amplitude was small enough, the zero amplitude approximation works fine.
- the sample thickness in nm (negative values means an infinite sample thickness).
- domain wall width in nm (can be calculated from equation (1.21)) if the wall width is unknown, a value of 0 should be used.

```
sxm_toplabel,6,'e';
```

*Look at the sample stray field z-derivative*

```
turkey_window,6,6,0.05;
```

*As explained above, before working in Fourier space, one must smooth out the edge of the image. turkey\_window is used to do this. The parameter 0.05 is fine for a 512 pixels image. However one can play a bit with this parameter if undesirable noise (regular low frequency line horizontal and vertical) appear while using the ICF to simulate an image.*

- turkey\_window,3,3,0.05;

```
sxm_fft,3,8,-1;
```

*If an unfiltered channel is used to get the calibration, it may be needed to smooth out the edges.*

- sxm\_fft,33,8,-1;

*If a slightly filtered channel is use to get the calibration, no additional modification is needed.*

```
sxm_fft,6,7,-1;
```

```
sxm_copy ,8,9;
```

```
image_9=image_8/image_7;
```

*As explained in section 2.2.3 the measurement is divided by the sample stray field z-derivative in Fourier space to get the ICF in the channel 9. Note that before performing the division, one must define the channel nine (mostly the size and the header) by copying either the channel 7 or 8 in channel 9*

```
image_9(0,0)=complex(0.0,0.0);
```

*This is a technical line to fix a bug at the point (0,0). Another way to fix it is to copy the point (0,1) at the position (0,0) :*  

```
image_9(0,0)=image_9(0,1)
```

```
sxm_fft,9,19,1;
```

```
image_19=shift(image_19,256,256);
```

```
sxm_toplabel,19,'g';
```

*The ICF channel cannot be directly plotted since it is complex. To have a look at it one has to do an inverse Fourier transform (same command but with parameter 1 instead of -1) and to shift the image by half the image size (because of the Fourier transform definition in SXM).*

```
sxm_copy,9,20;
```

- image\_20=shift(image\_9,256,256);

```
circ_mean_ampl,20,21;
```

- `circ_mean_ampl_k,20,21,zoom=3,shiftxy=[256,256];`

*A good way to represent the ICF (and to compare two different tips for example) is to perform a centre circular average of the complex channel. This can be done in either of the ways presented above. The second way have the advantage to allow the choice of a zoom, giving more points to plot a 1-D graph in an other software, without modifying directly the routine. However, this second routine calculates values of “x” meaningless. One have to recalculate the “x” axis using the following : The smallest wavelength one can see in an image is two pixels and the biggest is twice the image size. Doing that and plotting the graph in Igor<sup>©</sup> needs something like the following code :*

- `duplicate avgzoomx avgzoomcorr`
- `avgzoomcorr=avgzoomcorr/0.983277`
- `AppendToTable avgzoomcorr`
- `avgzoomcorr =avgzoomcorr*127`
- `avgzoomcorr=avgzoomcorr+1`
- `duplicate avgzoomcorr x avgzoomcorr k`
- `avgzoomcorr=(2*pi*avgzoomcorr*2)/(2*5000)`
- `duplicate avgzoomcorr k avgzoomcorr l`
- `avgzoomcorr l=(2*pi)/avgzoomcorr k`
- `display avgzoomy vs avgzoomcorr k`
- `appendtograph/T avgzoomy vs avgzoomcorr l`
- `modifygraph log=1;delayupdate`
- `setaxis/A/R top`
- `modifygraph mirror(left)=1`
- `SetAxis bottom 0.00251327,0.160849 ;DelayUpdate`
- `SetAxis/R top 2500,39.0625`
- `Label bottom "\ F'Times New Roman'k[1/nm]"`
- `Label top "\ F'Symbol'l\ F'Times New Roman'[nm]"`
- `Label left "| \ F'Symbol's\ \ F'Times New Roman'\ \ Btip\ \ M(k)[Am]"`

`sxm_lineview,21,'j',gauging_level=0;`

*A 1-D graph can be plotted in SXM. However a better plot is given by a log-log scale and this is easier to do with another software.*

```
sxm_write_ascii,21,'C:\...\directory\ICF.dat';
sxm_write_tiff,'j','C:\...\directory\ICF.tiff';
```

*The ascii as well as the tiff files can be saved*

```
sxm_fft,9,30,1;
sxm_write,30,'ICF.sxm',directory='F:\...\directory\';
```

*In order to use this ICF in the future to simulate an other image, it is good to save it in SXM format. However SXM can not save a complex channel. Therefore one have to inverse Fourier transform the channel before saving*

```
mfm_sim,5,9,10,1,0,z,a,12.0,0; sxm_toplabel,10,'g';;
```

*To feel confident about the ICF calculated, it is good to simulate the same image using the magnetisation pattern and the ICF. If the contrast and the qualitative aspect are not similar to the measurement, check the routine and try again  $\square$ . In a certain aspect this can show if the ICF is noisy (due to noise in the original measurement or due to an inappropriate turkey\_window)*

## D.2 Simulation

*This section shows how to use the tip calibration obtained in section D.1 in the channel 9 and exported as “D564.sxm” to simulate an MFM image at a certain average distance from the surface of a perpendicular magnetised sample with a well known magnetisation pattern, saturation magnetisation ( $M \frac{\text{A}}{\text{m}}$ ) and thickness (d nm). That can be used to estimate the frequency shift expected for a certain experiment to check whether the instrument is sensitive enough. That can also be used to test the hypothesis of a perpendicular magnetised sample (c.f. Chap. 3).*

```
M=660000.0;
```

```
d=12.0;
```

*The two parameters know of the sample to simulate are put in memory*

```
sxm_read, 'xxx.mag_norm',5, directory='C:\...\directory';
```

*The magnetisation pattern normalised ( $-1 \rightarrow 1$  or  $0 \rightarrow 1$  depending of the experiment) is read. The way to produce it is explain in section D.1. This corresponds to channel 5 before the multiplication by M.*

```

sxm_toplabel,5,'e';
image_5=image_5*M;
    The magnetisation can be plotted and then multiplied by the
    sample saturation magnetisation
sxm_read, 'ICF.sxm',8, directory='C:\...\directory\'
sxm_fft,8,9,-1;
    The calibration function is read into channel 8. It has to be
    transformed back into Fourier space.
mfmsim,5,9,10,1,0,30.0,0.0,d,0;
    The simulation routine is used from the magnetisation pattern
    (5) to the output channel (10) using the calibration function
    (9). The image is simulated for an average tip-sample distance
    of 30 nm, with a zero approximation amplitude of the cantilever
    using the known sample thickness d. If the domain wall size is
    known, it can be enter into the simulation in the last parameter
    (in nm)
sxm_minmax,10,1;
sxm_toplabel,10,'f';
    The result is plotted

```

## D.3 Tip Field

*Here will be described how to calculate the tip field from the instrument calibration function as described in section 2.2.3. Lets begin with the “ICF” channel coming from section D.1 in channel 20.*

```

sxm_copy,20,30
    To not interact with previous work, we copy channel 20 to chan-
    nel 30
image_30=conj(image_30)
    As we apply the equation (2.29) we have to the complex conju-
    gate (it have to be done in Fourier space).
sxm_fft,30,30,1
    We go back in real space.
image_30=image_30*(-2*0.032)/(16500.0*4.0*!pi*1e-7)
    We multiply by the factor  $-\frac{2c_L}{\mu_0 f_0}$  from equation (2.29). Here
     $c_L = 0.032 \text{ N/m}$  and  $f_0 = 16500 \text{ Hz}$  ( $\mu_0 = 4 \cdot \pi \cdot 10^{-7}$ ).
sxm_copy,30,31
image_31=shift(image_30,128,128)
    Due to the fourier transform definition in SXM©, one have to
    shift the image by half the image size (in pixel) in order to have

```

*the high frequencies in the middle of the image.*

```
image_31=image_31/(5.0e-6)^2
```

*We wish first to calculate a tip-equivalent surface charge pattern, with the surface charges located in a plane at the apex of the tip, parallel to the sample. Therefore one has to divide the channel by the picture area, in that case  $(5 \cdot 10^{-6})^2 \text{ m}^2$ . At that step, channel 31 contains  $\sigma_{m,tip}$  (the tip transfer function)*

```
image_31=(-0.5)*image_31
```

*To have the stray field of the tip (from the tip equivalent surface charge pattern) equation (2.30) must be used. In that case, we just calculate the  $z$  component in a plane at the apex of the tip and the equation is simplify to  $H_{z,tip}(z = z') = -1/2\sigma_{m,tip}(\vec{k})$ .*

```
image_31=image_31*4*!pi*1e-7
```

*It goes without saying that the channel being in  $\frac{\text{\AA}}{\text{m}}$  one have to multiply by  $\mu_0$  to have the stray field in tesla.*

```
lp_lambda_filter_sp,31,32,80.0,0.0
```

*Depending how noisy the image is (mainly depending how many images were averaged to get the ICF), one has to filter the channel. Here all frequencies smaller than 80nm (4 pixels) were filtered ( $\frac{5000}{256} \cdot 4 \approx 80 \text{ nm}$ ).*

```
sxm_toplabel,32,'b'
```

```
sxm_line,32,34,128,0
```

*A line profile can be extracted at position  $y=128$  in the direction  $x$ .*

```
sxm_lineview,34,'t'
```

*That line can be shown.*

```
***action from menu***
```

```
;from menu, do 3D-plot channel 32 (in e)
```

*The two above lines are just comments as the “;” is used. They are here to tell that, in order to get a 3D plot of the channel 32 in the window “e”, one has to select fom the menu.*

```
sxm_write,31,'C:\...\tip_field.sxm'
```

```
sxm_write,32,'C:\...\tip_field_filtered.sxm'
```

*Filtered and non-filtered SXM<sup>©</sup> channels are written in a chosen directory.*

```
sxm_write_ascii,34,'C:\...\tip_field_filtered_1D.dat'
```

*The 1D line profile is saved in a data format to be used by standard programs (Igor<sup>©</sup>, Origin<sup>©</sup>)*

```
sxm_write_tiff,'b','C:\...\tip_field_filtered_2D.tif'
```

```
sxm_write_tiff,'e','C:\...\tip_field_filtered_3D.tif'
```

*The 2D and 3D plot are saved as tiff files (grayscale 256 levels). Be careful that the actual window is saved. Namely, if the*



*window was resized to fit the screen, the saved file won't be full resolution. The only solution to overcome this limitation is to increase the screen resolution before starting PW-WAVE<sup>©</sup> (to get a reasonable 3D plot, one can use 1600x1200). The other solution in the case of a 2D plot is to use the procedure to write a 2D channel in Jef Poskanzer's "PGM" format for grayscale image, as shown in the next line.*

```
(sxm_write_pgm,channel,'C:\...\tip_field_2D.pgm')
```





## MAGNETOMETRY DATA ON Ni/SiO<sub>2</sub>/Si(100)

As presented in figure E.1, hysteresis curves have been measured by VSM at room temperature and at 8.3 K for 75 nm and 185 nm thick nickel films.

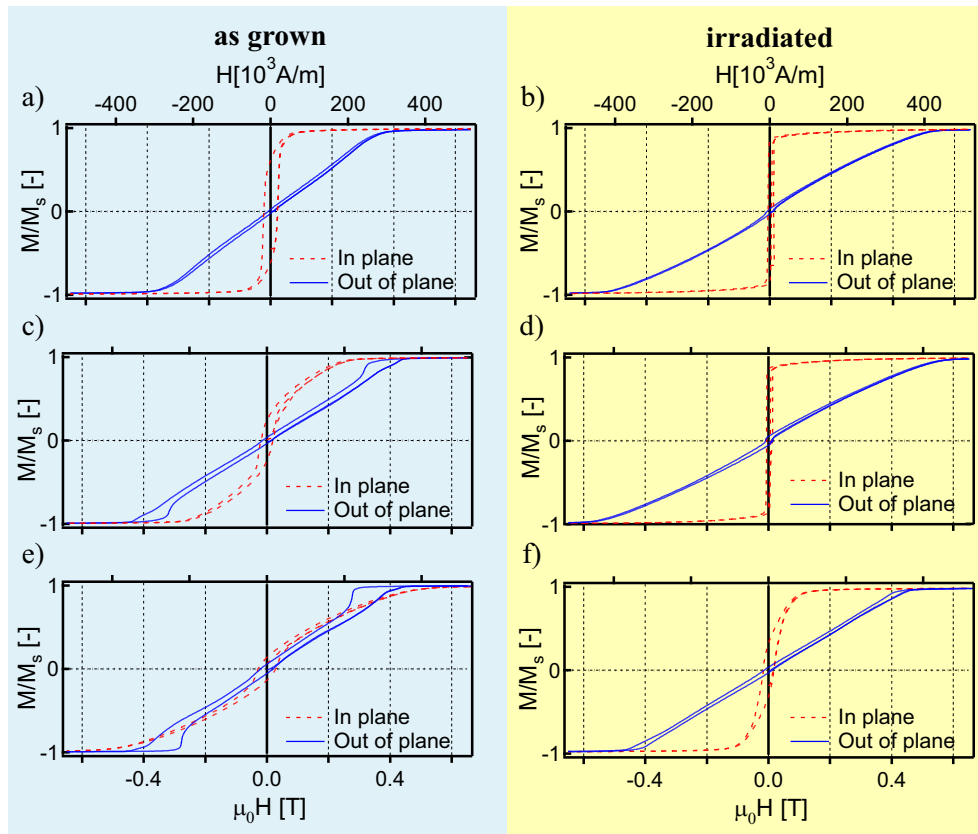


**Fig. E.1:** a)-d): Hysteresis loops measured at room temperature for the 70 nm thick nickel film (a)-b)) and the 185 nm thick nickel film (c)-d)). e)-f): Hysteresis loops for the 185 nm thick nickel film measured at 8.3 K.





## RPM AND CPM INFLUENCED BY FIELD COOLING

In order to investigate the origin of the difference between RPM and CPM values, we have recently performed further experiments where the ratio of  $\frac{\text{CPM}}{\text{RPM}}$  was compared for zero field and field-cooled samples. However the data is not yet fully analysed at the time of completion of this thesis. In this appendix are only reported raw counts for zero (Tab. F.3), positive (Tab. F.2) and negative (Tab. F.1) cooling field. The field cooled samples showed considerably more locations that have RPM but no CPM.

25/108 intermittent nucleation centres for $H > 0$			
23/109 intermittent nucleation centres for $H < 0$			
7 centres nucleating only for positive field			
8 centres nucleating only for negative field			
Point	Counts	$P_{\text{occur}}$	$\sigma_{P_{\text{occur}}}$
Positive			
1	111111111010001	0.73	0.11
2	110001100101111	0.60	0.13
3	111111111111111	1.00	0.00
4	111111110111111	0.93	0.06
5	111111111111111	1.00	0.00
6	000011101111111	0.67	0.12
7	111111111111111	1.00	0.00
Negative			
8	101110101111111	0.80	0.10
9	111111111111111	1.00	0.00
10	000001100001001	0.27	0.12
11	000001100101001	0.33	0.12
12	111111111111111	1.00	0.00
13	010000100100000	0.20	0.10
14	010000000000000	0.07	0.06
15	111111111111111	1.00	0.00

**Tab. F.1:** Counts and occurrence for intermittent nucleation centres in the Nickel film cooled in  $\mu_0 H = -2$  T.

23/120 intermittent nucleation centres for $H > 0$			
21/119 intermittent nucleation centres for $H < 0$			
6 centres nucleating only for positive field			
5 centres nucleating only for negative field			
Point	Counts	$P_{\text{occur}}$	$\sigma_{P_{\text{occur}}}$
Positive			
1	111111100101100	0.67	0.12
2	111111111011011	0.87	0.09
3	111101111111111	0.93	0.06
4	000000011000000	0.13	0.09
5	000000010000000	0.07	0.06
6	000101100111111	0.60	0.13
Negative			
7	101011010001000	0.40	0.13
8	000011000100000	0.20	0.10
9	000010000000000	0.07	0.06
10	000000010000000	0.07	0.06
11	111111111111111	1.00	0.00

**Tab. F.2:** Counts and occurrence for intermittent nucleation centres in the Nickel film cooled in  $\mu_0 H = +2$  T.

17/110 intermittent nucleation centres for $H > 0$			
16/110 intermittent nucleation centres for $H < 0$			
3 centres nucleating only for positive field			
3 centres nucleating only for negative field			
Point	Counts	$P_{\text{occur}}$	$\sigma_{P_{\text{occur}}}$
Positive			
1	01000000	0.13	0.11
2	01101011	0.62	0.16
3	01101011	0.62	0.16
Negative			
4	111111001	0.78	0.14
5	111100111	0.78	0.14
6	000000001	0.11	0.10

**Tab. F.3:** Counts and occurrence for intermittent nucleation centres in the Nickel film cooled in zero field.



## COMPLEMENTARY IMAGES TAKEN ON NANODOTS

Some of the images taken on 100 nm (Fig. [G.1](#)) and 50 nm (Fig. [G.2](#)) nanodots are presented here. These images are used to calculate the hysteresis and switching field distribution presented in chapter 7 (Fig. [7.5](#)).

A careful look reveals that the switching of a nanodot sometime happens in two steps. Some further study needs to be done in order to reveal if this is evidence of domain wall motion or if it is consistent with magnetisation rotation.

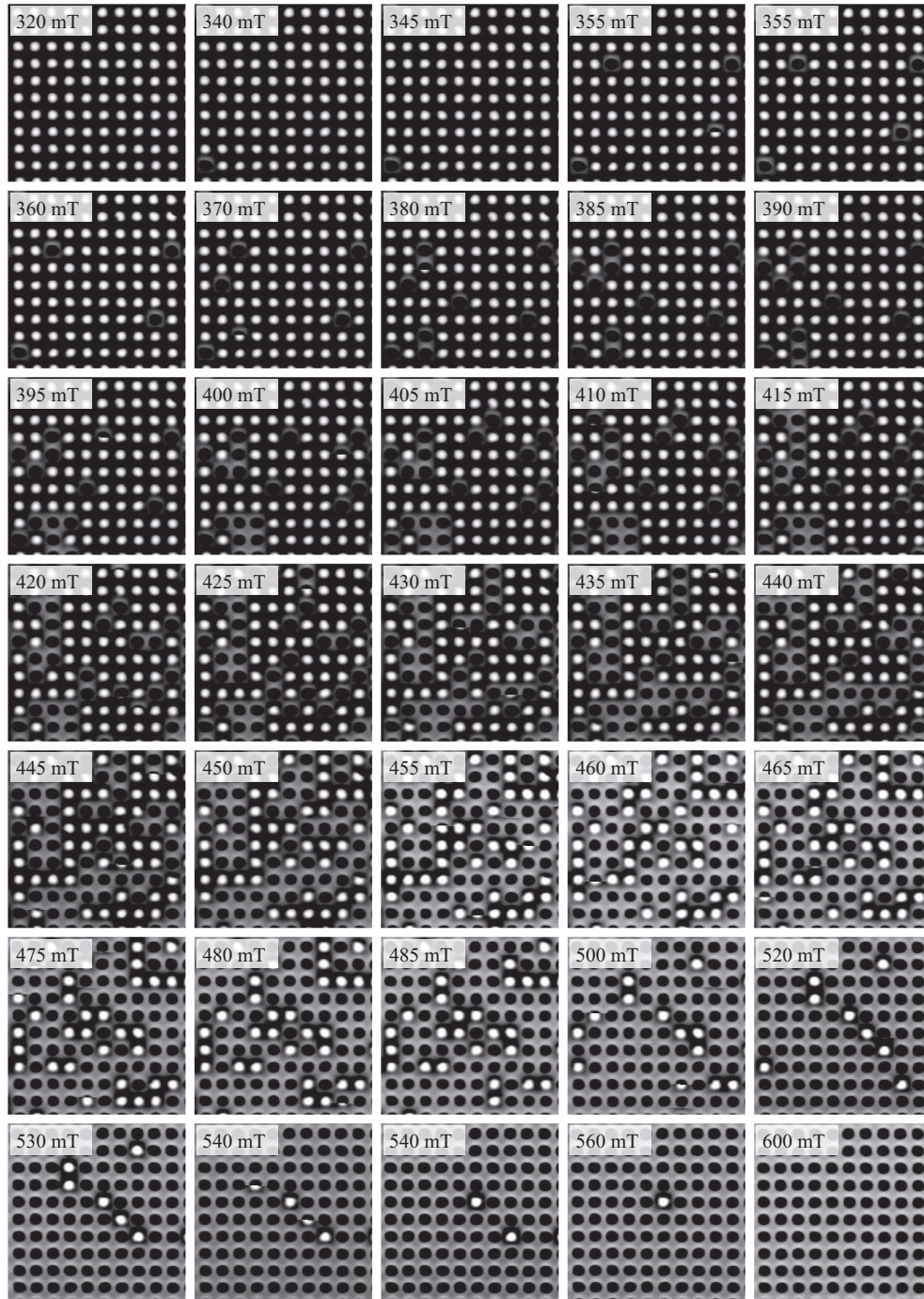


**Fig. G.1:** 100 nm nanodot array  $2 \times 2 \mu\text{m}^2$  MFM images at various field.



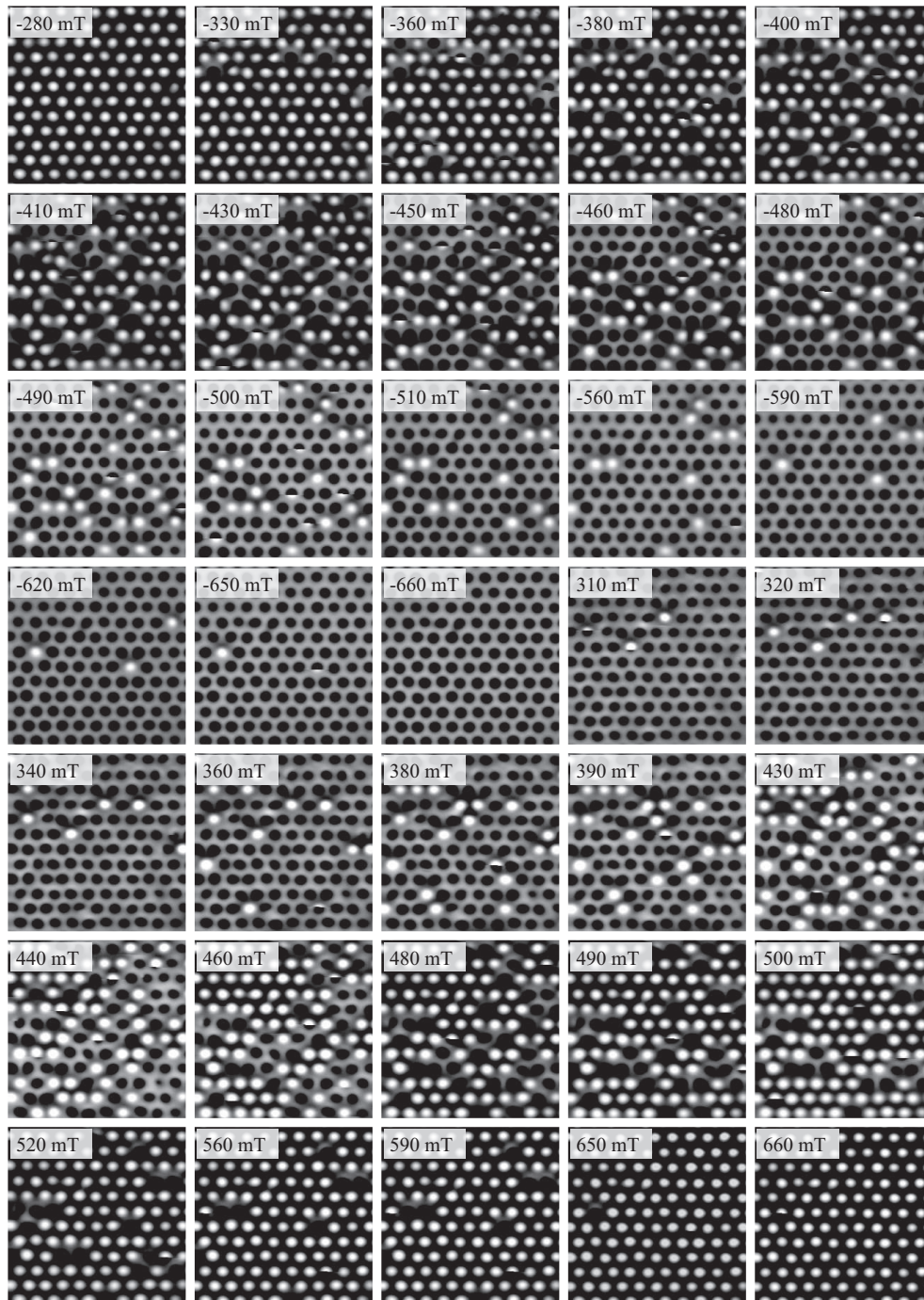


**Fig. G.2:** 50 nm nanodot array  $1 \times 1 \mu\text{m}^2$  MFM images at various field



# PUBLICATION AND PRESENTATION LIST

## Publications

- Ruihua Cheng, C.N. Borca, N. Pilet, Bo Xu, L. Yuan, B. Doudin, S.H. Liou, and P.A. Dowben, *Oxidation of metals at the chromium oxide interface*, Appl. Phys. Lett. **81** (2002), no. 11, 2109–2111.
- N. Pilet, C. Borca, A. Sokolov, E. Ovtchenkov, Bo Xu, and B. Doudin, *Interface composition and electronic properties of chromium (III, IV) oxides junctions*, Mater. Lett. **58** (2004), no. 14, 2016–2018.
- M.A. Marioni, N. Pilet, T.V. Ashworth, R.C. O’Handley, and H.J. Hug, *Remanence due to wall magnetisation and counterintuitive magnetometry data in 200 nm films of Ni*, Phys. Rev. Lett. **97** (2006), 027201 1–4.
- N. Pilet, T. V. Ashworth, M.A. Marioni, H.J. Hug, K. Zhang, and K.P. Lieb, *Effect of ion irradiation on domain nucleation and wall motion in Ni films*, J. Magn. Mater., in press (2006).
- K. Zhang, K.P. Lieb, D.G. Merkel, M. Uhrmacher, N. Pilet, T.V. Ashworth, , and H.J. Hug, *Ion-induced magnetic texturing of ni films: Domain structure and strain*, Nucl. Instr. Meth. B, in press (2006).
- B.D. Belle, F. Schedin, N. Pilet, T.V. Ashworth, E.W. Hill, P.W. Nutter, H.J. Hug, and J.J. Miles, *High resolution MFM study of e-beam lithography patterned Co/Pt nanodots*, J. Appl. Phys., in press, 2007.
- N. Pilet, T.V. Ashworth, M.A. Marioni, H.J. Hug, K. Zhang, and K.P. Lieb, *Microstructural and magnetic effects of Xe- and Ni-irradiation of Ni(70 nm)/Glass/Si(100) thin films*, in preparation, 2007.
- K. Zhang, K.P. Lieb, N. Pilet, T.V. Ashworth, M.A. Marioni, and H.J. Hug, *Microstructural and magnetic properties of thermally mixed Ni/Si layers*, in preparation, 2007.
- N. Pilet, T.V. Ashworth, M.A. Marioni, H.G. Katzgraber and H.J. Hug *Return Point Memory and Complementary Point Memory Presented in Real Space by in field MFM*, in preparation, 2007.

## Presentations

### ORAL

- N. Pilet, C. Borca, A. Sokolov, E. Ovtchenkov, P. A. Dowben and B. Doudin, *Interface composition and electronic properties of chromium oxide junctions*, European Materials Research Society (E-MRS), Strasbourg, **2002**
- N. Pilet, T. V. Ashworth, M. A. Marioni, H. J. Hug, K. Zhang, and K. P. Lieb, *An MFM Study of Perpendicular Magnetic Anisotropy in Nickel Films*, International Conference of Nanoscience and Technology (ICN+T), Basel, **2006**
- N. Pilet, T. V. Ashworth, M. A. Marioni, H. G. Katzgraber and H. J. Hug, *The Importance of Magnetic Memory: A Study of Microscopic Return Point Memory*, Swiss Physical Society (SPS) Annual Meeting, Zürich, **2007**
- N. Pilet (invited), *The Relation Between Magnetic Hysteresis and the Micromagnetic State Explored by Quantitative Magnetic Force Microscopy*, séminaire IPCMS / GEMME, Strasbourg, **2007**

### POSTER

- N. Pilet, T. V. Ashworth, M. A. Marioni, H. J. Hug, K. Zhang, and K. P. Lieb, *Quantitative MFM study of the role of strain in Ni films at room and low temperature*, NCCR Nanoscale Science Annual Meeting, Gwatt, **2005**
- N. Pilet, T. V. Ashworth, M. A. Marioni, H. J. Hug, K. Zhang, and K. P. Lieb, *The Micromagnetic Structure of Ni Films Modified by Ion Irradiation*, Swiss Physical Society (SPS) Annual Meeting, Lausanne, **2005**
- M. A. Marioni, N. Pilet, T. V. Ashworth, R. C. O'Handley, and H. J. Hug, *A quantitative MFM and VSM investigation of remanence due to wall magnetisation in capped nickel films*, Joint European Magnetic Symposia (JEMS), San Sebastian, **2006**
- N. Pilet, T. V. Ashworth, M. A. Marioni, H. J. Hug, K. Zhang, and K. P. Lieb, *The Micromagnetic Structure of Ni Films Modified by Ion Irradiation*, Joint European Magnetic Symposia (JEMS), San Sebastian, **2006**

# CURRICULUM VITAE

## Personal Data

---

Name	Nicolas Pilet
Nationality	Swiss, French
Place of birth	Montreux, Vaud, Switzerland
Date of birth	January 19 <sup>th</sup> 1977

## Education

---

2006	<b>Ph.D. in Physics</b> , University of Basel, Switzerland. Dissertation: <i>Micromagnetic study of Nickel films by MFM</i> , Superior: Prof. Dr. Hans Josef Hug, best distinction (Summa cum Laude).
2002	<b>Master of Science in Physics</b> , carried out at University of NE-Lincoln, Nebraska, USA, awarded by EPFL, Switzerland. Thesis: <i>Chromium oxide junction synthesis and electronic properties study</i> , Directed by Prof. Dr. Bernard Doudin and advised by Prof. Dr. Jean-Philippe Ansermet, Highest mark.
2002	<b>Bachelor of Science in Physics and Engineering (Phys. Dipl. EPF)</b> , Federal Polytechnical School of Lausanne (EPFL), Switzerland. Thesis: <i>Study of the Seebeck effect on Ni and multilayer Co-Cu nanowires under the influence of a magnetic field</i> , Advisor: Prof. Dr. Jean-Philippe Ansermet.
1996	<b>Baccalaureate in Mathematics and Sciences</b> , High School of Burier (CESSEV), Switzerland.

Research Experience

---

- 2003 – 2006 **Doctoral research**, University of Basel, Switzerland. *Scanning force microscopy measurements*: True non-contact atomic force microscopy (ncAFM) on Si and KBr. ncAFM on adamantane molecules deposited on gold. *Magnetic force microscopy measurements* Magnetic force microscopy (MFM) to study micromagnetic properties of Ni films. Study of Mn<sub>12</sub> Molecules by MFM. Investigation of hysteresis dependence versus shape of Co/Pt nanodots by tapping AFM and MFM. *Data analysis*: Quantitative analysis in fourier space of MFM measurements using SXM shell on PV-WAVE software. *Technical lab experience* Extensive use of ultra high vacuum chamber and liquid He cryostat. Use of optical fiber interferometer system, including laser replacement and installing a polarization maintaining fiber. Sensitive manipulation on cantilevers (CL) including ex-situ mounting of CL to micron accuracy. *Related Abilities* Development on new SXM and Labview programs.
- 2001 – 2002 **Master research**, University of NE-Lincoln, USA. Fabrication and characterization of spin-polarized electron transport in magnetic tunnel junctions based on CrO<sub>2</sub>/CrO<sub>3</sub> materials. *Fabrication* of magnetic junctions, involving wafer processing techniques, UV-lithography, metal sputtering and evaporation, electrodeposition, controlled oxidation and imaging by contact AFM. *Oxidation study* of the F/I/F junctions by X-ray photoelectron spectroscopy and angle-resolved inverse photoelectron spectroscopy. *Electrical transport and magnetic measurement* at variable temperature (1.5 K to RT).
- 2000 – 2001 **Diploma research**, EPFL, Switzerland. Study of heat and spin transport phenomena in metallic nanowires. Magnetic characterization by means of low-temperature systems. *Development* of a new setup for thermoelectric measurements with an applied magnetic field. *Study of the thermoelectric effect* and its influence on the magnetoresistance of the magnetic nanowires.
- 2000 **Internship in the company Tetra Pak**, Romont, Switzerland. *IR detection method in plasma physics* : Set-up and optimization of a CO<sub>2</sub> detector working inside an Oxygen plasma and based on infra-red absorption. Control of the CO<sub>2</sub> rate in the plasma.

Teaching Experience

---

- 2003 – 2006 Practical classes for students from Physics, Informatics and Nanosciences Departments
- 2002 Employment as "scientific collaborator" for a teaching program, physics department, EPFL : Production of a scientific manual, accurately describing the experiments and demonstrations presented to the students during physics lectures, designed for students use, as well as professors use.
- 1999 – 2001 General physics and Optics exercises teaching for 1<sup>st</sup> and 2<sup>nd</sup> year EPFL students from Physics and Informatics Departments.
- 1993 – 2001 Various physics and mathematics private lessons for various educational levels (from school to 2<sup>nd</sup> year university).







This work has been financed by the Swiss National Science Foundation (SNF) and the National Centre of Competence in Research (NCCR). Financial support for the printing of this thesis was provided by the University of Basel.



